

Characterization of microstructure in aluminum alloys based on electron backscatter diffraction

Der Fakultät Maschinenbau
der Technischen Universität Dortmund
zur Erlangung des Grades eines
Doktor-Ingenieurs
(Dr.-Ing.)
genehmigte Dissertation

von

Tobias Kayser

Dortmund 2011

Contents

Abbreviations	iv
Abstract	vii
1 Introduction	1
1.1 Influences of microstructure on material behavior	1
1.2 Aluminum in the field of engineering	5
1.2.1 Production of aluminum	5
1.2.2 Aluminum alloys	6
1.2.3 Strengthening of aluminum alloys	8
1.3 Crystal structures of metals	12
1.3.1 Crystal lattice types	12
1.3.2 Crystal orientations and symmetry	14
1.4 Dislocations and grain boundaries	21
1.5 Processes of grain microstructure evolution	26
1.5.1 Dynamic and static recovery	28
1.5.2 Static recrystallization	30
1.5.3 Dynamic recrystallization	31
1.6 Measurement techniques for grain microstructure characterization	33
1.6.1 Light optical microscopy	33
1.6.2 X-ray diffraction	34
1.6.3 Scanning electron microscopy	35
1.6.4 Electron Backscatter Diffraction	36
2 Software development	41
2.1 Discussion of existing EBSD software	41
2.1.1 OIM - Orientation Imaging Microscopy	41
2.1.2 MTEX - A Matlab Toolbox for Quantitative Texture Analysis	42
2.2 Microstructure plotter and analyzer Grainplot	42
2.2.1 Programming motivation	42
2.2.2 Microstructure visualization	43
2.2.3 Microstructure statistics	56
2.2.4 Verification	64

2.3	Synthetic microstructures	70
2.3.1	Synthetic microstructure generator Graingen	71
2.3.2	Generated synthetic microstructures	72
3	Experimental results and material characterization	77
3.1	Selection of aluminum alloys	77
3.2	Direct hot extrusion experiment	78
3.3	Sample preparation	81
3.3.1	Light optical microscopy	81
3.3.2	Electron Backscatter Diffraction	81
3.3.3	Scanning electron microscopy	82
3.4	Characterization of EN AW-6060	82
3.4.1	Deformation zones and mesoscopic microstructure development	82
3.4.2	EBSD measurements in different deformation zones	85
3.4.3	Microstructure evolution along middle axis	88
3.4.4	Microstructure statistics	92
3.5	Characterization of EN AW-6082	97
3.5.1	Deformation zones and mesoscopic microstructure development	97
3.5.2	EBSD measurements in different deformation zones	99
3.5.3	Microstructure statistics	102
3.6	Characterization of EN AW-7075	105
3.6.1	Deformation zones and mesoscopic microstructure development	105
3.6.2	EBSD measurements in different deformation zones	107
3.6.3	Microstructure statistics	108
3.7	Precipitations in partly extruded billets	114
4	Summary and outlook	117
A	Grain size histograms of all measurement points	122
A.1	EN AW-6060	123
A.2	EN AW-6082	126
A.3	EN AW-7075	128
B	Misorientation histograms of all measurement points	130
B.1	EN AW-6060	131
B.2	EN AW-6082	133
B.3	EN AW-7075	134
C	Discrete inverse pole figures of all measurement points	135

<i>Contents</i>	iii
C.1 EN AW-6060	135
C.2 EN AW-6082	138
C.3 EN AW-7075	140
References	143
Acknowledgements	151
Curriculum Vitae	153

List of Abbreviations

abbreviation	full designation
2-D	two dimensional
3-D	three dimensional
APF	atomic packing factor
BCC	body-centered cubic
BSE	backscattered electron
CDX	continuous dynamic recrystallization
CI	confidence index
CSL	coincidence site lattice
DMZ	dead material zone
DRV	dynamic recovery
DRX	discontinuous dynamic recrystallization
EBSD	electron backscatter diffraction
ECD	equivalent circle diameter
FCC	face-centered cubic
FE	finite element
FIB	focused ion beam
GBE	grain boundary engineering
GDX	geometric dynamic recrystallization
GNB	geometric nessecary boundary
GND	geometrically necessary dislocation
HAGB	high-angle grain boundary
HCP	hexagonal close-packed
IDB	incidental grain boundary
IPF	inverse pole figure
LAGB	low-angle grain boundary
LOM	light optical microscopy
MFZ	material flow zone

abbreviation	full designation
ODF	orientation density function
OIM A TM	orientation imaging microscopy – analysis tool
OIM DC TM	orientation imaging microscopy – data collection tool
PCG	peripheral coarse grains
RVE	representative volume element
SEM	scanning electron microscopy
SFE	stacking fault energy
SIZ	shear intensive zone
SRV	static recovery
SRX	static recrystallization
SSD	statistically stored dislocation
TEM	transmission electron microscopy
XDF	X-ray diffraction

Abstract

During the last decades, aluminum has been established as a common construction material especially in the fields of transportation, aircraft and light weight construction. In order to effect an economic efficiency in material and energy, not only the construction methods are continuously improved but also the material properties are adjusted according to the intended purpose. This includes the development of new alloy compositions and furthermore a controlled microstructure evolution inside the material. A large number of aluminum alloys facilitates a significant increase in strength by precipitation hardening. Through the techniques of grain boundary engineering the material's grain sizes as well as the type and distribution of the grain boundaries are also controlled to achieve an additional increase in strength.

The microstructure evolution is in this work exemplarily investigated for the three technological relevant aluminum wrought alloys EN AW-6060, EN AW-6082 and EN AW-7075 during thermo-mechanical processing by direct hot extrusion. The samples are prepared from partly extruded billets which are cut along the middle axis to reveal the microstructures in different deformation zones and at varying degrees of deformation.

Besides the classic light optical microscopy, the electron backscatter diffraction (EBSD) technique is applied for the microstructure analysis. In recent years, EBSD was widely established in the field of materials science and gives direct access to the grain and subgrain structures. Furthermore, it allows the determination of the relative misorientation between individual (sub-)grains and the investigation of the texture at the sample's surface. The final microstructure is the result of interacting dynamic and/or static evolution processes such as recovery and recrystallization. A detailed investigation of the type and distribution of the grain boundaries in the micrographs allows to identify the active microstructure evolution processes.

Based on existing EBSD measurement data sets, the visualization of the grain microstructure and the corresponding grain boundaries is performed by the newly developed and verified in-house program Grainplot. The main algorithms are explained in detail with a special focus on the restoring of incomplete data sets. The accessible and extensively commented program code then allows a further customization by the user. For the different deformation zones of the partly extruded billet, the microstructural evolution regarding grain and subgrain size distribution, relative grain misorientation and fraction of grain boundaries in the micrograph is determined and statistically evaluated. The texture evolution at the different measurement points is presented in the form of inverse pole figures.

Furthermore, the newly developed program Graingen is presented which is used to generate synthetic 2-D and 3-D microstructures with defined statistical properties based on previously analysed EBSD measurement results.

Kurzfassung

Der Werkstoff Aluminium hat sich in den letzten Jahrzehnten als gängiges Konstruktionsmaterial insbesondere im Bereich des Transportwesens, der Luftfahrt und des allgemeinen Leichtbaus bewährt. Um zukünftige Material- und Energieeinsparungen umsetzen zu können, werden neben der optimierten Konstruktion zunehmend die Werkstoffeigenschaften an die benötigten Anforderungen angepasst. Dies umfasst nicht nur die Legierungszusammensetzungen, sondern im zunehmenden Maße auch die gezielte Beeinflussung der Materialmikrostruktur. Bei einer großen Zahl von Aluminiumlegierungen lässt sich die Festigkeit durch Verfahren des Auslagerns signifikant steigern. Im Rahmen des so genannten Grain Boundary Engineerings kann darüber hinaus die Korngrößenverteilung sowie der Verlauf und die Art der vorhandenen Korngrenzen gesteuert werden, wodurch eine weitere Festigkeitszunahme erreicht wird.

Die Mikrostrukturentwicklung wird in dieser Arbeit exemplarisch für drei technologisch relevanten Aluminiumknetlegierungen EN AW-6060, EN AW-6082 und EN AW-7075 bei der thermo-mechanischen Umformung durch direktes Strangpressen untersucht. Als Proben dienen dabei teilverpresste Blöcke, die nach dem Trennen längs der Mittelachse die Mikrostrukturen in verschiedenen Umformzonen und bei unterschiedlichen Umformgraden offenlegen.

Neben einer lichtmikroskopischen Betrachtung wird zusätzlich das Verfahren der Electron Backscatter Diffraction (EBSD) zur Analyse der Kornmikrostruktur eingesetzt. Diese Technik hat sich im Laufe der letzten Jahre zunehmend etabliert und erlaubt neben der Identifizierung der Korn- und Subkornstruktur auch die Bestimmung der relativen Missorientierung benachbarter Körner und die Untersuchung der Textur. Eine detaillierte Betrachtung der Korngrenzentypen und ihrer Verläufe lässt Rückschlüsse auf die wirksamen dynamischen und statischen Entwicklungsmechanismen von Erholung und Rekristallisation zu.

Im Rahmen dieser Arbeit wurde das Programm Grainplot entwickelt und verifiziert, das ausgehend von vorliegenden EBSD-Messdaten eine Visualisierung der Kornmikrostrukturen und der beteiligten Korngrenzen ermöglicht. Die verwendeten Algorithmen insbesondere der Wiederherstellung unvollständiger Datensätze werden schwerpunktmäßig erläutert. Der einsehbare und ausführlich kommentierte Programmcode erlaubt so eine nachträglich Anpassung an verschiedene Aufgaben durch den Anwender. Unter Verwendung der neuen Software wird die Entwicklung der Mikrostruktur innerhalb der Deformationszonen in Hinblick auf Korn- und Subkorngrößenverteilung, relative Kornmissorientierung und Anteil der Korngrenzen im Gefüge statistisch erfasst und ausgewertet. Darüber hinaus werden die Texturentwicklungen an den Messpunkten als inverse Polfiguren dargestellt.

Zudem wird das neu entwickelte Programm Graingen vorgestellt, mit dem – ausgehend von zuvor charakterisierten EBSD-Messergebnissen – künstliche 2-D und 3-D Mikrostrukturen mit definierten statistischen Eigenschaften erstellt werden können.

Chapter 1

Introduction

Abstract – This introduction gives a short overview of the basic relationship between microstructure properties of aluminum alloys and the mechanical behavior of the final products. There is a short spotlight on the history of aluminum and its alloys, followed by a description of the main microstructure evolution mechanisms during forming. The physics of metal behavior depend on the crystal structure which is related to the unit cell geometry. Different unit cells and symmetry conditions are presented with a special focus on the face centered cubic structure of aluminum alloys. The influence of dislocations and their motion through the crystal lattice during plastic deformation is described as well as dislocation sourcing mechanisms and interaction processes. The development of grain size for example, is driven and influenced by a number of recovery and dynamic or static recrystallization processes. A distinction between these different microstructural mechanisms is essential to interpret and understand the micrographs and statistics during the material characterization. Finally the measurement techniques used in this work – light optical microscopy, X-ray diffraction and electron backscatter diffraction – are introduced.

1.1 Influences of microstructure on material behavior

The history of mankind is characterized by its development and use of innovative tools. Over the time the complexity of the devices increased and the preferred materials changed. Beginning with basic tools made of natural materials such as stone, wood and horn, advanced tools were made of metals like copper, bronze and iron. The knowledge of cleaning raw iron from interfering elements such as sulfur and controlling its contents of carbon significantly increased its strength and deformability. This combination of material properties nowadays makes steel the most common material for tools, machines and engines. Nevertheless, especially in the weight sensitive field of transportation and aircraft the application of steel faces its limits. This led to the development of lightweight alloys based on titanium, magnesium and aluminum. Generally, different alloy components allow to adjust various material properties and open a wide field of application for different materials.

Figure 1.1 gives a global overview of the development of new materials and alloys and their relative technical importance. The history of aluminum alloy being used as an engineering material started in the first decade of the 20th century which is indicated by the gray mark in Figure 1.1. Since then integral lightweight constructions based on aluminum alloys became more and more crucial, especially in the field of energetically expensive automotive and aircraft transport. Therefore, the techniques and software obtained during this work are used to characterize a group of widely used aluminum alloys.

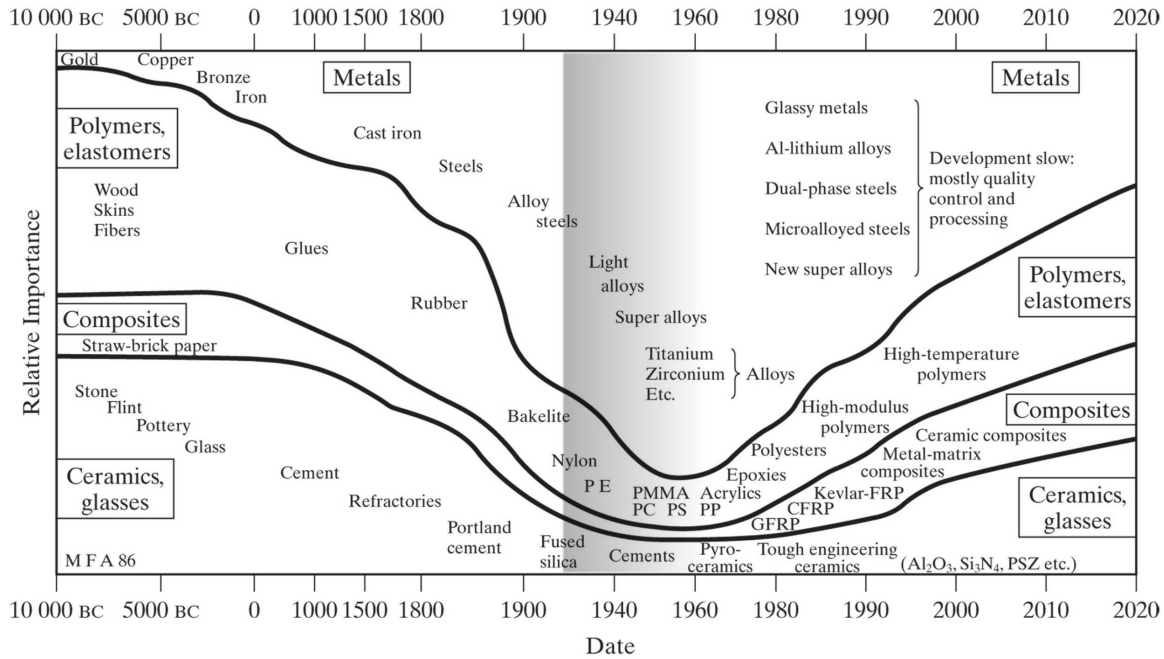


Figure 1.1: Evolution of engineering materials on a non-linear time scale (Ashby, 2005).

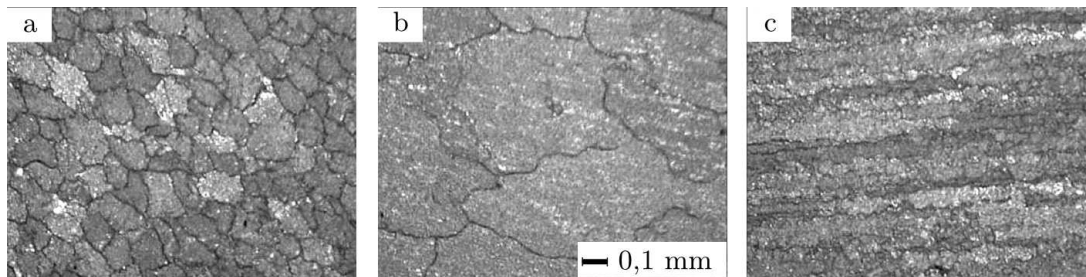


Figure 1.2: LOM micrographs of EN AW-6060. a) initial undeformed microstructure; b) recrystallized grains after large shear deformation; c) banded grain structure resulting from plastic material flow during an direct hot extrusion process. Courtesy of the Institute of Forming Technology and Lightweight Construction (IUL), TU Dortmund University, see Schikorra et al. (2007) for details.

Generally, the material properties of an alloy depend on several chemical and physical effects which are firstly based on alloy composition and element concentration. Secondly, the macroscopic material properties are linked to the local microstructure which for example, is a result of the material's deformation and temperature history. An example of different microstructures taken from the same sample of an direct hot extrusion process is given in Figure 1.2. The light optical microscopy (LOM) images show in Figure 1.2a the initial globular grain structure of an EN AW-6060 aluminum alloy. In Figure 1.2b the plastic shear deformation exceeds the limit of internal energy to initialize static recrystallization as described in Section 1.5.2. This results in significantly larger grains which also have a globular shape. Finally, the banded microstructure in Figure 1.2c arises from plastic material flow along the middle axis of the extrusion billet. Here, the grains reveal a banded texture in direction of extrusion while their grain size has not significantly changed compared to the initial state presented in Figure 1.2a.

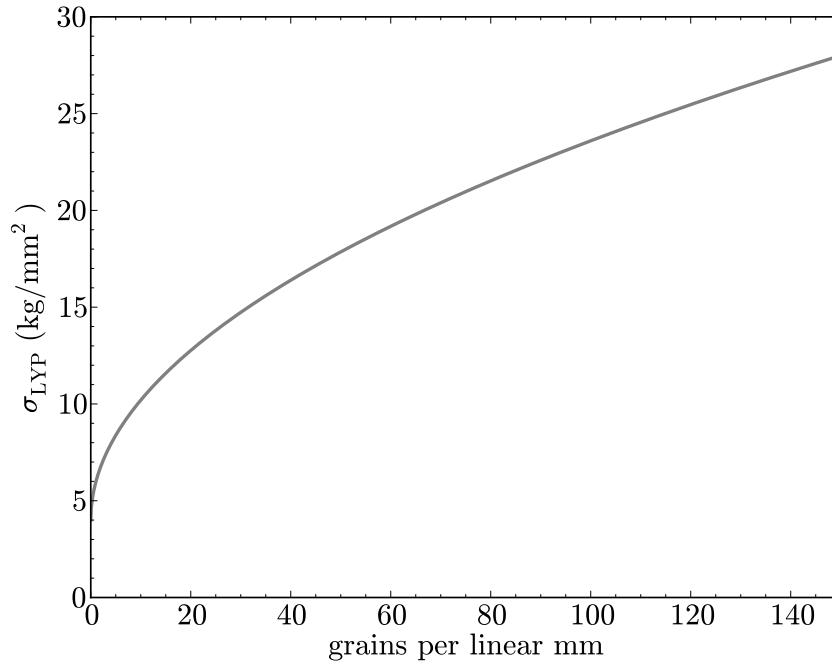


Figure 1.3: Development of lower yield stress σ_{LYP} as a function of grain size for a mild steel examined by Hall (1951).

Comparing the grain sizes and grain shapes given in Figure 1.2, it is obvious that the deformation process leads to significant changes in the microstructure which is linked to the mechanical properties of the material. A well known expression linking microstructure properties with the mechanical response of the material is the equation $\sigma = \sigma_0 + c_1 D^m$ independently formulated in the early 1950s by Hall (1951) and Petch (1953). Here, the yield stress σ is related to the grain diameter D with an exponent $m = -0.5$ and a material dependent constant c_1 . The part σ_0 is the material dependent minimum lattice friction stress which is required to move dislocations inside existing grains. This increase in yield stress results from a dislocation interaction and their pile-up at the grain boundaries as explained in Section 1.4.

Although this relation was originally found on low-carbon steels, it also holds for a large number of other materials such as copper, titanium and aluminum, as shown in Gottstein (2004) and Kammer (2009). Figure 1.3 exemplifies the results of the work of Hall (1951). It shows the development of the lower yield stress σ_{LYP} of an mild steel as a function of the number of grains per linear mm. Here, the grain size is measured by applying a number of straight lines onto the micrograph image and dividing the number of intersecting grains by the length of the line in mm. To convert the shown results into the commonly used SI units σ_{LYP} has to be multiplied with the factor 9.81 N/kg. The Hall-Petch equation also holds for the relationship between smaller scaled subgrain size and yield stress if choosing the exponent $-1 \leq m \leq -0.5$ as indicated by McQueen and Celliers (1996) and Humphreys and Hatherly (2004). The exact value depends on the alloy composition.

The method of grain refinement directly uses the described relationship between grain size and yield stress. The grain refinement during casting can be achieved by adding grain refining

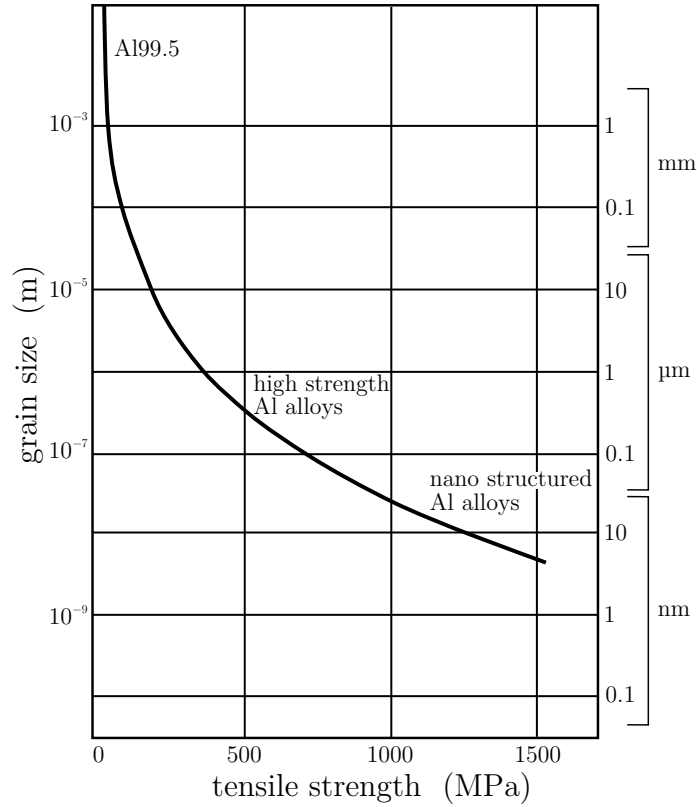


Figure 1.4: Development of tensile strength as a function of grain size for different types of aluminum alloys. Re-drawn from Kammer (2009).

elements to the alloy, e.g. zirconium in case of aluminum alloys as shown in the work of Li et al. (2005). Furthermore a grain refinement and subgrain development due to plastic deformation leads to an increase of the yield stress due to dislocation pile-up at the grain and subgrain boundaries. This effect is commonly known as cold work hardening and plays a significant role during extrusion of aluminum alloys which is described in detail in Section 1.4. Grain refinement as shown in Figure 1.4 is only one aspect of the so-called grain boundary engineering (GBE), the importance of which is summarized in an editorial by Kumar and Schuh (2006). In GBE different measurement techniques and processes are combined to achieve desired mechanical properties by controlling the types and distribution of grain and subgrain boundaries inside the material. As an example for GBE, Owen and Randle (2006) used the electron backscatter diffraction (EBSD) technique in combination with strain-anneal cycles of steel samples to record the change in grain and subgrain structure.

Generally, simulations of microstructure behavior, for example by finite element (FE) simulations, require initial microstructures obtained by different measurement methods. To reduce the number of time and cost intensive experiments and sample preparations, measurement results can be used to reproduce synthetic microstructures with similar statistical characteristics in grain size and misorientation distribution. By using representative volume elements (RVE) which are geometrically periodic it is also possible to assemble several RVE to simulate larger structures based on small scale measurements. A method of generating synthetic microstructures in 2-D and 3-D by cellular automata is described in Section 2.3.

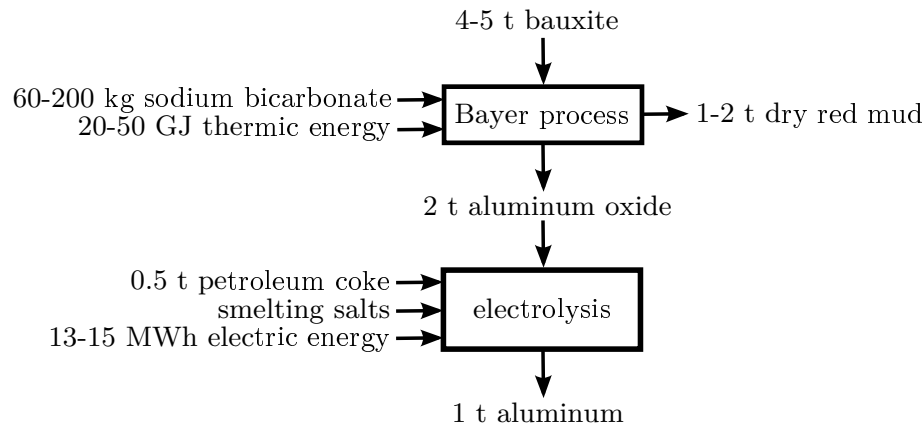


Figure 1.5: Classical aluminum production with preceding Bayer process and electrolytical reduction with necessary additives and consumed energy (Kammer, 2009).

1.2 Aluminum in the field of engineering

1.2.1 Production of aluminum

The element aluminum has an overall weight fraction of 8.23 wt.% of the Earth's crust. This is even more than iron (5.63 wt.%) but the third rank behind oxygen (46.1 wt.%) and silicon (28.2 wt.%) according to Lide (2010). Due to its high affinity to oxygen, aluminum is naturally found in chemical composition, mainly in form of aluminum silicates (feldspars) or oxides (corundum). Aluminum in its elemental state is extremely rarely found on Earth. This explains why it was firstly identified as a separate element by Sir Humphry Davy in 1808. The first reduction to the metal phase was successfully done in 1825 by the Danish physicist and chemist Hans Christian Ørsted from a mixture of Aluminum chloride (AlCl_3) and potassium amalgam (KHg/KHg_2). Two years later the German chemist Friedrich Wöhler replaced the reducing agent potassium amalgam by metallic potassium which led to a clean metallic form of aluminum following the reaction $4 \text{AlCl}_3 + 3 \text{K} \rightarrow \text{Al} + 3 \text{KAlCl}_4$.

Today almost all primary aluminum is produced by electrolysis from bauxite $\text{AlO}_x(\text{OH})_{3-2x}$. The reduction of bauxite needs a large amount of energy which was firstly provided after the invention of the electric power generator by Werner von Siemens in 1886. This led to the independent patents of Charles Martin Hall and Paul Hroult which describe the fused-salt electrolysis of bauxite to melted metallic aluminum. This process was finally improved by Carl Josef Bayer in 1889 and is still used in large scale production of aluminum as depicted in Figure 1.5. Here, a simplified overview of the production process of aluminum from bauxite is given according to Kammer (2009). Depending on its chemical purity 4 ~ 5 t bauxite can be converted into 2 t of pure aluminum oxide by the Bayer process while consuming 20 ~ 50 GJ of thermic energy. The additive sodium bicarbonate converts the bauxite into aluminum hydroxide and red mud which binds the iron parts of the bauxite in form of Fe_2O_3 which is responsible for its characteristic red color. Two tons of aluminum oxide reduce to 1 t of metallic aluminum under addition of smelting salts and 0.5 t petroleum coke as reducing agent. The reduction process consumes 13 ~ 15 MWh of electric energy which makes the production process of primary aluminum from bauxite energetically expensive compared to steel for example.

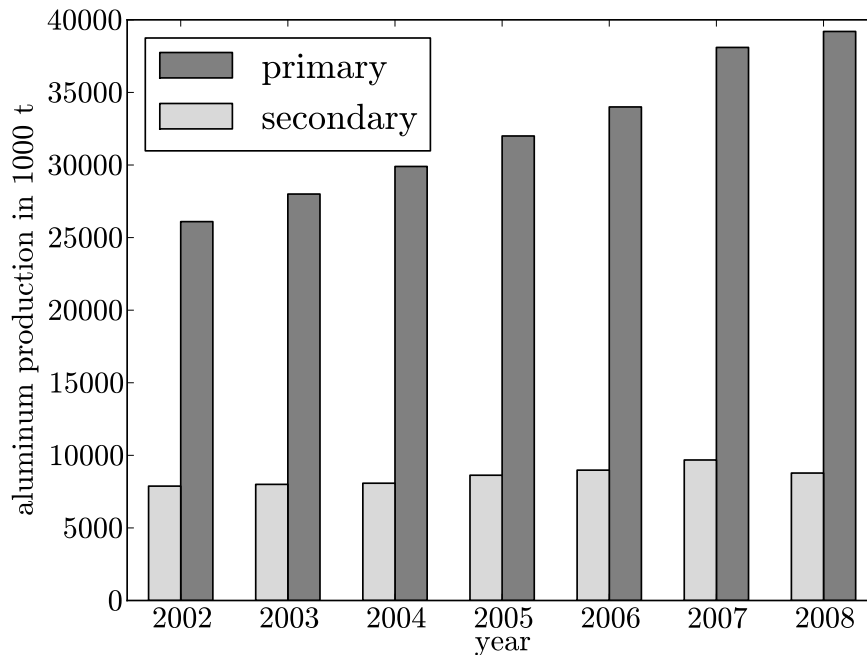


Figure 1.6: World wide production of primary and secondary aluminum (Kammer, 2009).

Since the production of aluminum reached an industrial scale the consumption of electric energy significantly decreased from 21 kWh per kg primary aluminum in the 1950s to 13 ~ 15 kWh per kg nowadays. During the recycling of aluminum the Bayer process and the reduction of aluminum oxide is obsolete. In this case the energy consumption for secondary aluminum reduces to less than a fifth of the energy previously required to produce primary aluminum from bauxite. Taking into consideration that aluminum allows an endless recycling without losing quality in combination with the comparable low energy costs for recycling, the use of aluminum dramatically increased in the last decades and is now used for a number of different products. This is reflected in Figure 1.6 which shows the world wide production of primary and secondary aluminum in 1000 tons. While the production of aluminum remains on a constant level in the western world, the production of primary aluminum is still growing in China. Here, the production increased more than tenfold from 963,000 t in 1991 to 12,600,000 t in 2007 (Kammer, 2009).

1.2.2 Aluminum alloys

Pure aluminum shows excellent chemical resistance based on a thin but dense aluminum oxide layer at the surface. Due to aluminum's high affinity to oxygen a damage of this layer heals itself by oxidizing the aluminum below. Chemical anodizing increases the thickness and density of the oxide layer and offers an improved protection of the underlying material against chemical corrosion. Nevertheless, the comparably low strength of pure aluminum limits its field of application to special purposes in chemical industry. Depending on the demands requested by a specific product, different alloy components are added to improve the mechanical properties

of an aluminum alloy. Typically one or more of the following properties are needed for special applications:

- high tensile strength
- high tensile yield strength
- high temperature strength
- high fatigue strength
- high creep resistance
- high chemical corrosion resistance
- high or low ductility (depending on application)
- high or low elasticity (depending on application)
- high or low heat conductivity (depending on application)
- low thermal expansion
- ability of age hardening
- good pourability
- good machining ability

Since the addition of a specific element improves one or more of these properties, it may also influence other ones in an undesired way. Therefore a large number of different aluminum alloys basing on a number of alloy elements is commercially available. In the following the most commonly used alloy elements are listed and the main influences on the resulting aluminum alloy are summarized according to Bargel et al. (1999); Kammer (2009); Sheppard (1999):

Magnesium fractions below 5 % increase the tensile strength of an AlMg alloy by solid solution strengthening. Fractions larger than 5 % additionally lead to precipitation hardening based on the intermediate phase Al_3Mg_2 (compare Section 1.2.3). Furthermore magnesium positively influences fatigue strength and high temperature strength. Primary precipitates of Al_3Mg_2 that occur in alloys with high magnesium fractions larger than 15 % reduce corrosion resistance and stress concentration since this oversized precipitates facilitate crack initiation.

Silicon is the main alloy component for aluminum cast alloys. AlSi alloys near to the eutectic composition of 11.7 % silicon are characterized by a suitable solidification behavior combined with acceptable tensile strength. In contrast to most other materials silicon expands during solidification which is used to reduce the solidification shrinkage from about 7 % of pure aluminum to handy values around 3 %.

Apart from its benefits for cast alloys silicon also increases the tensile strength by solid solution strengthening. In presence of magnesium the solid solution strengthening can be significantly enhanced by the development of Mg_2Si precipitates during heat treatment.

Copper increases the tensile strength due to solid solution strengthening and precipitation hardening based on the intermediate compound Al_2Cu . The development of primary Al_2Cu precipitates during solidification should be avoided since these oversized particles act as nuclei for crack initiation and reduce the material's strength. Holding the copper fraction in an alloy below 4.5 % ensures that the copper is completely resolved in the aluminum matrix. Due to significant differences in the electro-potential of aluminum and copper, their alloys have a reduced corrosion resistance which is related to galvanic corrosion around Al_2Cu precipitates.

Zinc is usually combined with copper and/or magnesium for high strength aluminum alloys of the EN AW-7xxx alloy family. Here, the maximum tensile strength values for aluminum alloys of 650 MPa are reached. The precipitation hardening is caused by particles of MgZn_2 and/or Al_2CuMg depending on the alloy composition.

Manganese as single alloy element only supports solid solution strengthening. In combination with iron the tensile strength is also increased by precipitation hardening. The high temperature strength is positively influenced by raising the recrystallization temperature.

Nickel significantly increases the high temperature strength. Together with copper and magnesium it is part of special alloys for aluminum pistons in combustion engines.

Iron is usually not used as single alloy element because of the formation of brittle, needle shaped Al_3Fe precipitates. Iron just shows a very little solution in the aluminum matrix.

Lead, tin and bismuth are added to special machining alloys where they act as chip breaker.

Boron, chromium, titanium and zirconium increase the recrystallization temperature depending on the combination with other alloy elements. The suppression of recrystallization results in a grain refinement with improved mechanical properties of the specific aluminum alloy.

Generally, aluminum alloys can be subdivided into casting (AC) and wrought alloys (AW). Only the latter ones are usable in the field of extrusion. All AW alloys are grouped in different series named by a four digit number. The assignment to the alloy series is normed by the standard DIN EN 573-1 and depends on the main alloy components as shown in Table 1.1. The chemical composition of individual wrought alloys is stated in the standard DIN EN 573-3. This work focuses on the characterization of two alloys of the 6000 series, i.e. 6060 and 6082, and the high strength alloy 7075. A detailed description of the alloy compositions and their properties is given in Section 3.1.

1.2.3 Strengthening of aluminum alloys

Solid solution strengthening

Aluminum shows an excellent ratio of density and Young's modulus but the strength of pure aluminum is very low compared to other metals used in the field of engineering. Its Young's modulus of approximately 70 GPa is less than a third compared to steel while the tensile strength varies at a comparably low level between 40 and 120 MPa depending on heat treatment and

Table 1.1: Aluminum wrought alloy series according to DIN EN 573-1 and ability of precipitation hardening.

series No.	main alloy components	precipitation hardening
1000	aluminum > 99.00 %	no
2000	copper	yes
3000	manganese	no
4000	silicon	no
5000	magnesium	no/yes
6000	magnesium and silicon	yes
7000	zinc	no/yes
8000	other elements	no

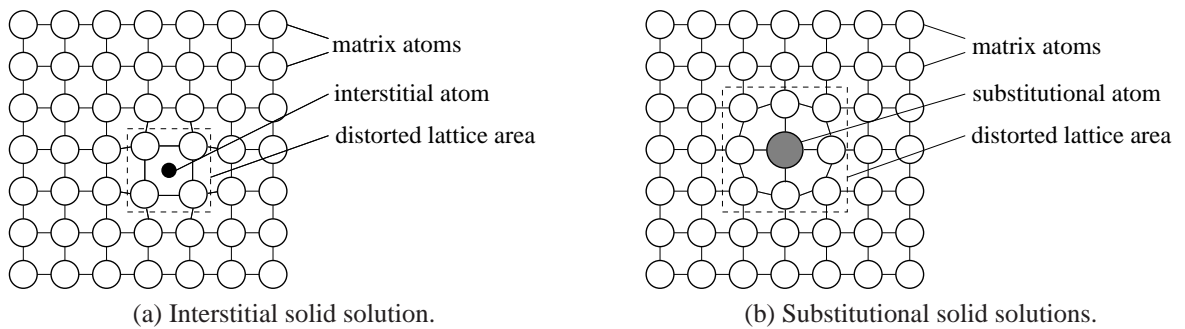
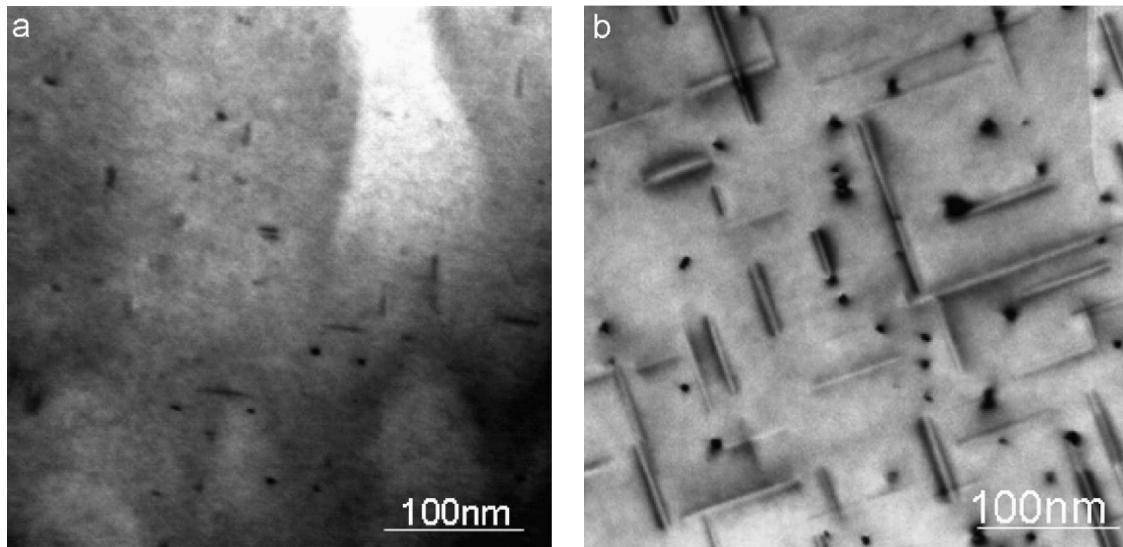


Figure 1.7: Schematic illustration of solid solution types.

alloy composition (Kammer, 2009). The tensile strength can be increased by adding alloy components as already described in Section 1.2.2. Most of the alloy components increase the tensile strength by the solid solution strengthening effect. Here, atoms of the alloy components are placed inside the atomic matrix and cause an elastic distortion of the matrix lattice. These distorted regions then act as obstacles for passing dislocations.

There are two types of solid solutions: In the interstitial solid solution the alloying atoms are placed in between the matrix atom lattice as shown in Figure 1.7a. This is only possible for small sized atoms like hydrogen, bromine, carbon or nitrogen. In consequence of the small dimensions of the interstitial located atoms the region elastic distorted regions in interstitial solid solution are rather small. If the alloying element and the matrix element have a similar atomic radius, which only differs by less than 15 %, substitutional solid solution occurs. Figure 1.7b indicates that in this case matrix atoms are replaced by alloying atoms (Gottstein, 2004). Usually the elastic distortions of substitutional solid solutions are larger than those of interstitial solid solution which lead to a more increasing strength. Since the alloy composition does not change during thermo-mechanical processes, the influence of solid solution strengthening on the overall tensile strength remains constant. It is also independent from the microstructure evolution.



(a) Globular-shaped precipitates after artificial aging at 180 °C for 1.5 h.

(b) Needle-shaped precipitates after artificial aging at 180 °C for 8 h.

Figure 1.8: TEM images of precipitates in an Al-Mg_{0.4}-Si_{0.4} alloy after different artificial aging times at constant temperature (Chang et al., 2009).

This influence of solid solution strengthening on the material properties by varying the fraction of alloy components in an 6000-series aluminum alloy is investigated , e.g. by Bergsma et al. (1998).

Precipitation hardening

The effect of solid solution strengthening alone is not sufficient to reach material strengths which facilitate a use of aluminum alloys in the field of engineering. The success of aluminum as a light weight construction material started in 1906 when the effect of precipitation hardening was accidentally discovered by Alfred Wilm. He experimented which different heat treatment processes on different aluminum alloys. One specific alloy with the composition AlCu4Mg1 – today known as Duralumin or DURAL® of the 2000-series – showed a significant increase in tensile strength upon resting some days after quenching. Duralumin has the ability of precipitation hardening at room temperature due to its high content of copper. Due to the strong time dependency of the resulting mechanical properties, the precipitation hardening is also denoted as age hardening. Later on numerous aluminum alloys with this ability were identified and suitable heat treatment processes were developed to achieve optimal mechanical material properties. Precipitations are not in the focus of this work but, as the handled alloys EN AW-6060, EN AW-6068 and EN AW-7075 are precipitation hardenable, this process is briefly described in the following.

The precipitation hardening results from the disperse of small scaled intermediate compound particles inside the crystals. Depending on the alloy composition, the thermal conditions and the aging time different shapes and sizes of precipitates evolve. In a recent work Chang et al. (2009) investigated an Al-Mg_{0.4}-Si_{0.4} alloy which is similar to EN AW-6060 and observed a dramatical change in the precipitate shape while extending the aging time. Figure 1.8 reveals

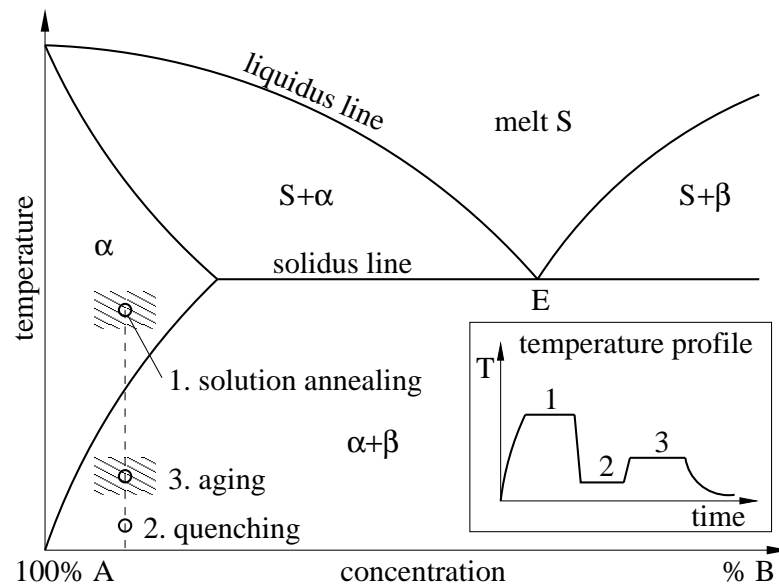


Figure 1.9: Scheme of artificial precipitation hardening for a two component alloy and corresponding temperature profile over time.

how the globular precipitates change their shape into needles with increasing aging time at constant temperature. Parallel to the change in the precipitate shape, the hardness increased from ~ 40 HV up to ~ 60 HV. Depending on the compound of the precipitates and the surrounding matrix, different types of the particle boundaries are possible (Bargel et al., 1999). The most effective ones are coherent and partly coherent precipitates which induce stress into the surrounding atom matrix. This leads to an elastic deformation of the matrix and extends the effective range in which passing dislocations are stuck.

All precipitation hardenable aluminum alloys require at least one alloy component whose solid solution decreases with decreasing temperature. Some alloys such as Duralumin show a natural aging behavior so that, after annealing, the strength increases over time at room temperature. Usually the strength can be more efficiently increased by a special heat treatment. A scheme of this artificial precipitation hardening procedure is depicted in Figure 1.9. Firstly, already existing intermediate compound particles are solved in the matrix by solution annealing (1) between solubility and solidus line. Annealing temperature and time depend on the alloy composition. Secondly, the solid solution state is frozen by quenching (2) to a temperature below the solubility line. The material strength now increases exclusively by solid solution strengthening. Finally, the temperature is raised again (3) to allow precipitation from the supersaturated solid solution. Number and distribution of the new evolving precipitates depend on aging temperature and time. The aging time is crucial because the precipitates become oversized with time and that significantly reduces the material strength.

Table 1.2: The seven basic crystal systems. Axes and angles according to Figure 1.10.

system	axis lengths	angles
cubic	$a = b = c$	$\alpha = \beta = \gamma = 90^\circ$
tetragonal	$a = b \neq c$	$\alpha = \beta = \gamma = 90^\circ$
orthorhombic	$a \neq b \neq c$	$\alpha = \beta = \gamma = 90^\circ$
rhombohedral	$a = b = c$	$\alpha = \beta = \gamma \neq 90^\circ$
monoclinic	$a \neq b \neq c$	$\alpha = \gamma = 90^\circ \neq \beta$
triclinic	$a \neq b \neq c$	$\alpha \neq \beta \neq \gamma \neq 90^\circ$
hexagonal	$a = b \neq c$	$\alpha = \beta = 90^\circ; \gamma = 120^\circ$

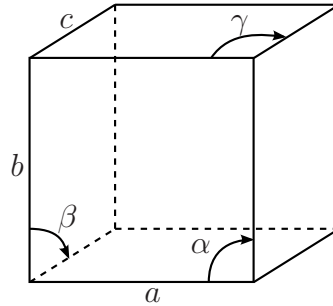


Figure 1.10: Reference crystal geometry.

1.3 Crystal structures of metals

1.3.1 Crystal lattice types

Basically all technical metals and alloys can be categorized by their unit cell geometries. Ideally, the unit cells form a perfect lattice throughout a single grain. But, as described in Section 1.4, this is rather an exception than the rule where point defects, dislocations and impurities disturb the ideal regular crystal lattice. Nevertheless, the structure of the basic unit cell defines the general behavior of the material. Table 1.2 lists the seven basic crystal systems and their corresponding characteristic angles and lengths as defined in Figure 1.10. A comprehensive introduction and overview of crystal structures can also be found in Shackelford (2009).

The seven basic crystal systems can be extended by adding additional atoms in the unit cell interior or on the faces. This results in a total of 14 individual crystal lattices – also called Bravais lattices. All crystal systems vary in their structure, the number and positioning of closed-packed planes, the number of atoms per unit cell and the atomic packing factor (APF). The APF specifies how much volume fraction of a unit cell is occupied by the atom's volumes. Unlike Figure 1.11 implies, usually atoms do not belong to a single unit cell alone, but are shared with adjacent unit cells. For example, atoms at the corners of cubic unit cells belong to 8 neighboring cells at the same time. In the context of metals only 3 Bravais lattices are relevant:

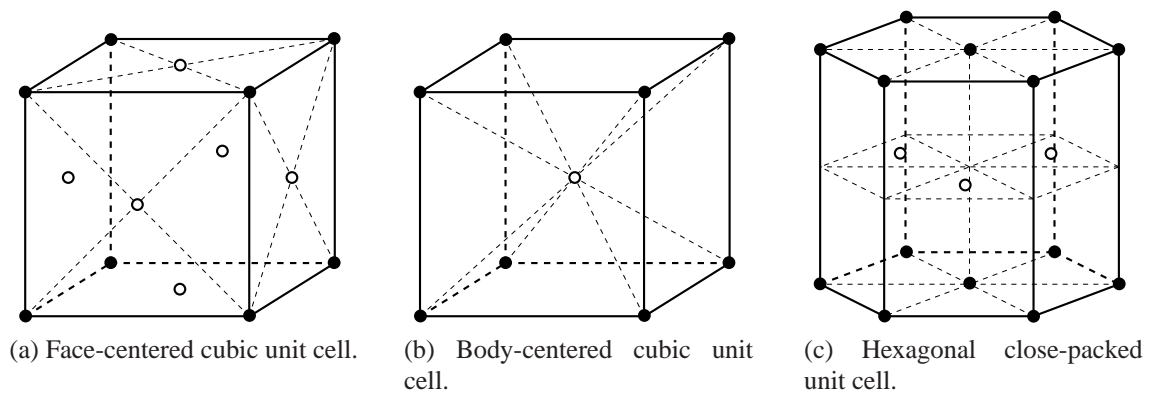


Figure 1.11: Crystal structures of metals.

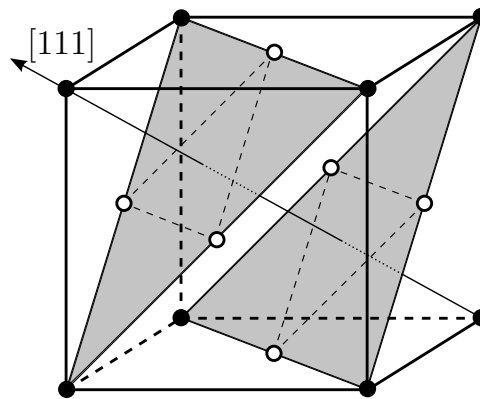


Figure 1.12: Close-packed planes of a FCC unit cell.

face-centered cubic (FCC): In the center position of each face of a cubic lattice an additional atom is placed as shown in Figure 1.11a. A unit cell contains 4 atoms and has an APF of 0.74 which is the highest possible value to be reached by packing spheres of same diameter. Typical metals with FCC lattice are aluminum, nickel, copper and iron in austenite phase (γ -Fe).

body-centered cubic (BCC): Here, an additional atom is located in the body center of a cubic lattice as pictured in Figure 1.11b. Although the volume of the center atom completely belongs to the BCC unit cell, the APF is with 0.68 lower as for the FCC lattice. In sum a unit cell with BCC lattice contains only 2 atoms. This crystal system can be found in tungsten, vanadium, chromium and the ferrite phase of iron (α -Fe).

hexagonal close-packed (HCP): This crystal lattice is characterized by two hexagonal layers, each with an additional atom in the face centers and an intermediate layer holding 3 atoms. Although a HCP unit cell contains only two atoms, it reaches an APF of 0.74 which is equal to the FCC lattice. Example metals with a HCP lattice are zinc, zirconium, α -titanium and magnesium.

The previous list already indicates that some metals such as iron change their unit cell configuration depending on temperature and alloy composition. In contrast to this, aluminum alloys

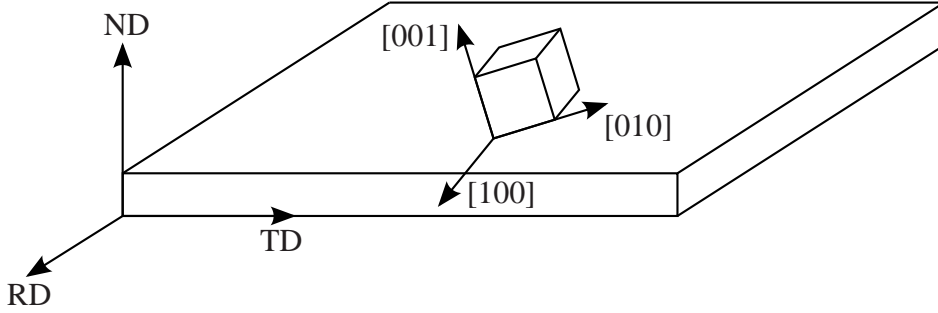


Figure 1.13: Definition of sample and crystal coordinate systems.

constantly remain in the FCC lattice so that the symmetry operations described in the following section are valid for the whole range of temperature occurring during the observed hot forming processes. The lattice structure directly influences the number and positioning of closed-packed planes which act as slip planes during plastic deformation as discussed in detail in Section 1.4. FCC unit cells have 4 closed-packed planes, two of which are exemplarily emphasized by gray shadings in Figure 1.12, with 3 directions each. Due to the high number of 12 glide systems and their orientation towards each other, a number of slip planes is active during plastic deformation of aluminum alloys. This facilitates a good deformability in combination with moderate ram forces at comparably low processing temperatures during thermo-mechanical processing by hot extrusion.

1.3.2 Crystal orientations and symmetry

Euler angles

There are different ways to mathematically describe the orientation of crystal lattices \mathbf{C} in an orthogonal three dimensional (3-D) space that hold $\mathbf{C} \in \text{Orth}^+(\mathbb{E}_3)$. In the following, orientations are given in form of the Euler angles following the notation by Bunge (1981). Using the passive rotation matrix \mathbf{R} which rotates the sample coordinate system \mathbf{C}_S into the crystal coordinate system \mathbf{C}_C by

$$\mathbf{C}_C = \mathbf{R} \mathbf{C}_S, \quad (1.1)$$

as indicated in Figure 1.13, the rotation is defined by the Euler angles φ_1 , Φ , φ_2 . The sample coordinate system \mathbf{C}_S is usually related to significant surfaces of the sample or directions during specimen processing. RD indicates the rolling direction which is equivalent to the direction of the ram movement during direct extrusion. The normal direction ND is defined perpendicular to RD and the surface of a rolled blank. The transverse direction TD completes the orthogonal 3-D coordinate system. In the case of rotationally symmetric parts, the direction of ND is arbitrary. The directions of the local crystal coordinate system are given in Miller indices pointing towards the directions of a unit cell [100], [010] and [001].

According to Figure 1.14 the angle φ_1 rotates around the normal direction ND which transforms the transverse direction TD into the intermediate direction TD' and the rolling direction RD into the intermediate direction RD'. Φ then rotates around the new intermediate rolling direction RD' which brings the normal direction ND in coincidence with the crystal direction [001] and transforms TD' into TD''. Finally, a rotation with the angle φ_2 around the [001]

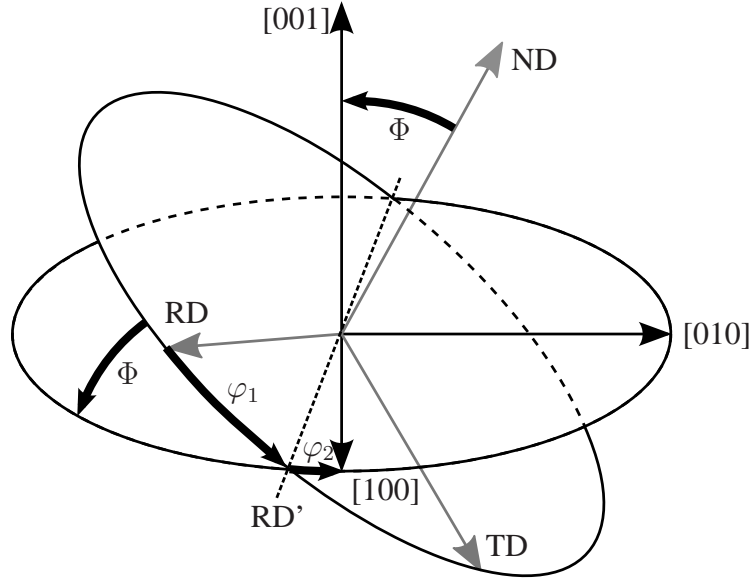


Figure 1.14: Euler angles in Bunge's notation. Passive rotation: Crystal coordinate system in black, sample coordinate system in gray. Re-drawn from Randle and Engler (2009).

direction brings both RD' and TD'' into coincidence with [100] and [010], respectively. These individual rotations can be expressed by the matrices

$$\begin{aligned}
 \mathbf{R}_{\varphi_1} &= \begin{pmatrix} \cos \varphi_1 & \sin \varphi_1 & 0 \\ -\sin \varphi_1 & \cos \varphi_1 & 0 \\ 0 & 0 & 1 \end{pmatrix}, \\
 \mathbf{R}_{\Phi} &= \begin{pmatrix} 1 & 0 & 0 \\ 0 & \cos \Phi & \sin \Phi \\ 0 & -\sin \Phi & \cos \Phi \end{pmatrix} \text{ and} \\
 \mathbf{R}_{\varphi_2} &= \begin{pmatrix} \cos \varphi_1 & \sin \varphi_1 & 0 \\ -\sin \varphi_1 & \cos \varphi_1 & 0 \\ 0 & 0 & 1 \end{pmatrix}.
 \end{aligned} \tag{1.2}$$

The rotation matrix \mathbf{R} then derives from the multiplication of the the three rotations

$$\mathbf{R} = \mathbf{R}_{\varphi_2} \cdot \mathbf{R}_{\Phi} \cdot \mathbf{R}_{\varphi_1} \tag{1.3}$$

which gives the complete expression

$$\mathbf{R} = \begin{pmatrix} c\varphi_1 c\varphi_2 - s\varphi_1 s\varphi_2 c\Phi & s\varphi_1 c\varphi_2 + c\varphi_1 s\varphi_2 c\Phi & s\varphi_2 s\Phi \\ -c\varphi_1 s\varphi_2 - s\varphi_1 c\varphi_2 c\Phi & -s\varphi_1 s\varphi_2 + c\varphi_1 c\varphi_2 c\Phi & c\varphi_2 s\Phi \\ s\varphi_1 s\Phi & c\varphi_1 s\Phi & c\Phi \end{pmatrix} \tag{1.4}$$

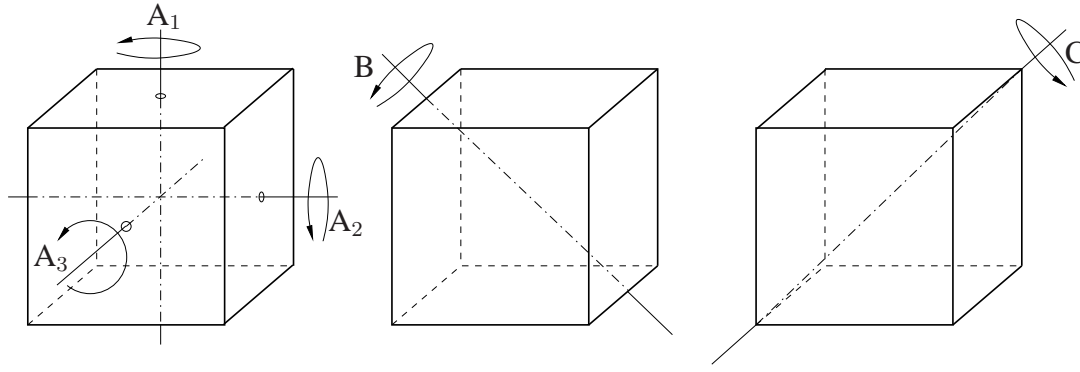


Figure 1.15: Crystal symmetries for cubic unit cells. Symmetric rotations around axis of type A: 90° , 180° , 270° ; axis type B: 180° ; axis type C: 120° , 240° .

where s is the sine and c is the cosine function. By definition, the Euler angles are periodic with a period of 2π which can also be seen in Figure 1.14. To enforce uniqueness in the Euler angle representation the three angles are only defined in the bounds of $0^\circ \leq \varphi_1 \leq 360^\circ$, $0^\circ \leq \Phi \leq 180^\circ$, $0^\circ \leq \varphi_2 \leq 360^\circ$ which also limits the orthogonal Euler space $\text{Orth}^+(\mathbb{E}_3)$ (Randle and Engler, 2009).

Axis/angle pair

Depending on their unit cell architecture, metallic crystals show certain symmetries which are displayed in Figure 1.15 for the cubic unit cells of FCC and BCC crystals. Around each of the three rotation axes $A_1 = [001]$, $A_2 = [010]$ and $A_3 = [100]$ – which belong to the direction family $\langle 100 \rangle$ – three possible rotations of 90° , 180° , 270° lead to the same orientation of the unit cell again. Additionally, rotations around the six rotation axes of type B $\langle 110 \rangle$ with each 180° and two rotations of 120° and 240° around the three rotation axes of type C $\langle 111 \rangle$ also result in the original orientation of the crystal. Including the identity, i.e. no rotation at all, this leads to 24 symmetric orientations for cubic unit cells (Randle and Engler, 2009).

Figure 1.15 also reveals the opportunity to use an axis/angle pair to describe the orientation of unit cells. For cubic unit cells a single rotation with an angle θ around a suitable normalized rotation axis \mathbf{r} is necessary to bring two structures into coincidence. Following Santoro and Mighell (1973) θ and \mathbf{r} can be derived from the rotation matrix \mathbf{R} by solving the eigenvalue problem

$$(\mathbf{R} - \lambda \mathbf{I})\mathbf{r} = \mathbf{0} \quad (1.5)$$

with the eigenvalue $\lambda = 1$ and the identity matrix \mathbf{I} . Thus, the resulting rotation angle θ is

$$\theta = \arccos\left(\frac{1}{2}(\text{tr}(\mathbf{R}) - 1)\right) \quad (1.6)$$

and the corresponding normalized rotation axis vector \mathbf{r} consists of the components

$$\begin{aligned} r_1 &= \frac{R_{23} - R_{32}}{2 \sin \theta} \\ r_2 &= \frac{R_{31} - R_{13}}{2 \sin \theta} \\ r_3 &= \frac{R_{12} - R_{21}}{2 \sin \theta}. \end{aligned} \quad (1.7)$$

If the rotation angle holds $\theta = 180^\circ$, the axis vector cannot be determined by the equations 1.8. In this particular case the corresponding rotation axis vector \mathbf{r} is determined by

$$\begin{aligned} r_1 &= \left(\frac{1}{2}(R_{11} + 1) \right)^{\frac{1}{2}} \\ r_2 &= \left(\frac{1}{2}(R_{22} + 1) \right)^{\frac{1}{2}} \\ r_3 &= \left(\frac{1}{2}(R_{33} + 1) \right)^{\frac{1}{2}} \end{aligned} \quad (1.8)$$

With respect to the possible symmetries of cubic unit cells the rotation axis vectors and rotation angles are known. From this it is possible to generate each of the 24 symmetry orientation matrices of the symmetry group \mathcal{G}_S by

$$\mathbf{O}_S = \begin{pmatrix} r_1^2(1 - \cos \theta) + \cos \theta & r_1 r_2(1 - \cos \theta) - r_3 \sin \theta & r_1 r_3(1 - \cos \theta) + r_2 \sin \theta \\ r_1 r_2(1 - \cos \theta) + r_3 \sin \theta & r_2^2(1 - \cos \theta) + \cos \theta & r_2 r_3(1 - \cos \theta) - r_1 \sin \theta \\ r_1 r_3(1 - \cos \theta) - r_2 \sin \theta & r_2 r_3(1 - \cos \theta) + r_1 \sin \theta & r_3^2(1 - \cos \theta) + \cos \theta \end{pmatrix} \quad (1.9)$$

where r_1, r_2, r_3 are the components of one of the normalized rotation axes belonging the direction families $\langle 100 \rangle, \langle 110 \rangle, \langle 111 \rangle$ and θ is one of the corresponding rotation angles $90^\circ, 120^\circ, 180^\circ, 240^\circ$ or 270° according to Figure 1.15.

Misorientation

A misorientation describes the difference in orientation of two crystals or grains. The misorientation is commonly determined between adjacent grains while analysing a micrograph. It is given by the misorientation matrix \mathbf{M}_{12} via

$$\mathbf{R}_2 = \mathbf{M}_{12} \mathbf{R}_1 \quad (1.10)$$

which transforms the orientation matrix \mathbf{R}_1 of grain 1 into the orientation matrix \mathbf{R}_2 of grain 2. Since the rotation matrices are orthogonals it follows that $\mathbf{R}^{-1} = \mathbf{R}^T$, thus,

$$\mathbf{M}_{12} = \mathbf{R}_2 \mathbf{R}_1^T. \quad (1.11)$$

While determining the misorientation angle θ_{12} between two grains, all symmetries have to be taken into account to identify the minimum angle. Therefore all symmetry orientations of the symmetry group \mathcal{G}_S have to be evaluated by the equation

$$\theta_{12} = \min_{\mathbf{O}_S \in \mathcal{G}_S} \left| \arccos \left(\frac{1}{2} \{ \text{tr}(\mathbf{O}_S \mathbf{M}_{12}) - 1 \} \right) \right|. \quad (1.12)$$

Depending on the relative orientation of the grains, the misorientation angle can be negative which simply means that the corresponding rotation axis vector has to point in the opposite direction. Due to the symmetries of materials with cubic crystal structure the misorientation angle is limited to $\theta_{12} \leq 62.8^\circ$ which was shown by Mackenzie (1958).

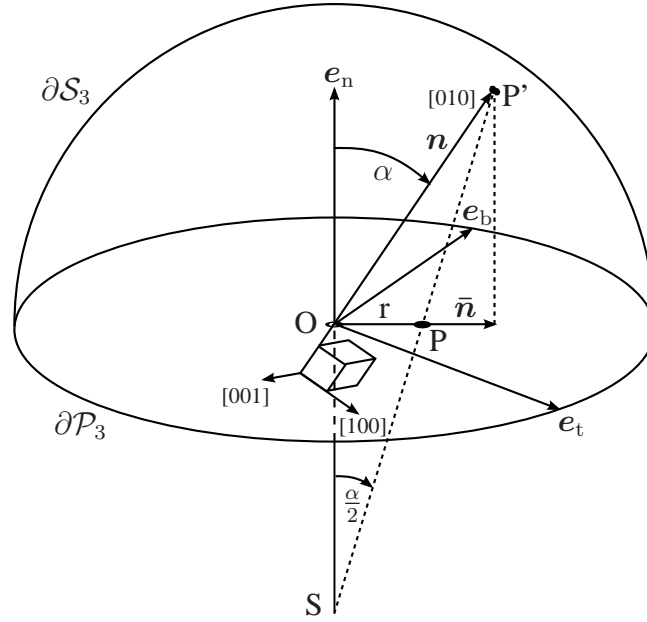


Figure 1.16: Stereographic projection. Re-drawn from Kraska (1998).

Pole figures and inverse pole figures

For a two dimensional (2-D) representation of the 3-D orientation of a crystal in space an appropriate projection is necessary. In crystallography the stereographic projection is widely used which is also known from generating a world map. The stereographic projection preserves the angle between different points which is especially important in the field of misorientations.

The principle of stereographic projection is explained by following the example given in Figure 1.16. As indicated in Figure 1.13 an individual coordinate system C_C can be assigned to each grain according to the orientation of its crystal lattice. One coordinate of the crystal's system, e.g., [010], is now projected onto a surrounding unit sphere ∂S_3 through the sphere center O. The projected point P' defined by its position vector \mathbf{n} is connected to the south pole S of the sphere which finally gives the intersection point P on the equatorial plane ∂P_3 . The pole P is then specified by the direction $\bar{\mathbf{n}}$ and the distance r from the sphere center O by

$$\bar{\mathbf{n}} = \begin{cases} (\mathbf{I} - \mathbf{e}_n \mathbf{e}_n) \cdot \mathbf{n} & \text{if } \mathbf{n} \cdot \mathbf{e}_n \geq 0 \\ -(\mathbf{I} - \mathbf{e}_n \mathbf{e}_n) \cdot \mathbf{n} & \text{else} \end{cases} \quad (1.13)$$

$$\alpha = \arcsin |\mathbf{n} \times \mathbf{e}_n| \quad (1.14)$$

$$r = \tan\left(\frac{\alpha}{2}\right) \quad (1.15)$$

If ∂P_3 is defined by the coordinate system $(\mathbf{e}_t, \mathbf{e}_b)$ the position (x, y) of P can be acquired by

$$x = \frac{r}{|\bar{\mathbf{n}}|} \bar{\mathbf{n}} \cdot \mathbf{e}_t; \quad y = \frac{r}{|\bar{\mathbf{n}}|} \bar{\mathbf{n}} \cdot \mathbf{e}_b \quad (1.16)$$

as given in Figure 1.17 which shows the complete pole figure for an example pole P with its coordinates (x, y) on ∂P_3 . According to the symmetry conditions of cubic unit cells, the stereographically projected pole P has 24 redundant positions on ∂P_3 as indicated in Figure 1.17.

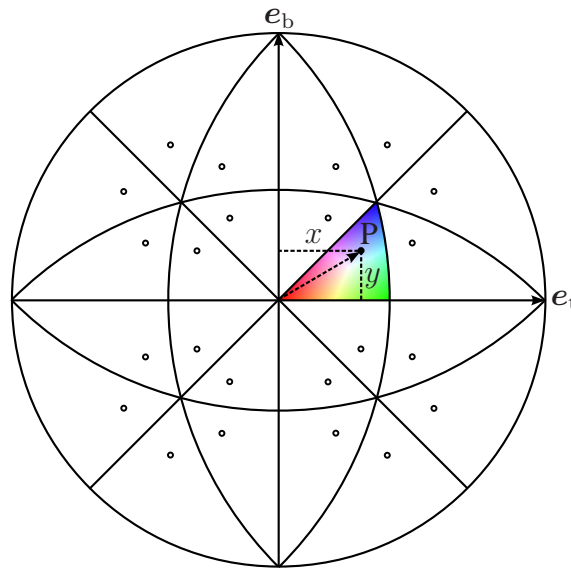


Figure 1.17: Position of a sample point P in a pole figure with respect to symmetry during stereographic projection.

Therefore $\partial\mathcal{P}_3$ can be reduced to a single section of the pole figure which is emphasized by a color gradient in Figure 1.17.

Instead of projecting the orientation of the crystal coordinates in a sphere based on the sample coordinate system, one can also invert this procedure by representing an arbitrary direction in a system defined by the crystal coordinates system as shown in Figure 1.18. For the inverse stereographic projection a unit sphere $\partial\mathcal{S}_3$ is placed relative to a cubic unit cell so that its center O is coincident with the origin of crystal coordinate system $\{[001], [010], [001]\}$. In Figure 1.18 only an eighth of the sphere located inside the cubic unit cell is shown. Firstly, the intersection point P' , the desired direction n and the unit sphere $\partial\mathcal{S}_3$ are constructed. The intermediate point P' is then stereographically projected onto the equatorial plane $\partial\mathcal{P}_3$ by connecting it to the south pole S of $\partial\mathcal{S}_3$ yielding the pole P . With respect to the symmetry conditions, the inverse stereographic projections of all directions end up in the light gray shaded area of $\partial\mathcal{P}_3$ – the inverse pole figure (IPF). The IPF as shown in Figure 1.18 is then spanned between the projection points of the crystal directions $[100]$, $[101]$ and $[111]$. By filling the IPF with an appropriate color gradient, it allows to encode the orientation of a specific point by its color as described in detail in Section 2.2.2.

Orientation distribution functions

When reducing the 3-D orientation of a crystal into the 2-D coordinates of a pole by stereographic projection, some of the original information is lost. Pole figures and inverse pole figures only hold the complete orientation information for single crystals or an assembly of few grains as long as all pole positions can be observed separately. With increasing number of crystals or grains which are investigated, the pole positions may overlay which results in uncertain interpretation of the pole figures. This uncertainty is additionally intensified by measurement

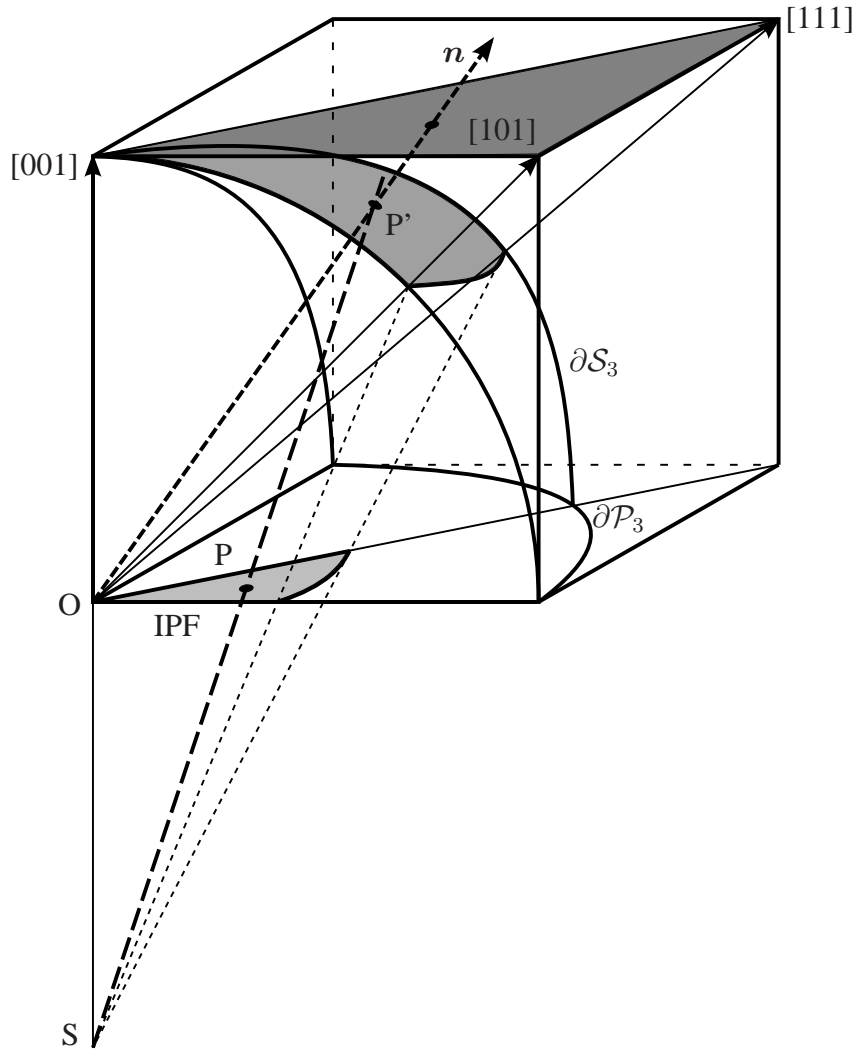


Figure 1.18: Inverse stereographic projection of a cubic unit cell. Re-drawn from Kraska (1998).

deviations which arise dependently on the used measurement technique, e.g. X-ray diffraction or electron backscatter diffraction.

The orientation distribution function (ODF) $f(\mathbf{R})$ generally describes the ratio of the volume fraction dV of grains with an orientation \mathbf{R} which have a maximum angular variation of $d\mathbf{R}$ and the total volume V of grains in the sample:

$$\frac{dV}{V} = f(\mathbf{R}) d\mathbf{R}. \quad (1.17)$$

If the orientation is described by Euler angles as previously introduced in Section 1.3.2, the angular variation $d\mathbf{R}$ depends on the variation of the three Euler angles $\varphi_1, \Phi, \varphi_2$:

$$d\mathbf{R} = \frac{1}{8\pi^2} \sin \Phi d\varphi_1 d\Phi d\varphi_2 \quad (1.18)$$

and the ODF must also fulfill the normalization condition

$$\oint f(\mathbf{R}) d\mathbf{R} = 1. \quad (1.19)$$

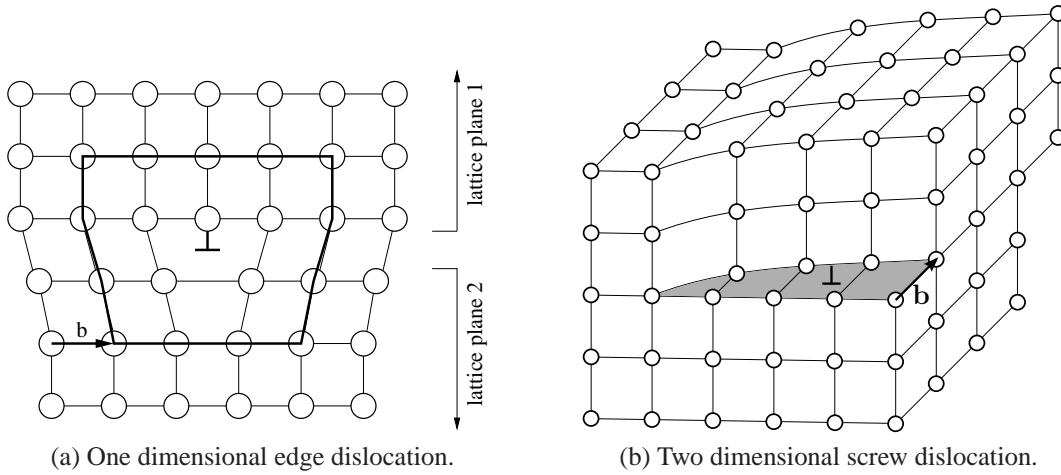


Figure 1.19: Schematic dislocations in FCC crystal structures. Burger's vector \mathbf{b} indicated by vector \mathbf{b} .

In practice the 3-D ODF is obtained from 2-D pole figures P_h by determination of the volume fraction $\frac{dV}{V}$ of all grains whose direction h is oriented parallel to a sample direction y accepting an angular variation of dy :

$$\frac{dV}{V} = \frac{1}{4\pi} P_h(y) dy. \quad (1.20)$$

Here, the sample direction y is given by the pole figure angles α and β as specified in Figure 1.16 and its variation is $dy = \sin \alpha d\alpha d\beta$. The pole figure intensities have to be normalized so that:

$$\frac{1}{4\pi} \oint P_h(y) dy. \quad (1.21)$$

Since the pole figure $P_h(y)$ is a reduced 2-D projection of the full qualified 3-D ODF $f(\mathbf{R})$, it represents a set of rotations around the sample direction y with an angle $0 \leq \gamma \leq 2\pi$. The relationship between $P_h(y)$ and $f(\mathbf{R})$ is then expressed by the pole figure inversion equation

$$P_h(y) = \frac{1}{2\pi} \int_{\gamma=0}^{2\pi} f(\mathbf{R}) d\gamma. \quad (1.22)$$

The factor $\frac{1}{2\pi}$ ensures the compatibility of the normalization conditions of ODF and pole figure (Randle and Engler, 2009). Finally, the ODF can be obtained by solving the fundamental equation 1.22. However, the ODF cannot be completely derived from a single pole figure so that additional pole figures have to be taken into account. The inversion equation cannot be solved analytically but numerous numerical approaches have been developed and published in literature, (e.g. Hielscher (2007); Hielscher and Schaeben (2008); Pospiech et al. (1993); Schaeben et al. (2007)).

1.4 Dislocations and grain boundaries

The crystal structure of technical materials is not perfectly built of unit cells but contains a number of defects. Point wise lattice defects include vacancies by missing atoms as well as

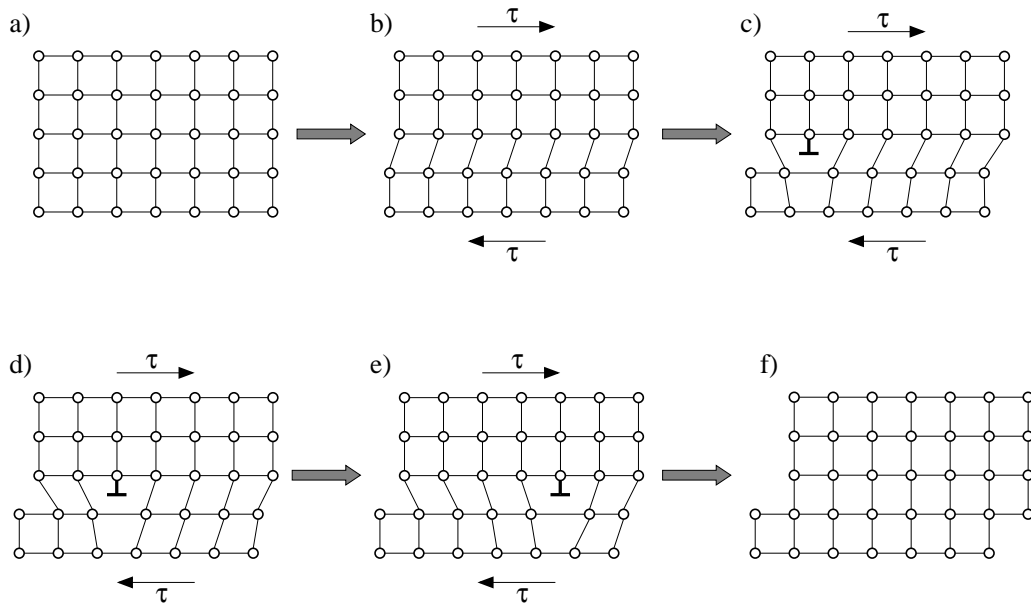


Figure 1.20: Plastic deformation by edge dislocation gliding. a) undeformed lattice; b) elastically deformed lattice under shear load; c) forming of edge dislocation; d)-e) dislocation gliding; f) plastically deformed lattice.

alloy atoms at positions of the crystal lattice or in-between as shown for solid solutions in Figure 1.7. These types of defects are also known as zero dimensional defects. Higher dimensional defects are called dislocations which significantly influence the materials' response on plastic deformation. The linear one dimensional edge dislocation occurs between two lattice planes with a different number of atoms as depicted in Figure 1.19a. Its absolute value and direction are modeled by the Burger's vector \mathbf{b} which is determined by comparing the length of a closed line around the dislocation with a closed line of the same height in a perfect reference crystal. The Burger's vector and the corresponding closed line are also shown in Figure 1.19a. If the dislocation line is not straight but curved instead, the resulting planar two dimensional lattice defect is a screw dislocation. An example including the defining Burger's vector is given in Figure 1.19b.

Dislocations do not statically remain in one position but can glide along the plane where they initiated. This effect leads to a dislocation motion during plastic deformation which is energetically much more efficient than a discrete motion of two lattices planes relative to each other. In Figure 1.20 a small crystal section undergoes plastic shear deformation. At a low shear loading level, the initial crystal lattice in 1.20a is elastically deformed while the atomic bindings remain intact as shown in 1.20b. With increasing shear load, an edge dislocation forms at a specific lattice plane in 1.20c and glides along this plane parallel to the direction of shearing in 1.20d - 1.20f. During the plastic deformation only the dislocations move while the rest of the crystal lattice remains connected. Due to the natural principal of energy reduction, dislocation gliding is favored along crystal planes with a high packing density. For materials with FCC crystal structure, such as aluminum, the highest packing density is found on planes perpendicular to the direction $[111]$ as shown by the gray shaded areas in Figure 1.12. Each of the close-packed planes in an FCC unit cell is then enclosed by six atoms. Depending on the

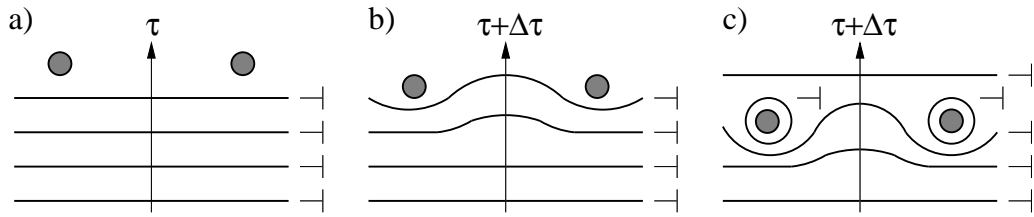


Figure 1.21: Scheme of Orowan type dislocation source. a) pile-up of edge dislocations in front of two obstacles; b) bending of the dislocation fronts; c) formation of dislocation rings around obstacles. Re-drawn from Bargel et al. (1999).

loading conditions and the initial orientation of the crystal towards the loading direction other glide systems are activated as well. Under severe plastic deformation the grains rotate and align to direction of load so that the energetically most favorable glide planes are active.

The dislocation gliding can be hindered by various effects such as solid solution atoms which distort the surrounding lattice, precipitates, stacking faults, grain boundaries or other dislocations. Two dislocations of the same type with inverse Burger's vectors annihilate each other when they meet on the same gliding plane. Each dislocation distorts the surrounding lattice as exemplarily shown in Figure 1.19. This distortion acts as a back stress on dislocations of the same type and direction and keeps them apart from each other. Depending on the type of obstacle, the edge dislocations can leave their initial gliding plane by climbing, and screw dislocations by cross-slipping to move perpendicular to their previous direction until a free motion in the original direction is possible. If the obstacle is too large or other interacting dislocations prevent a climbing or cross-slipping by their back stress, the arriving dislocations pile-up in front of the obstacle. Already piled-up dislocations also hinder the motion of following dislocations on the same lattice plane due to their back stress. The book of Hirth and Lothe (1982) gives a comprehensive overview on the modeling of dislocations and their interactions.

Small scale obstacles in the crystal lattice are passed by arriving dislocations. In Figure 1.21 a wave of edge dislocations encounter two small scale particles in the crystal lattice. The parts directly in front of the obstacles pile-up while the rest of the dislocation bends during motion in Figure 1.21b. With increasing plastic deformation dislocation rings are produced around the particles while the original edge dislocation proceeds on its way. Due to the remaining fixed dislocation ring, the effective diameters of the obstacles increase as indicated in Figure 1.21c. This process continues until the effective diameter of the particles prevents following dislocations from bypassing and forces them to climb or pile-up.

If an edge dislocation is pinned on both ends by small scale particles, a Frank-Read dislocation source develops, the mechanism of which is schematically depicted in Figure 1.22 (Frank and Read, 1950). Under plastic deformation the straight dislocation pinned by the particles A and B in 1.22a starts to bend into the configuration in 1.22b. With increasing deformation the dislocation undercuts the particles (see 1.22c and 1.22d) and finally reunites in Figure 1.22e. The detached dislocation ring then expands while the remaining pinned dislocation starts to bend again and the whole process repeats itself under continuing deformation load. In contrast to the dislocations produced by the Orowan mechanisms, the new dislocations of a Frank-Read source are mobile and depart from the sourcing particles. Due to the active dislocation sources,

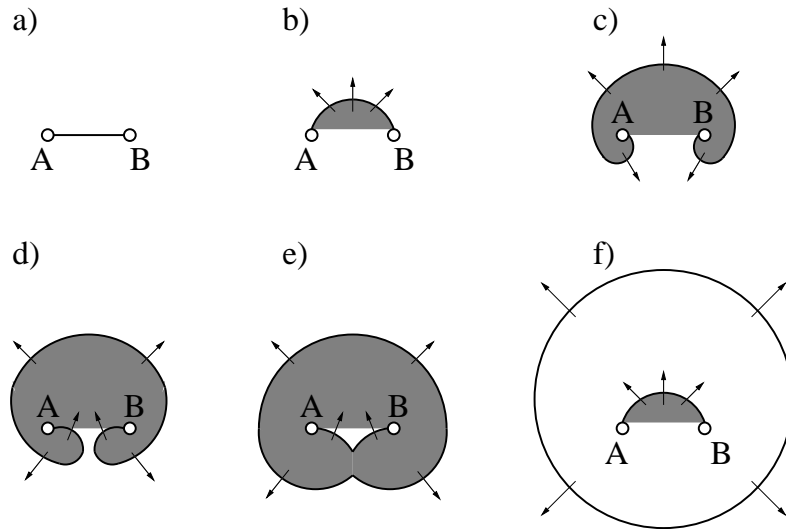


Figure 1.22: Scheme of Frank-Read type dislocation source. a) dislocation pinned between obstacles A and B; b)-d) bending of dislocation during plastic deformation leads to undercutting of the obstacles; e) detaching of dislocation ring; f) restart of periodic process. Re-drawn from Bargel et al. (1999).

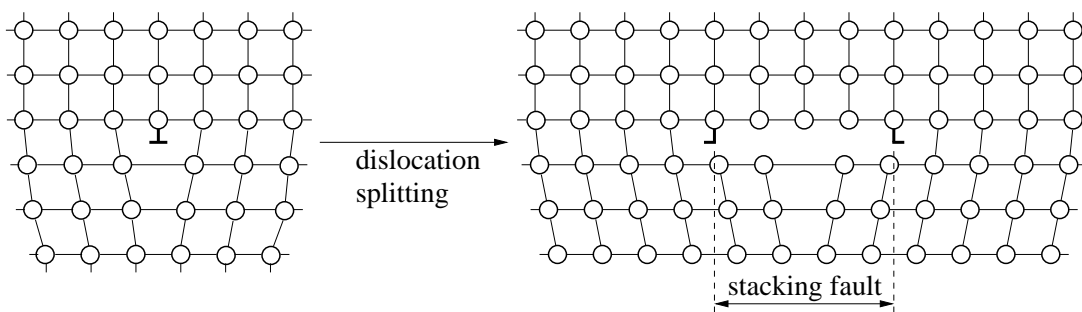


Figure 1.23: Stacking fault development by dislocation splitting. Re-drawn from Bauser et al. (2006).

the number of dislocations and the effective dislocation density (dislocation length per volume) increases during plastic deformation. As an example, the dislocation density of a soft-annealed metal increases by cold work hardening from 10^6 mm/mm^3 up to 10^{10} mm/mm^3 according to Bargel et al. (1999). By this dislocation density rise by several magnitudes, the internally stored energy in the distorted crystal lattices increases by 10^{-12} J/mm . Here, the length of the dislocations inside a reference value is measured.

One dimensional edge dislocation can form planar stacking faults by splitting as schematically depicted in Figure 1.23. The tendency of dislocation splitting is described by the characteristic stacking fault energy (SFE) which is material and temperature dependent. In materials with high SFE, the forming of stacking faults is energetically unfavorable and the number of occurring stacking faults is consequently low. The stacking fault energy of aluminum alloys treated in this work is comparably high. In pure aluminum the SFE is approximately 0.2 J/mm^2 almost completely suppresses the forming of stacking faults (Kammer, 2009). The influence of SFE on the forming behavior is crucial since stacking faults effectively prevent dislocation

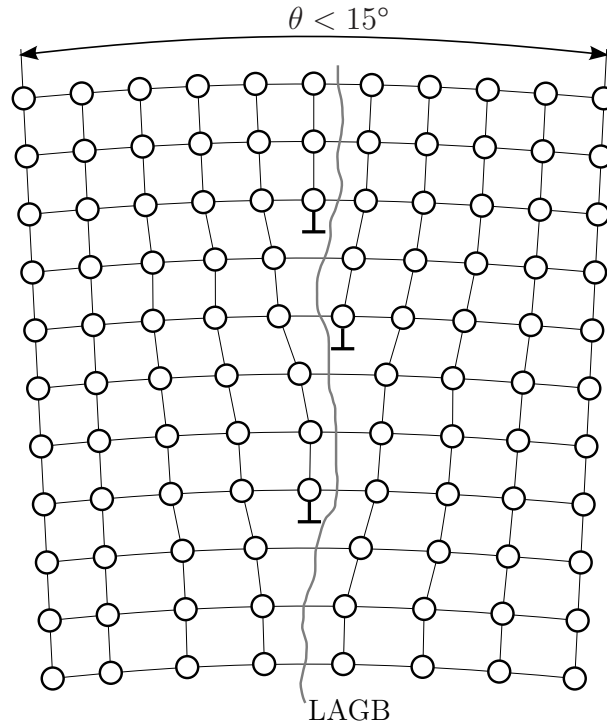


Figure 1.24: LAGB formation by dislocations. Re-drawn from Kammer (2009).

climbing and cross-slipping so that the existing dislocations are forced to remain in the original gliding plane even if they are hindered in their motion. This leads to an interaction between the already existing dislocations due to their back stresses and to a pile-up of dislocations in front of stacking faults which cannot be overcome. During continuous plastic deformation this dislocation pile-up raises the internal energy of the distorted crystal lattice until an energy level is reached to drive dynamic recrystallization as described later in Section 1.5.3.

The dislocations are generally necessary to keep the crystal lattice consistent under plastic deformation and to enable an angular variance in the shape of existing grains. The dislocations inside grains during plastic deformation can be categorized into statistically stored dislocations (SSDs), described by their density ρ_S , and geometrically necessary dislocations (GNDs) with a density ρ_G according to Ashby (1970) and Hughes et al. (2003). The SSDs are trapped by statistically distributed obstacles inside grains while the GNDs arrange themselves to long geometrically necessary boundaries (GNBs) inside the grains to compensate the change of the grain shape (Hansen et al., 2001). The resulting low angle grain boundary (LAGB) structure itself is subdivided into more or less equiaxial cells by incidental dislocation boundaries (IDBs) perpendicular to the GNBs (Godfrey and Hughes, 1997; Hughes, 2001; Hughes et al., 2003).

The formation of LAGBs by regular accumulation of edge dislocations is schematically depicted in Figure 1.24. Naturally this type of symmetric tilt LAGBs separates grain zones, the relative lattice misorientation of which is only a few degrees but may increase during plastic deformation. Following Gottstein and Shvindlerman (1999), the geometry of symmetric tilt LAGBs is described with the magnitude $b = |\mathbf{b}|$ of Burger's vector of the involved edge dislo-

cations, their mean distance d to each other, and the misorientation angle θ of the two separated grains by

$$\frac{b}{d} = 2 \sin \frac{\theta}{2} \approx \theta. \quad (1.23)$$

The energy stored of a single edge dislocations (ED) per unit length is

$$E_{\text{ED}} = \frac{\mu b^2}{4\pi(1-\nu)} \ln \frac{d}{r_0} + E_c \quad (1.24)$$

and depends on the material's shear modulus μ , its Poisson ratio ν , the specific energy of the dislocation core E_c and the dislocation core radius r_0 . The dislocation core radius can be approximated by the magnitude of the corresponding Burger's vector $r_0 \approx b$, so that, in combination with Equation 1.23, the stored energy of the symmetric tilt boundary (STB) per unit area depends on the misorientation θ of the adjacent grains according to

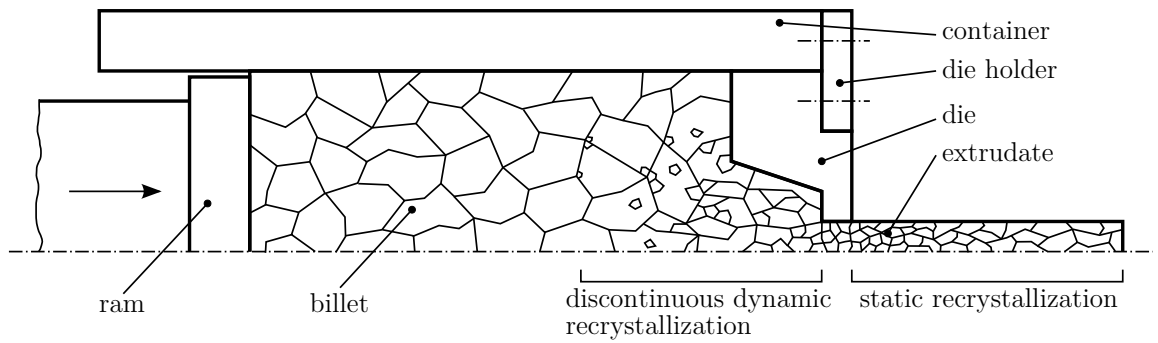
$$\gamma_{\text{STB}} = \frac{\theta}{b} E_{\text{ED}} = \frac{\theta}{b} \cdot \left(\frac{\mu b^2}{4\pi(1-\nu)} \ln \frac{1}{\theta} + E_c \right). \quad (1.25)$$

Since the dislocations defining an LAGB are not necessarily fixed, the boundary can move as a whole inside the hosting grain. The interior of cells and subgrains formed by LAGBs is dislocation poor and mainly contains trapped SSDs (Kocks, 1966). The formation of subgrain structures inside the existing grain is essential for most of the dynamic microstructure evolution processes discussed in the next section. A recent work describing a modelling approach covering the different types of dislocations and the resulting subgrain boundary types is published by Rezvanian et al. (2007).

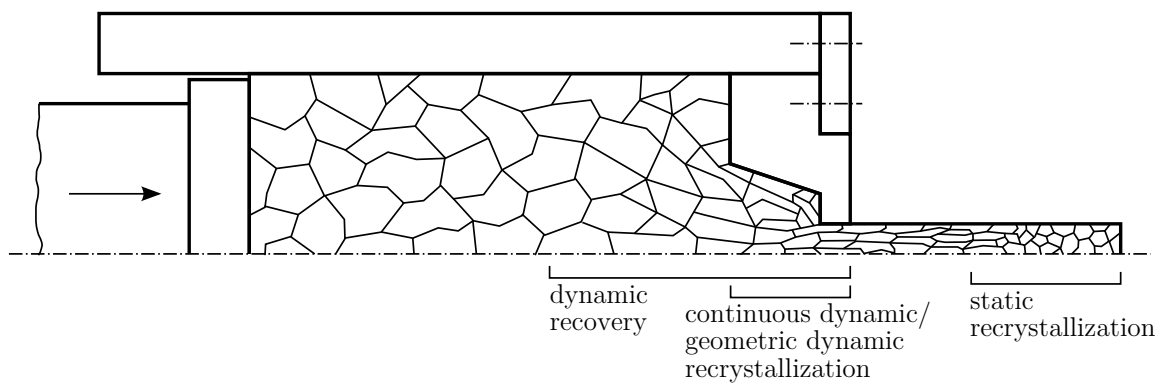
Grain boundaries exceeding a misorientation $\geq 15^\circ$ are denoted as high angle grain boundaries (HAGBs) which separate grains of the initial microstructure (Gottstein, 2004; Hughes et al., 2003). Above this threshold an increase of the misorientation of the adjacent grains no longer contributes to the grain boundary energy by Equation 1.25 (Gottstein and Shvindlerman, 1999). In contrast to LAGBs, the lattices of the adjacent grains at a HAGBs are not defined by a regular assembly of dislocations, but the transition from grain to grain contains a rather complex systematic atomic structure except for coincidence site lattice (CSL) boundaries, such as $\Sigma 3$ twin boundaries. Due to their regular structure, CSL boundaries contain much less energy per unit area than irregular HAGBs. Compared to LAGBs, the mobility of HAGBs is restricted and mainly driven by deformation induced energy or grain boundary energy (Gottstein and Shvindlerman, 1999; Humphreys and Hatherly, 2004). Dislocations are not capable of passing an HAGB from one grain to a neighboring one but pile-up in front of the grain boundary instead if they are not annihilated or rearranged by the microstructure evolution processes described in the following.

1.5 Processes of grain microstructure evolution

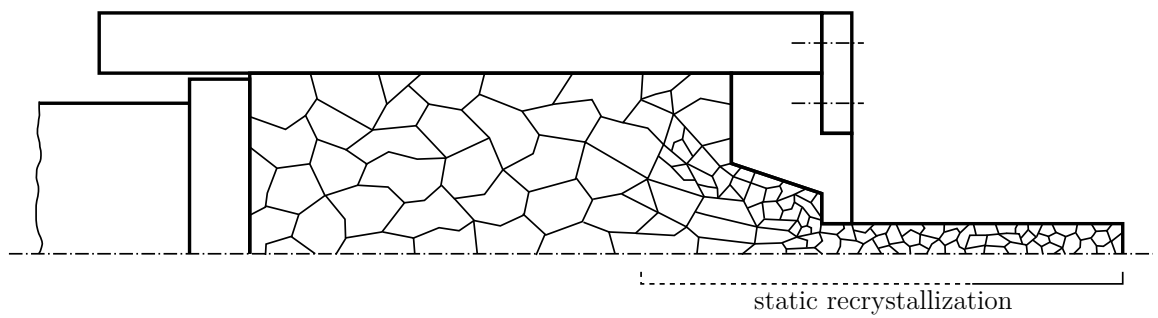
During plastic deformation the initial material's microstructure undergoes a number of evolution processes by recovery and different types of recrystallization. The microstructure evolution is generally divided into a dynamic part which is only active under continuous energy input due



(a) Low stacking fault energy. Continuous extrusion process.



(b) High stacking fault energy. Continuous extrusion process.



(c) High stacking fault energy. Extrusion process interrupted.

Figure 1.25: Recovery and recrystallization processes during extrusion of materials with high and low stacking fault energy. Partly re-drawn from Bauser et al. (2006).

to plastic deformation, and a static part which is evident after the deformation and driven by the induced energy already stored in the material. All types of evolution depend on a number of processes and material parameters such as temperature ϑ , strain ε , strain rate $\dot{\varepsilon}$ and SFE which is related to the alloy composition. Focussing on an exemplary extrusion process, Figure 1.25 depicts the active microstructure evolution processes of materials with low and high SFE. At this point only a rough distinction of the observed microstructures is given and a detailed description of the occurring processes follows in the next sections. An overview of the different microstructure evolution processes can also be found in the comprehensive review of Doherty et al. (1997) and in the book of Humphreys and Hatherly (2004).

During plastic deformation of materials with low SFE, the material dynamically recrystallizes in areas with high strains and strain rates as shown in front of the die in Figure 1.25a. The large number of stacking faults in the material prevents dislocation climb and the number of induced dislocations increases during deformation. When a critical temperature dependent energy level is reached, a discontinuous nucleation is initiated and the existing grain microstructure recrystallizes. After passing the die, no further plastic deformation is evident and the microstructure of the extruded rod undergoes static recrystallization to minimize the induced energy stored in the grains. At every stage of the extrusion process a large number of recrystallized, globular-shaped grains is observed in the billet and the extrudate.

The microstructure evolution of materials with high SFE, such as aluminum, differs due to enhanced dislocation climb as presented in Figure 1.25b. Here, dynamic recovery processes are energetically more favorable which efficiently reduce the induced internal energy of the grains by forming subgrain structures. With increasing strain, the new LAGBs continuously turn into HAGBs and elongated grains are fragmented by pinching off during continuous geometric dynamic recrystallization. Since no plastic deformation acts on the extruded rod, static recrystallization can be initialized under the given temperature conditions, resulting in new equiaxed grains and destroying the original fibrous grain microstructure.

The microstructure evolution of a high SFE material during an interrupted extrusion process is shown in Figure 1.25c. In the absence of plastic deformation, all dynamic microstructure evolution processes stall. However, the material of the billet near to the die inflow already experienced severe plastic deformation which increased the internal energy in this zone. This energy now drives the static recrystallization facilitated by the high temperature conditions inside the heated container. If the static recrystallization is not prevented by alloy additives for example, the fibrous grain microstructure is not preserved but replaced by globular-shaped, dislocation poor recrystallized grains.

1.5.1 *Dynamic and static recovery*

During hot working of polycrystalline materials with high SFE at elevated temperatures $\vartheta > 0.4 \vartheta_M$ (40% of melting temperature), the existing grains are deformed and a distinct subgrain structure evolves in the grain interior to ensure the lattice consistency even with severe changes of the grain shape. The dislocations' rearrangement to form LAGBs results from the restorative mechanism of dynamic recovery (DRV), the basic concepts of which can be found in the publication of McQueen (2001). DRV requires a relatively free motion of dislocations

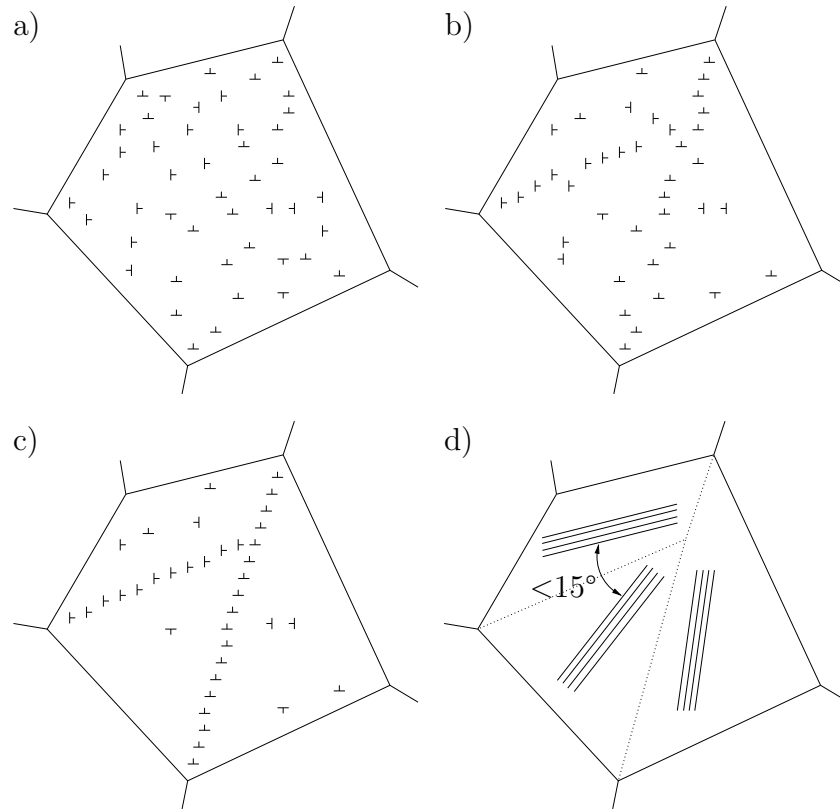
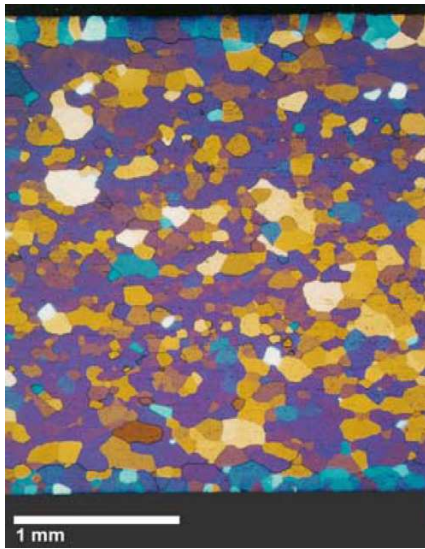


Figure 1.26: Subgrain formation during recovery. a) randomly distributed dislocations; b)-c) dislocation rearrangement and dislocation annihilation during dislocation gliding; d) misorientation of evolving cells does not exceed 15° .

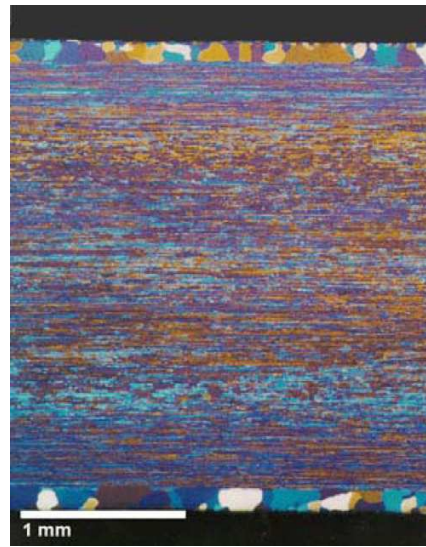
including dislocation glide, climb and cross-slip which is facilitated in materials with high SFE so that the number of hindering stacking faults is low.

DRV is the dominant mechanism which limits the flow stress in a steady-state forming process and is responsible for the good hot workability of materials with high SFE due to a permanent annihilation and rearrangement of dislocations into LAGBs. Figure 1.26 schematically depicts the annihilation of newly produced dislocations and their rearrangement into dislocation rich cell walls forming LAGBs. During plastic deformation the mobility of the LAGBs inside the grains and a permanent rearrangement forms predominantly globular-shaped subgrains. Generally, with increasing temperature ϑ or decreasing strain rate $\dot{\epsilon}$, the evolving subgrains are characterized by increasing diameter d , lower internal dislocation density ρ_i and larger dislocation spacing s . In the work of McQueen and Blum (2000) the influences of DRV during hot deformation of Al 99.9 are discussed and compared to alternative microstructure evolution processes presented in later sections.

If a high SFE material is kept at an elevated temperature directly after thermo-mechanical processing, static recovery (SRV) is activated. During annealing above the critical activation temperature, SRV remedies crystal defects arising from previous cold working while conserving the existing HAGB structure. In principle, the mechanisms of dislocation annihilation as well as LAGB evolution and migration during SRV are comparable to DRV. According to McQueen (2001), SRV takes much longer to reach an equivalent subgrain structure than DRV so that other



(a) Globular-shape recrystallized grains.



(b) Conserved fibrous grain structure due to recrystallization preventing Zr alloy additive.

Figure 1.27: LOM images of grain microstructure of an EN AW-71XX series alloy after extrusion (Li et al., 2005).

effects such as static recrystallization (SRX) might be more favorable, depending on the process parameters such as temperature, true strain, internal dislocation density, etc.

1.5.2 Static recrystallization

The grains of a plastically deformed microstructure contain a large number of dislocations which distort the crystal lattice and induce energy into the material. In order to minimize this internal energy, new dislocation free grains are formed by static recrystallization (SRX) at an elevated temperature. Starting from certain nucleation points at the existing HAGBs, newly formed grain boundaries migrate equiaxially into the surrounding distorted grains. This process is driven by the energy gradient between the dislocation poor recrystallized lattice and the energy rich deformed grains beyond the HAGBs. SRX stops if two already recrystallized grains touch, due to lacking driving energy difference.

The resulting grain microstructure consists of globular-shaped grains of similar size as exemplarily shown in Figure 1.27. In contrast to this, Figure 1.27b depicts a sample of the same EN AW-71XX alloy which additionally contains Zirconium to prevent any SRX. Here, the microstructure inside the extruded rod consists of the original deformed and elongated grains. However, at the surface of the rod a thin layer of recrystallized peripheral coarse grains (PCG) can be observed, resulting in inhomogeneous strains during extrusion as described by Geertruyden et al. (2005).

The modelling of static recrystallization over the time usually follows a Avrami-type equation $X(t) = 1 - \exp(-\beta t^k)$ as presented, e.g., by Gutierrez et al. (1988). The recrystallized fraction $X(t)$ of the microstructure depends on the time t and a parameter β which usually in-

cludes strain, temperature, initial grain size, etc. The time exponent k can be set to 2 in most cases.

If the recrystallized grain microstructure is not yet stable, secondary recrystallization and grain growth may occur which is now driven by the energy stored in the grain boundaries and not by dislocations in the grain interior (Humphreys and Hatherly, 2004). This driving force is usually much smaller than in the case of primary recrystallization so that HAGB migration during growth is much slower and more sensitive to temperature. Normal grain growth is a continuous process and results in homogeneously coarsened grain microstructure. Depending on temperature and alloy composition, also abnormal grain growth is possible where only a few grains discontinuously start to grow at the expense of their smaller neighbors.

1.5.3 Dynamic recrystallization

Discontinuous dynamic recrystallization

Materials with low SFE do not show a dynamic restorative mechanism such as DRV due to the large number of stacking faults efficiently preventing the necessary dislocation climb and cross-slip. Instead of dislocation annihilation or rearrangement into a subgrain structure, the dislocations induced during plastic deformation pile-up as GNDs in the interior of the existing grains. This leads to a continuous increase in internal energy of the deformed grains. At a critical internal energy level reached by a critical strain ε_c , nucleation along the existing HAGBs is initialized, depending on temperature ϑ and strain rate $\dot{\varepsilon}$. The subsequent recrystallization by grain boundary migration driven by the stored deformation energy is comparable to SRX already described in the previous section. Since the critical energy for nucleation is reached for individual grains at different times, the observed microstructure consists of a mixture of original dislocation rich deformed grains and newly formed dislocation poor grains. The two distinct phases of nucleation and growth define this type of dynamic recrystallization as a discontinuous process called discontinuous dynamic recrystallization (DRX). A detailed overview of the history of the DRX theory can be found in McQueen (2004) and more general information also in Humphreys and Hatherly (2004).

Under continuous plastic deformation new dislocations are also induced into the new recrystallized grains until sufficient deformation for a new nucleation is reached. Starting from the grain sizes of the initial microstructure, a specific mean grain size evolves with increasing strain leading to an equilibrium fraction of deformed and currently recrystallizing grains. The mean size of the recrystallized grains in steady state is independent on the initial grain size and remains constant throughout the deformation. In the stress-strain curve of low SFE materials a characteristic peak can be observed at the critical strain ε_c until the softening effect of DRX lowers the flow stress to a steady-state level.

The microstructure characteristics of DRX can be expressed by the Zener-Hollomon parameter $Z = \dot{\varepsilon} \cdot \exp\left(\frac{Q}{R\vartheta}\right)$ which includes the process parameters strain rate $\dot{\varepsilon}$ and temperature ϑ . Here, Q is the characteristic activation energy and R is the gas constant. With decreasing stress σ or decreasing Z , also the critical strain ε_c generally reduces except for very low strain rates $\dot{\varepsilon}$, for example during creep (Humphreys and Hatherly, 2004). As proposed by McQueen and Imbert (2004) and others, the flow stress follows the equation $\sigma = \frac{1}{\alpha} \cdot \operatorname{arsinh}\left(\left[\frac{Z}{A}\right]^{\frac{1}{n}}\right)$ for

a broad range of σ with the material constants A , α and n . Nevertheless, several other descriptions depending on the true stress level are possible, as for example given by McQueen (2001). In materials with high SFE such as aluminum, the internal energy level to initialize nucleation is never reached due to competitive DRV processes which continuously reduce the internal energy and number of free dislocations.

Continuous dynamic recrystallization

Materials of high SFE also show a significant reduction in grain size during plastic deformation which cannot be explained by DRV that only forms new LAGBs by dislocation rearrangement but no HAGBs. DRV requires a high mobility of these LAGBs which facilitates their annihilation and continuous rearrangement leading to a equiaxed subgrain structure. If the mobility of the LAGBs is prevented, the existing subgrains have to rotate to follow the deformation of the hosting grain. The strain induced subgrain rotation proceeds until the misorientation exceeds the critical angle and until the LAGBs continuously turn into HAGBs (Kaibyshev et al., 2005). This process is denoted as continuous dynamic recrystallization (DRX) (Humphreys and Hatherly, 2004). Due to the globular shape of the former subgrains, the newly developed grains are also mainly equiaxial. With increasing strain these new grains undergo DRV followed by CDX so that the number of grains rises with increasing strain while the mean grain diameter decreases. Since the CDX mechanism shows no nucleation like the classical SRX and DRX, the name “recrystallization” is a little misleading. Nevertheless, this mechanism also produces new globular-shaped grains with low dislocation density so that at least the resulting newly formed grains justify the designation as recrystallization process.

The concept of CDX has been applied to the simulation of thermo mechanical processing of pure aluminum or aluminum alloys by several groups. Huang and Humphreys (1997) describe CDX as a transient microstructure evolution process with a strong strain rate dependency which is superposed by DRV. The microstructural results of CDX based on EBSD measurements after equal-channel angular extrusion of a grain refining Al-Li-Mg-Sc are discussed by Kaibyshev et al. (2005). The grain size evolution of a commercial-purity aluminum during an equal-channel angular extrusion process is modelled via CDX and simulated by Hallberg et al. (2010).

Geometric dynamic recrystallization

However, a number of groups disagree that the microstructure evolution of aluminum alloys can be efficiently modelled by the mechanisms of CDX. For example, the publication by Gourdet and Montheillet (2003) presents a model of CDX for aluminum alloys which is criticized by McQueen and Kassner (2004). They present a geometrical mechanism which leads to a significant grain refinement and increasing fraction of HAGBs denoted as geometric dynamic recrystallization (GDX). Here, the globular shaped subgrains do not turn into grains by relative rotation. Instead, they force the existing HAGBs of the initial grains to serrate during elongation under plastic deformation as schematically depicted in Figure 1.28a. If the short diameter of the original grains reaches a thickness of 2 or 3 subgrains, the opposite HAGBs touch and the grain fragments by pinching-off. In contrast to CDX, the LAGBs formed during previous DRV do not turn into HAGBs during GDX.

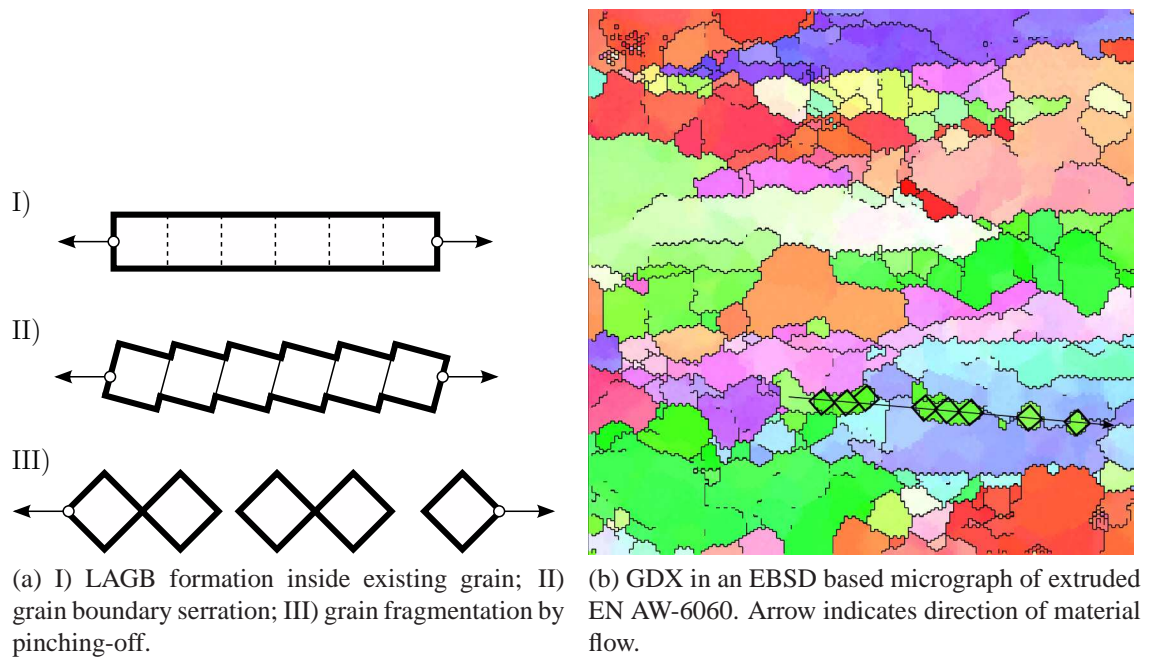


Figure 1.28: Schematic geometric dynamic recrystallization.

A chain of grain fragments with almost identical orientation as shown at stage III in Figure 1.28 can also be found in an exemplary EBSD based micrograph in Figure 1.28b. Similar structures of small grains of same orientation which are aligned in direction of material flow are found in several micrographs presented in Chapter 3 of this work. Furthermore, the characteristic serrated shape of the deformed initial grains proves the presence of GDX during the experiments. Comparable to CDX, the categorizing of GDX as recrystallization process is misleading due to the absence of nucleation. McQueen (2004) therefore proposes to describe GDX as grain refining DRV instead.

1.6 Measurement techniques for grain microstructure characterization

1.6.1 Light optical microscopy

The oldest technique used for microstructure characterization of metallic material is the light optical microscopy (LOM). In order to reveal the grain microstructure, the surface of the sample has to be prepared by mechanical polishing and chemical etching. Depending on the material, several etching reagents are known which attack the surface of the grains and HAGBs with different intensity due to their different atomic structure. This improves the contrast between grains and boundaries in the obtained LOM image. Especially for aluminum alloys common etching reagents are based on the recipe published by Flick (1925). A further contrast improvement can be achieved by the usage of polarized light. Here the lattice orientation of the individual grains influences the light reflection and the filtered image shows the grains in different colors.

The grain microstructure characterization is performed manually by the operator or by automated image processing. The characterization techniques include a visual comparison of the microstructure LOM image with test images, planimetric and intercept procedures which are

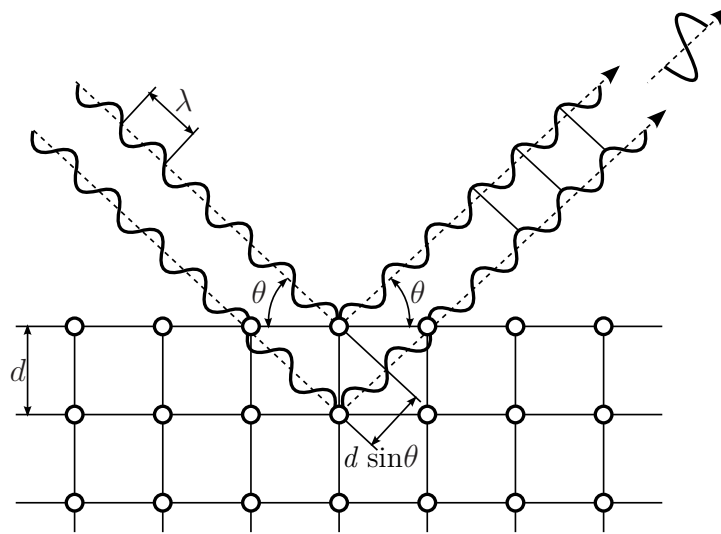


Figure 1.29: Bragg diffraction of an X-ray beam on a crystal lattice.

defined in (ASTM International, 2004), for example. In the planimetric procedure the number of grains inside a defined testing area is counted and the mean grain size is derived from the size of the testing area. For the intercept method a test line of a defined length is overlaid to the picture and the number of intersected grains or grain boundaries is counted to determine the mean grain size. The quality of the statistical results is influenced by the grain structure and the chosen characterization method.

Since the light is reflected by the surface, the sample dimensions are only limited by the microscope device used. The reflected light is not influenced by the outer atmosphere so that a vacuum chamber is not necessary. LOM images allow a quick access to the grain microstructure statistics but do not provide any information regarding the grain orientations and texture. Furthermore, LAGBs inside the grains are normally not emphasized during etching so that a characterization of the subgrain structure is usually not possible.

1.6.2 X-ray diffraction

To reveal information on the texture of a sample, X-ray instead of light can be used. By filtering the X-rays produced by an X-ray tube, monochromatic X radiation of a rather discrete wave length spectrum is produced and focused on the sample surface. An introduction to this technique is given by Gottstein (2004), for example. During reflection of the X-rays by the crystal lattice of the sample the radiation is intensified or annihilated due to the Bragg condition $2d \sin \theta = n\lambda$. The distance between the atomic lattice layers is d and the direction towards the sample surface is described by the angle θ and the characteristic wave length of the monochromatic X radiation is λ . Figure 1.29 schematically visualizes the Bragg diffraction of X-rays during reflection by two atomic lattice layers. During X-ray diffraction (XRD) the angle θ is continuously varied by rotating the mounted sample under a fixed X-ray beam or by a circular motion of the X-ray source around the specimen.

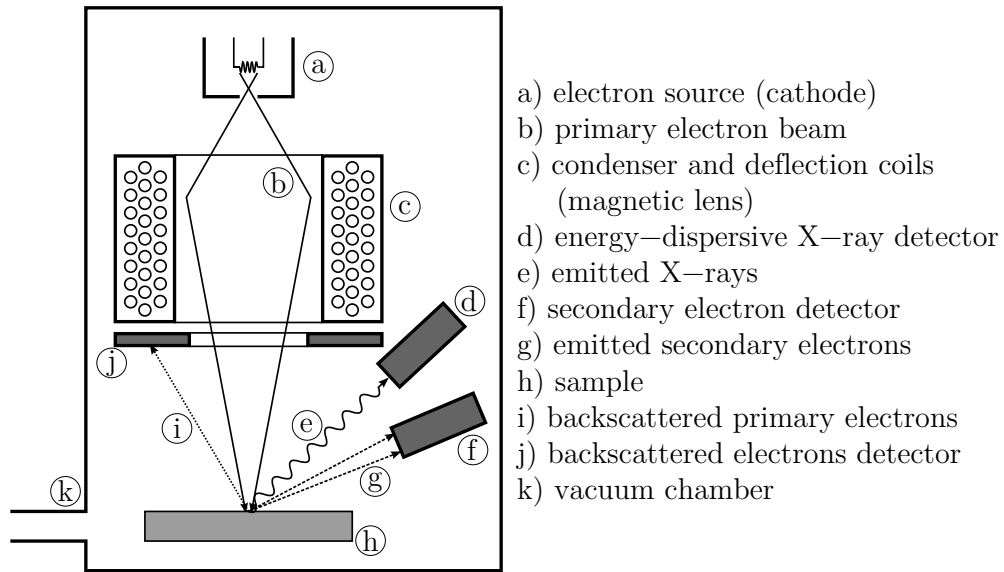


Figure 1.30: Simplified scheme of a scanning electron microscope.

1.6.3 Scanning electron microscopy

The maximum detail resolution of LOM is limited to ~ 200 nm due to the mean wave length $\lambda = 550$ nm of visual light. The use of electrons instead of light allows a higher magnification of 500'000 which reveals details of a minimum size of 1 nm. In contrast to light, the incident electrons interact with the sample atoms allowing further determination of material characteristics such as density and chemical composition. In the field of materials science the scanning electron microscope (SEM) is a widely used technique for microstructure characterization. The simplified scheme of an SEM is depicted in Figure 1.30 following the introduction into SEM technique of Vernon-Parry (2000). A primary electron beam (b) is emitted by a tungsten cathode (a) and accelerated to an energy of $0.5 \sim 40$ keV. Condenser coils (c) are used as magnetic lenses to focus the electron beam onto the sample surface (h). Deflection coils allow to move the beam in a raster over the sample surface. Some SEM devices use a fixed electron beam and a movable sample holder, the position of which is controlled by stepping motors.

When the primary electrons interact with the sample atoms near the surface of the sample, they are repeatedly scattered and partially absorbed. The absorption of high-energy primary electrons initiates electromagnetic radiation in form of characteristic X-rays. The energy of the emitted X-rays is individual for each element. Therefore the energy-dispersive X-rays (EDX) (e) are detected to determine the exact chemical material composition (chemical fingerprint) at the current measurement point on the sample surface. In contrast to XRD, only the intensity of the X-rays is measured in (d). Orientation information due to diffraction effects is not evaluated. The topology visualization of the sample is obtained by the emitted low energy secondary electrons (g) resulting from inelastic scattering. The number of the secondary electrons detected in (f) depends on the tilt of the sample surface towards the primary electron beam so that the obtained image appears as if the surface were illuminated from the direction of the electron source. Depending on the sample material density, a number of primary electrons are backscattered with still high energy (i). The backscattering angle towards the incident beam

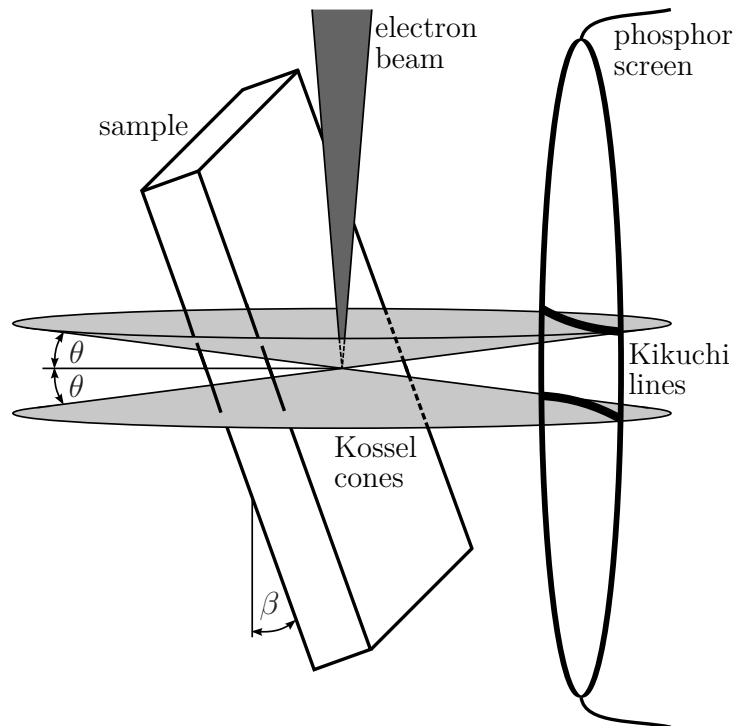


Figure 1.31: Formation of Kikuchi lines by electron backscatter diffraction according to Randle and Engler (2009).

is quite low and specifies the position of the backscattered electron (BSE) detector (j) around the primary beam. BSE-SEM images reflect the density contrast in the sample rather than the sample topology. This feature can be used to identify precipitates in a metal matrix due to their different densities.

To prevent any interaction of the primary electron beam, the response electrons and radiation emitted from the sample with the outer atmosphere, the whole SEM is enclosed inside a vacuum chamber (k). The maximum dimensions of the sample are limited due to the size of the vacuum chamber. Furthermore, the measurement area is limited due to the maximum primary beam deflection or the area covered by the stepping motors drives. The sample has to be electrically conductive at least at its surface. For biological materials and tissues this enforces a thin coating of metal, e.g. of gold, which improves the image contrast due to its high density.

1.6.4 Electron Backscatter Diffraction

The backscattered primary electrons of an SEM can also be used to obtain information on the lattice orientation at the current measurement point. A review of different electron diffraction based techniques applied to bulk samples is given by Wilkinson and Hirsch (1997). The electron backscatter diffraction (EBSD) technique requires an additional phosphor screen and an attached CCD camera system to identify the Kikuchi bands (Nishikawa and Kikuchi, 1928) resulting from Bragg diffraction of the backscattered electrons (see also Section 1.6.2). These diffraction patterns produced by an SEM were first reported by Coates (1967).

The backscattered electrons are emitted from the surface near lattice atoms in the form of two symmetric Kossel cones as depicted in Figure 1.31. By a tilt sample orientation with an

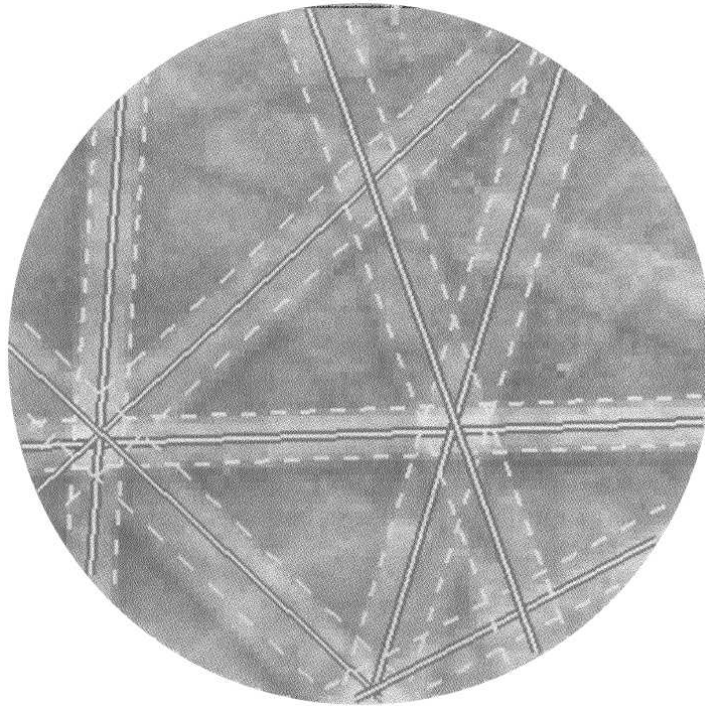


Figure 1.32: Band recognition of Kikuchi pattern (Kunze et al., 1993).

angle of $\beta \approx 70^\circ$ towards the direction of the primary electron beam, the Kossel cones cut the electron sensitive phosphor screen attached perpendicular to the electron beam. Position and direction of the produced Kikuchi pattern depend on the crystal lattice orientation at the current measurement position on the sample surface and are recorded by a CCD camera system located behind the phosphor screen. Sharp diffraction patterns can only be achieved by an intact atomic lattice structure at the specimen's surface. Therefore the sample has to be electrolytically or chemically polished to remove the top layers, the atomic lattice of which is distorted by previous mechanical machining and polishing.

The EBSD scan follows a fixed user defined raster on the specimen's surface and the recorded pattern remains constant as long as the raster points belong to the same crystal. Therefore a full scan requires an automated and fast pattern recognition and indexing software. The first automatic Kikuchi band recognition was introduced by Wright and Adams (1992) using the algorithm proposed by Burns et al. (1986) to identify the straight lines in the diffraction pattern. Later the band recognition algorithm was replaced by the faster and more robust Hough transform (Kunze et al., 1993; Wright, 2000). Each line of an image can be parameterized by the rotation angle θ and the distance ρ towards the origin of a coordinate system by $\rho = x \cos \theta + y \sin \theta$. Here, $\{x, y\}$ is a set of all coordinates forming a line. When parameterizing the complete Kikuchi pattern image and adding the brightness intensity of each pixel to the Hough parameters (ρ, θ) results in a gray scale image where the intersection points of the Kikuchi bands appear as characteristic peaks in the Hough space.

For the pattern identification the contrast of the Kikuchi bands is improved by additional image processing steps including background subtraction. An exemplary improved Kikuchi pattern with identified bands is depicted in Figure 1.32. The orientation of the crystal lattice at

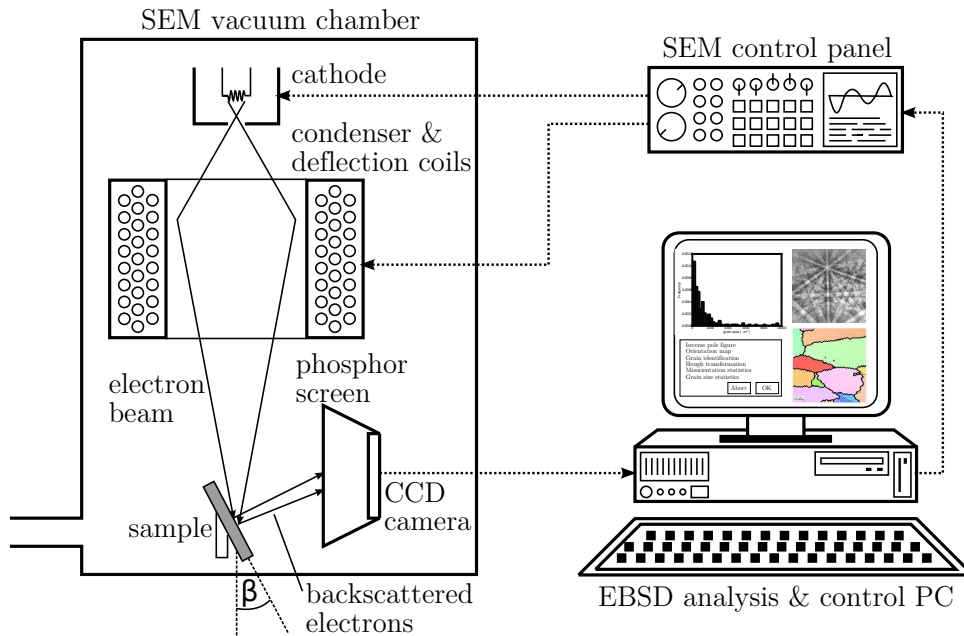


Figure 1.33: Simplified scheme of an EBSD system.

the current measurement point is then derived by identification of the band intersection points and assignment of the corresponding Miller indices by a voting scheme with help of a look-up table as described by Wright (2000). The reliability of the obtained Miller indices is expressed by the confidence index (CI) value which is discussed in Section 2.2.2.

A fully automated EBSD scanning system as schematically depicted in Figure 1.33 was used by Wright et al. (1993) and Adams et al. (1993) for the pattern analysis of polycrystalline aluminum samples. The connected analysis and control PC performs the indexing of the Kikuchi pattern obtained from the CCD camera system of the SEM. Furthermore, the PC controls the positioning of the SEM electron beam on the sample surface according to the user defined scanning raster. Due to the tilt mounting of the sample, this also includes a focus adjustment depending on the current measurement point position. Two types of scanning modes during data acquisition are generally possible which are subjected to the used SEM device. During beam scanning, the sample position inside the SEM remains fixed and the direction of the incident electron beam is controlled by the deflection coils. At the perimeter of a large scanning raster this may lead to an additional measurement error of $\sim 1^\circ$ in the obtained lattice orientation, since the geometry of the incident electron beam on the specimen surface is distorted into an elliptic shape (Humphreys, 2001). The stage scanning mode uses a fixed primary electron beam in the SEM and moves the sample by stepping motors instead. Here, the electron beam geometry remains constant but the speed of data acquisition is much slower compared to beam scanning.

The angular resolution of the minimum misorientation between two adjacent data points is limited by the image quality of the diffracted Kikuchi pattern and the implemented band recognition algorithm. The contrast of the Kikuchi bands increases for material with higher density and higher acceleration voltage of the incident electron beam. The density of the sample material is immutable and the acceleration voltage is bounded by the SEM device. With a

properly calibrated EBSD system Humphreys (1999) determined a minimum misorientation threshold for aluminum alloys of $1 \sim 1.5^\circ$. A method to improve the angular resolution by reduction of the orientation noise caused by IDBs is presented by Godfrey (2004).

The identification of small scale grain and subgrain structures requires a sufficient spatial resolution which depends on the positioning accuracy of the beam or sample and the geometry of the electron beam on the sample surface. If the area of the electron beam covers more than only one grain, the overlapping diffraction pattern inhibits a correct orientation indexing. A minimum step size of 20 nm perpendicular to the tilt axis of the sample was reached for aluminum by Humphreys et al. (1999) with a field emission gun SEM in beam scanning mode. The usage of an SEM with tungsten filament reduces the spatial resolution by a factor of $2 \sim 3$. In directions parallel to the sample tilt axis the spatial resolution is lower if the electron beam geometry is not adapted by the SEM control software. The limitations of the EBSD technique for the characterization of fine-scale microstructure in the context of angular and spatial resolution are discussed by Humphreys (2004a).

Comparable to XDF, the EBSD technique allows to determine the texture and misorientation distribution of the observed sample microstructure (Baba-Kishi, 2002; Davies and Randle, 1996). But apart from pole figure plots it also facilitates a detailed representation of the grain and subgrain microstructure by grain orientation maps. For each measurement point the relative misorientation towards its neighbors can be evaluated which gives an insight to the orientation variance inside grains investigated by He et al. (2008) for cold-rolled aluminum. The generation of grain orientation maps, grain size and misorientation statistics as well as texture representation by IPFs are all topics of Chapter 2.

The diffraction patterns of the SEM are emitted from the atomic layers directly under the surface of the specimen. In consequence, single EBSD based micrographs only reflect the grain microstructure of the thin surface layer. The integration of a focused ion beam (FIB) canon allows a sequential removal of the top layers after the EBSD scan and gives access to the layers below. The application of combined EBSD-FIB systems as well as several possible arrangements for an FIB mounting inside the SEM are presented and discussed by Schwartz et al. (2009). The obtained sectional EBSD scans are finally assembled into a 3-D microstructure representation in an additional postprocessing step. Further information on the recent developments in the field of EBSD can be found in the publications of Randle (2008) and Randle (2009).

Chapter 2

Software development

Abstract – The orientation angles obtained by the EBSD technique allow a graphical visualization and statistical analysis of the investigated microstructure. Before presenting the in-house software package Grainplot which is used to generate the micrographs and microstructure statistics presented in this work, two already available software packages are briefly introduced. The programming motivation then highlights the differences and limits of the existing programs which initiated the development of an own code. The basic features of Grainplot are described in detail and the core algorithms are given in pseudo-code. The results obtained by the new code are verified against a commercial software package and an open source solution. Finally, the newly developed synthetic microstructure generator Graingen and some exemplary synthetic micrographs in 2-D and 3-D are presented.

2.1 Discussion of existing EBSD software

2.1.1 OIM - Orientation Imaging Microscopy

The widely used commercial software Orientation Imaging Microscopy (OIM™) of the TSL/EDAX company combines the work of scientific groups at the universities in Bristol and Sussex. In both groups the basics of automated diffraction scanning and pattern recognition have been investigated in the years from 1973 to 1983. At the end of the 1980s other groups at the universities in Oxford, Yale, Clausthal and the Risø Laboratory lead their focus on similar topics, too. Especially the concepts developed during 1991 and 1993 by a team at Yale University under supervision of B.L. Adams found their way in the early versions of the OIM software. A description of the first fully automatic EBSD pattern recognition system was published in Adams et al. (1993). A detailed overview of the basic capabilities of the OIM software can be found in the publications of Schwartz et al. (2000) and Wright et al. (2000).

Nowadays the OIM software consists of two independent packages called OIM Data Collection (OIM DC) and OIM Analysis (OIM A). The former one is often part of integrated EBSD systems and controls the data acquisition in the SEM appliance. During the EBSD measurements, OIM DC gives an instant access to SEM image of the specimen and the Kikuchi pattern diffracted at the current measurement point. Furthermore, OIM DC improves the pattern image by contrast enhancement, noise reduction, background subtraction and other image manipulation techniques. Finally the pattern recognition is performed by using the Hough transform as outlined in Section 1.6.4. The resulting orientation angles in Euler representation at certain coordinates, as well as additional information such as image quality, phase and confidence index (CI) are stored in a binary file format or optionally in a list styled ASCII file. If necessary,

the angle representation in the output file may vary but, in the context of this work, only the Euler representation is used.

The microstructure visualization and statistical analysis is done by OIM A on the basis of the input files provided by OIM DC. The visualization modes offer different color schemes to clearly distinct individual grains in the micrographs, but also allow a coding of grain orientation based on different types of standard orientation triangles. In addition to micrograph plots, the orientation of each data point of the EBSD measurement can be used to fit an orientation density function (ODF). The basic microstructure statistics include number and sizes of individual grains separated by grain boundaries with an arbitrary angle, e.g., the standard value for HAGB is 15° (Humphreys, 1999). Since the EBSD method gives direct access to the spacial orientation at each measurement point, this information is used to determine the mean misorientation between all grains in the measurement area, for example. Micrographs and microstructure statistics such as grain size and misorientation distribution are used to compare and validate the results obtained by the newly developed in-house code Grainplot, as described in Section 2.2.

2.1.2 MTEX - A Matlab Toolbox for Quantitative Texture Analysis

MTEX is an open source collection of functions and objects to handle microstructure characteristics such as grains, orientations, ODFs and texture which are bundled in a toolbox for the commercial numerical computing environment Matlab. In contrast to the OIM software package, MTEX has its roots in the field of pole figure and ODF generation and their visualization based on the work of Schaeben et al. (2007) and Hielscher (2007). A detailed description about the newly implemented ODF estimation scheme is presented in the work of Hielscher and Schaeben (2008). In contrast to the commercial OIM software package, MTEX only allows the analysis of existing EBSD measurement data but is not capable of controlling an EBSD-SEM system to perform measurements. It features micrograph plotting, determination of grain sizes and grain misorientation distribution as well as ODF generation.

All functions, objects and data types defined in MTEX are accessible to the user by the applications programmers interface (API) and can also be embedded into a self-written Matlab code. This allows a flexible handling of EBSD data sets, but requires an installed Matlab environment and the coding of own programs if statistics besides the supported standard features are required. In the context of this work, especially the micrographs and statistics produced by MTEX in the version 3.0 are used for a qualitative and quantitative validation of the results of the new program Grainplot.

2.2 Microstructure plotter and analyzer Grainplot

2.2.1 Programming motivation

A software package such as OIM shares the same problem with almost all other commercial software: its closed source. This means that the user has no influence or knowledge on how specific tasks are performed by the software code. The whole program acts like a black box which requires certain user information and input data in order to produce a specific output. In contrast to this, the project wherein this work is embedded requires full access to all internal

data processing steps. As part of an integrated simulation chain it is necessary to hand over data from one program to the next by providing appropriate interfaces. The coding of an in-house stand-alone program for micrograph representation and microstructure analysis allows to deal with both issues:

- Full access to all data processing steps by directly varying the Grainplot code.
- Direct implementation of necessary interfaces for data exchange between different programs.

The first versions of Grainplot were written when MTEX only poorly supported the handling of EBSD data. However, in the current versions it is still necessary to write additional input/output parser programs which would allow to integrate this program into the existing integrated simulation chain. Both OIM A and MTEX only deal with existing EBSD data files. However, Grainplot also allows to characterize artificial microstructures, e.g., produced by the in-house software Graingen introduced in Section 2.3.1. The grain detection algorithm can also be extended to characterize micrographs obtained by ordinary LOM or LOM with polarized light if the contrast between adjacent grains is sufficient. In the current versions this still requires a manual contrast improvement.

All parts of the introduced software Grainplot are written in Python if not explicitly stated otherwise in the text. Python is a high level object-oriented script language which is highly extensible and offers free access to a large number of multipurpose modules, e.g., image manipulation, database handling, mathematical routines, etc. Although it is an interpreted programming language, the drawback of slower code execution compared to compiled programs is more than compensated by its intuitive and clear code structure which supports a fast prototyping and programming process. The progress of programming development and a selected collection of obtained results by different program versions can be comprehended in the publications of Kayser et al. (2010, 2009, 2008); Parvizian et al. (2010a); Svendsen et al. (2009).

2.2.2 *Microstructure visualization*

Input file format

The visualization of EBSD measurement results in the form of colorized micrograph plots in Grainplot is generally performed by the following scheme. A raw data set provided by OIM DC in a list styled ASCII file format contains the three Euler angles φ_1 , Φ , φ_2 ($0 \leq \varphi_1, \varphi_2 < 2\pi$, $0 \leq \Phi < \pi$) for a passive rotation in Bunge's notation for each measurement point. This describes the orientation of the local crystal coordinate system in space at the coordinates of the current measurement point on the specimen's surface. Furthermore, OIM DC provides additional information such as identified phase, detector signal quality and CI. The first lines of a sample ASCII input file including its header are given in listing 2.1. Comment lines in the header are marked by a preceding hash sign ('#') and ignored during data processing.

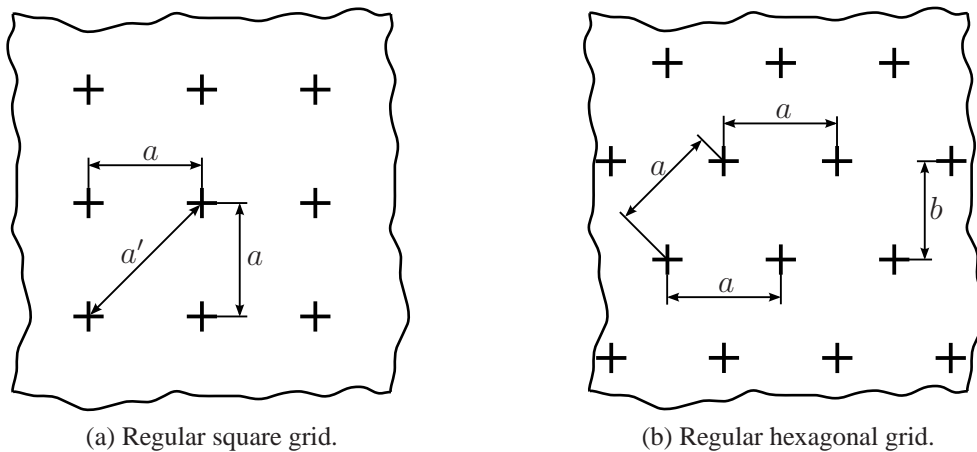


Figure 2.1: Types of scanning rasters for EBSD measurements. Measurement points are marked by crosses.

Listing 2.1: Header lines (1-9) and first four data sets (lines 10-13) of an exemplaric OIM DC input file in ASCII format.

```

1 # Header:  Project1 :: Punkt6 :: All data :: Grain Size    6/12/2007
2 #
3 # Column 1–3: phi1, PHI, phi2 (orientation of point in radians)
4 # Column 4–5: x, y (coordinates of point in microns)
5 # Column 6:   IQ (image quality)
6 # Column 7:   CI (confidence index)
7 # Column 8:   Fit (degrees)
8 # Column 9:   phase (index identifying phase)
9 # Column 10:  sem (detector signal value)
10 4.63998    2.11299    2.66515      0.00000      0.00000    64.9
    0.514     0          1    1.063
11 3.35111    1.10465    0.57819      4.00000      0.00000    87.3
    0.357     0          1    1.365
12 3.35423    1.10831    0.57006      8.00000      0.00000    76.7
    0.952     0          1    0.728
13 3.35243    1.11980    0.55998     12.00000     0.00000    76.5
    0.369     0          1    1.102

```

As described in Section 1.6.4 EBSD is a raster scanning technique. The measurement point distribution depends on the material, expected grain sizes and the hardware equipment. Different strategies for EBSD data acquisition with a special focus on data point reduction are discussed by Humphreys (1999, 2001). OIM DC supports different types of measurement point grids, two of these being significant in the context of this work. The simplest distribution is a regular square grid of measurement points on the specimen's surface with a constant step size a as shown in Figure 2.1a. This grid allows a direct representation of each measurement point by a quadratic pixel or a group of pixels. In addition, the regular hexagonal distribution of measurement points is widely used in the field of EBSD measurements. In the hexagonal grid three measurement points form an equilateral triangle as indicated in Figure 2.1b. Here, the reduced

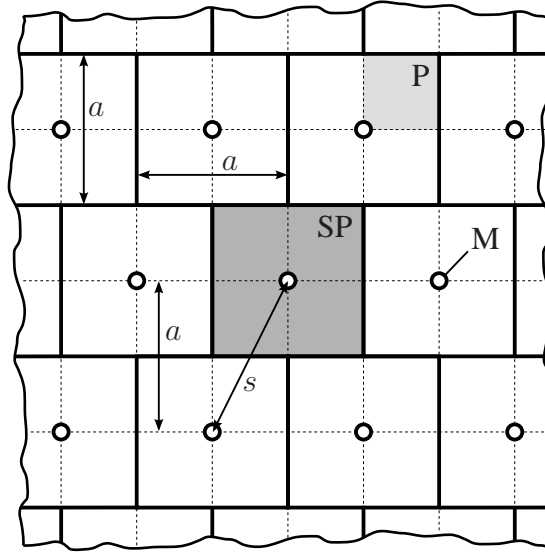


Figure 2.2: Assembly of pixels (P) and super-pixels (SP). Measurement points (M) are indicated by circles.

vertical line spacing $b = \sqrt{\frac{3}{4}} a$ increases the measurement point density by 15.4 % compared to the square grid. The advantage of the hexagonal grid over the square grid is the constant distance between a measurement point and its six direct neighbors. In contrast to this, a point in the square grid has four direct neighbors (to the right, left, below and above) in the distance a and for neighbors at the edges in the distance $a' = \sqrt{2} a$. The change in distance between these two groups has to be compensated by an appropriate weighting function during the analysis.

In the case of a hexagonal or other non-quadratic grid of measurement points, it is necessary to superpose a grid consisting of grouped pixels which allows to represent the micrograph with naturally quadratic shaped pixels. Figure 2.2 shows an assembly of pixel groups – named super-pixels – which represent a hexagonal grid of measurement points indicated by circles. Each super-pixel (SP) consists of 2×2 pixels (P) located around a measurement point M. This representation preserves the horizontal distance a between adjacent measurement points but stretches the distance s . The vertical distance a between the grid lines is increased by a factor of $\sqrt{\frac{4}{3}}$ in comparison to the original distance $a' = \sqrt{\frac{3}{4}} a$. The original ratio of the micrograph is finally restored by an additional image processing step. By adapting the shape and dimensions of the super-pixel groups it is possible to handle various non-quadratic measurement point rasters. In this work all EBSD data sets follow a hexagonal scanning raster in which even rows of the grid hold n measurement points while odd rows hold $n - 1$. The number of rows and data sets are determined during data read-in.

Confidence index map

The automatic Miller-indexing during pattern recognition may be affected by inclusions, precipitates or grain boundaries at a measurement point where the back scattered electrons do not yield sharp Kikuchi bands. The produced pattern images are enhanced by using different techniques of image manipulation, but there is still a minimum amount of information necessary to identify individual Kikuchi bands. To capture these influences on the index assignment,

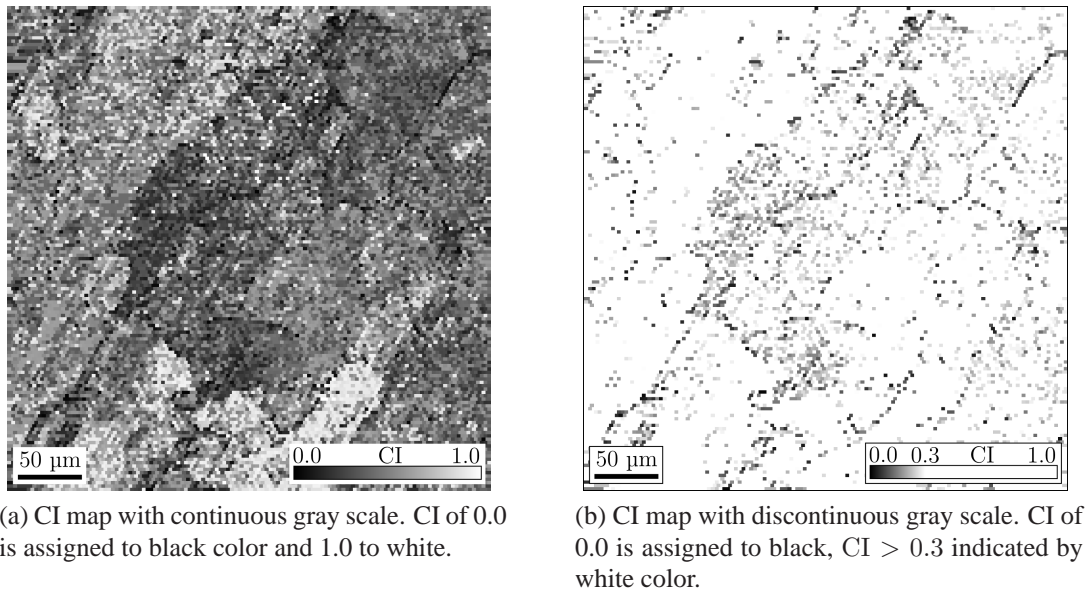


Figure 2.3: Exemplary maps of EBSD measurement on an EN AW-6060 specimen highlighting CI with different gray scales.

OIM DC additionally computes the confidence index CI. Usually a number of suitable possibilities exist while assigning the Miller indices to the detected bands. Therefore a voting scheme is implemented to OIM DC to decide which set of Miller indices to use in a particular case. The CI then is a quality measure on how confident the chosen Miller indices are at that specific measurement point. Wright (2000) showed that, in the case of FCC materials such as aluminum, a CI of 0.1 ensures an confidence level of 95 % for the pattern. Lower CIs imply a decrease in the confidence level. Thus, a CI of 0.05 corresponds to about 80 % confidence, and a CI of 0.025 to about 60 % confidence. Data points with a CI less than a variable threshold are ignored during micrograph generation. An established standard threshold for the CI in the field of aluminum alloys is 0.1.

The CI value can be used to print a gray scale map indicating all regions in the measurement area which have a low CI. This allows to intentionally raise the threshold value or to come to the decision that the selected measurement area does not allow reliable EBSD results. Figure 2.3 depicts two CI maps of the same measurement point. In Figure 2.3a the CI is represented by gray scale values which continuously change from black to white while the CI increases from 0.0 to its maximum value of 1.0. Figure 2.3b selectively emphasizes measurement points with a CI less than 0.3 where the color changes from black to white while the CI increases from 0.0 to 0.3. In extreme cases the pattern recognition completely fails at some measurement points if the specimen surface is damaged or non-metallic or intermetallic inclusions prevent a sufficient backscattering of the electrons. Depending on the settings of OIM DC, these points are marked by a CI value of zero or are simply not added to the EBSD data file. Figure 2.4 shows the distribution of measurement points with different CIs of 0.3 and 0.1 as well as the reconstructed micrograph ignoring all measurement points with a CI less than 0.1. Choosing a CI threshold of 0.1 reveals that many points with a low CI are located along HAGB which can be seen in Figure 2.4b.

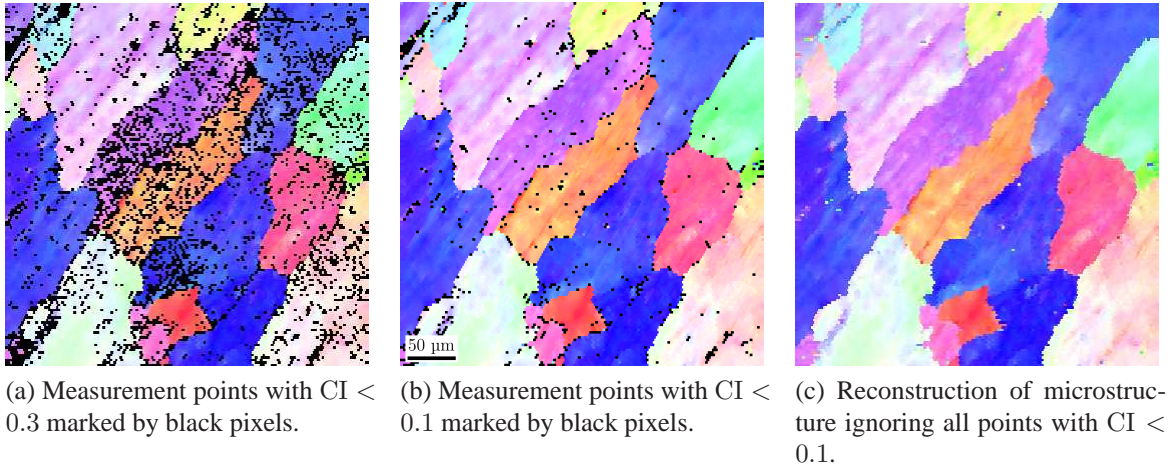


Figure 2.4: Exemplary micrographs of EN AW-6060 emphasizing measurement points with low CI by black pixels. Colors depending on grain orientation determined by EBSD scans of $\sim 18,000$ measurement points.

Grain orientation map

Since the orientation information is the key feature of the EBSD technique, the Euler angles can be converted into color values for a graphical representation of the orientation yielding the grain orientation map or micrograph. The raw input data file indistinctively contains all measurement points regardless of the quality. While reading in the EBSD data file, all points with a CI of less than a specific threshold are fixed by setting the CI values to a magic value of zero. Depending on the user settings in OIM DC, missing data points are also marked by a CI of zero or the data set line is completely missing. In the latter case this gap is compensated by copying the previous data set, adapting the coordinates and setting the CI to a magic value of zero. Depending on the user settings, data sets with a low CI are filtered out as described in Section 2.2.2.

Early versions of the Grainplot software package exclusively used an Euler space based color scheme for the color coding of the orientations. Here, each of the color channels red (R), green (G) and blue (B) represents one of the Euler angles φ_1 , Φ , φ_2 . The RGB color scheme uses three bytes, one for each of the colors red, green and blue. By this representation every color channel can adopt 256 discrete values (0 to 255) and allows to display more than 16.7 million color combinations (so-called True Color). An additive combination of the three color channels with the RGB value (0, 0, 0) leads to black and (255, 255, 255) to white. By definition, φ_1 is assigned to the red color channel, Φ to green and φ_2 to blue by the equations

$$c_R = \frac{\varphi_1}{2\pi} 250; \quad c_G = \frac{\Phi}{\pi} 250; \quad c_B = \frac{\varphi_2}{2\pi} 250. \quad (2.1)$$

The combined color then represents the crystal lattice orientation in space at a specific data point. To prevent conflicts with further image processing operations, e.g., providing color space for reserved signal colors, the color channels are limited to a range between 0 and 250. Additional color schemes with different color offsets or inverted color sets are available for special purposes, e.g., to increase contrast or brightness.

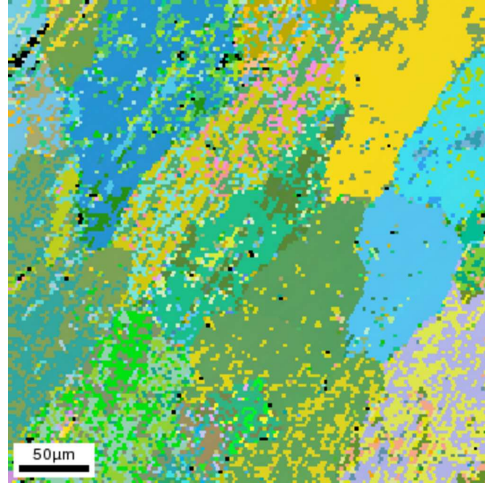


Figure 2.5: Sample microstructure image obtained from raw EBSD data without symmetry check (Euler space based colors according to Equation 2.1; missing data points marked in black).

The Euler angles obtained for each data point result from the automatic Miller indexing algorithm in OIM DC, regardless of the symmetry conditions of the crystals which are introduced in Section 1.3.2. In consequence, by simply assigning the color according to Equation 2.1 leads to a noisy micrograph as shown in Figure 2.5. Most of the noise can be removed by choosing a color scheme based on the orientation triangle presented in Figure 2.6. It is almost identical to the one used by the commercial software OIM A by default and therefore all other EBSD based micrographs presented in this work are colored according to this color scheme. This supports the visual comparison of the micrographs obtained by different programs during verification later on in Section 2.2.4. The position of the area representing the orientation triangle inside a complete pole figure is shown in Figure 1.17. During micrograph generation the orientation of each data point is checked concerning its symmetry conditions to determine the pole P which is projected into the orientation triangle. Hereby, it is ensured that measurement points with similar orientations are displayed in similar colors.

In particular, the area of the orientation triangle is sub-divided into three sectors designated as R, G and B. In each of the sectors either the color channel red c_R , green c_G or blue c_B is set to a constant maximum value of 255 while the intensity of the remaining two color channels depends on the pole position P inside the sector. By definition, the colors at the edges of the IPF are pure red (255, 0, 0) at position [001] in sector R, pure green (0, 255, 0) at position [101] in sector G and pure blue (0, 0, 255) at position [111] in sector B. In the gravity center of the orientation triangle the three color channels sum up to (255, 255, 255) – defining in the white point W. The specific color at a pole then results from the area fractions inside the sector. For the given example pole P in Figure 2.6 the color channels are

$$\begin{aligned}
 c_R(P) &= \left(1 - \frac{2A'_R}{A_G}\right) \cdot 255 \\
 c_G(P) &= 255 = \text{const.} \\
 c_B(P) &= \left(1 - \frac{2A'_B}{A_G}\right) \cdot 255
 \end{aligned} \tag{2.2}$$

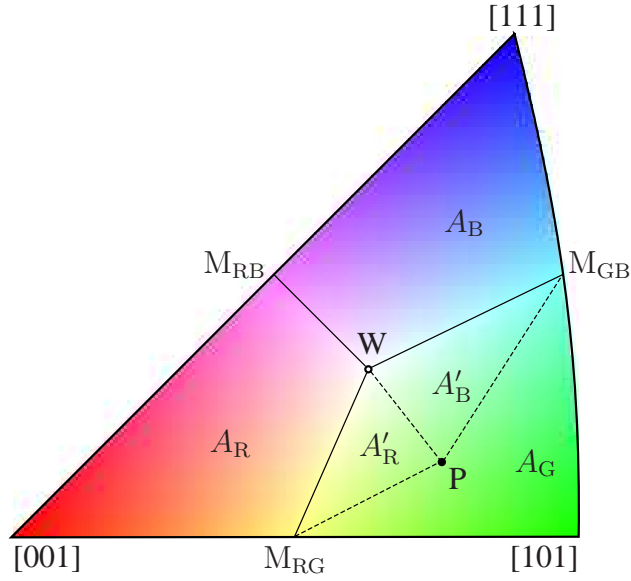


Figure 2.6: Colored inverse pole figure representing an orientation triangle for EBSD based micrographs. Significant points and areas for color determination are labeled. See text for details on color gradient.

where A_G is the area of sector G including the circular segment:

$$A_G = \frac{1}{2} \left| \overrightarrow{WM_{RG}} \times \overrightarrow{WG} \right| + \frac{1}{2} \left| \overrightarrow{WM_{GB}} \times \overrightarrow{WG} \right| + \frac{1}{2} \left[2 \arcsin \left(\frac{|\overrightarrow{GM_{GB}}|}{2} \right) - \sin \left(2 \arcsin \left(\frac{|\overrightarrow{GM_{GB}}|}{2} \right) \right) \right]. \quad (2.3)$$

A'_R and A'_B are the sub areas related to the color channels red and blue, respectively, which depend on the position of the pole P by

$$A'_R = \frac{1}{2} \left| \overrightarrow{PM_{GB}} \times \overrightarrow{PW} \right| \quad \text{and} \quad A'_B = \frac{1}{2} \left| \overrightarrow{PM_{RG}} \times \overrightarrow{PW} \right|. \quad (2.4)$$

If the pole is located in sector R or B, the sector area and sub areas have to be determined accordingly inside the sector to obtain the color channels.

The basic algorithmic formulation of the grain orientation map generation is summarized in Algorithm listing 1. Here, and in the following algorithm listings, the prefix “Lo” always indicates a list of elements and “No” stands for an integer meaning “Number of”. The function `CheckSymmetries` identifies the pole located inside the orientation triangle according to the description in Section 1.3.2. To improve the performance of the computational expensive symmetry check, this function is not implemented in Python but in Cython which compiles the code into a fast execution shared library. The color representation of the identified symmetric orientation of a data point following the strategy described in this section is performed by the `GetColor` function. The color scheme is defined in the orientation mapping triangle shown in Figure 2.6. The Function `PutPixel` is responsible for the correct mapping of the super-pixels inside the micrograph according to scanning raster of the input file. Furthermore, it completes the look-up table which allows a quick assignment of data point to micrograph pixels and vice versa later on.

Algorithm 1: Basic micrograph generation.

Data: OIM DC generated input file in ASCII format; CI threshold.

Result: Micrograph image; look-up table *data point* \leftrightarrow *assigned pixels*; basic file statistics dictionary; list of EBSD data sets.

```

1 Initialization:
2   CITreshold  $\leftarrow$  user defined CI threshold
3   open input file
4   LoDataSets  $\leftarrow$  read in data set lines into list
5 /* restore missing data sets and check CI threshold */
6 foreach Set in LoDataSets do
7   if Set missing then
8     | add copy of previous data set and change CI  $\leftarrow$  0
9   else if CI of Set  $\leq$  CITreshold then
10  | CI  $\leftarrow$  0
11 NoEvenPoints  $\leftarrow$  number of data sets in first row of scanning raster
12 NoRows  $\leftarrow$  number of rows of scanning raster
13 /* iterate over each row, determine pole color from
    orientation triangle and set super-pixel to micrograph */
14 EvenRow  $\leftarrow$  True /* first row is even by definition */
15 foreach Row in NoRows do
16   foreach Set in Row do
17     | SymmetricEulerAngles  $\leftarrow$  CheckSymmetries(EulerAngles of Set)
18     | append SymmetricEulerAngles to LoDataSets
19     | Color  $\leftarrow$  GetColor(SymmetricEulerAngles)
20     | if EvenRow then
21       | ShiftFactor  $\leftarrow$  False
22       | update LookUpTable  $\leftarrow$  PutSuperPixel(PointCoordinates of Set,
23         | Color, SuperPixelDimensions, ShiftFactor)
24     | else
25       | ShiftFactor  $\leftarrow$  True
26       | update LookUpTable  $\leftarrow$  PutSuperPixel(PointCoordinates of Set,
27         | Color, SuperPixelDimensions, ShiftFactor)
28   EvenRow  $\leftarrow$  not EvenRow
29 return LookUpTable, LoDataSets
30 Postprocessing:
31   fill empty border pixels at odd rows
32   correct micrograph dimensions: MicrographHeight  $\leftarrow$  MicrographHeight  $\cdot \sqrt{\frac{3}{4}}$ 
33   micrograph restoring and clean-up

```

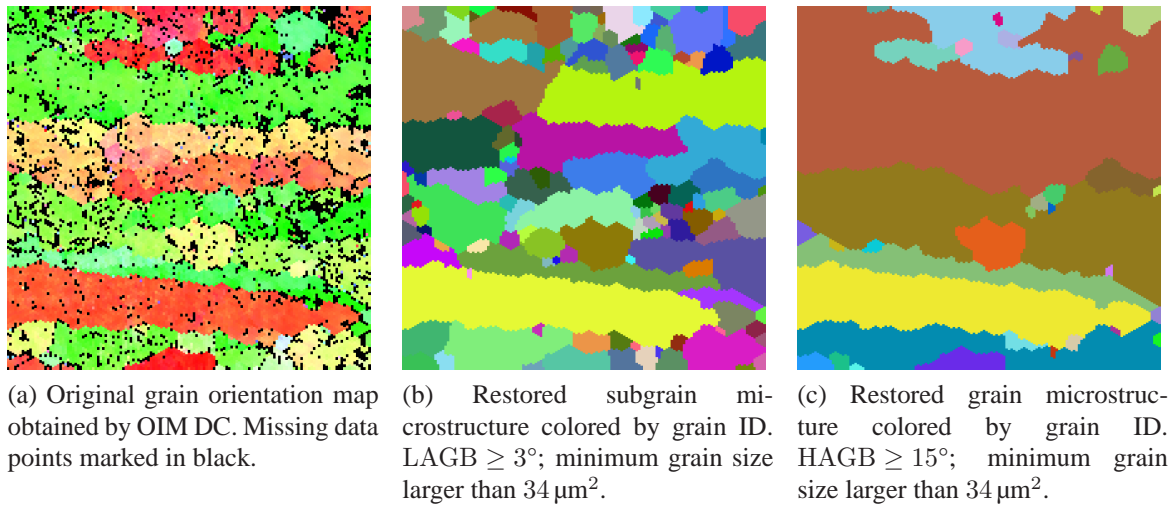


Figure 2.7: Micrograph restoration and clean-up applied to exemplary EBSD based micrograph of EN AW-6060. Micrograph dimensions $350 \mu\text{m} \times 350 \mu\text{m}$.

Micrograph restoration and clean-up

Depending on the sample material and its preparation, the quality of the obtained micrographs varies in CI, number of points, the orientation of which is indeterminable, and grain fragments. The first two topics are discussed in Section 2.2.2 and relate to EBSD technique itself. The grain fragments result from the 3-D character of the microstructure. All grains in the scanned area are cut at an arbitrary plane so that the real grain size has to be determined statistically from the grain areas of the micrograph. If the cut plane of the specimen lies parallel to a grain boundary, peaks of the grain underneath the surface occur as individual grain fragments of equal orientation in the micrograph. An equivalent situation arises when a grain is almost completely removed during preparation but some fragments remain at the specimen's surface. During micrograph generation these fragments are treated indistinctively as "normal" grains.

Missing data points and grain fragments reduce the mean grain size of the investigated measurement area and negatively affect the misorientation analysis. Therefore Grainplot offers different methods to restore and clean-up the final micrograph images before determining the main microstructure statistics. Figure 2.7a shows the original grain orientation map obtained by OIM DC. Missing data points are indicated by black pixels. In Figure 2.7b data points with a CI < 0.1 and individual grains smaller than the given area threshold of five data points, i.e. $34 \mu\text{m}^2$, are restored. A sweeping algorithm is used to check the misorientation and the CI of each measurement point with its neighbors. Due to the hexagonal scanning grid, each point has six neighbors as indicated in Figure 2.2. If the CI is lower than the allowed threshold, all adjacent points with a sufficiently high CI are checked for their misorientation relative to each other. A voting scheme then selects those points with the lowest misorientation, and the mean value of their orientation is assigned to the currently checked data point.

Algorithm 2: Micrograph outliner and CI restoring.

Data: List of EBSD data sets; CI threshold; misorientation threshold.

Result: Restored list of EBSD data sets for micrograph generation.

```

1 Initialization:
2   LoDataSets ← list of EBSD data sets
3   CITreshold ← user defined CI threshold
4   MisorientationTreshold ← user defined misorientation threshold
5 /* iterate over all data sets and check CI threshold and
   identify outliner points */
6 foreach Set in LoDataSets do
7   LoAdjacentPoints ← copy data sets of adjacent points into list /* ignore
   missing data sets at sample edges */
8   LoRelativeMisorientations ← check misorientation of adjacent points
9   /* check for CI */
10  if CI of Set ≤ CITreshold then
11    MeanOrientation ← determine adjacent points with lowest misorientation
   towards Set from LoRelativeMisorientations and compute mean orientation
12    assign MeanOrientation to Set
13  /* identify and restore outliners */
14  Counter ← 0
15  foreach Neighbor in LoAdjacentPoints do
16    MisorientationAngle ← CheckMisorientations(EulerAngles of Set,
   EulerAngles of Neighbor)
17    if MisorientationAngle > MisorientationTreshold then
18      Counter ← Counter +1
19      LoFittingNeighbors ← append Neighbor
20  if Counter ≥ 4 then
21    MeanOrientation ← mean orientation of all points in LoFittingNeighbors
22    assign MeanOrientation to Set
23  else
24    Keep point for further filtering
25 Postprocessing:
26   generate restored grain orientation map
27   optional further filtering

```

If a single point is surrounded by adjacent points which all have a misorientation larger than the misorientation threshold, it can be assumed that this individual point is an outlier and does not belong to the current grain. Again, the misorientation of the adjacent points relative to each other is checked. If four or more adjacent points have a misorientation smaller than the specified misorientation threshold, it is assumed that they all belong to the same grain. The orientation of the outlier point is then changed to the mean of the orientation of the adjacent points belonging to one grain. The restoring algorithm is summarized as pseudo code in Algorithm listing 2. Here, the function `CheckMisorientations` determines the minimum misorientation between two points with respect to the symmetry conditions.

The misorientation threshold specifies the distinction of individual grains. A low threshold complicates the visual differentiation of grains in the grain orientation plot since the colors of similar oriented grains are represented by similar colors. To overcome this problem the grains in the micrograph are plotted in arbitrary colors depending on their individual identification number (ID) as shown in Figures 2.7b and 2.7c. The figures differ from each other by the used misorientation threshold of 15° and 3° , respectively, so that Figure 2.7c shows more individual grains than Figure 2.7b. Both micrographs are filtered by grain size and all grains consisting of five or less data points, i.e. smaller than $34 \mu\text{m}^2$, have been removed.

Algorithm 3: Simplified burn algorithm.

Data: List of EBSD data sets; start point; misorientation threshold.

Result: List of EBSD data sets belonging to grain with specified start point.

```

1 Initialization:
2   LoDataSets ← list of EBSD data sets
3   LoGrainPoints ← append start point to list of points belonging to grain
4   MisorientationTreshold ← user defined misorientation threshold
5 /* loop stops if all points are assigned to grain */
6 while True do
7   LoNewGrainPoints ← empty list
8   foreach Point in LoGrainPoints do
9     LoAdjacentPoints ← GetAdjacentPoints(LoDataSets, Point)
10    /* ignore missing points at sample edges */
11    foreach AdjacentPoint in LoAdjacentPoints do
12      MisorientationAngle ← CheckMisorientations(EulerAngles of
13      Point, EulerAngles of AdjacentPoint)
14      if MisorientationAngle ≤ MisorientationTreshold then
15        LoNewGrainPoints ← append AdjacentPoint
16
17    foreach NewPoint in LoNewGrainPoints do
18      if NewPoint not in LoGrainPoints then
19        LoGrainPoints ← append NewPoint
20
21    if length of LoNewGrainPoints == 0 then
22      break /* no further points found */
23
24 return LoGrainPoints

```

The ID assignment requires an identification of individual grains which can be performed by different strategies as described by Wright et al. (2000) and Humphreys (2004b). Grainplot uses a burn algorithm which starts at an arbitrary point inside a grain and searches in all directions for points with a misorientation smaller than the specified misorientation threshold. Comparable to a spreading fire the algorithm proceeds until no further adjacent points with similar orientation are found¹. Because the misorientation is only checked between adjacent points, the burn algorithm belongs to the group of relative methods. Grain boundaries with a smooth transition are not found but unconnected grain fragments of same or similar orientation are identified and indexed as individual grains. The core code of the burn algorithm is presented in the Algorithm listing 3. For speed improvement the implemented universal burn algorithm supports sub lists for different search directions. These sub lists prevent a backward search of points which are already indexed. For clarity the sub lists are not included in the given pseudo code. The burn algorithm is repeated with a shifting starting point until all measurement points in the EBSD input file are grouped to indexed grains. Furthermore, the universal burn algorithm can also be applied to image files by using a color threshold instead of the misorientation threshold and by iteration over the image pixels. A similar method of grain identification of individual grains in EBSD based micrographs or appropriate LOM images is the watershed image segmentation presented by Rauch et al. (2010).

The grouping of measurement points with similar orientation into grains with individual grain IDs also facilitates further filtering of the micrograph by grain size or grain shape. The grain shape filtering is performed by moving a search window of variable dimensions over the micrograph. All grains fitting into the search window are removed and the gap is closed by growth of the adjacent grains. The current implementation only allows a rectangular search window which is orientated parallel to the micrograph edges. Especially for banded microstructures, it is useful to choose a search window the dimensions of which are adapted to the predominant grain alignment. Furthermore, the fraction of grain area and grain perimeter length can be used as a filter criterion. This allows a separate handling of globular and elongated shaped grains. Both presented filter methods primarily aim at the application on microstructures with distinct textures, e.g., thin and elongated grains.

However, filtering by grain size has a more general purpose. It is especially useful to clean up the micrograph from grain fragments and wrongly indexed EBSD data sets. A list of all grain IDs and the according grain sizes is generated during the grouping of points as grains. This list of grain sizes is used to delete all grains of the micrograph which are smaller than a specified grain area threshold. Afterwards the remaining grains grow into the resultant gaps. The Algorithm listing 4 summarizes the basic method of generating a grain size filtered grain ID map including the growth of grains to close occurring gaps. Here, the `GetAdjacentPoints` function simply reads the IDs of the adjacent points and returns the ID assigned to the majority of them. The removal of grain fragments is not yet fully automated. All described filter methods still need user interaction by defining search window dimensions or size thresholds depending on the microstructure characteristics. The returned list of grain IDs and the generated grain ID

¹The burn algorithm is independent from the Burns algorithm which is used to identify straight lines or edges in image files and is used for the automatic Kikuchi pattern recognition described in Section 1.6.4.

Algorithm 4: Micrograph clean-up by grain size filtering.

Data: List of EBSD data sets; list of grain IDs and associated EBSD data sets; minimum grain area threshold.

Result: Updated lists of grain IDs and sizes; cleaned micrograph image.

1 Initialization:

2 LoDataSets \leftarrow list of EBSD data sets

3 LoGrainIDs \leftarrow list of grain IDs and associated data sets

4 AreaTreshold \leftarrow user defined minimum grain area threshold

5 /* generate map of grain IDs ignoring grains smaller than area threshold */

6 foreach Grain in LoGrainIDs do

7 NoGrainPoints \leftarrow number of associated data sets in Grain

8 **if** NoGrainPoints > AreaTreshold **then**

9 **foreach** Point in Grain **do**

10 MapGrainIDs \leftarrow add Point

11 /* find and fill gaps in grain ID map; loop stops if no unassigned points left */

12 while True do

13 NoNonIndexedPoints \leftarrow 0

14 foreach Point in LoDataSets do

15 **if** Point **not in** MapGrainIDs **then**

16 LoAdjacentPoints \leftarrow GetAdjacentPoints(Point, MapGrainIDs)

 /* ignore unassigned points and missing ones at map edges */

17 NewID \leftarrow GetDominantID(LoAdjacentPoints)

18 MapGrainIDs \leftarrow assign NewID at position of Point

19 NoNonIndexedPoints \leftarrow NoNonIndexedPoints + 1

20 **if** NoNonIndexedPoints == 0 **then**

21 **break** /* no unassigned points found */

22 **return** MapGrainIDs

23 Postprocessing:

24 generate size filtered grain id map from MapGrainIDs

25 optional further filtering

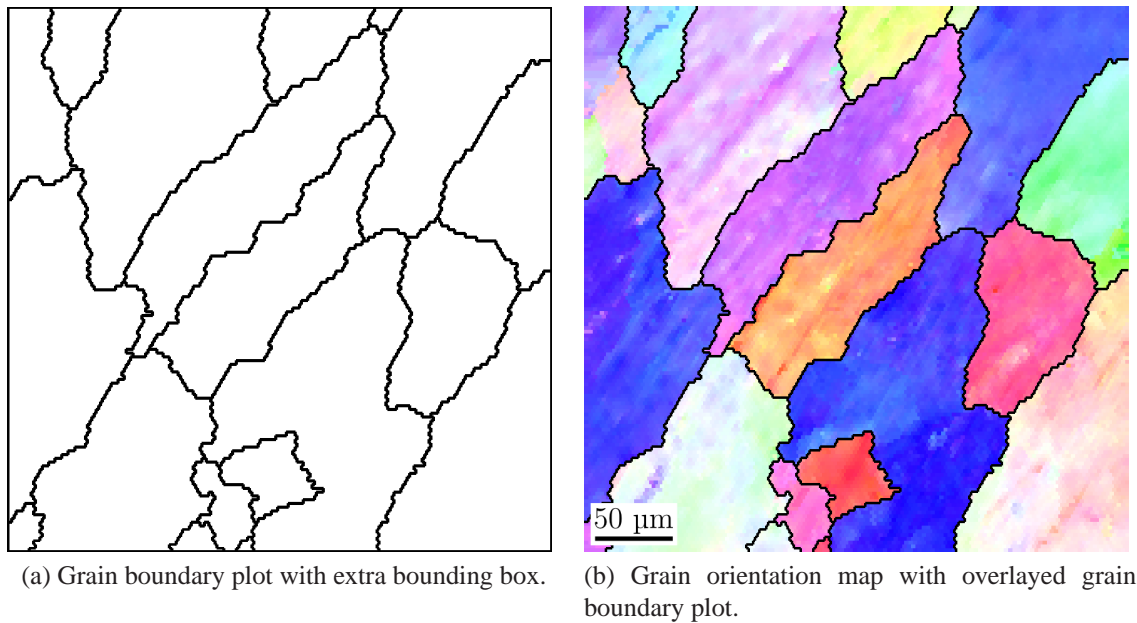


Figure 2.8: Exemplary grain boundary plot obtained from EBSD measurement of EN AW-6060. Grain boundaries distinct HAGB $\geq 15^\circ$.

micrographs then serve as the basis for determination of the grain size statistics and are also used for the generation of grain boundary plots described in the following.

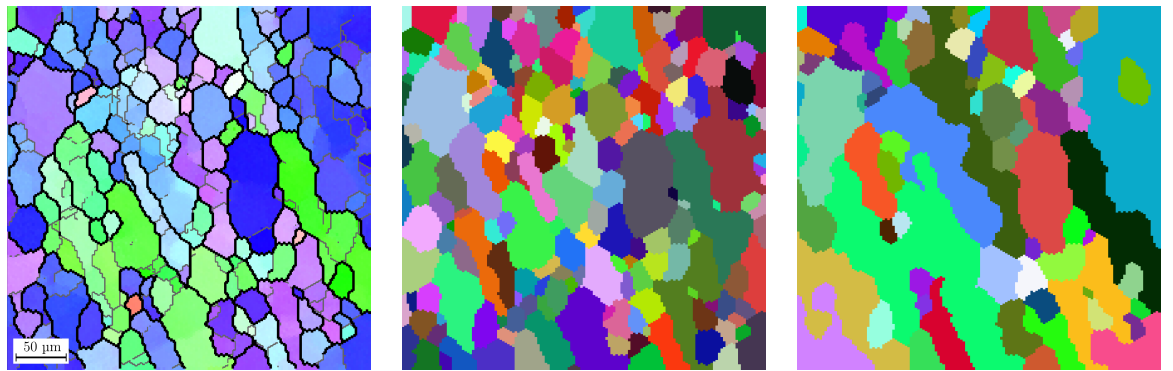
Grain boundary plots

Besides the coloring by grain IDs, an overlaid grain boundary plot can also be used to visually emphasize the main microstructure characteristics. Analogously to the grain identification a specified misorientation threshold distinguishes the individual grains. In particular, the grain boundary plots are produced by application of an adapted sweep algorithm. Here, for all points in the EBSD data file the orientation of the current point is compared to its neighbors to the right and below. If the misorientation between the compared points exceeds the given threshold value, e.g., 15° for HAGB, the position is marked in the generated grain boundary plot. Sweeping over the entire EBSD data file then produces a map of all grain boundaries for the given misorientation angle. An example for a grain boundary map for HAGB $\geq 15^\circ$ of a nearly undeformed sample of EN AW-6060 is shown in Figure 2.8a. If the boundary plot has a transparent background, it can be placed on top of a regular grain orientation map as presented in Figure 2.8b.

2.2.3 *Microstructure statistics*

Grain size distribution and evolution

In contrast to the common micrograph based methods, e.g., (ASTM International, 2004), the EBSD measurements allow an exact determination of grain and subgrain sizes. The distinction as to whether grain or subgrain sizes are measured is completely independent from the EBSD data file but only depends on user defined misorientation threshold values. A value of 15° misorientation is commonly used to define HAGBs which separate individual grains in alu-



(a) Restored grain orientation map with reconstructed data points with a CI < 0.1.

(b) Randomly colored subgrain micrograph with LAGB $\geq 3^\circ$; minimum grain size larger than $34 \mu\text{m}^2$.

(c) Randomly colored grain micrograph with HAGB $\geq 15^\circ$; minimum grain size larger than $34 \mu\text{m}^2$.

Figure 2.9: Grain and subgrain identification applied to exemplary EBSD based micrograph of EN AW-6060.

minimum alloys (Gottstein, 2004). In this work LAGBs between 3° and 15° are identified as grain boundaries separating individual subgrains. The lower limit of 3° is chosen to ensure a certain distance to the measurement inaccuracy of the EBSD technique which lies in the range of $1^\circ \sim 2^\circ$ (Humphreys, 2004a) and depends on the alloy composition and position of the focused electron beam inside the measurement area. According to Humphreys (2001), the additional angular error due to distortion of focused electron beam in the used fast beam scanning mode can reach up to 1° . The definition of the minimum misorientation angle treated as LAGB between subgrain varies in different publications but is usually assumed to be less than 5° as stated by Humphreys et al. (1999) for example.

The used method of grain and subgrain reconstruction from EBSD measurement data follows the approach of relative referencing as discussed in the work of Humphreys (2004b). Here, the misorientation between adjacent data points is evaluated, allowing a limited variation of orientation inside individual identified grains, which is natural for most of the observed micrographs. With respect to the symmetry operations and grain size filtering applied during the micrograph restoration, all data points with a misorientation less or equal than the user defined threshold are grouped as grains which are referenced by a unique ID during further processing. Based on the EBSD results of an exemplary measurement point in the SIZ of an EN AW-6060 billet, Figure 2.9a shows a restored and cleaned orientation map with overlaid HAGB $\geq 15^\circ$ as black lines and $3^\circ \leq \text{LAGB} \leq 15^\circ$ in gray. Figures 2.9b and 2.9c show the identified subgrains and grains which are colored corresponding to their grain ID.

Based on the ID assignment, the number of data points of each grain is known. In the graphical representation each data point covers a specific area depending on the micrograph dimensions and the number of data points in the measurement raster. From this, the area covered by each grain can directly be derived and plotted into a histogram, as exemplarily depicted in Figures 2.10a and 2.10b, for the grain and subgrain sizes in the micrograph in Figure 2.9a. This gives a quick quantitative overview if the observed microstructure is dominated by small-scale grains or by coarse grains. Furthermore, the grain sizes of each micrograph can be statistically

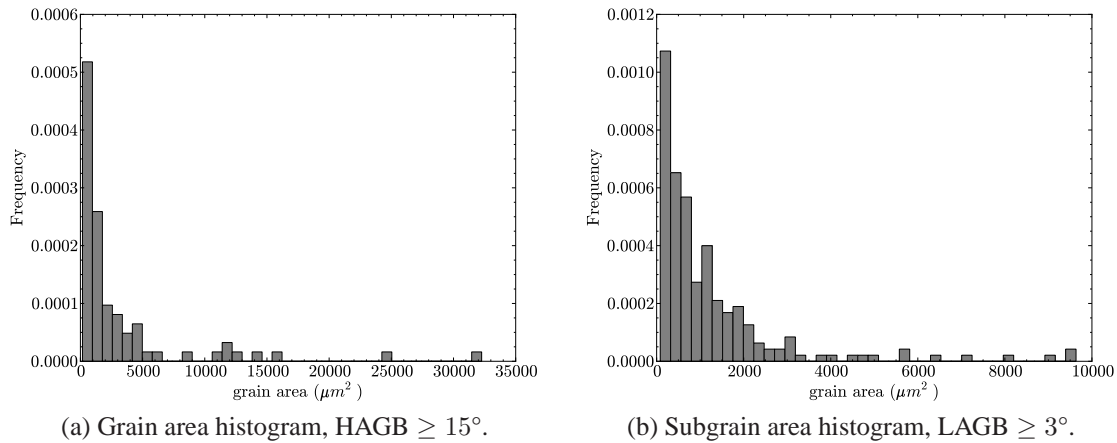


Figure 2.10: Grain size distribution histograms of exemplary micrograph in Figure 2.9a.

analyzed regarding mean and median values as well as standard variance or standard error. To analyze the grain size evolution for selected measurement points of a partly extruded billet specimen, the obtained grain area values are post-processed and presented by bar plots of the mean grain and subgrain sizes and their according standard errors. The mean grain area size \bar{A} is the arithmetic mean value of the sum of all n considered grain areas A in the micrograph:

$$\bar{A} = \frac{1}{n} \sum_{i=1}^n A_i. \quad (2.5)$$

The standard error $\sigma(\bar{A})$ of the statistical grain area population A derives from the standard variance σ_A^2 by $\sigma(\bar{A}) = \sigma_A \cdot n^{-\frac{1}{2}}$ with

$$\sigma_A^2 = \frac{\sum_{i=1}^n (A_i - \bar{A})^2}{n}. \quad (2.6)$$

In order to catch subgrains which are partially enclosed by HAGBs in the grain interior, all HAGBs are taken into account while determining the subgrain sizes. In consequence, also those grains completely surrounded by HAGBs are included in the subgrain size statistics which shifts the determined sizes to larger values since grains are treated like subgrains. In the case of microstructures with weak subgrain structures, for example statically recrystallized regions, this leads to a significant increase in subgrain size, especially if only very few small subgrains are evident because the grains are also automatically treated as subgrains. The influence of this unwanted side effect on the subgrain size is discussed in the corresponding grain size statistics sections in Chapter 3.

In general, the grain size determination based on the grain area obtained by image processing is fast and more accurate compared to other methods such as the intercept procedure or the comparison method proposed by ASTM International (2004), for example. By application of the equation $G = c_1 \cdot \log_{10}((\bar{A} \cdot 10^{-6})^{-1}) - c_2$ based on the ASTM planimetric procedure, the equivalent grain size number G can be obtained from the mean grain area size \bar{A} in μm^2 . The constants are defined as $c_1 = 3.321928$ and $c_2 = 2.9542$. If necessary, the determined grain area size A_i can also be easily converted into the equivalent circle diameter (ECD) d_i of

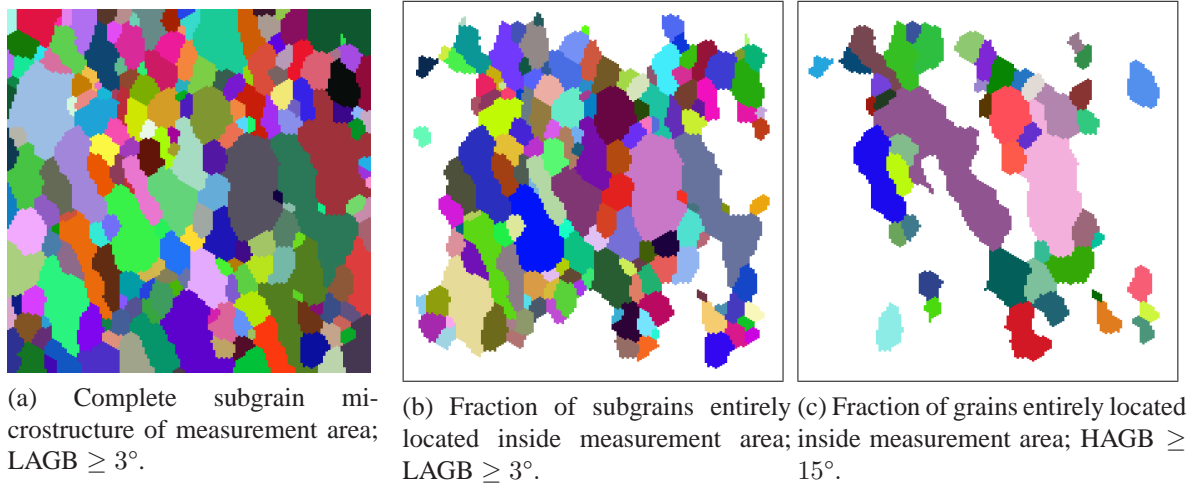


Figure 2.11: Fraction of complete (sub-)grains entirely located inside exemplary EBSD based micrograph of EN AW-6060.

a grain designated by the index i by $d_i = \sqrt{4A_i\pi^{-1}}$. However, this simple conversion does not consider the grain shape if applied to micrographs with a banded microstructure. In this case a grain approximation by ellipses with respect to the shape factor is more useful.

Grains located at the outer edges of the micrograph as shown in Figure 2.11a are partly cut and their real grain size is obviously larger than determined from the EBSD measurement data. Therefore the grain area results are underestimated by including these incomplete grains into the statistics. If the investigated microstructure mainly consist of similar size grains and a sufficiently large number of grains is entirely located inside the measurement area, this effect can be eliminated by consideration of complete grains only. Figure 2.11b exclusively contains subgrains with $\text{LAGB} \geq 3^\circ$ which have no contact to the micrograph margin. In this example the mean subgrain area size decreases from $614 \mu\text{m}^2$ in Figure 2.11a to $529 \mu\text{m}^2$ in Figure 2.11b because comparably large grains at the perimeter are now ignored while small grains in the interior are still captured. In this case the exclusion of grains leads to an additional underestimation. In fact, the underestimation caused by this effect increases for larger grains and fibrous microstructures where a large number of grains are cut by the micrograph margins. The influence of increasing grain size is illustrated in Figure 2.11c which contains complete grains with $\text{HAGB} \geq 15^\circ$. Compared to Figure 2.11b the number of evaluable grains significantly decreases. Quantitatively the mean grain area size decreases by about 44% from $1587 \mu\text{m}^2$ including incomplete grains to $880 \mu\text{m}^2$ obtained for the micrograph in Figure 2.11c. In consequence, all grain area size statistics presented in chapter 3 also include incomplete grains located at the micrograph edges while keeping in mind that this systematically underestimates the determined mean grain sizes.

Normed fraction of grain boundaries

The development of grain boundaries and their nature as GNBs, IDBs, coincident $\Sigma 3$ twin boundaries or random grain boundaries are in the focus of recent works in the field of GBE as described by Hughes et al. (2003); Rezvaniyan et al. (2007); Schuh et al. (2003) and Humphreys

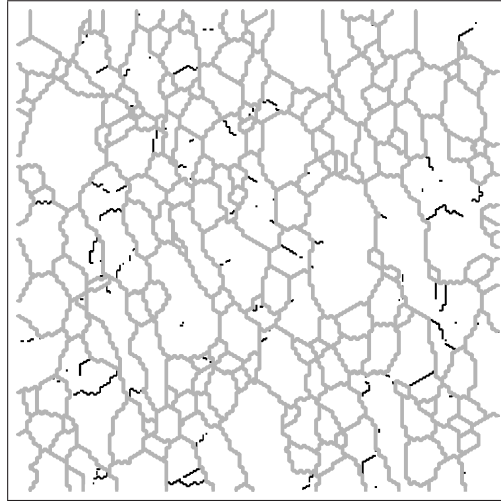
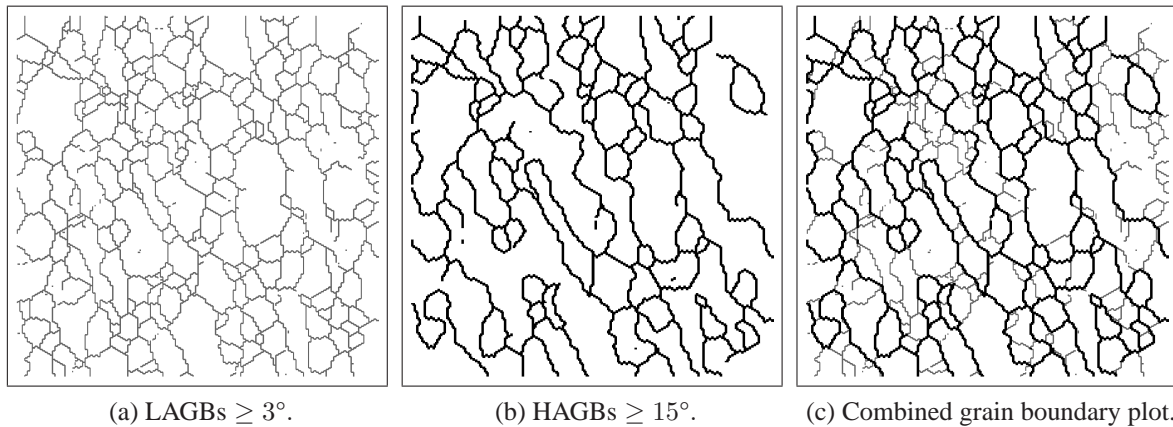


Figure 2.12: LAGBs $\geq 3^\circ$ of exemplary EBSD based micrograph of EN AW-6060 in Figure 2.9a. LAGBs enclosing subgrains marked gray, free LAGBs plotted in black.



(a) LAGBs $\geq 3^\circ$.

(b) HAGBs $\geq 15^\circ$.

(c) Combined grain boundary plot.

Figure 2.13: Grain and subgrain boundary plots of exemplary EBSD based micrograph of EN AW-6060 in Figure 2.9a. $3^\circ \leq \text{LAGBs} \leq 15^\circ$ indicated by gray lines, HAGBs $\geq 15^\circ$ marked in black.

(2004b), for instance. However, the grain and subgrain statistics only indirectly describe the evolution of grain and subgrain boundaries. Naturally, the grain size based statistics exclusively include HAGBs and LAGBs which are part of a closed network separating individual grains. Depending on its evolution history, a specific grain microstructure may additionally contain partial grain boundaries which have an unconnected free end inside existing grains. As an example, Figure 2.12 shows the free unconnected LAGBs of an exemplary subgrain microstructure in black color. Since this type of boundaries do not belong the grain and subgrain structure, they are not captured by the ordinary grain size statistics.

A different way of statistically capturing the grain boundary evolution is based on the analysis of the grain boundary micrographs by methods of image processing. Figure 2.13 illustrates the assembly of the grain and subgrain boundary plots to create a combined boundary image. The grain boundary fraction derives from the area A_{GB} covered by grain boundaries in the plots in Figure 2.13a and 2.13b. Since the areas of LAGBs and HAGBs directly depend on the user

defined line thickness l_{GB} , the obtained fraction is at first normed to this variable value. The boundary fraction is subsequently normed according to the image resolution. The subsequent equation for the normed grain boundary fraction f_{GB} as implemented into Grainplot is then $f_{GB} = A_{GB} \cdot l_{GB}^{-1} \cdot A_M^{-1}$ where A_M is the size of the entire micrograph. All values are given in pixels.

By evaluation of the grain boundary fractions at different measurement points of a sample, qualitative statistics about the evolution of all LAGBs and HAGBs can be acquired. The described norming procedure filters influences of varying image sizes due to the EBSD raster resolution and ensures the quantitative comparability of the non-dimensional boundary fraction value for different micrographs. For the subgrain boundary structure in Figure 2.13a, the determined normed LAGB fraction is 0.0643, and the grain boundary structure in Figure 2.13b consists of approximately half of the grain boundaries resulting in a normed HAGB fraction of 0.0375. In combination with the grain size statistics, the normed grain boundary fraction also offers information on the grain shape of a specific micrograph. The length of a grain boundary generally depends on the grain shape. With increasing grain elongation the normed grain boundary fraction decreases as well. A larger impact on the normed grain boundary fraction is found for grain boundaries with irregular geometry or serrated grain shapes as observed in the presence of GDZ.

Misorientation distribution and evolution

During plastic deformation the microstructure tends to reach the energetically optimal configuration under the given process conditions in the meaning of total strain, strain rate, temperature, etc. Depending on these conditions and the composition of the processed aluminum alloy, a textured microstructure can be observed at different measurement points in the samples. This does not only include the change in grain shape from initially globular-shaped grains to a banded or fibrous grain structure but also affects the grain orientation due to the activated glide systems in the material. Especially under severe shear load observed in the SIZ, the existing more or less randomly orientated grains rotate into a more parallel orientation. The degree in rotation and the resulting preferred orientation depend on the material's crystal structure.

The relative angle between two unit cell orientations with respect to their possible symmetries is expressed by the misorientation angle θ which is introduced in Section 1.3.2. In the previous sections the misorientation is used to distinguish individual grains or subgrains if the observed misorientation exceeds a given threshold. Generally, the misorientation can be evaluated between two adjacent data points in the micrograph or between neighboring individual (sub-)grains identified in the previous microstructure visualization steps. For the latter method, the mean orientation of each grain has to be determined since the orientations of data points belonging to a grain still vary in the limits of grain boundary threshold misorientation. Smoothing the orientation leads to a distortion in the determined misorientation angles. This method usually does not capture any misorientation angles below the grain boundary threshold angle. The applied method of relative referencing during grain identification allows an exception if the orientation smoothing of two grains accidentally leads to an alignment of the orientations so that their misorientation can decrease below the grain boundary threshold. The misorientation of each grain is determined once for all neighboring grains regardless of their sizes. During this

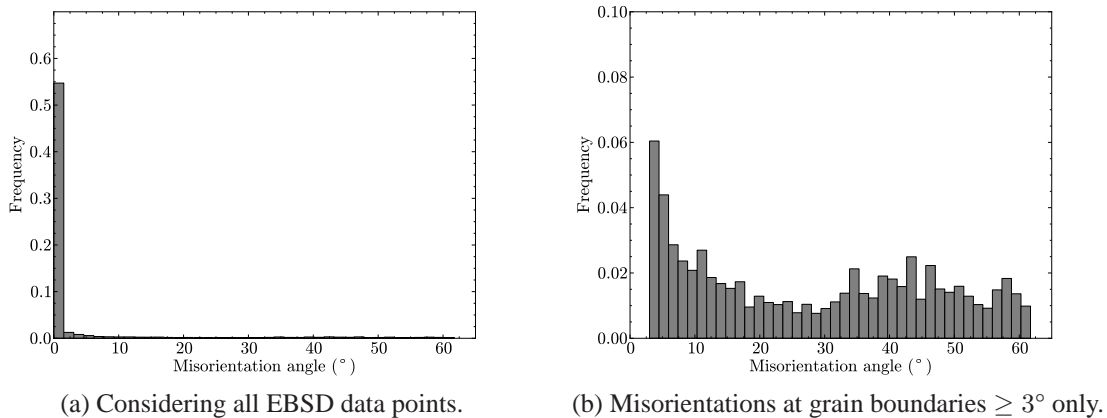


Figure 2.14: Misorientation histograms of exemplary EBSD based micrograph of EN AW-6060 in Figure 2.9a.

unweighted procedure, the influence of significant smaller grains in the microstructure usually shifts the obtained misorientation angles towards higher values.

The point-wise misorientation results from a point-wise evaluation of Equation 1.12. Due to the hexagonal measurement point distribution in the scanned area as shown in Figure 2.2, it is sufficient to sweep line-wise from point to point and to determine the misorientations to the right neighboring data point (designated as super-pixel in the figure) and to the data points left and bottom right in the next line. The obtained misorientation results are plotted as a frequency histogram as given in Figure 2.14a. The example shows that 90 % of the adjacent data points have a misorientation below 15° but that misorientations $> 45^\circ$ are also observed at a very few grains. In contrast to the grain based misorientation statistics, the point-wise determination covers the low level misorientations inside the individual grains. Furthermore, the number of data points along the grain boundaries is considered in the misorientation frequency.

A mixture of both algorithms is to determine the misorientation angle only between adjacent data points belonging to different grains. In this case the results are also strongly influenced by the chosen angular grain boundary threshold. By definition, misorientation angles below the grain boundary threshold are not determined by this method. Therefore the frequency of the remaining misorientations above the threshold is increased as exemplarily shown in the corresponding histogram in Figure 2.14b for a grain boundary threshold of 3° . With respect to the symmetry conditions of the FCC unit cell structure in the aluminum alloys of interest here, the maximum misorientation between two points is limited to $\theta_{12} \leq 62.8^\circ$ (Mackenzie, 1958). The misorientation evolutions at different measurement points in the samples are analyzed on the basis of the arithmetic mean values derived from the misorientation histograms. The corresponding misorientation histograms for each measurement point can be found in Section B in the appendix of this work. It has to be considered that only misorientations larger than the LAGB threshold of 3° are plotted in the histograms.

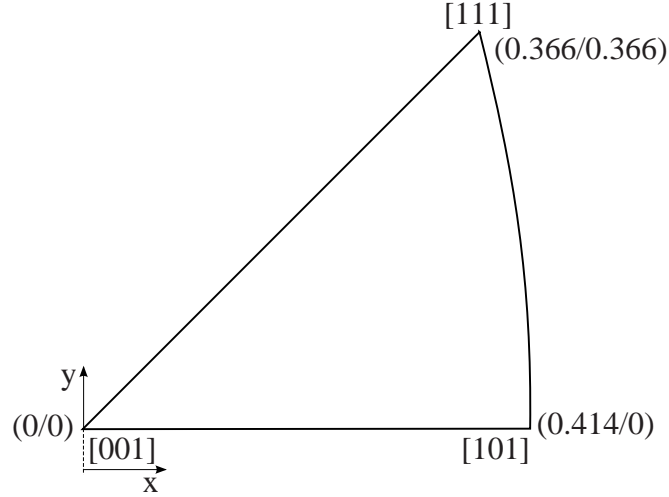


Figure 2.15: Inverse pole figure outline with edge coordinate labels.

Discrete inverse pole figure plot

A graphical representation of the grain orientations obtained by EBSD measurements is implemented in form of inverse pole figures, the fundamental basics of which have been introduced in Section 1.3.2. For a full texture representation of the 3-D orientation, the stereographic projection of three orthogonal sample directions denoted as normal direction (ND), transverse direction (TD) and rolling direction (RD) is necessary. The direction perpendicular to the measurement surface is defined as ND (sample $[001]$ coordinate). The color coding of the orientation triangle in Figure 2.6, used for the presented EBSD based micrographs, is defined with respect to this direction. By definition, RD points to the right (sample $[100]$ coordinate) in the EBSD based micrographs so that the material flow in the MFZ in the center of the billet is parallel to RD which results in a sharp texture pattern in the corresponding IPFs. A complete orthogonal right-hand sample coordinate is completed by TD which points vertically upwards in the micrographs (sample $[010]$ coordinate).

According to Randle and Engler (2009), the projection direction \mathbf{n} can be directly extracted from the orientation matrix \mathbf{R} . With respect to the previous definitions of the directions RD, TD and ND, these are equivalent to the first, second and third columns of \mathbf{R} , respectively. The obtained directions automatically are unit vectors. Due to the 24 equivalent symmetric rotations of FCC unit cells, 24 symmetric poles on the on the equatorial plane $\partial\mathcal{P}_3$ are possible as indicated in Figure 1.17. Therefore it is sufficient to focus on a specific triangle on $\partial\mathcal{P}_3$, e.g., between the points $[001]$, $[101]$ and $[111]$, instead of taking the whole equatorial plane into account.

While checking the symmetry conditions between adjacent data points for the misorientation statistics by Equation 1.12, the orientation matrix \mathbf{R} of each data point is multiplied with each of the 24 symmetry matrices \mathbf{O}_S given in Equation 1.9. For each symmetry the projected pole coordinates are also determined for each of RD, TD and ND. Should the pole coordinates x_p

and y_P be located inside the IPF triangle, these values are stored. For a stereographic projection inside a unit sphere, the area of the IPF sector is specified by the equations

$$\begin{aligned} y_P &\geq 0, \\ y_P &\leq x_P, \\ y_P^2 &\leq 2 - (x_P + 1)^2 \end{aligned} \tag{2.7}$$

which define the edge point coordinates at [001], [101] and [111] as given in Figure 2.15.

In the case of homogeneously orientated grains in the observed measurement area, the overlaid poles project a sharp pattern for each grain inside the IPF due to missing orientation variance. In contrast to this, a large number of grains with a distinct subgrain structure leads to diffuse pattern which makes it hard to identify texture tendencies. By variation of the pole diameter and the usage of transparency in the IPF plot, the contrast can be increased as demonstrated in Figure 2.16. The strong texture in the RD related plot is clearly visible in all three variants. In the ND related IPF in Figure 2.16a, for example, a preferred direction somewhere between [100] and [101] cannot be distinguished. The reduced transparency in Figure 2.16b reveals two orientation concentrations near [100] and [101]. By increasing the pole diameter in Figure 2.16c the contrast of orientation distribution inside the IPF is additionally enhanced.

The problems of overlying patterns can be avoided by using ODFs according to Section 1.3.2. However, the comparably small number of grains in the investigated measurement areas still allow the use of discrete IPFs. Therefore an ODF based representation of the stereographic projected pattern is not yet implemented to Grainplot.

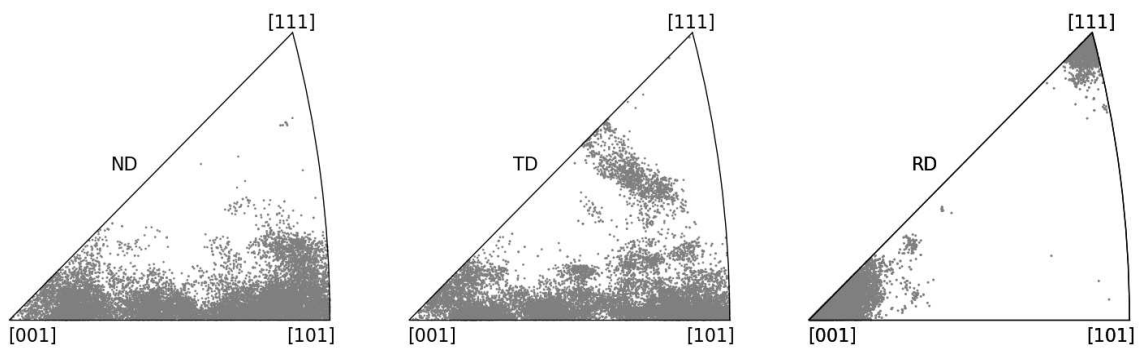
2.2.4 Verification

The results produced by the in-house code Grainplot are verified by comparison with results from the commercial software OIM Analysis and MTEX, briefly introduced in Section 2.1.1. Due to variations in several implementation details, especially during grain fragment filtering and handling of data points with low CI, the statistical results of the different programs are not identical but show a good qualitative agreement.

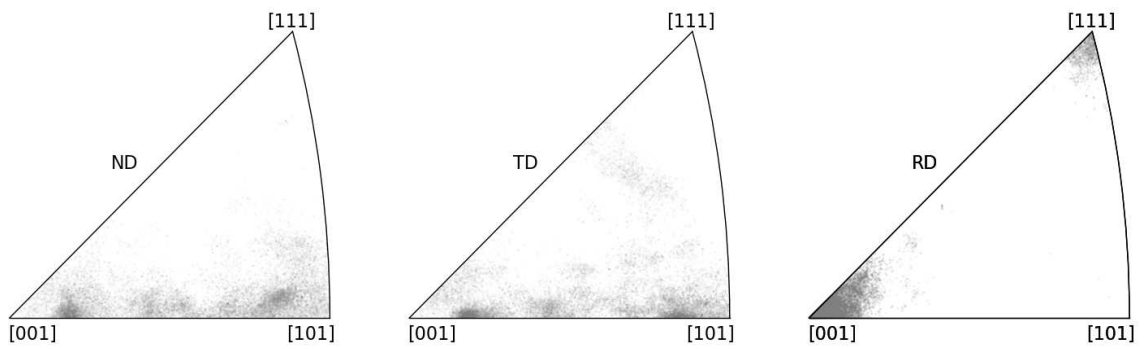
Micrographs

The quality of the produced grain orientation maps can be verified by visual comparison of the different micrographs in Figure 2.17. The maps of Grainplot in Figure 2.17a and OIM A in Figure 2.17b are almost identical including the HAGBs $\geq 15^\circ$ marked by black lines and the LAGBs $\geq 2^\circ$ in gray and red, respectively. The result of OIM A includes some small grains in the dimensions of less than five data points which are filtered out in the micrograph of Grainplot. The slight difference in the color coding is an effect of the used color maps. A misconfiguration of OIM DC during the data acquisition lead to a wrong dimension scale in Figure 2.17b. This effect is compensated in the micrograph of Grainplot.

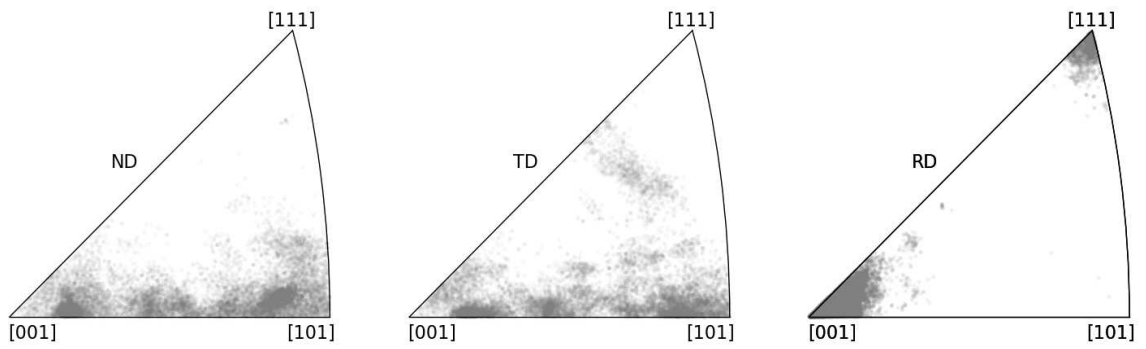
By default the color coding of MTEX is different from the orientation triangle in Figure 2.6 which is used by Grainplot and in a very similar form also in OIM A. In MTEX the direction [101] is coded by the color blue and [111] in green which results in the orientation color map shown in Figure 2.17. In the current version of MTEX HAGBs and LAGBs are determined



(a) Pole diameter 3, alpha 1.0 (no transparency).

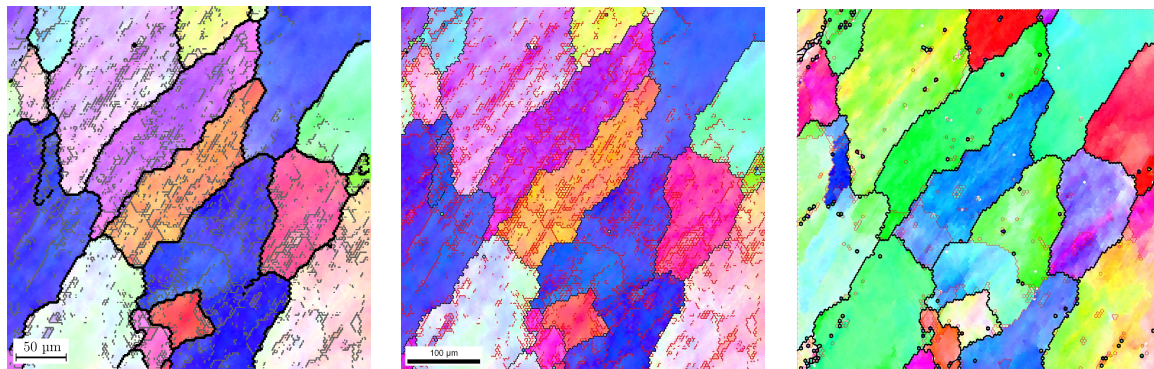


(b) Pole diameter 3, alpha 0.05.



(c) Pole diameter 10, alpha 0.05.

Figure 2.16: Variation in pole diameter and transparency (alpha value) for exemplary IPFs.



(a) Restored grain orientation map by Grainplot. (b) Grain orientation map by OIM A. Note: Due to a misconfiguration the displayed scale has to be multiplied with a factor of 0.7. (c) Grain orientation map by MTEX with different color map and closed grain boundaries only.

Figure 2.17: Grain orientation maps of exemplary EBSD based micrograph of EN AW-6060. HAGBs $\geq 15^\circ$ indicated by bold black lines, LAGBs $\geq 2^\circ$ marked by narrow lines in gray or red.

from identified grains and subgrains. Therefore only grain boundaries which completely enclose grains or subgrains are plotted in the micrographs. In consequence, evolving GNB during plastic deformation are not covered in the micrographs and the according microstructure statistics.

Depending on the grain microstructure and the predominant orientations inside a grain orientation map, it is often useful to emphasize individual grains by high contrast colors for a more obvious distinction as exemplarily shown in Figure 2.18. Here, the colors assigned to the grains are independent from their orientations. The grain detection algorithms of Grainplot, OIM A and MTEX basically identified the same grains. The small differences result from the adopted filtering of small grain fragments and the handling of data points with low CI. Nevertheless, these small scale grains affect the grain size statistics as discussed in the next section.

Statistics

The presentation of grain size and misorientation distribution of a micrograph in form of histogram plots is comparably sensitive towards user settings such as CI threshold, minimum grain size filtering and LAGB/HAGB angle definition. Therefore the presented histograms may vary but the effect of the listed settings is usually much smaller during determination of mean values. The grain area histograms produced by Grainplot, OIM A and MTEX for the exemplary micrograph in Figure 2.18 are depicted in Figure 2.19. Since the grain micrographs contain a different number of small scale grain fragments, the resulting grain size histograms differ from each other. The efficient grain size filter of Grainplot significantly reduces the number fraction of grains with an area size less than $1000 \mu\text{m}^2$ in Figure 2.19a compared to the grain area histogram obtained by OIM A in Figure 2.19b. The grain size filter automatically increases the size of the remaining large scale grains and leads to small variance in the remaining bars for larger grain sizes. This effect is also evident in the histogram by MTEX in Figure 2.19c.

The misorientation histograms obtained by the three programs and presented in Figure 2.20 show a good qualitative coincidence. For the given measurement point, the dominance of

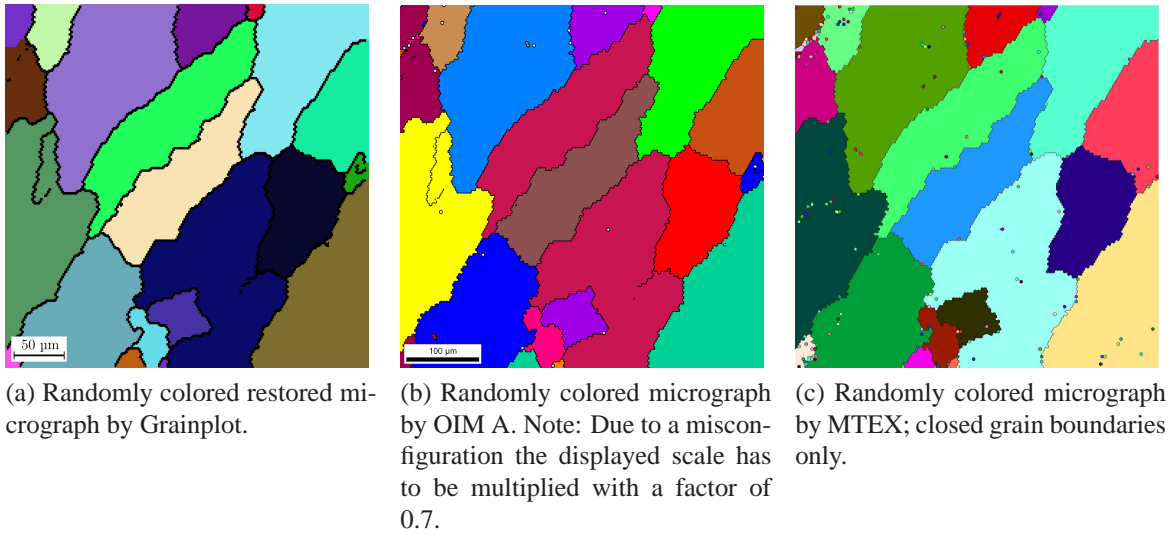


Figure 2.18: Grain identification in exemplary EBSD based micrograph of EN AW-6060. HAGB $\geq 15^\circ$ indicated by black lines.

LAGB $\leq 15^\circ$ is clearly visible in the full histograms in the left column (sub figures a, c, e). All programs also show some misorientation fractions between 1 % and 5 % between $30^\circ \sim 60^\circ$ which are emphasized in histograms in the right column (sub figures b, d, f) in which the HAGB $\geq 15^\circ$ are exclusively considered. Here, the individual bar heights are very sensitive to the applied filtering and the implemented histogram plotting functions so that a complete quantitative coincidence cannot be achieved. However, the general tendencies in the misorientation distributions plotted by Grainplot in Figures 2.20a and 2.20b show a good qualitative agreement with the results of OIM A in Figures 2.20c and 2.20d.

The misorientation handling routines implemented in the current version of MTEX only support limited features which do not facilitate the misorientation determination between individual data points but only between grains instead. By defining an extremely low misorientation threshold for the grain identification, almost all data points are identified as individual grains to simulate this feature. Filtering of the misorientation histograms is not implemented, leading to significant differences in Figures 2.20e and 2.20f compared to the results of the other programs. Nevertheless, the qualitative misorientation distribution is similar to the one obtained by Grainplot and OIM A. Since MTEX ships with accessible Matlab code, the missing functions can be added by the user himself.

A statistical evaluation of the EBSD measurements regarding the fraction of grain boundaries in a micrograph as described in Section 2.2.2 is not available in OIM A or MTEX. But since grain boundary plots serve as input data for the normed grain boundary fraction determination, it is possible to use those images from OIM A or MTEX as well. As previously shown, the produced misorientation maps of Grainplot and OIM A are almost identical and, in consequence, the obtained normed grain boundary fractions are equal. Partial LAGBs which freely end up inside a grain without enclosing a subgrain are not taken into account by MTEX. Therefore they are missing in the orientation maps, and the corresponding normed grain boundary fraction is systematically underestimated compared to Grainplot and OIM A.

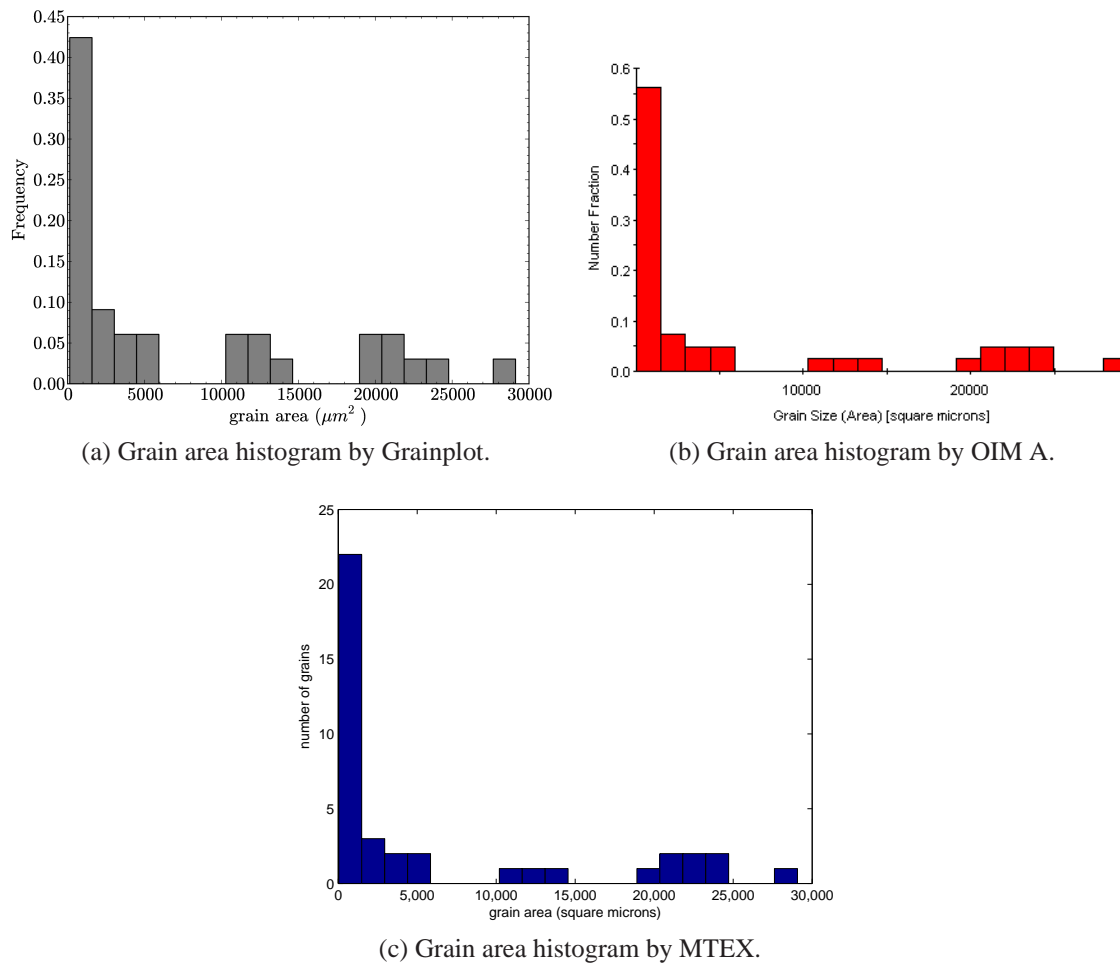
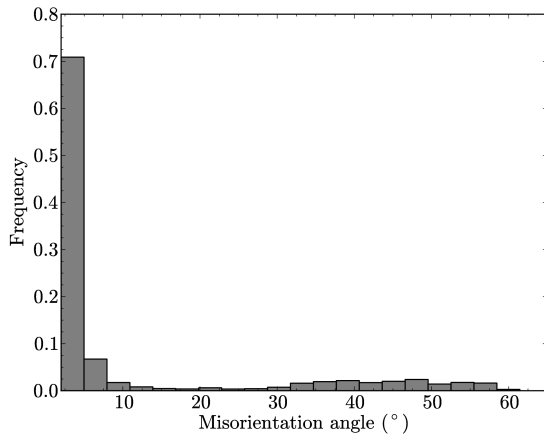


Figure 2.19: Grain area histograms of exemplary EBSD based micrograph of EN AW-6060.

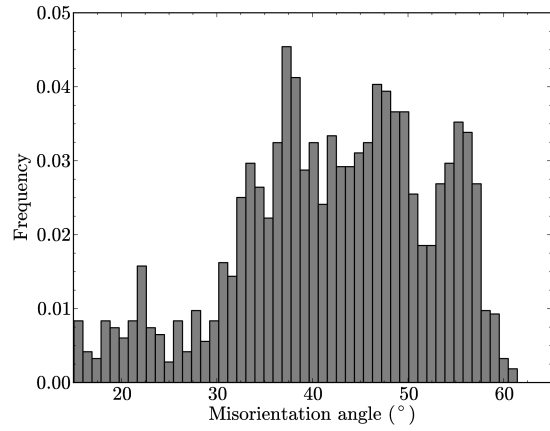
Inverse pole figures

To verify the quality of the discrete IPFs produced by Grainplot, the results of an exemplary measurement point are compared with IPFs from MTEX and OIM A in Figure 2.21. The discrete IPFs of Grainplot and MTEX in Figures 2.21a and 2.21b, respectively, show a clear qualitative agreement. The observed variance derives from the data restoration algorithm which filters outline results in Grainplot but not in MTEX. Furthermore, the restoration of points with low CI has a significant influence on the resulting stereographic projected pole pattern. The ODF based IPFs of OIM A in Figure 2.21c reflects the same texture. Here, in the [100] IPF, i.e. RD, the orientation density in [111] direction is weaker than expected from the results in Figures 2.21a and 2.21b. The directions between [001] and [111] in the [101] IPF also appear weaker than in the corresponding IPFs of the other programs. Again, the produced IPFs depend on the filter settings for data restoration and the chosen CI threshold.

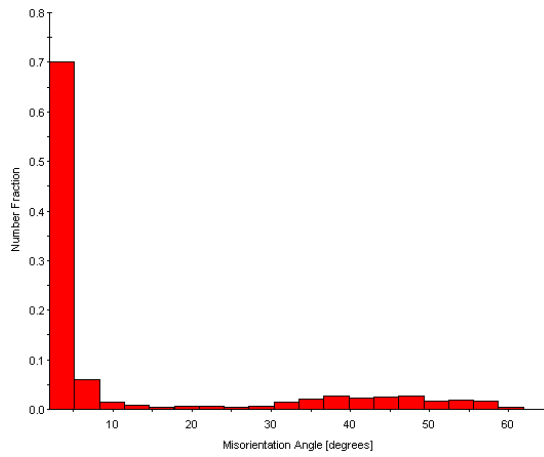
The additional IPFs in Figure 2.21d result from an X-ray diffraction measurement performed in the billet center near the die region which also covers the position of the exemplary measurement point used for verification. A comparison of the IPFs produced by the different programs proves that the texture identified from the small area EBSD measurements shows a good qualitative coincidence with the texture obtained by X-ray diffraction measurements over a larger



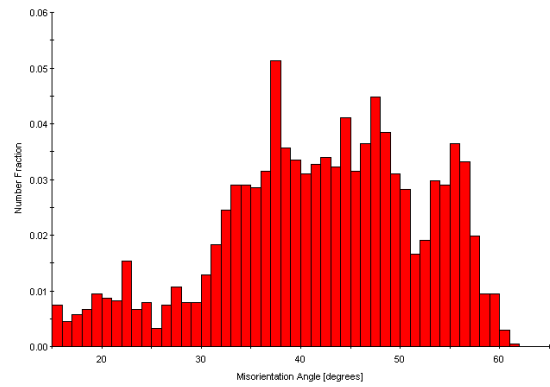
(a) Misorientation histogram by Grainplot.



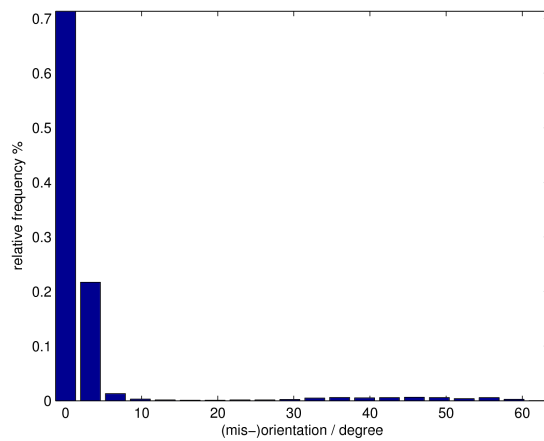
(b) Reduced misorientation histogram by Grainplot.



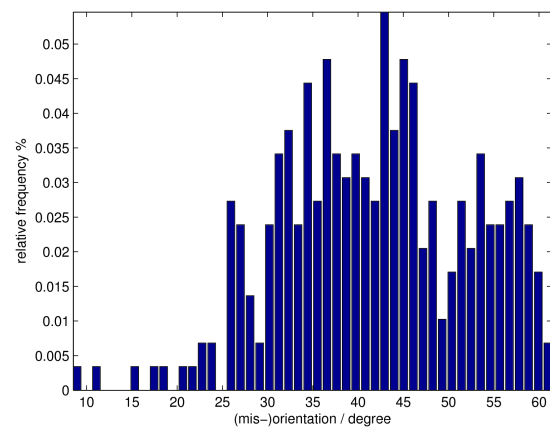
(c) Misorientation histogram by OIM A.



(d) Reduced misorientation histogram by OIM A.



(e) Misorientation histogram by MTEX.



(f) Reduced misorientation histogram by MTEX.

Figure 2.20: Misorientation histograms of exemplary EBSD based micrograph of EN AW-6060. Histograms in the right column are limited to HAGB $\geq 15^\circ$.

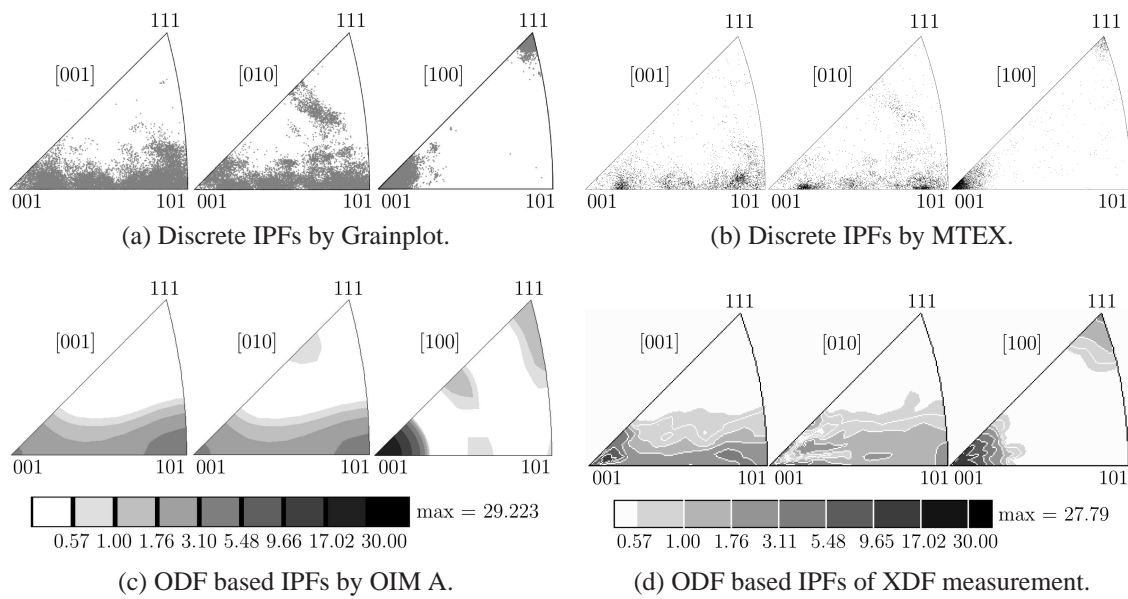


Figure 2.21: Discrete and ODF based inverse pole figures of an exemplary measurement point at die inflow area nearby middle axis of partly extruded billet of EN AW-6060.

area. This confirms the validity of the EBSD technique for microstructure investigations for aluminum EN AW-6060 under the given experimental conditions.

2.3 Synthetic microstructures

The characterization data obtained from the microstructures is used as input parameter for simulations of the microstructural evolution. A general overview on different models such as phase field and Monte Carlo Potts models as well as cellular automata to simulate grain growth and recrystallization in aluminum alloys is given by Miodownik (2002). The concept of phase field modeling applied to grain growth is also presented in the works of Fan and Chen (1997) as well as Krill III and Chen (2002) while the publication of Chen (2002) describes a more general application for the simulation of microstructure evolution. Cellular automata are used to model grain growth in the works of Liu et al. (1996) in 2-D and Ding et al. (2006) in 3-D. Dynamic recrystallization is simulated by an extended cellular automata approach by Ding and Guo (2002).

Independent from the used model, a simulation of microstructure evolution requires an initial 2-D or 3-D micrograph. These micrographs can be acquired by measurements but especially the measurements of 3-D microstructures, e.g. by using a combined FIB-EBSD device, are time and cost intensive. Through synthetic microstructure generation, several statistically equivalent micrographs can be produced from a single characterization data set. The generation of a 3-D polycrystalline microstructure model based on multi-layer EBSD images is described in the work of Bhandari et al. (2007). St-Pierre et al. (2008) uses a combination of Voronoi tessellation and grain representation by overlapping ellipses to generate 3-D microstructure models from EBSD based micrographs. A complete framework of automated microstructure characteriza-

tion and generation of corresponding 3-D microstructure models is presented in the publication series (Groeber et al., 2008a) and (Groeber et al., 2008b).

2.3.1 Synthetic microstructure generator Graingen

The burn algorithm introduced in Section 2.2.2 is quite similar to the approach of cellular automata already used to simulate recrystallization and grain growth as previously described. Therefore, the already implemented module for grain identification is modified so that a synthetic microstructure grows starting from a defined set of nuclei based on the previous microstructure characterization. The resulting stand-alone program Graingen generates synthetic 2-D and 3-D microstructures of variable size and resolution which are only limited by the available memory. Here, single grains are defined as grain object instances which are addressable by unique identification numbers (IDs). This allows an individual adjustment of growth laws and the tracking of growth history during all time steps. A grain object instance contains a list of all volumetric pixels (voxels) already belonging to this specific grain and further lists defining the grain periphery. During the grain growth simulation only the lists of boundary pixels are processed.

The main growth algorithm implemented to Graingen can be summarized as follows:

1. Define empty microstructure volume.
2. Define and initialize grain objects:
 - (a) Set grain nuclei according to user defined spatial grain distribution function.
 - (b) Assign individual grain orientations.
 - (c) Define global or individual grain growth control functions.
 - (d) Initialize all grain boundary groups with nuclei coordinates.
3. Grain growth by iterating over all grains in order of their IDs:
 - (a) Iterate over grain boundary groups.
 - (b) For each voxel listed in current boundary group iterate over neighboring voxels.
 - (c) Append free neighboring voxel to current grain if growth condition holds. Else, continue with next voxel in list.
 - (d) Update boundary lists
4. Grain growth automatically stops if no free neighboring voxels are found.
5. Close pores.

The grain object contains a list of all voxels belonging to an instance and two additional boundary sub lists for each direction in space, e.g. four sub lists in 2-dimensions and six sub lists in 3-dimensions. The sub lists also denoted as grain boundary groups are indexed as shown in Figure 2.22. The grain boundary lists contain all voxels at the grain surface which have the

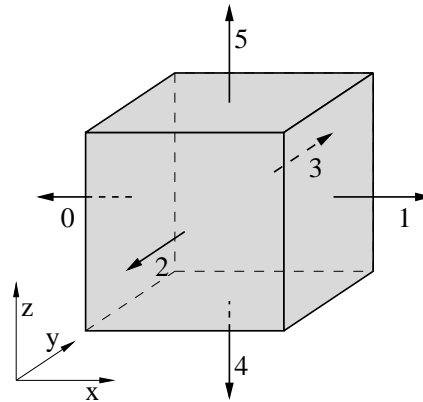


Figure 2.22: Indexing of grain boundary groups.

opportunity to expand into their neighborhood in the next time step. In order to increase the processing speed, separate sub lists for each direction in space are used instead of one global surface list for each grain. For all voxels in a specific boundary list it is known that the neighboring voxel in negative normal direction (reverse growth direction) already belongs to the specific grain. This direction is therefore not checked during growth. Under certain conditions this algorithm encloses free voxels inside the growing grains. These pores are closed in a final post-processing step by applying the grain restoring algorithm of Grainplot presented in Algorithm listing 2.

The currently implemented growth law is not deterministic but influenced by a variable randomized factor defining whether a voxel of the current grain is expanding into its neighborhood. In consequence, this provokes several 'dry runs' in the code where all conditions for grain growth except the grow factor are met. This procedure is still efficient since all previous conditions are dominated by fast if-statements so that the interrupted randomized growth shows an acceptable time consumption during code execution. The simplified pseudo code of the modified burn algorithm implemented in Graingen is presented in Algorithm listing 5. Here, only a single list of boundary voxels is used to limit the number of loops for reasons of clarity. The geometric periodicity is taken into account by the function `FindFreeNeighbors`. There is no algorithmic difference in the generation of a synthetic 2-D or 3-D micrograph by the shown code because a 2-D micrograph has simply one layer of voxels in one of the three micrograph's dimensions. The progress during grain growth of a synthetic microstructure based on the Graingen algorithm is exemplarily depicted in Figure 2.23. The initial nuclei of the 40 grains after 10 time steps in Figure 2.23a are randomly distributed, and the random grain orientation is represented by the grain color. With a chosen growth fraction of 0.3, the grains circularly expand as shown in Figure 2.23b for time step 51. The final periodic micrograph after 102 time steps and pore filling in the postprocessing is given in Figure 2.23c.

2.3.2 Generated synthetic microstructures

The characteristics of the generated synthetic microstructure are mainly controlled by the initial distribution of the grain nuclei and the individual growth laws of the grains. The exemplary synthetic micrograph depicted in Figure 2.24 generated by Graingen contains 10,000 grains.

Algorithm 5: Modified burn algorithm of synthetic grain generator Graingen.

Data: List of grain nuclei coordinates; List of grain orientations, List of global or individual grain growth laws; growth fraction; List of microstructure dimensions.

Result: Synthetic microstructure as ASCII type VTK file with orientation look-up table.

1 Initialization:

2 initialize LoGrainObjects

3 **foreach** Grain **in** LoGrainObjects **do**

4 Grain.Nucleus \leftarrow LoGrainNucleiCoords [Grain]

5 Grain.Orientation \leftarrow LoGrainOrientations [Grain]

6 Grain.GrowthLaw \leftarrow LoGrainGrowthLaws [Grain]

7 Grain.GrowthFraction \leftarrow GrowthFraction

8 Grain.LoVoxels \leftarrow Grain.Nucleus

9 Grain.LoBoundaryVoxels \leftarrow Grain.Nucleus

10 /* Grain growth - loop stops if no free voxels found */

11 Marker \leftarrow 1 /* magic value */

12 **while** Marker **not** 0 **do**

13 Marker \leftarrow 0 /* reset Marker */

14 **foreach** Grain **in** LoGrainObjects **do**

15 LoNewVoxels \leftarrow empty list /* reset list */

16 **foreach** BoundaryVoxel **in** Grain.LoBoundaryVoxels **do**

17 LoFreeVoxels \leftarrow FindFreeNeighbors (BoundaryVoxel,
18 LoDimensions)

18 Marker \leftarrow Marker + lenght of LoFreeVoxels

19 **foreach** Voxel **in** LoFreeVoxels **do**

20 **if** Grain.CheckGrowthFraction (Grain.GrowthLaw) == **True**
21 **then**

21 LoNewVoxels \leftarrow append Voxel

22 Grain.LoVoxels \leftarrow append Voxel

23 Grain.LoBoundaryVoxels \leftarrow LoNewVoxels /* update list */

24 **return** LoGrainObjects

25 Postprocessing:

26 ClosePores (LoGrainObjects)

27 write voxel coordinates from LoGrainObjects into VTK file

28 generate orientation look-up table from LoGrainObjects and add to VTK file

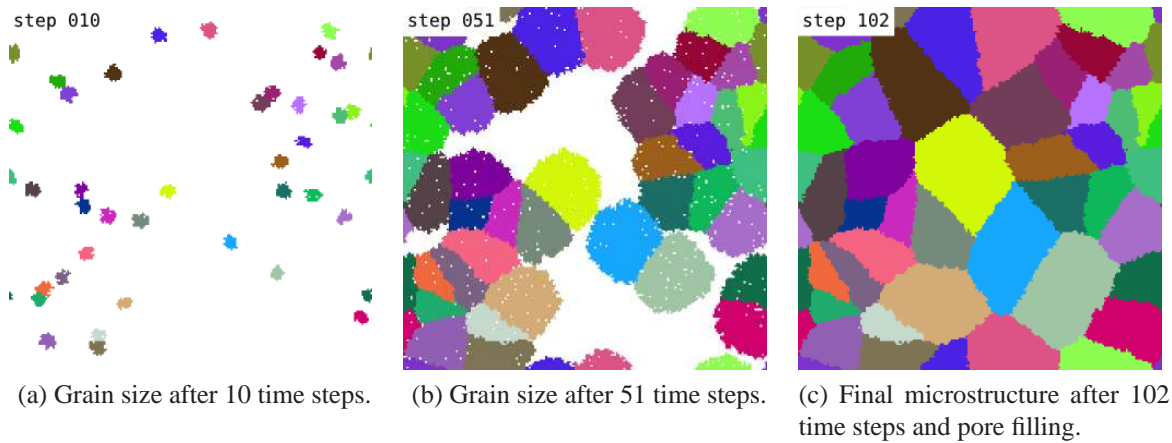


Figure 2.23: Grain growth of a synthetic microstructure based on the Graingen algorithm with random grain nuclei and orientation distribution.

Here, the growth fraction of 1.0 ensures that the grains continuously grow during each time step which leads to a grain boundary shape with preferred horizontal/vertical alignment and directions rotated by 45° .

Figure 2.25a shows a periodic synthetic microstructure consisting of 40 randomly distributed and oriented grains generated by Graingen. Grains which are cut at the micrograph's edges are continued on the opposite edges due to the geometric periodicity which allows to assemble several periodic micrographs to a larger structure. The growth fraction is 0.3 so that the grain boundaries are not straight but frayed and partly curved. The overlaid grain boundary adaptive FE mesh in Figure 2.25b is generated by the open source software OOF2 published by the United States National Institute of Standards and Technology (NIST) (Chawla et al., 2002; Langer et al., 2001; Reid et al., 2008).

An example for a geometrically periodical synthetic 3-D microstructure generated by Graingen is given in Figure 2.26. The microstructure data is stored in the .vtk file format of the free Visualization Toolkit (VTK) as structured points. Here, the grain orientations are embedded in a look-up table. This file format is independent from the operation system, and predefined read-in functions are available for a number of program languages.

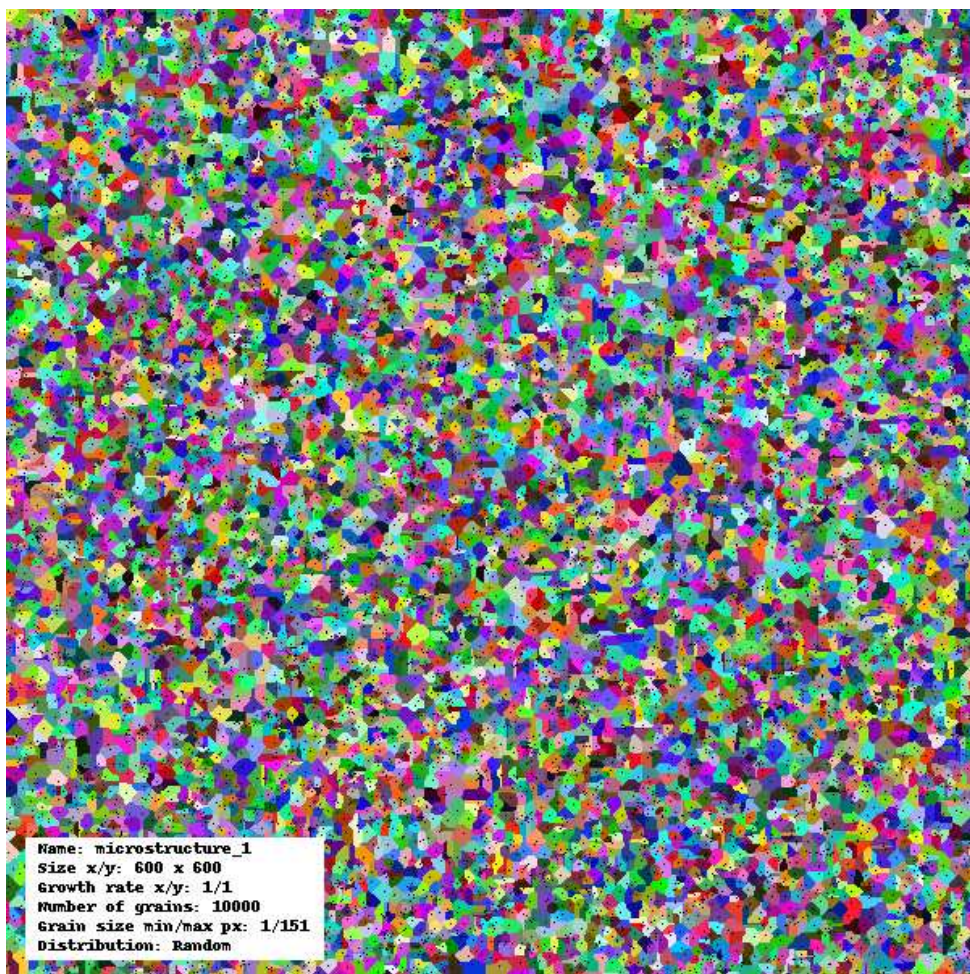
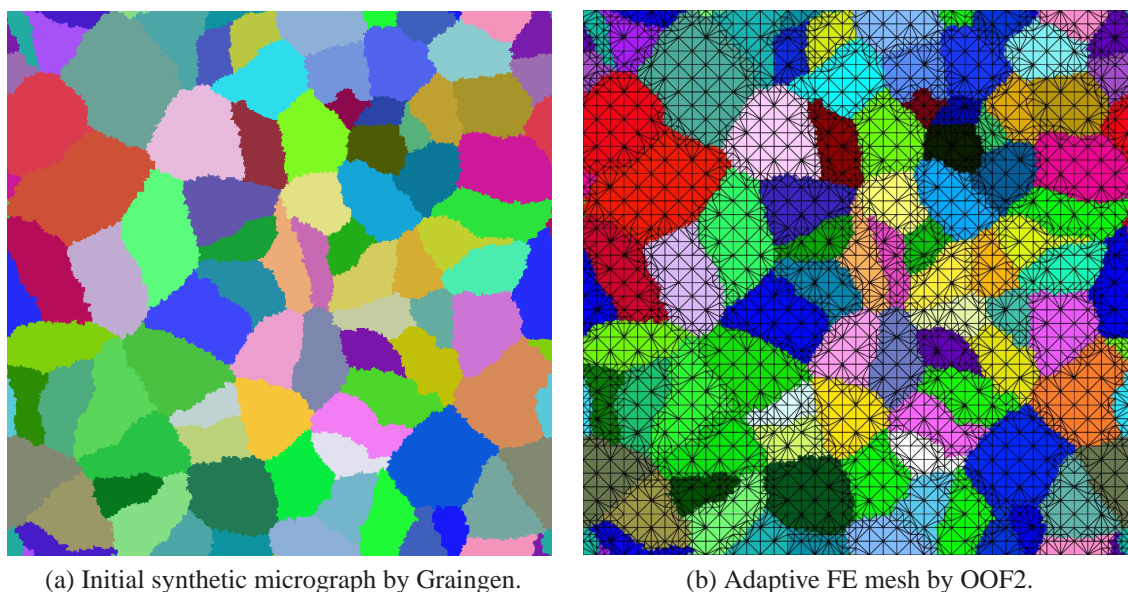


Figure 2.24: Synthetic micrograph of 10,000 randomly distributed and orientated grains generated by Graingen. Growth fraction 1.0; grain nuclei indicated by black dots.



(a) Initial synthetic micrograph by Graingen.

(b) Adaptive FE mesh by OOF2.

Figure 2.25: Grain boundary adaptive meshing of microstructures.

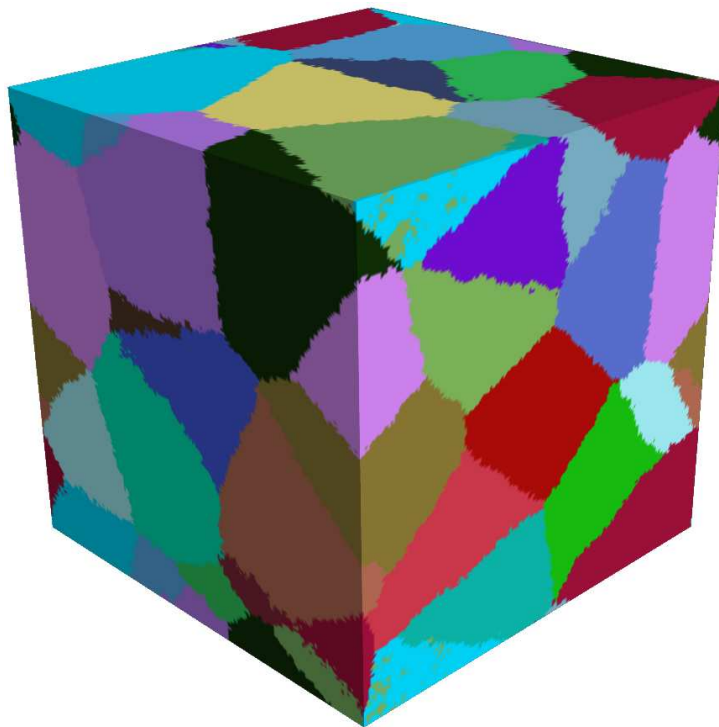


Figure 2.26: Synthetic periodic 3-D microstructure with 40 randomly distributed and oriented grains generated by Graingen. Cube dimensions $200 \times 200 \times 200$ voxels.

Chapter 3

Experimental results and material characterization

Abstract – For the characterization the aluminum wrought alloys EN AW-6060, EN AW-6082 and EN AW-7075 are exemplarily selected and their mechanical properties are briefly summarized. To reveal the microstructure evolution at different degrees of deformation, partly extruded billets are produced by direct hot extrusion and prepared by cutting along the middle axis. The characterization of the different partly extruded billet obtained by the experiments is based on mesoscopic LOM images as well as on selective EBSD measurements. The general formation of different deformation zones inside the billets is emphasized and, especially for EN AW-6060, the microstructure gradient observed in the extruded rod is discussed. EBSD measurements at representative points inside the distinctive deformation zones are presented and analyzed for each billet. For EN AW-6060 this additionally includes a path of measurement points along the rotation symmetry axis of the billet to trace the grain microstructure evolution in the center of the billet. Based on the EBSD results, the main grain microstructure characteristics are summarized in diagrams for each of the three alloys. Besides the grain size and texture development a normed fraction of grain boundaries (HAGB and LAGB based) is introduced which indicates the formation of GNB and the development of new (sub-)grains. Finally, the development of precipitates in the dead metal zone (DMZ) is briefly described on the basis of BSE SEM images.

3.1 Selection of aluminum alloys

The software tools developed in this work are used to characterize the three aluminum wrought alloys EN AW-6060, EN AW-6082 and EN AW-7075. The composition of these alloys according to the standard DIN EN 573-1 is listed in table 3.1. Alloy elements not listed in the table each have a weight fraction of less than 0.05 wt.% and not more than 0.15 wt.% in total. Both wrought alloys of the 6000 series are characterized by good warm forming ability which makes

Table 3.1: Aluminum wrought alloy compositions according to DIN EN 573-1; in wt.%, shortened.

alloy name	alloy elements							
	Si	Fe	Cu	Mn	Mg	Cr	Zn	Ti
EN AW-6060	0.3-0.6	0.1-0.3	0.1	0.1	0.35-0.6	0.05	0.15	0.1
EN AW-6082	0.7-1.3	0.5	0.1	0.4-1.0	0.6-1.2	0.25	0.2	0.1
EN AW-7075	0.4	0.5	1.2-2.0	0.3	2.1-2.9	0.18-0.28	5.1-6.1	0.2

them widely used for extruded products even with complex profile shapes. In combination with an acceptable corrosion resistance due to comparably low fraction of copper, the field of application reaches from window or door casings in civil engineering to interior equipment in the automotive and transportation sector, including even sailing boat masts. Due to their capability of surface finishing, mechanical polishing and anodization of these alloys is also used for a variety of house-ware products. The low copper content supports the weldability of these alloys, especially if using gas tungsten arc welding or gas metal arc welding.

In annealed condition both EN AW-6060 and EN AW-6082 provide a high deformability but also allow a significant increase in strength by suitable heat treatment as shown in Figure 3.1. The main material characteristics are then dominated by the main alloy components magnesium and silicon and their intermediate phase Mg_2Si which is responsible for the general hardening behavior of Al–Mg–Si alloys. Furthermore, each of the main alloy components silicon, copper and magnesium supports solid solution strengthening based on the mechanisms described in Section 1.2.3. The properties of the high strength Al–Zn–Mg–Cu alloy EN AW-7075 are mainly influenced by the zinc fraction. Zinc supports the development of intermediate phase Al_2CuMg which acts as precipitate nucleus and significantly increases the precipitation rate especially at low temperatures that are already reached during hot deformation processes. Additional contents of chromium and manganese suppress static recrystallization effects under certain process conditions so that a persistent grain refinement takes place during plastic deformation. Although this alloy shows a high tensile strength, its field of application is limited since the high copper fraction reduces the corrosion resistance and dramatically increases hot cracking during fusion welding. Typical application for profiles and plates of EN AW-7075 are high stress materials in aerospace industry or high quality light weight sports equipment.

Figure 3.1 exemplarily compares the material properties tensile strength R_m , tensile yield strength $R_{p0.2}$ and R_{eH} , respectively, for the three described aluminum alloys and two steels. Additionally shown is the maximum fracture strain at which specimens fail at tensile tests. S235JR is a typical mild steel widely used in civil engineering, and 42CrMo4v is a high strength quenched and tempered steel for gear wheels and other high stressed materials in the field of mechanical engineering. The values vary depending on different heat treatments leading to grain fining and/or precipitation hardening. As shown, aluminum alloys of the 7000 series reach strengths in the range of mild steels but generally aluminum alloys are defeated by high strength steels. This has to be compensated by construction layout, e.g., increasing wall thicknesses of aluminum parts.

3.2 Direct hot extrusion experiment

The extrusion experiments dealt with in this section have been performed at the Institute of Forming Technology and Lightweight Construction (IUL) at TU Dortmund University. A complete description of the process conditions is given in the work of Schikorra et al. (2007). For the aluminum alloys EN AW-6060 and EN AW-6082 billets with 139 mm in diameter and 295 mm in length are prepared. The billet made of EN AW-7075 has the same diameter but a shortened length of 140 mm to reduce the punch forces which are limited by the extrusion press.

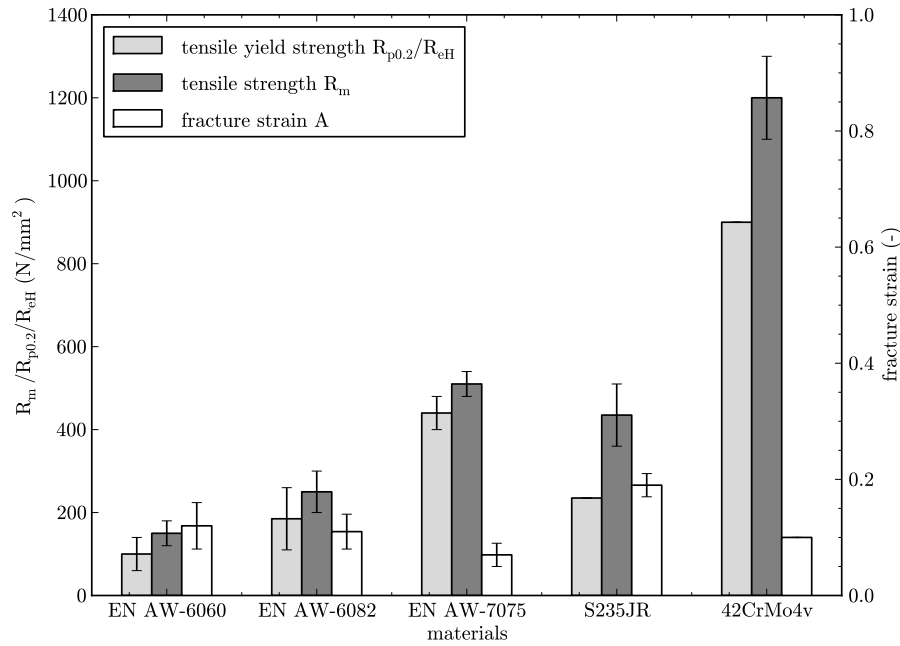


Figure 3.1: Tensile and tensile yield strength and fraction strain of aluminum alloys compared to steel. Values vary according to heat treatment following the standards DIN EN 755-2, DIN EN 10025-2 and DIN EN 10083-3.

The main experimental steps are summarized in table 3.2. Firstly, the billets are preheated and homogenized in a separate oven at a constant temperature of 550 °C for 8 hours. The handling of the specimen during insertion into the press takes approximately 2 min while the billet temperature decreases by 10 °C which is monitored by applied thermo-elements. The direct extrusion process is sketched in Figure 3.2 and takes 7 min for the billets of the EN AW-6060 and 6068 but 4 min for the EN AW-7075 billet with a constant ram speed of 0.3 mm/s in all three experiments. In the beginning, the billet diameter widens from the initial diameter of 139 mm to the inner diameter of the container which is 146 mm. Afterwards it is extruded through a die with a diameter of 36.5 mm (extrusion ratio 16) and a bearing length of 12 mm finally resulting in a solid rod of 36 mm in diameter after cooling. During the extrusion process the die

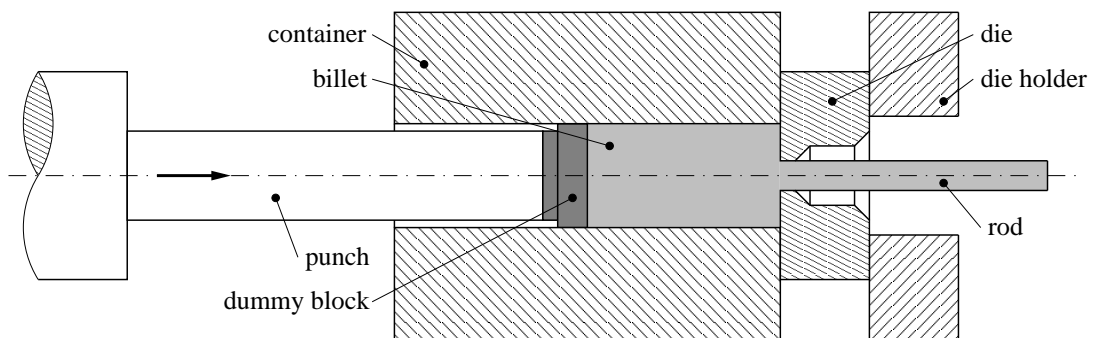


Figure 3.2: Schematic direct extrusion process.

Table 3.2: Temperature profile during direct extrusion process according to Schikorra et al. (2007).

process description	time [min]	billet temperature
preheating in separate oven	480	550 °C
handling, billet insertion into press	2	550 °C → 540 °C
extrusion process	4/7	540 °C → 450 °C
billet removal from extrusion press	15	450 °C → 400 °C
air cooling to room temperature	—	400 °C → 20 °C

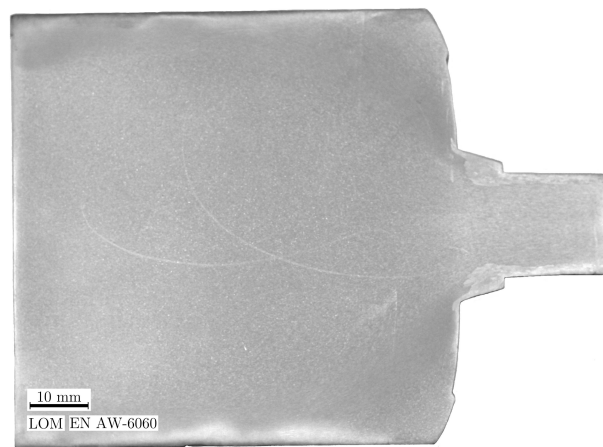


Figure 3.3: Etched cross section of a partly extruded billet of EN AW-6060. Underlying LOM image by courtesy of the Institute of Forming Technology and Lightweight Construction (IUL), TU Dortmund University.

temperature is permanently monitored showing values of 420 °C for EN AW-6060, 380 °C for EN AW-6082 and 365 °C for EN AW-7075. Sporadic temperature measurements of the exiting profile near the die show that the material temperature deviates no more than 5 °C from the die temperature. Before the billet can be released from the extrusion press, the die and the die holder have to be removed. During the 15 min needed to open the press, the billet temperature remains at an elevated level and continuously decreases from 450 °C to 400 °C. Finally, the retrieved profile cools down to room temperature on ambient air.

To allow an investigation of the microstructure at different stages of plastic deformation, the process is stopped when approximately 40 % of the original billet length has been extruded. A partly extruded billet is exemplarily given in Figure 3.3 and shows distinct areas of different material flow history which are discussed in detail later in this chapter. From left to right the image shows the billet, the die region with a funnel-shaped die inflow and the extruded solid rod. The die inflow acts as a welding chamber for continuous billet-on-billet extrusion. The outer shape of the partly extruded billet is influenced by experimental conditions. The bulge on the initially plane front surface results from friction during the ejection of the billet from the container after removing the die and die holder. The concentric kink located on the

front face ~ 10 mm from the outer billet diameter originates from the die design of the die which facilitates the use of replaceable containers with different diameters. Due to the design of the used press, it is not possible to quickly unload the partly extruded billet after stopping the process and the billet remains heated by the surrounding container for 15 min at elevated temperatures above 400 °C. Depending on the alloy composition and deformation history, at this temperature level SRX effects may occur and falsify the grain size and misorientation statistics. These influences on the microstructure are not evident during the active extrusion process since the profile continuously leaves the die and cools down in ambient air.

3.3 Sample preparation

3.3.1 Light optical microscopy

Following the extrusion and the cool-down process, the partly extruded billets of the different alloys are prepared for microstructure investigations. They are cut along the symmetry axis in direction of extrusion to provide access to the microstructure at different zones inside the billet and extruded rod. A constant water cooling in combination with a reduced cutting speed minimizes the thermal and mechanical influences of the cutting process on the microstructure at the section surfaces. The possibly affected top layer at the surface of the cut specimen is then removed by wet-sanding. One cross section of each billet is prepared for LOM investigation by mechanically polishing and chemically etching the surface as described in Schikorra et al. (2007). The etching reagent consists of 8.7 % concentrated hydrofluoric acid solution and 13 % concentrated hydrochloric acid solution in water according to Flick (1925). The etching time varies between 5 and 8 min at room temperature to reveal a high-contrast micrograph which allows to distinguish individual grains. Finally the surface is sealed with transparent varnish to prevent oxidation and staining. A sample LOM image of a prepared partly extruded billet is given in Figure 3.3.

3.3.2 Electron Backscatter Diffraction

The EBSD measurements require small specimens, the size of which allow a placement inside the vacuum chamber of the used Philips XL 40 ESEM with tungsten filament operating at a nominal acceleration voltage of 20 kV. Therefore, small parts of 20 mm \times 20 mm \times 12 mm are cut out at points of interest from the mid-plane surface of the partly extruded billet. As discussed in Section 1.6.4, the EBSD technique requires a high surface quality to ensure a correct orientation determination. The necessary surface preparation includes several mechanical polishing steps with increasing abrasive grain sizes down to 5 μ m. The cutting and polishing processes are performed under special consideration of preventing any undesired thermal and/or mechanical effects. Subsequently, electro-polishing in a 5 % perchloric acid solution in water under an applied potential of 30 V at -25 °C is performed to remove the mechanically influenced atomic layers at the specimen's surface. A further sealing of the surface with transparent varnish is not possible.

All EBSD measurements presented in this work and the corresponding sample preparations have been performed at the Lehrstuhl für Werkstoffkunde (Materials Science) at the University of Paderborn. The scan area size varies between 250 μ m \times 250 μ m and 1200 μ m \times

1200 μm depending on the expected grain size for the different alloys and deformation zones inside the billet. The used scan raster is a regular hexagonal grid with variable number of steps and step sizes. EBSD measurement results obtained from the experimental samples discussed in the previous section are also presented in Schikorra et al. (2008).

3.3.3 Scanning electron microscopy

The SEM device Philips XL 40 ESEM used for the EBSD measurements can also be applied to generate images of the precipitate distribution. The sample preparation is basically the same as described in the previous section. By using the backscattered electrons (BSE mode) the image contrast depends on the material density at the measurement points. Since the precipitate particles have a significantly higher density than the aluminum matrix, they can be identified with a good contrast. Furthermore, the intensity of the BSE signal allows to draw conclusions on the elemental particle composition.

3.4 Characterization of EN AW-6060

3.4.1 Deformation zones and mesoscopic microstructure development

Figure 3.4 shows a scanned half section of a partly extruded billet of EN AW-6060 with an overlaid 5 mm raster. During preparation this specimen was cut ~ 11 mm from the symmetry axis to preserve the microstructure of the other half section for the EBSD sample preparation. The experimental conditions of the direct hot extrusion process and cooling conditions can be found in Section 3.2. In the remaining billet, three different zones of microstructural development are evident which are separated by the black lines in the upper half of Figure 3.4. The forming of deformation zones according to the plastic deformation is discussed by Valberg (1992) who performed direct extrusion experiments with marked billets to visualize the material flow. Further information is also given by Bauser et al. (2006).

In the Dead Material Zone (DMZ) which forms a cone at the front of the block, friction between the billet, container and die results in little material deformation and concomitant microstructural development as shown by Misiolek and Kelly (1992); Trogolo et al. (1996); Valberg (1992) and others. Under ideal conditions the microstructure in the DMZ remains almost unchanged from its state after preheating (Saha, 2000). However, due to undesired loading of the billet during release from the press, the material in the DMZ is plastically deformed. This is indicated by the bulk shape of the front face on the right side in Figure 3.4. The influence of the plastic deformation in this zone is discussed in Section 3.4.2. In the neighboring Shear Intensive Zone (SIZ) the material undergoes significant and predominantly shear deformation. As a result, the microstructural evolution in this region is quite complex during both extrusion and cooling and can be influenced by various process parameters as shown by Peng and Sheppard (2004a,b). A visual comparison of the microstructure of the SIZ compared to the DMZ reveals that the grain size significantly decreases under shear load which is later statistically evaluated based on the EBSD measurements. Generally, the high stacking fault energy of aluminum alloys and the high temperature conditions during the extrusion process facilitate dislocation climb resulting in DRV and GDX in the SIZ. Furthermore, friction and material sticking between billet and container wall also produce a thin layer of shear deformed material

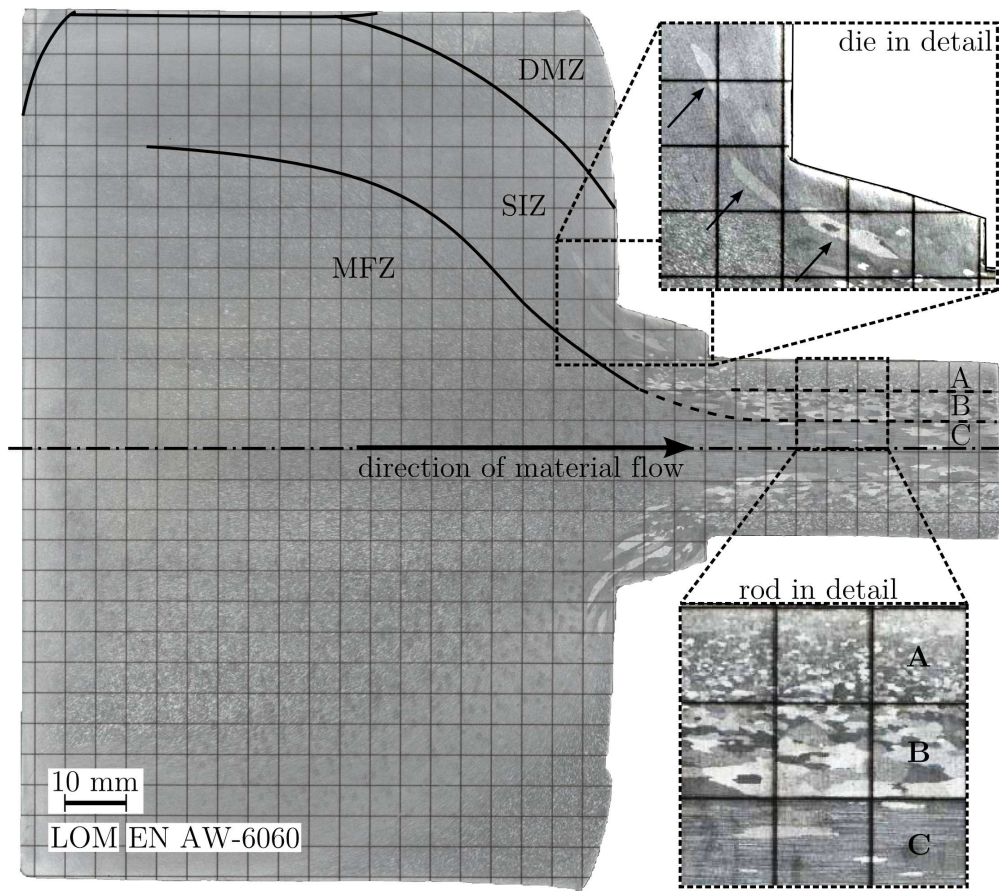


Figure 3.4: Half section of a partly extruded billet of EN AW-6060 with overlaid 5 mm raster. Detail images of die and rod regions are contrast improved. Underlying LOM macro scan image by courtesy of the Institute of Forming Technology and Lightweight Construction (IUL) at TU Dortmund University.

in the area beneath the billet's surface which is indicated by extension of the black line separating DMZ and SIZ. The central region of the block is denoted as Material Flow Zone (MFZ). Here, the material flows towards the center of the extruded rod. With decreasing distance to the die the material is mainly stretched in direction of extrusion and individual grains elongate into a banded microstructure. A discussion on the grain microstructures in the different deformation zones based on LOM images can be found in the work of Schikorra et al. (2007).

The detailed view of the extrudate shown in Figure 3.4 (right) reveals that the grain size distribution is not homogeneously perpendicular to the direction of extrusion. Indeed, three different axisymmetric zones labeled A, B and C are discernible which are comparable to the zones observed by Ishikawa et al. (2006) during direct extrusion of the aluminum-copper alloy EN AW-2013. The central zone C exclusively contains material from the MFZ. Here, the minimum stored energy needed to drive SRX upon extrusion is generally not achieved. Consequently, the elongated-grain fibrous texture developed during the extrusion process in this region persists after the extrudate exits the die. In fact, SRX occurs only in a few isolated regions near the middle axis. In contrast, the neighboring zone B is characterized by larger grains

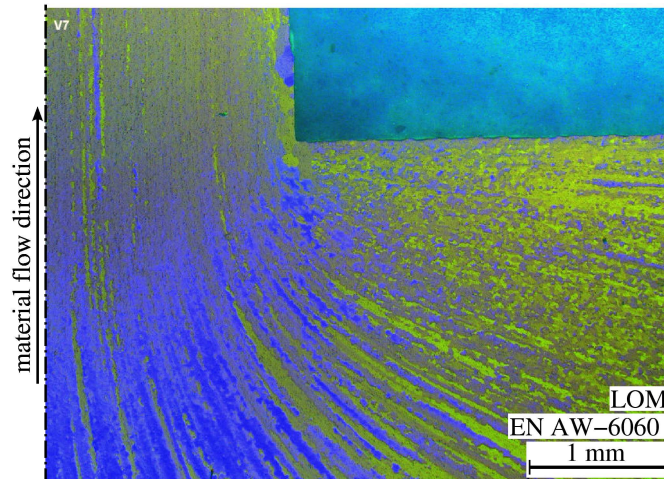


Figure 3.5: Detailed view on die area of a partly extruded block of EN AW-6060 from miniature extrusion experiment. Dot-dashed line on the left marks rotation symmetry axis. Underlying LOM image by courtesy of the Institute of Forming Technology and Lightweight Construction (IUL) at TU Dortmund University.

resulting from SRX. This material originates in the SIZ where sufficient energy is stored by shear deformation during extrusion to facilitate SRX. Lastly, in the outer zone A, a finer grain microstructure develops. Both zones A and B contain material emanating from the SIZ. Zone B material originates in the SIZ nearer to the MFZ whereas material of zone A has its source near to the DMZ. Since the material in the DMZ does not flow at all, SIZ material located near the DMZ undergoes even more severe shearing in the die direction than material near the MFZ. This results in a larger number of recrystallization nuclei in the grains which store the deformation induced energy, finally leading to a smaller average grain size (Humphreys and Hatherly, 2004). The smooth increase in mean grain size from zone A to B is primarily related to the varying deformation history inside the SIZ. However, the significant difference in grain size between zones B and C results from the different origins of the material involved (i.e., SIZ and MFZ).

A closer look at the microstructure near the die (see detailed view of die region in Figure 3.4) reveals elongated, abnormally large recrystallized grains in this area (marked by arrows). Such a microstructure is not expected to result from dynamic recovery and CDX/GDX. This is caused by the special environmental conditions arising in this part of the die. Indeed, this region remains at high temperature and zero loading for 15 min during removal of the partly extruded billet. During this time, primary and secondary recrystallization occurs in the SIZ material near the die which already exhibits enough stored energy to drive SRX. To determine the influence of SRX on the final microstructure observed in the partly extruded billets, small scaled miniature extrusion experiments were performed by . Here, the small dimensions of the billet (diameter 20 mm) combined with a disposable container allows water quenching of both parts directly after interrupting the extrusion process. Afterwards the container with the remaining billet is cut in along the direction of extrusion and prepared for LOM observation. An LOM image with polarized light of a partly extruded miniature billet of EN AW-6060 is shown in Figure 3.5. The color contrast emphasizes the elongation of grains while flowing towards the die of 4 mm in

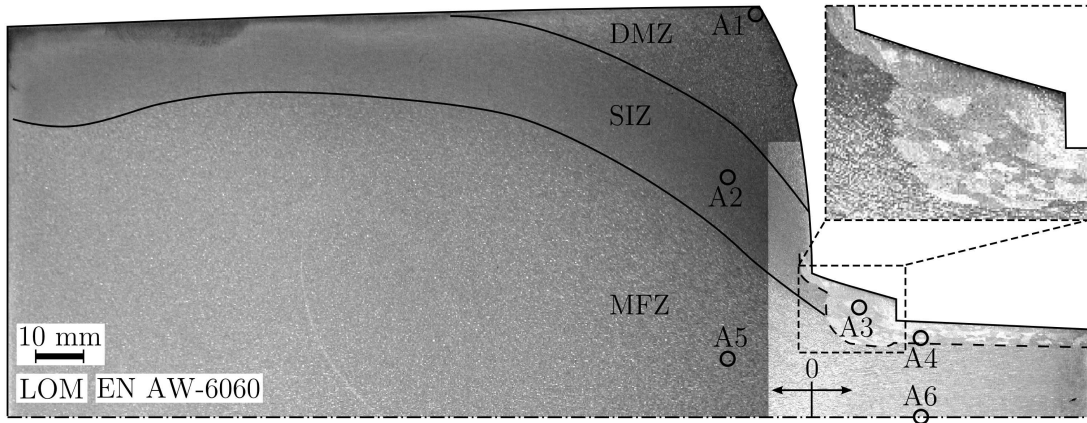


Figure 3.6: Half section of a partly extruded billet of EN AW-6060. EBSD measurement point positions marked by circles. Black lines separate labeled deformation zones. Detailed view on inflow region is contrast improved. Underlying LOM macro scan image by courtesy of the Institute of Forming Technology and Lightweight Construction (IUL) at TU Dortmund University.

diameter during extrusion with a ram velocity of 2 mm/s. Only a few globular shaped grains resulting from SRX can be found exclusively at the surface of the extruded grains. The influences of the extrusion process parameters on the resulting microstructure of the related alloy EN AW-6082 are described in detail in the work of Parvizian et al. (2011). The quick quenching of the sample prevents further SRX and freezes the microstructure at the die area during the extrusion process. This proves that the oversized recrystallized grains observed at the die areas of the partly extruded large scale billets result from SRX during the resting time while opening the press for release.

3.4.2 EBSD measurements in different deformation zones

In contrast to the LOM image previously presented, the EBSD analysis gives access to more details of the evolving microstructure in the partly extruded billet. In a first step the evolution of the subgrain structures and the orientation of individual grains in the different deformation zones are analyzed and discussed. Figure 3.6 shows half of the counter part of the partly extruded billet also presented in Figure 3.4. Here, the cut of the half section in direction of extrusion lies exactly in the center of the billet, and the deformation zones DMZ, SIZ and MFZ are defined by black lines. Again, the detailed view with improved contrast value at the inflow and die area reveals large globular-shaped grain resulting from SRX during the resting time under high temperature. The die area and the extrudate appear to be brighter in the LOM image due to image improvement.

The grain microstructure evolution in the different zones is discussed for the six sample points A1–A6 marked by circles in Figure 3.6. Point A1 is located in the outer corner of the DMZ and is used as reference point showing the microstructure in the most original state before the extrusion process. The points A2, A3 and A4 approximately follow a streamline of material flow inside the SIZ from billet over inflow into the extruded rod. Finally, the points A5 and A6 are representative for the microstructure evolution inside the MFZ. The obtained EBSD

results at the measurement points are summarized in Figure 3.7 with marked grain boundaries. HAGB are depicted by bold black lines and distinct individual grains with a misorientation $\geq 15^\circ$. For LAGB, indicated by narrow gray lines, the limit is set to $\geq 3^\circ$. To emphasize the underlying grain microstructure, grain fragments consisting of five or less data points have been removed from the micrograph. Corresponding to the expected grain sizes estimated from the LOM images, the scale for the EBSD micrographs of points A1, A3 and A4 differs from the others. All micrographs are rotated according to the billet orientation shown in Figure 3.6.

The grain microstructure of point A1 located in the DMZ is presented in Figure 3.7a and dominated by globular-shaped grains. There is also an impressed structure of subgrain structure which forms a banded structure with a tilt angle of 45° . This subgrain structure evolves due to the undesired plastic deformation also leading to the bulge shape of the front face while the partly extruded billet is released from the press. At the elevated temperature level in the billet, the dislocations induced by plastic deformation arrange to LAGB by DRV processes. It can be assumed that the forming LAGB are GNB which split the existing grains into smaller fragments. A further increase in misorientation between the individual subgrains yielding newly formed grains separated by HAGB due to CDX is not observed at point A1. The color coding of the grains according to the orientation triangle given in Figure 3.7a shows no preferred grain orientation which is supported by the misorientation analysis in Section 3.4.4. When excluding grains which are not entirely placed inside the micrograph, the mean subgrain size results in $\sim 2035 \mu\text{m}^2$ and the mean grain size is $7570 \mu\text{m}^2$.¹

In contrast to the globular-shaped grains in the DMZ, the EBSD based micrograph at point A2 in Figure 3.7b reveals elongated grains and a distinct subgrain structure. The elongation of the individual grains follows the direction of shear load which induces the necessary energy to drive the grain microstructure evolution inside the SIZ. With respect to the image scale, the mean grain size of $\sim 1590 \mu\text{m}^2$ at point A2 is significantly smaller compared to the more original state observed in the DMZ. Due to DRV, the elongated grains split into several – in the cut plane globular-shaped – subgrains with a mean size of $\sim 610 \mu\text{m}^2$. The serrated shape of the HAGB and the orientation of LAGB perpendicular to the grain's long axes indicate the influence of arising GDX at this measurement point. The color shading of the EBSD micrograph at point A2 indicates a grain orientation alignment especially towards the $\langle 111 \rangle$ and $\langle 101 \rangle$ directions.

As visible in the detailed view onto the inflow and die section in Figure 3.6, this region is dominated by abnormally large grains compared to the initial grain sizes observed in the DMZ. Although the scanned area of the micrograph shown in Figure 3.7c is more than 30 times larger than for point A2 for example, the number of grains entirely placed inside the micrograph is too low for a statistical grain size analysis. Taking incomplete grains into account, the mean grain size in the micrograph of point A3 is increased by a factor of more than 300 in comparison to the SIZ from which the material originated. When the extrusion process is interrupted the material located in the outer inflow region contains enough energy – induced

¹The results of the microstructure evolution along the middle axis and in the different deformation zones for a partly extruded billet of EN AW-6060 are also presented in Kayser et al. (2010). However, due to applied grain size filtering and the exclusion of incomplete grains at the micrograph's edges, the obtained grain sizes differ from the values reported here.

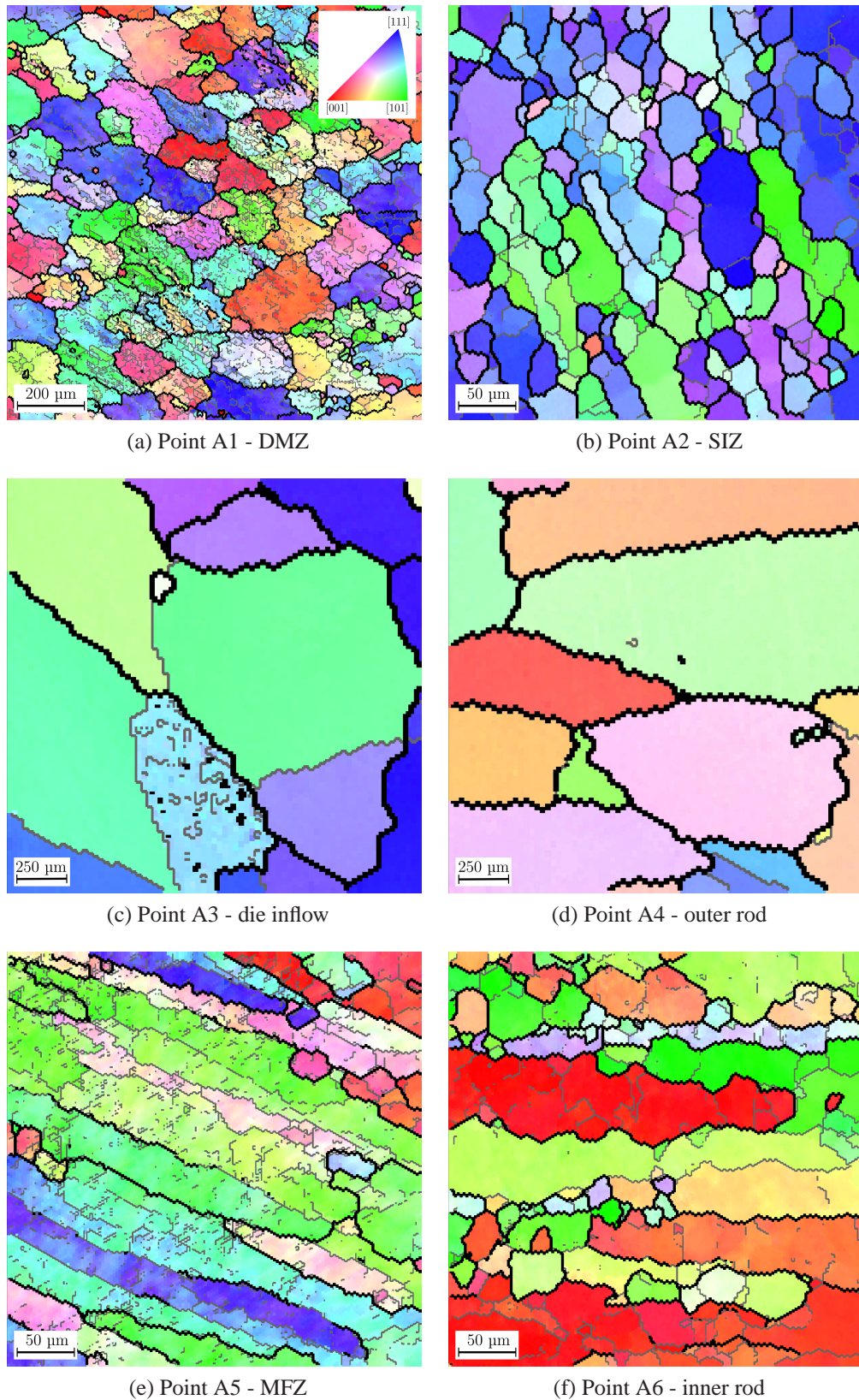


Figure 3.7: Restored EBSD based micrographs by Grainplot for different deformation zones in partly extruded billet of EN AW-6060. See Figure 3.6 for measurement point positions. Grain colors according to orientation triangle in subfigure a. Bold black lines indicate HAGB $\geq 15^\circ$, narrow gray lines indicate LAGB $\geq 3^\circ$. Minimum grain size filter is $155 \mu\text{m}^2$ in (a), $34 \mu\text{m}^2$ in (b), (e), (f) and $3827 \mu\text{m}^2$ in (c), (d); minimum CI of 0.1.

by the shear deformation in the SIZ – to drive primary nuclei based SRX. The resting time at an elevated temperature then facilitates additional grain growth by secondary recrystallization which is driven by the surface energy of the newly formed grains. In consequence, existing subgrain structures inside the grains are mostly annihilated. The HAGB grain structure in the SIZ mainly consists of elongated grains which channelize the recrystallization by following the present HAGB so that the elongated structure is partly conserved, but in a less distinctive form. The region containing recrystallized grains extends into the SIZ as far as the grains already contain sufficient deformation energy and dislocations to initialize nucleation and to drive SRX. Since the nucleation of primary SRX starts inside existing grains from the SIZ, the aligned orientation observed at point A3 in Figure 3.7c remains rather unaffected predominantly towards the $\langle 111 \rangle$ and $\langle 101 \rangle$ directions.

The coarse grain structure of point A4, depicted in Figure 3.7d, results from the same recrystallization mechanisms of primary and secondary recrystallization leading to the grain microstructure evolution acting at point A3. Here, the grain elongation rotates into the direction of extrusion and the texture is weaker than found at point A3. The scale of the micrograph of point A4 is equivalent to the one also used for point A3. Due to SRX only very few LAGB remain.

In comparison to the material of the SIZ, the rate of plastic deformation of the material inside the MFZ is significantly lower. Hence, the representative grain microstructure at point A5 in Figure 3.7e shows elongated grains, the mean size of which is $\sim 4360 \mu\text{m}^2$ under consideration of incomplete grains at the micrograph's edges. Since this reduces the effective mean grain size, it can be expected that the true grain size lies somewhere in the range of the initial grain size obtained in the DMZ. In contrast to the observations in the SIZ, the subgrain structure in the MFZ consists of GNB (mainly oriented parallel to the existing HAGB) and randomly orientated LAGB fragments inside the grains which do not yet form a closed subgrain structure yet. According to the orientation triangle, the grain orientation varies between $\langle 001 \rangle$ and $\langle 101 \rangle$.

A similar microstructure is found at the middle axis of the extruded rod which is displayed in Figure 3.7d. At this point the HAGB of the elongated grains already show the characteristic serrated shape which indicates the presence of GDX. Furthermore, the LAGB are now less fragmented and more oriented perpendicularly to the HAGB. The location of point A6 leads to the conclusion that the microstructure in the center of the billet largely remains in this condition since no further plastic deformation occurs. During the continuous extrusion process, the decrease in temperature due to radiation and air cooling conserves the microstructure when the temperature falls below the activation temperature of SRX. Consequently, on average, the deformation-dominated, elongated-grain texture microstructure developed during the extrusion process persists after the extrudate exits the die. Only in a few isolated regions near the middle axis where the deformation induced energy reaches the necessary level, some recrystallized grains are found in the detailed view on the extruded rod in Figure 3.4.

3.4.3 Microstructure evolution along middle axis

For a further investigation on the grain microstructure evolution based on EBSD measurements, a number of additional points along the symmetry axis in the center of the billet are selected. In this section the material faces a rather moderate plastic deformation and it can be assumed

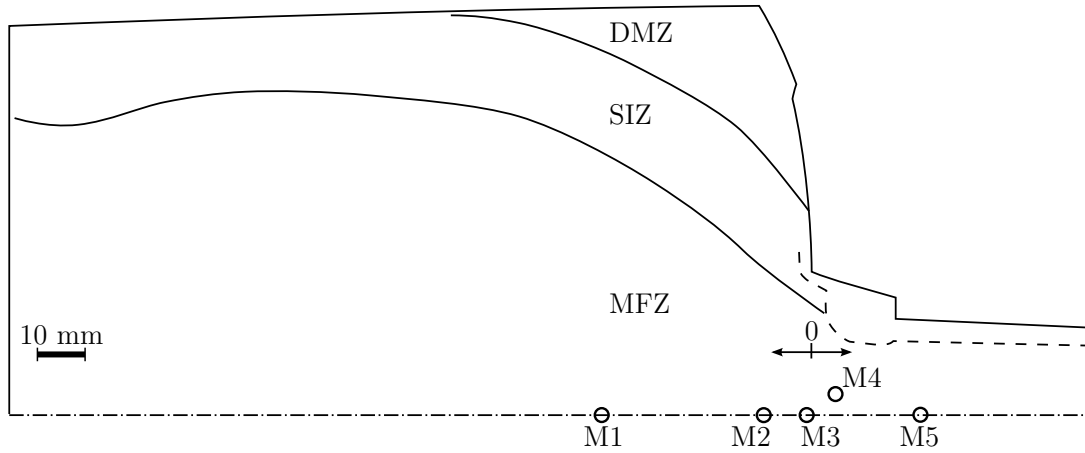


Figure 3.8: Contour of half section of a partly extruded billet of EN AW-6060. EBSD measurement point positions marked by circles. Black lines separate labeled deformation zones. Dashed line marks zone of recrystallized grains at die inflow and inside extruded rod.

that SRX caused by the experimental conditions has only a minor influence on the final microstructure. Exemplary of the general microstructural development as a whole in this region, the five measurement points are placed as follows: M1 is located 40 mm in front of the die inflow according to the point of origin indicated in Figure 3.8. M2 has a distance of 10 mm towards the die inflow. Points M3 and M4 are located directly in front of and inside the die inflow respectively. The position of point M4 is shifted 3.5 mm from the middle axis due to specimen preparation but is still located in zone C introduced in Figure 3.4. Finally, M5 is located 5 mm away from the die inflow. Point M5 is identical to point A6, the EBSD based micrograph of which has already been discussed in the previous section.

The grain and subgrain evolution along the middle axis of the billet is reflected by the EBSD micrographs shown in Figure 3.9. Grain fragments smaller than the threshold of five data points, i.e. $34 \mu\text{m}^2$, and data points with a $C < 0.1$ are filtered. The microstructure at point M1 in Figure 3.9b is still dominated by grains with a moderate elongation towards the die. The subgrain structure evolution is in an early stage and the LAGBs $\geq 3^\circ$ do not form a generally closed mesh. There is a weak tendency of the LAGB arranging parallel to the direction of extrusion. With increasing deformation the misorientation of these LAGB continuously increases, finally leading to an assembly of parallelly aligned thin elongated grains separated by HAGB due to CDX. The majority of grains show an orientation towards $\langle 101 \rangle$ but a number of grains with random orientation can be found as well. The mean grain size is $6430 \mu\text{m}^2$, if including incomplete grains, so that the effective grain size is comparable to the initial grain size.

At point M2 the elongation of the existing grains proceeds and leads to a banded microstructure shown in Figure 3.9c. A distinct subgrain structure caused by DRV can be observed especially in the most elongated grains. Here, the LAGB are oriented perpendicularly to the longitudinal direction. In combination with the serration of the HAGB this leads to a detachment of grain fragments when the opposite HAGB get in contact which represents the GDX mechanism. Detached grain fragments with an approximate dimension of the former subgrains are marked by arrows in Figure 3.9c. Additionally, evolving LAGB parallel to the HAGB are

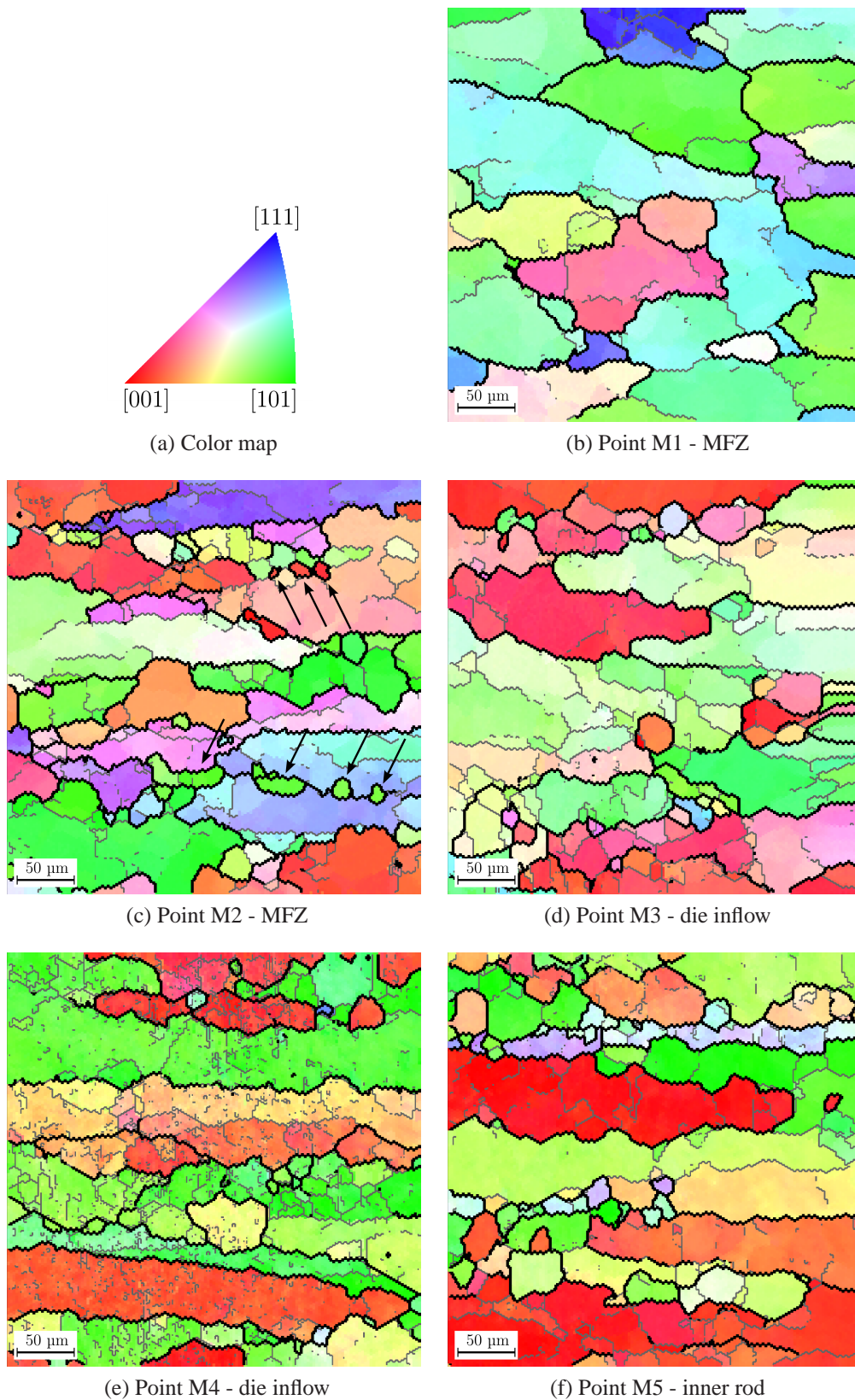


Figure 3.9: EBSD based micrographs by Grainplot at measurement points following a path along the middle axis of a partly extruded billet of EN AW-6060. See Figure 3.8 for measurement point positions. Grain colors according to orientation triangle in subfigure a. Bold black lines indicate $HAGB \geq 15^\circ$, narrow gray lines indicate $LAGB \geq 3^\circ$. Minimum grain size filter is $34 \mu\text{m}^2$; minimum CI of 0.1.

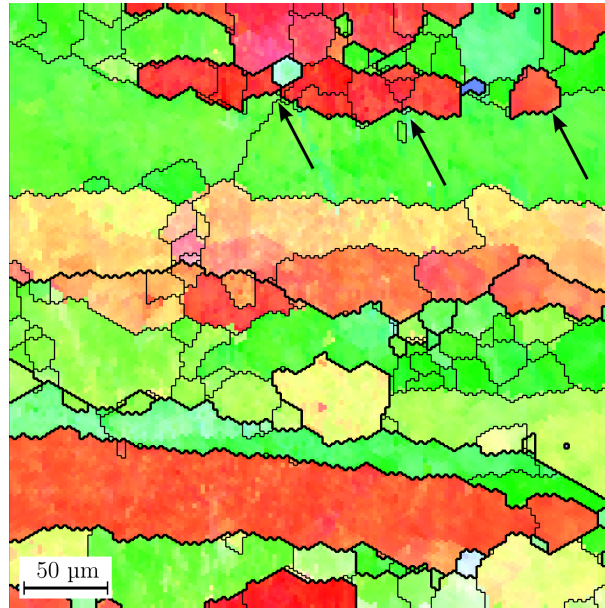


Figure 3.10: Restored and filtered EBSD micrograph by Grainplot at point M4 in partly extruded billet of EN AW-6060. See Figure 3.8 for measurement point positions. Grain colors according to orientation triangle in Figure 3.9 a. Bold black lines indicate $\text{HAGB} \geq 15^\circ$, narrow gray lines indicate $\text{LAGB} \geq 3^\circ$. Only closed LAGB shown. Minimum grain size filter is $34 \mu\text{m}^2$; minimum CI of 0.1.

found which start to lengthwise split the existing grains. The orientations of the individual grains vary between several directions.

In the micrograph of point M3 given in Figure 3.9d a similar grain microstructure to the one at point M2 can be observed. The grain elongation is less distinctive, but again numerous LAGB split the existing grains into subgrains. The grain orientations now tend more to $\langle 001 \rangle$ and $\langle 101 \rangle$ directions.

The microstructure of point M4 in Figure 3.9e shows that the bands of parallel HAGB become finer. A large number of small scale LAGB fragments is found inside the existing grains. A further comparison with a filtered micrograph depicted in Figure 3.10 reveals a subgrain structure inside the grains which is however comparable to points M3 and M4, though. The serrated shape of the HAGB and the LAGB structure indicate the influences of GDX. In the upper quarter of the micrograph a detached fragment and the necking of the originating grain are marked by arrows.

After passing the smallest diameter of the die, the grain microstructure is not affected by dynamic processes such as DRV/GDX or CDX. Therefore, the microstructure consisting of elongated grains and globular-shaped subgrains at point M4 also remains preserved in point M5 as shown in Figure 3.9f. Nevertheless, at this temperature level, SRX may occur if sufficient energy is stored inside the grains due to the previous plastic deformation.

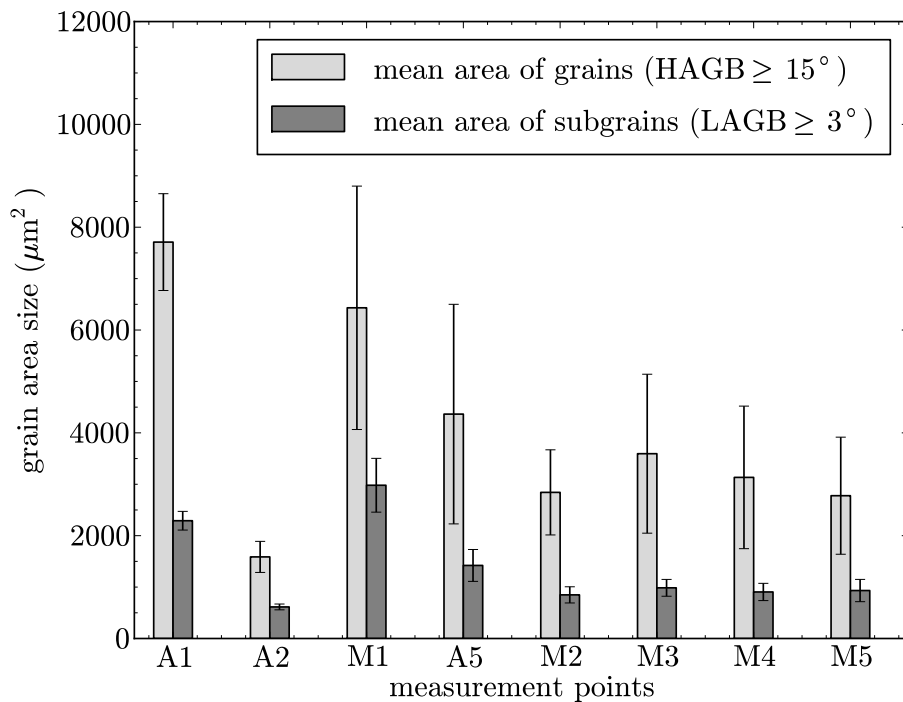


Figure 3.11: Mean grain area size at different measurement points in partly extruded billet of EN AW-6060. See Figures 3.6 and 3.8 for measurement point positions. Statistics by Grainplot include grains and subgrains which are not completely located inside the micrographs.

3.4.4 Microstructure statistics

Grain size evolution

The micrographs of the different deformation zones and along the middle axis shown in Figures 3.7 and 3.9 already indicate a significant reduction in grain size while the material moves towards the die. The grain size evolution inside the billet of EN AW-6060 during extrusion is statistically summarized in the diagram in Figure 3.11. The light gray bars represent the mean grain area size of grains separated by HAGBs $\geq 15^\circ$ and the dark gray bars indicate the mean area size of subgrains separated by LAGBs $\geq 3^\circ$. The mean grain area in the diagram includes grains and subgrains which are not completely located inside the micrograph. Especially large and elongated grains at the outer regions of the micrograph are cut. Thus, the grain size is generally underestimated and the variance in grain sizes is indicated by the standard error bars. Nevertheless, the tendency of grain refinement during the extrusion process can be clearly seen in Figure 3.11. The grain areas of the static recrystallized points A3 and A4 are not included in this discussion since their microstructure results from static recrystallization processes which occurred after interrupting the extrusion process.

The mean grain size of $7710 \mu\text{m}^2$ at point A1 in the DMZ is comparable to the initial grain size in the billet before starting the extrusion process. In contrast to this, the mean grain area size $1587 \mu\text{m}^2$ of point A2 reflects the significant grain refinement by a factor of 4.85 in the SIZ due to DRV and GDX processes. The other points are all located in the MFZ in decreasing distance to the die. Starting with moderately elongated grains with a mean grain size of $6432 \mu\text{m}^2$

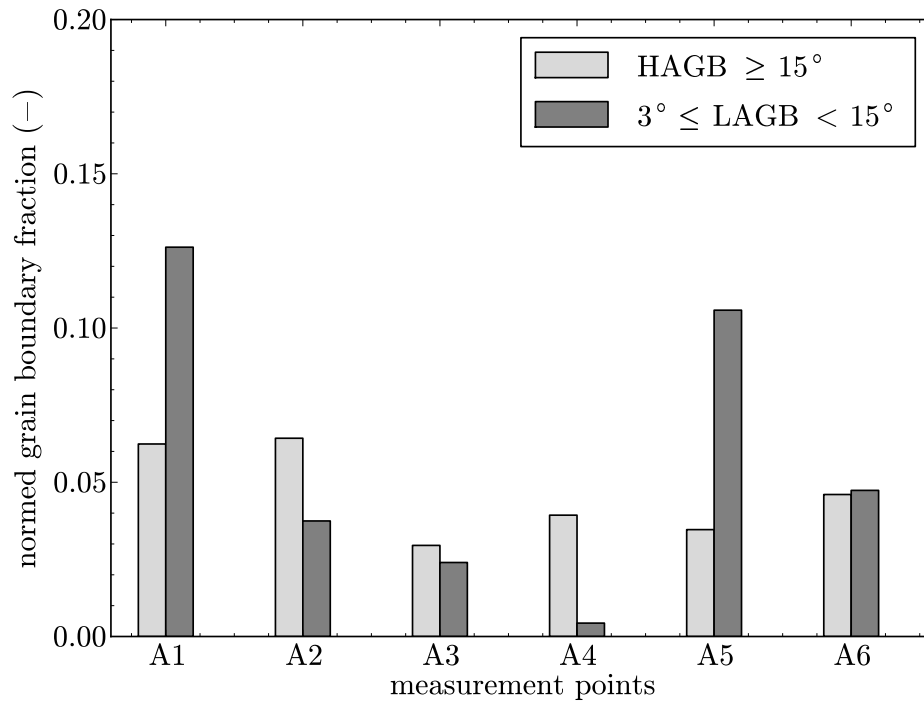


Figure 3.12: Normed grain boundary fraction development at measurement points in different deformation zones of partly extruded billet of EN AW-6060. See Figure 3.6 for measurement point positions inside billet.

at point M1, the mean grain area continuously decreases to a value of $2777 \mu\text{m}^2$ at point M5. Only in point M2 a reduced mean grain size is observed which is already at a level comparable to point M6. This also corresponds to the distinct subgrain structure observed in the micrograph of this point in Figure 3.9c which indicates presence of dynamic microstructure evolution processes. Generally, the tendency of decreasing areas can also be observed for subgrains in Figure 3.11. The smallest subgrain size is found at point A2 in the SIZ with a mean area of $614 \mu\text{m}^2$. In the MFZ the subgrain evolution starts with a mean size of $1421 \mu\text{m}^2$ at point M1 and quickly saturates at a mean subgrain size of $900 \mu\text{m}^2$ which is detected at the points M2 – M5.

Besides the grain size development, the evolution of grain boundaries can also be analyzed on the basis of EBSD data. The normed grain boundary fractions depicted in Figure 3.12 are obtained from the EBSD micrographs shown in Figure 3.7 with respect to grain size filtering. The fractions of LAGB and HAGB contained in the micrographs area extracted and normalized according to line thickness and micrograph dimensions. The normed grain boundary fraction is generally influenced by the grain shapes, since elongated grains with jagged boundaries have a longer grain boundary as a globular-shaped grain of equal grain area size. A detailed description on the generation of normed grain boundary fractions is given in Section 2.2.3.

The grain boundary fractions determined from the micrographs in Figure 3.7 have to be analyzed group-wise since different evolution processes result in incomparable microstructures. The points A1 and A2 located in the DMZ and SIZ respectively, have a comparable normed HAGB fraction of ~ 0.063 , although the mean grain size of point A2 is less than 25% com-

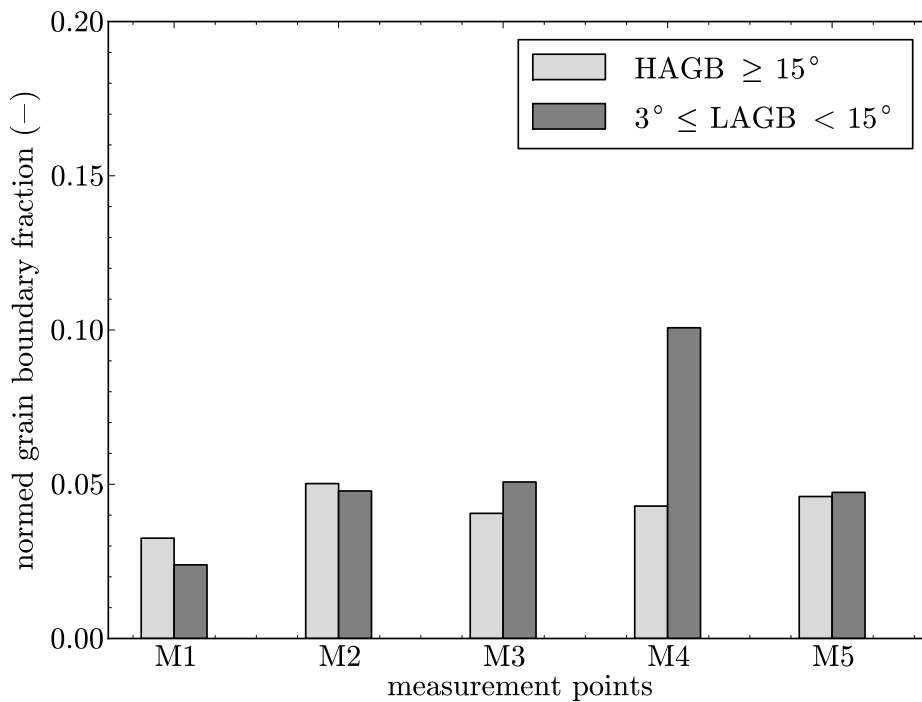


Figure 3.13: Normed grain boundary fraction development at measurement points along middle axis of a partly extruded billet of EN AW-6060. See Figure 3.8 for measurement point positions inside billet.

pared to point A1. Both micrographs differ in scaling but any influences caused by this disappear during normalization according to the micrograph size. Furthermore, the micrograph of point A1 given in Figure 3.7a contains a number of small grains which compensate the increase of the normed HAGB fraction due to grain elongation observed in the micrograph of point A2 in Figure 3.7b. Although the shear deformation in the SIZ leads to distinct subgrain structure at point A2, the large number of partial LAGB at point A1 results in a normed LAGB fraction of 0.126 which is almost three times higher than the value of 0.037 observed at point A2.

The coarse grain microstructure at points A3 and A4 in the die inflow and die region develops during nucleation based grain growth SRX which consumes the subgrain structures in the initial grain interior. Only at point A3 some LAGB remain while the micrograph of point A4 in Figure 3.7d is almost free from LAGB which is reflected by its low normed LAGB fraction of 0.004. The influence of a different scaling is again suspended by normalization. Since both micrographs consist of only a few large globular-shaped grains, the corresponding normed HAGB fraction of 0.04 is significantly lower compared to point A2, for example. On the one hand the microstructure at point A5 in the MFZ mainly consists of elongated grains with a comparable low normed HAGB fraction of 0.035. On the other hand the subgrain structure features a large number of short partial LAGB which is expressed by the high normed LAGB fraction value 0.106. The proceeding GDX leads to more serrated shape of the grains and to partial fragmentation which increases the normed HAGB fraction up to 0.046. At the same time the partial LAGB attach, and separate subgrains which are free of LAGB evolve. In consequence the normed LAGB fraction drops to 0.047.

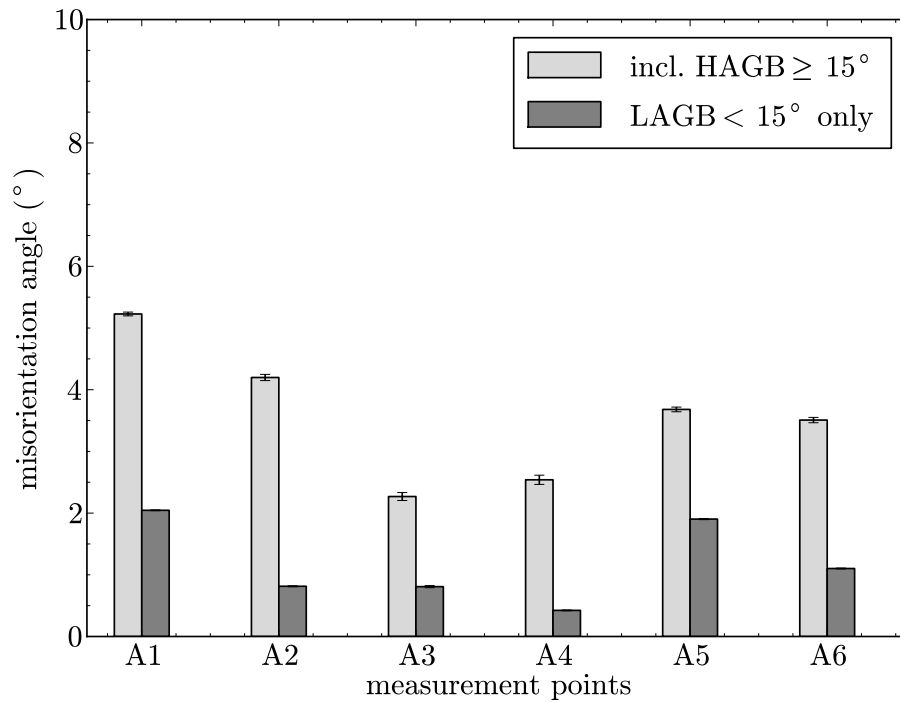


Figure 3.14: Evolution of misorientation at measurement points in different deformation zones in partly extruded billet of EN AW-6060. See Figure 3.6 for measurement point positions inside billet.

With a coincident decrease in mean grain and subgrain area size given in Figure 3.11, the grain boundary fractions tendentially increase for both $\text{HAGB} \geq 15^\circ$ and $3^\circ \leq \text{LAGB} \leq 15^\circ$. The weakly distinctive subgrain structure in the micrograph shown in Figure 3.7a, obtained at point M1 in the MFZ, is reflected by the significantly smaller normed LAGB fraction of 0.024. In the micrograph of point M2 in Figure 3.7c several detached grain fragments due to GDX can be found which are partly marked by arrows. The comparably high number of these small grains additionally raises the normed HAGB fraction of point M2 to 0.05. In contrast to this, the micrograph of point M4 in Figure 3.7e shows a subgrain structure containing a large number of short LAGB which do not entirely enclose subgrains. Nevertheless, these partial LAGB contribute to the normed LAGB fraction of 0.1 obtained at point M4.

Misorientation evolution

The orientation information offered by the EBSD technique is used to determine the misorientations between each data point and its neighbors. The mean misorientation for each measurement point in the different deformation zones of the EN AW-6060 sample is given in Figure 3.14 for $\text{LAGB} < 15^\circ$ only, as well as for $\text{HAGB} \geq 15^\circ$. Generally, for microstructures with large homogeneous orientated grains with no or only weak subgrain structures, both misorientation values tend towards low values. This is evident for the recrystallized microstructures of both points A3 and A4, the mean misorientation values of which are 2.269° and 2.54° . Since the formally existing subgrain structures mostly vanished during SRX, the mean misorientation of LAGB only stagnated at significantly lower levels of 0.808° for A3 and 0.423° for A4.

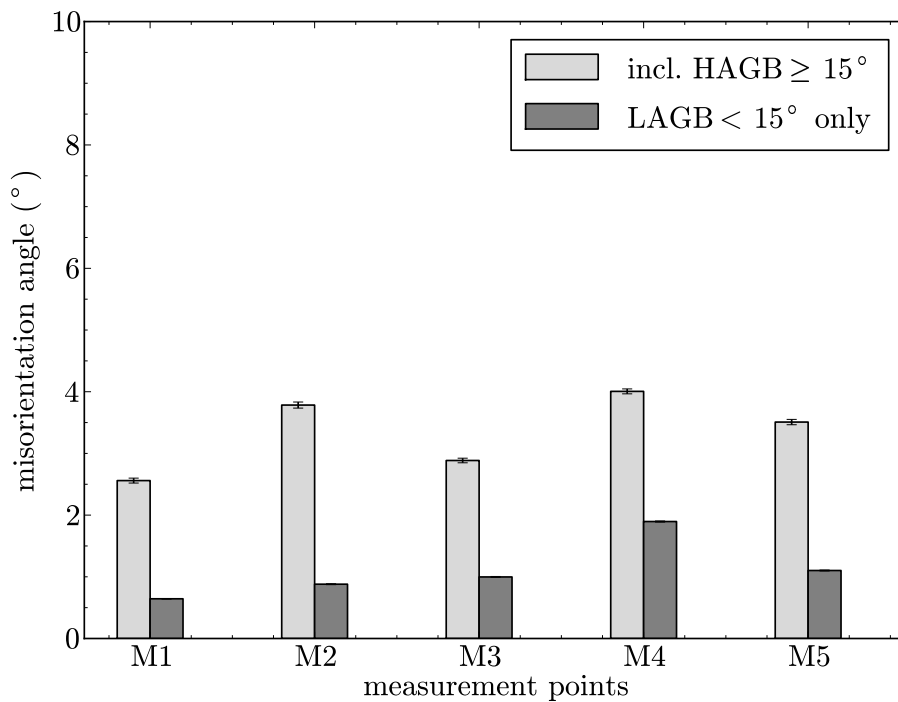


Figure 3.15: Evolution of misorientation at measurement points along middle axis of partly extruded billet of EN AW-6060. See Figure 3.8 for measurement point positions inside billet.

The mean misorientation values 5.228° and 2.045° of the initial microstructure at point C1 in the DMZ are comparably high due to the large number of partial LAGB inside the existing grains. The reorientation of the grains during plastic shear deformation in the SIZ then reduces the mean misorientation to 4.198° . The main contribution here is the large number of HAGB between the elongated and partially refined grains. The number of LAGB is now significantly lower leading to a mean LAGB misorientation of only 40 % compared to point A1. Regarding the mean misorientation angle, the points A5 and A6 in the MFZ of the billet show similar values of $\sim 3.50^\circ$. A significant reduction of LAGB from point A5 to A6, however, leads to a decrease in the mean LAGB misorientation of more than 40 % from 1.903° to 1.102° . A large difference in the orientation is only expected at the grain and subgrain boundaries. As shown in Figure 3.12 the maximum fraction of boundaries in the microstructure lies between 10 ~ 15 %. Therefore the variance and the derived standard error of the misorientation is one to two orders of magnitude smaller than the observed misorientation values.

The misorientation evolution at the measurement points along middle axis of a partly extruded billet of EN AW-6060 summarized in Figure 3.15 reveals no clear tendency if taking HAGB into account. Depending on the measurement point the mean misorientation angles vary between 4.00° and 2.56° . The mean LAGB misorientation angle slightly increases during the material flow from the billet center towards the die from 0.644° at point M1 up to 1.102° at point M5. Since the micrograph of point M4 contains a high LAGB fraction according to Figure 3.13, an increased mean misorientation angle of almost 2° is also observed. The mean values of the misorientation are derived from the corresponding misorientation histograms of

each measurement point. All misorientation histograms of the points A1–A6 and M1–M5 can be found in Section B.1 in the appendix of this work.

Inverse pole figures

For a correct interpretation of the IPFs the directions ND, RD and TD have to be defined in the corresponding micrographs. In the following, the RD points to the right of all EBSD micrographs, and therefore the impact of grain orientation alignment on the microstructure, can be most significantly determined at measurement points in the MFZ and especially along the middle axis of the billets where the material flow is parallel to RD. In order to obtain a right-hand orthogonal sample coordinate system, TD points upwards in the micrographs while ND is orientated perpendicularly to RD and TD pointing out of the image plane. All discrete IPF plots presented in this chapter are produced by Grainplot using the algorithmic implementation described in Section 2.2.3.

A representative selection of IPFs of the different deformation zones in the partly extruded billet of EN AW-6060 is depicted in Figure 3.16. Smearing of the usually concentrated pattern in all IPFs in Figure 3.16a is caused by the subgrain structure observed in Figure 3.7a. The resulting homogeneous shading of the IPFs proves the random grain orientation of the initial microstructure in the DMZ at point A1. The IPFs of point A2 in Figure 3.16b reveal the starting texture development during plastic deformation in the SIZ. Although the EBSD based micrograph in Figure 3.7b contains a large number of elongated grains, the evolving texture due to grain alignment is rather diffuse. For point A2 it has to be considered that the RD is rotated by an angle of $\sim 45^\circ$ related to the direction of material flow.

Representative for the MFZ and the measurement points along the middle axis of the billet, the IPF of point A6 located in the center of the exiting rod is shown in Figure 3.16c. The IPF related to RD shows a strong texture in the directions $\langle 100 \rangle$ and $\langle 111 \rangle$, found with different intensities for all points in the MFZ and the exiting profile center. According to Bunge (1971), this kind of texture is typical for rotationally symmetric plastic deformation in RD which can be expected in the MFZ nearby the middle axis of the billet. The complete collection of discrete IPFs obtained for the points A1 – A6 and M1 – M4 can be found in the appendix in Section C.1. Here, especially the recrystallized grain microstructure due to SRX at points A3 and A4 lead to less distinctive texture. Since the recrystallization consumed almost all LABGs in the grain interiors, the stereographic projections of the individual grains produce sharp patterns.

3.5 Characterization of EN AW-6082

3.5.1 Deformation zones and mesoscopic microstructure development

The half section of the partly extruded billet of EN AW-6082 is depicted in Figure 3.17. The general shape is comparable to the partly extruded billet of EN AW-6060. The differences in contrast in the scanned image allow to identify the three deformation zones DMZ, SIZ and MFZ which are labeled and indicated by black lines in Figure 3.17. The brightness of the die area and the extruded rod makes it hard to recognize the microstructure especially at the die inflow. Nevertheless, the rod shows a banded texture of elongated grains throughout the complete diameter. In contrast to the sample of EN AW-6060 no individual zones with different grain sizes

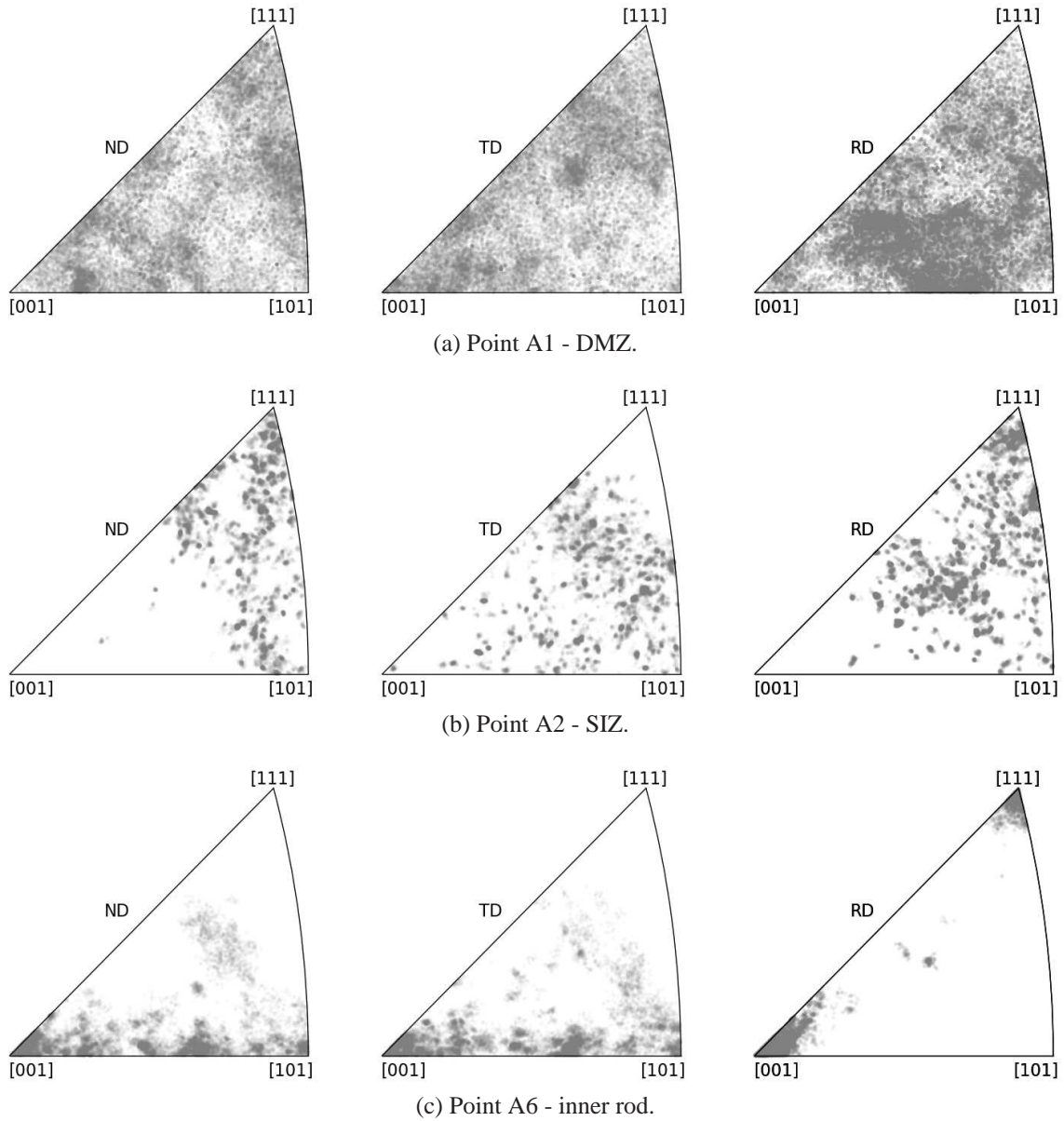


Figure 3.16: Selected discrete inverse pole figures by Grainplot of measurement points in different deformation zones in partly extruded billet of EN AW-6060. See Figure 3.6 for measurement point positions.

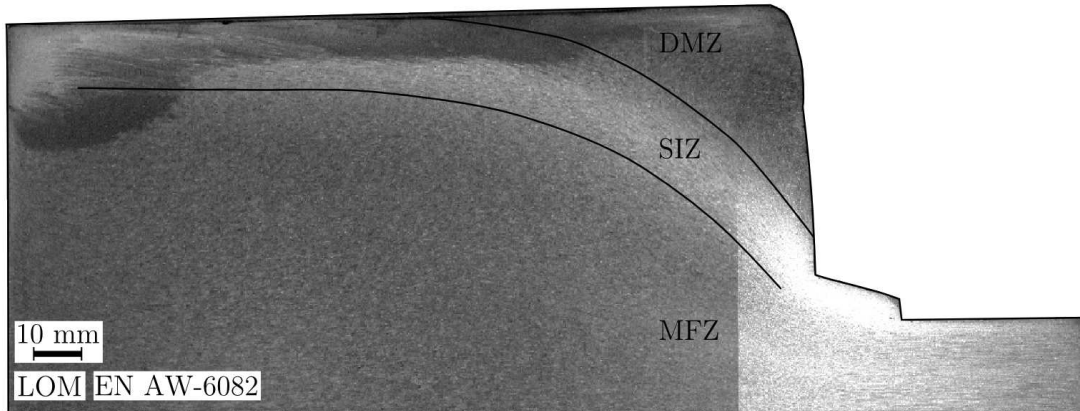


Figure 3.17: Half section of a partly extruded billet of EN AW-6082. Black lines separate labeled deformation zones. Underlying LOM macro scan image by courtesy of the Institute of Forming Technology and Lightweight Construction (IUL) at TU Dortmund University.

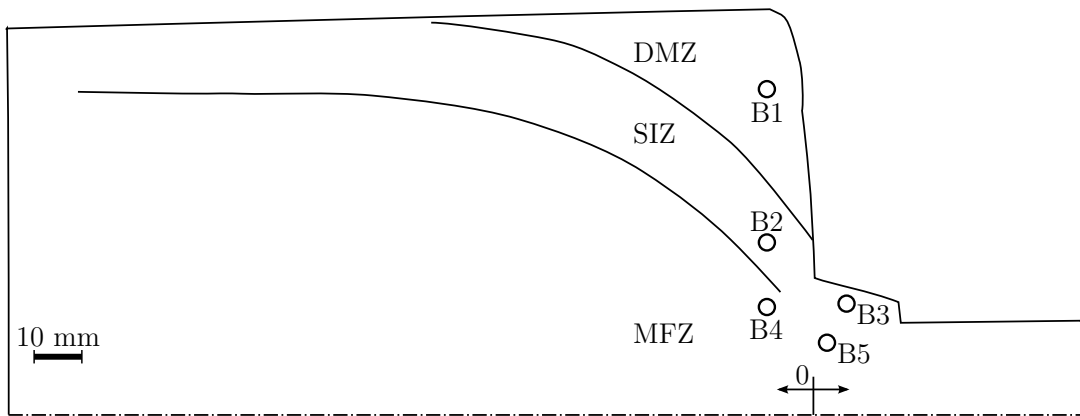


Figure 3.18: Contour of half section of a partly extruded billet of EN AW-6082. EBSD measurement point positions marked by circles. Black lines separate labeled deformation zones.

or shapes are visible. Large grains indicating the appearance of SRX and secondary recrystallization are not found at the observed cutting surface of the extruded profile and remaining billet.

3.5.2 EBSD measurements in different deformation zones

The positions of the EBSD measurement points in the partly extruded billet of EN AW-6082 are given in Figure 3.18 which shows the outline of the billet and the deformation zone boundaries for orientation. Point B1 is located inside the deformation zone with a distance of ~ 13 mm towards the SIZ. The points B2 and B3 are located in a distance of ~ 21 mm following the material flow from the SIZ into the die inflow. Furthermore, the points B4 and B5 are located at a stream line segment with ~ 15 mm in length inside the MFZ.

The EBSD results obtained at the five measurement points in the different deformation zones in partly extruded billet of EN AW-6082 are presented in Figure 3.19. Instead of undeformed globular-shaped grains, the microstructure of point B1, located inside the assumed DMZ, shows a banded structure of elongated grains. The longitudinal axes of the grains point towards the die

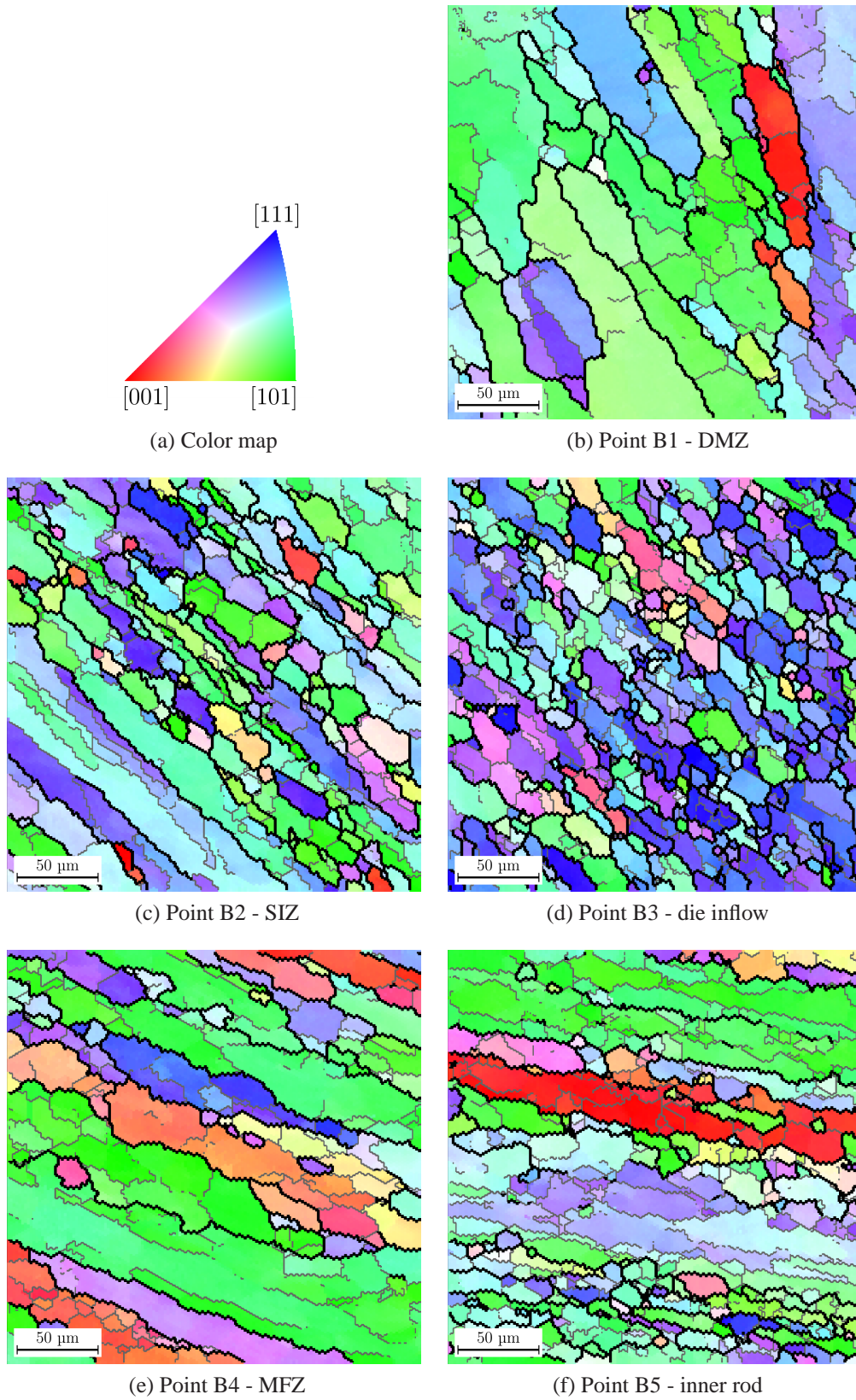


Figure 3.19: Restored EBSD based micrographs by Grainplot for different deformation zones in partly extruded billet of EN AW-6082. See Figure 3.18 for measurement point positions. Grain colors according to orientation triangle in subfigure a. Bold black lines indicate $HAGB \geq 15^\circ$, narrow gray lines indicate $LAGB \geq 3^\circ$. Minimum grain size filter is $17 \mu m^2$; minimum CI of 0.1.

inflow and the distinct subgrain structure implies the presence of plastic deformation. Although located in significant distance to the SIZ as identified in the LOM macro scan image of the billet, the characteristic influences of material flow on the grain microstructure can be found at the position of point B1. In contrast to the subgrain structure identified at point A1 in the DMZ of the billet of EN AW-6060, this deformation is primarily caused by shear during the extrusion process and does not result from the extraction of the billet from the press. The grain microstructure evolution induced by the plastic deformation at point B1 prohibits its use as undeformed reference microstructure. According to the color coding of the orientation triangle given in Figure 3.19a, the grain orientation of point B1 is dominated by the directions $\langle 101 \rangle$ and $\langle 111 \rangle$ as well as variations in between.

The grain microstructure inside the SIZ is exemplarily shown by the micrograph at point B2 in Figure 3.19. The vast majority of grains separated by HAGB are characterized by an elongated shape with longitudinal axes orientated parallel to the direction of shear. The subgrain structure consists of several GNB which lie parallel to the longitudinal axes to compensate the shear deformation. Furthermore, the existing stretched grains are split into subgrains by LAGB perpendicular to the direction of elongation. Together with the observed serrated shape of the HAGB this indicates the influence of DRV and GDX on the grain microstructure evolution. The fragmentation of the existing grains leads to significant grain area size reduction of approximately two-thirds compared to point B1.

With further material flow inside the SIZ, the process of GDX proceeds which leads to the grain microstructure of Figure 3.19d observed at point B3 in the outer region of the die inflow. The former microstructure consisting of elongated grains at point B2 now evolves into an assembly of moderately elongated grains of half mean area. Grains which are not already fragmented show a sub structure of numerous subgrains of similar size. The orientation of the majority of grains tends towards direction $\langle 111 \rangle$. The grain microstructure observed at point B3 significantly differs from that found at point A3 in the EN AW-6060 alloy shown in Figure 3.7c. In contrast to EN AW-6060 the experimental conditions in the outer region of the die inflow of the partly extruded billet of EN AW-6082 do not facilitate SRX. In consequence the refined microstructure at this point remains conserved.

The EBSD based micrograph of point B4 in the MFZ depicted in Figure 3.19e reveals a grain microstructure quite similar to the one found at point B1 in the assumed DMZ. This includes comparable sizes in grain and subgrain sizes and the tendency of grain orientation towards $\langle 111 \rangle$ as discussed in the following microstructure statistics section. The similarity of the microstructures of points B4 and B1 suggest that both points experienced a similar deformation history although located in different deformations zone with a distance of more than 40 mm as shown in Figure 3.18.

The primary characteristic of the micrograph in Figure 3.19f, observed at point B5, is the distinct subgrain structure. Existing elongated grains separated by HAGB are split into several subgrains which are also predominately elongated in direction of material flow to the right. Especially in the lower section of the micrograph, the LAGB turned into HAGB due to CDX leading to a significant reduction in grain size.

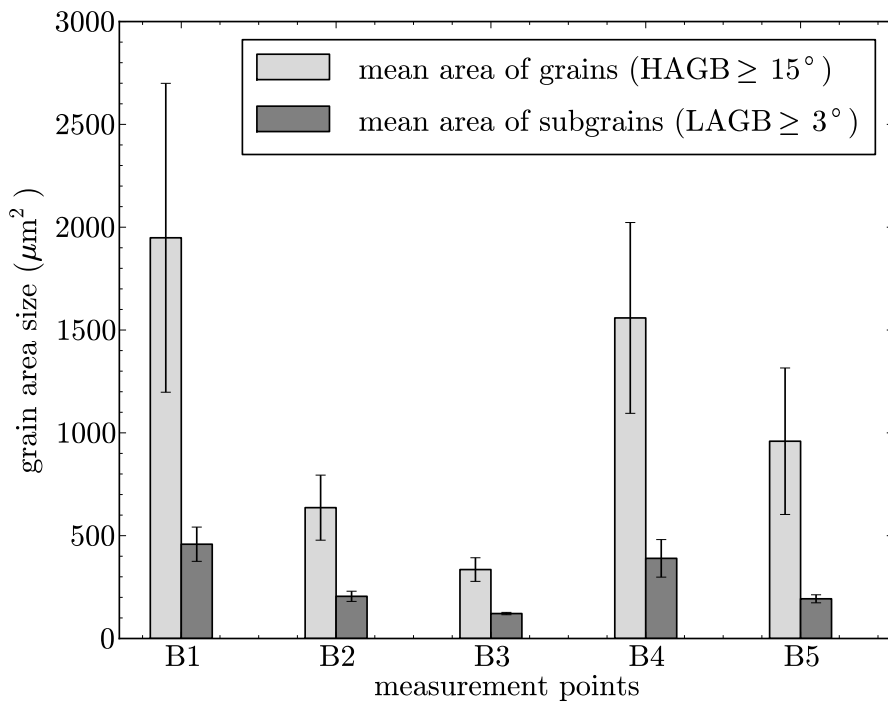


Figure 3.20: Mean grain area size in different deformation zones in partly extruded billet of EN AW-6082. See Figure 3.18 for measurement point positions. Statistics include grains and subgrains which are not completely located inside the micrographs.

In contrast to the samples of EN AW-6060, the EBSD based micrographs obtained from the partly extruded billet of EN AW-6082 show no significant evidence of SRX during the resting time in the heated press until release of the billet. The original elongated grain shapes as well as the subgrain structures inside the existing grains are found at each of the measurement points. The absence of SRX is also reflected by the grain size statistics discussed in the following.

3.5.3 Microstructure statistics

Grain size evolution

The mean grain sizes depicted in Figure 3.20 are obtained from the micrographs in different deformation zones shown in Figure 3.19. Generally, the mean grain area sizes in the partly extruded billet of EN AW-6082 are 25% of the size found at the comparable measurement points in the EN AW-6060 billet. Point B1 in the DMZ shows the largest grain area size of $\sim 1950 \mu\text{m}^2$ but the elongated grain shapes in the micrograph in Figure 3.19 implies the occurrence of significant plastic deformation in the proximity of this measurement point. The plastic deformation is also responsible for the evolution of subgrains with a mean area size of $\sim 460 \mu\text{m}^2$. In the SIZ at point B2 the grain elongation is even more evident and the processes of DRV and GDX lead to a reduction of grain and subgrain size down to $636 \mu\text{m}^2$ and $205 \mu\text{m}^2$, respectively. This tendency proceeds during the material flow towards the die resulting in a minimum grain area size of $335 \mu\text{m}^2$ at point B3 located in the die inflow. Coincident with the mean grain area reduction, the subgrain area size also decreases to $121 \mu\text{m}^2$. A saturation of minimum grain and subgrain area size can be expected in the order of the values obtained for point B3. The mean grain

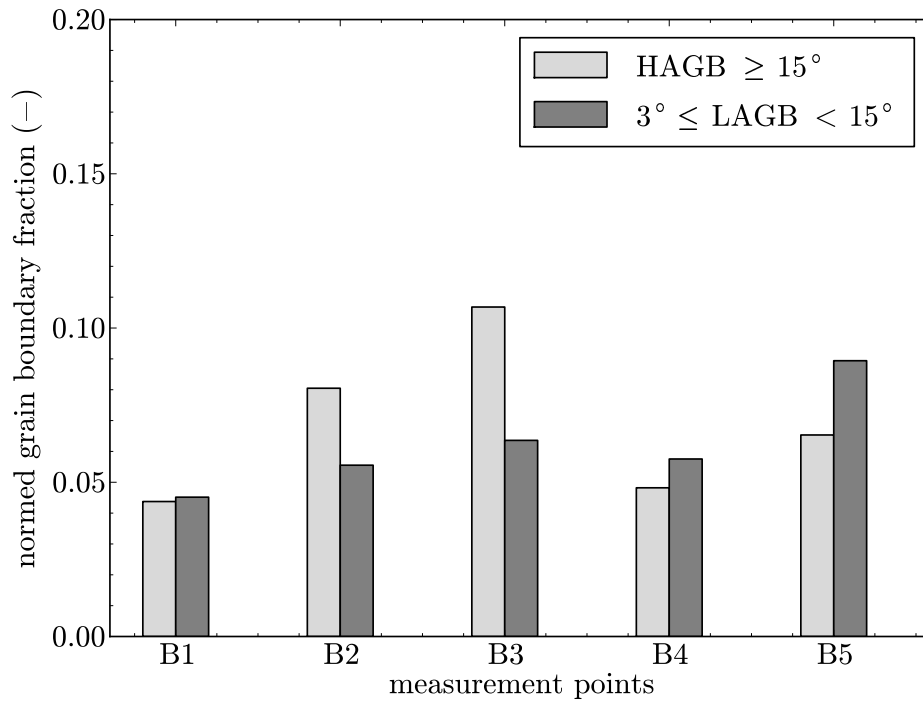


Figure 3.21: Normed grain boundary fraction development in different deformation zones of a partly extruded billet of EN AW-6082. See Figure 3.18 for measurement point positions inside billet.

and subgrain area sizes determined at point B4 in the MFZ are comparable to those obtained at point B1 but approximately decreased by 20 % and 15 %, respectively. Due to DRV and GDX the grain and subgrain sizes in MFZ evolve similarly to the SIZ so that the mean grain area size reduces to $960 \mu\text{m}^2$ and the mean subgrain area size decreases to $193 \mu\text{m}^2$ at B5 at the die inflow region. Due to the large variation in grain size especially of the elongated grains at points B1, B4 and B5, the mean grain area sizes show a comparably high standard error indicated by the black bars in the diagram in Figure 3.20. This effect is even intensified by also taking the incomplete grains which are cut at the micrographs edges into account.

The grain microstructure evolution based on the fractions of grain and subgrain boundaries in the micrograph depicted in Figure 3.19 is summarized by the diagram in Figure 3.21. Obviously no SRX takes place after interrupting the extrusion process of the EN AW-6082 billet. Accordingly, the development of the normed grain boundary fractions inside the different deformation zones is more comparable to the fraction evolution along the middle axis of the EN AW-6082 billet shown in Figure 3.13 than inside the deformation zones given in Figure 3.12.

The microstructure of point B1 is already affected by plastic deformation predominantly leading to elongated grains similar to those observed in the MFZ. Therefore, the points B1, B4 and B5 are handled as a group of points with decreasing distance towards the die. This grouping is also based on the results of the mean grain area size statistics in Figure 3.20. In this case, the normed HAGB fraction continuously increases from 0.044 at point B1 to 0.048 at point B4 and finally up to 0.065 at point B5. This fraction growth results from the grain refinement and the more serrated shaped grain boundaries due to GDX. The normed LAGB fraction

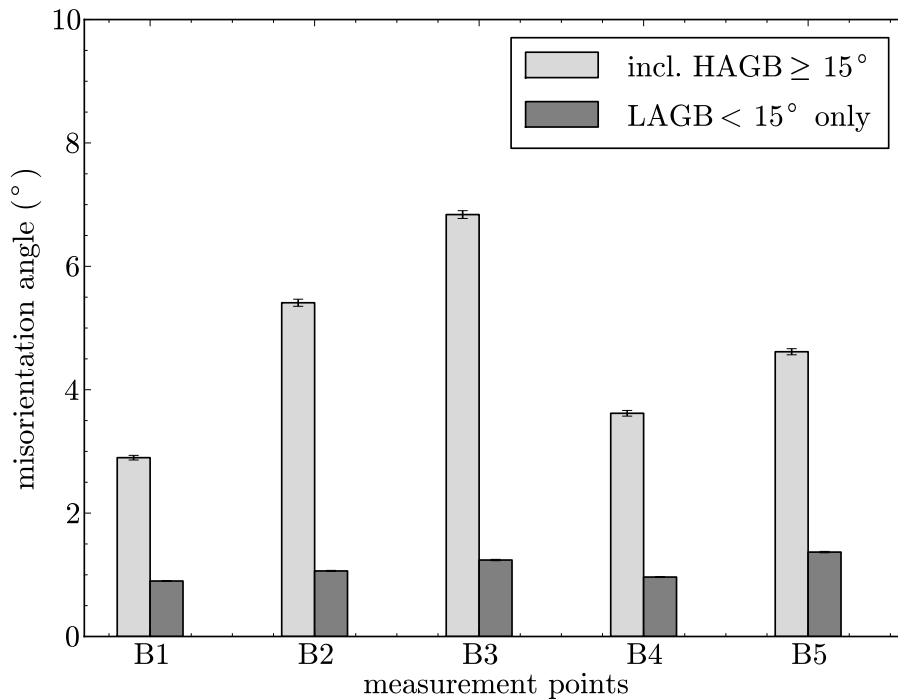


Figure 3.22: Evolution of misorientation at measurement points in different deformation zones in partly extruded billet of EN AW-6082. See Figure 3.18 for measurement point positions inside billet.

correspondingly increases from 0.045 to 0.057 and finally to 0.089. At all the points there is a distinct subgrain structure inside the grains, the fraction of which is constantly higher than the normed HAGB fraction. A comparable tendency in the grain boundary fraction development is also evident for the remaining points B2 and B3 both located on a stream line of material flow inside the SIZ. Here the shear deformation already leads to fibrous grain structure with small globular-shape grain fragments due to GDX. In consequence, the normed HAGB fraction at these points of 0.08 and 0.107 is significantly higher than in the MFZ. Also the normed LAGB fraction increases from 0.056 at point B2 to 0.064 at B3 but remains lower than the normed HAGB fraction due to the comparably small mean grain area sizes.

Misorientation evolution

The evolution of misorientation in the different deformation zones in the partly extruded billet of EN AW-6082 in Figure 3.22 shows a different behavior than observed for EN AW-6060 in Figure 3.14. The absence of SRX preserves the evolved subgrain structure after interrupting the extrusion process so that the mean subgrain misorientations at all points lie between 0.9° at B1 and 1.37° at point B5.

Basing on the same grouping of points used in the discussion of the grain size evolution in EN AW-6082 during extrusion, the mean HAGB misorientation of the points B1, B4 and B5 continuously increase from 2.90° to 3.62° and finally to 4.61° . This misorientation growth goes along with the HAGB newly formed during grain refinement due to GDX. The plastic deformation in the SIZ intensifies the grain refinement at the points B2 and B3 which is also

reflected in the increase of the mean HAGB misorientation from 5.41° to 6.84° on a comparably high level. The misorientation histograms of the measurement points B1–B5 which are the basis of the mean misorientation angles presented here can be found in Section B.2 in the appendix of this work.

Inverse pole figures

The texture development inside the different deformation zones in the partly extruded billet of EN AW-6082 is depicted in the IPFs in Figure 3.23. In comparison to the observed random microstructure at point A1 in the DMZ of the EN AW-6060 specimen, the microstructure at DMZ point B1 in Figure 3.23b already shows a weak texture towards $\langle 101 \rangle$ and $\langle 111 \rangle$ so that the IPF in RD is more similar to the one found at point A2 in Figure 3.16. Furthermore the direction of material flow and related grain elongation is comparable at these two points.

Focussing on the RD IPF, the texture at point B2, located in the SIZ of the billet and presented in Figure 3.23b, forms in the directions $\langle 100 \rangle$ and $\langle 111 \rangle$. This tendency is more evident in Figure 3.23c which depicts the IPFs of point B5 located at the inner rod near the die orifice. The points B3 and B4 show a less distinctive texture evolution in their RD IPFs which can be found in the appendix Section C.2.

3.6 Characterization of EN AW-7075

3.6.1 Deformation zones and mesoscopic microstructure development

Figure 3.24 shows a scanned LOM image of the half section of the partly extruded billet of EN AW-7075 which has the same diameters for the billet and extruded rod as the billets of EN AW-6060 and EN AW-6082. The initial billet length is shortened to 140 mm, which is almost half the length of the other billet, to keep the ram forces during the extrusion process inside the limits specified by the used press. The reduced length of the billet does not influence the general development of the deformation zones which are labeled and separated by black lines in Figure 3.24. Position and shape of the deformation zones are both comparable to the other experiments discussed in the sections before. The dashed line overlaying the extruded rod marks the transition between two zones with different grain microstructure in the profile. The outer zone is characterized by small scaled fine grains at the surface, the size of which continuously increases until a depth of ~ 5 mm inside the profile. The microstructure inside a diameter of 15 mm around the symmetry axis of the extruded rod is dominated by a mixture of globular-shaped recrystallized grains and elongated grains, the fraction of which increases towards the rod center. The detailed view of the die inflow area reveals no evidence of SRX which massively influences the grain microstructure of EN AW-6060 in this region as visible in the detailed view in Figure 3.6. The cross section reduction at the die leads to the development of a miniature DMZ and SIZ which are marked by arrows in the detailed view. A similar development of secondary deformation zones inside the die inflow is not evident in the partly extruded billets of EN AW-6060 and EN AW-6082.

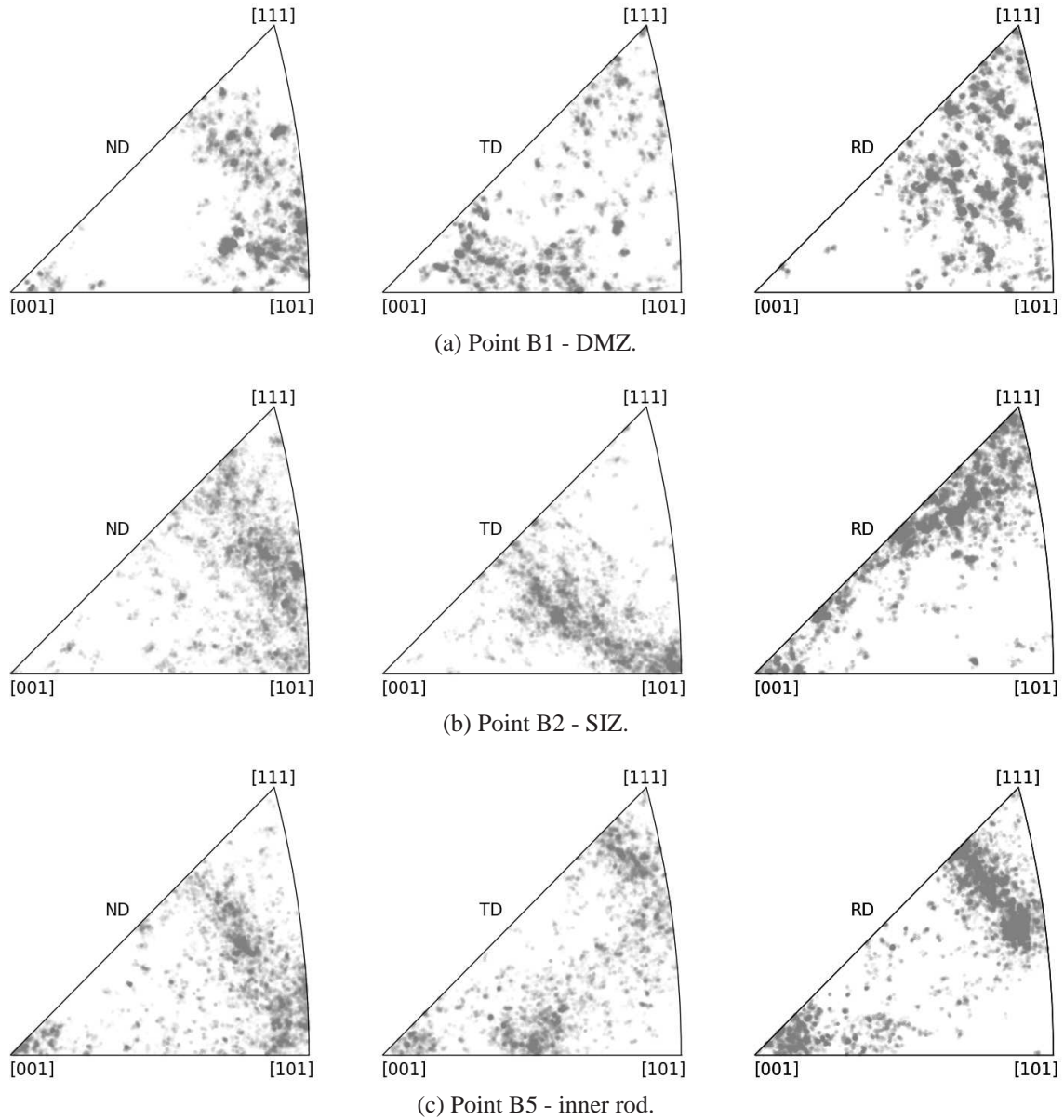


Figure 3.23: Selected discrete inverse pole figures by Grainplot of measurement points in different deformation zones in partly extruded billet of EN AW-6082. See Figure 3.18 for measurement point positions.

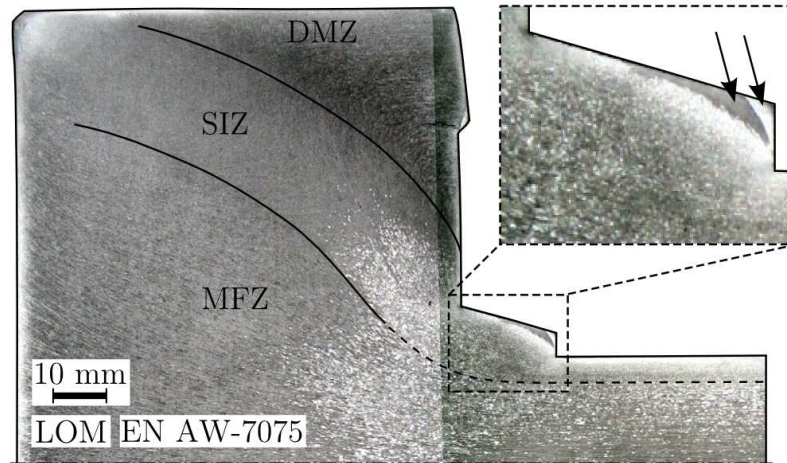


Figure 3.24: Half section of a partly extruded billet of EN AW-7075. Black lines separate labeled deformation zones. Detailed view on inflow region is contrast improved. Underlying LOM macro scan image by courtesy of the Institute of Forming Technology and Lightweight Construction (IUL) at TU Dortmund University.

3.6.2 EBSD measurements in different deformation zones

In Figure 3.25 the positions of the EBSD measurement points in the partly extruded billet of EN AW-7075 are marked by black circles. Point C1 is placed inside the DMZ and has a distance of ~ 20 mm to the border between DMZ and SIZ. Inside the SIZ the point C3 in the outer region of the die inflow follows point C2 in a distance of ~ 45 mm. Taking the secondary deformation zones inside the die inflow into account, the position of C3 is MFZ equivalent inside. The points C4 and C5 are both placed inside the MFZ with a distance of ~ 30 mm from each other. As indicated by the dashed line at the die inflow, C5 is placed in a region in which predominantly globular-shaped recrystallized grains are found in the mesoscopic LOM image in Figure 3.24.

The grain microstructure at point C1 in the DMZ of the partly extruded billet of EN AW-7075 in Figure 3.26b consists of globular-shaped grains with a mean grain area size of $\sim 1200 \mu\text{m}^2$. The subgrain structure is only weakly developed which indicates the absence of plastic deformation in this region. According to the color coding in the orientation triangle in Figure 3.26a, the grains at point C1 are randomly orientated.

The mean grain and subgrain sizes at point C2 in the SIZ as shown in Figure 3.26c are approximately half the size compared to the initial microstructure in the DMZ. Except one large elongated grain in the micrograph center, all other grains are significantly smaller and only slightly elongated. The arrangement of the subgrain structures indicate that this decrease in grain size is a result of DRV and GDX. The subgrain structure inside the single, still existing large elongated grain sketches this process of grain fragmentation. The grains observed at point C2 have only a weak orientation preference and vary between $\langle 001 \rangle$ and $\langle 111 \rangle$.

At point C3 in the die inflow region in Figure 3.26d the observed grain microstructure is very similar to the one obtained at point C1 in the DMZ regarding the observed grain and subgrain sizes. The majority of grains is characterized by a globular-shape and a sporadic distribution of

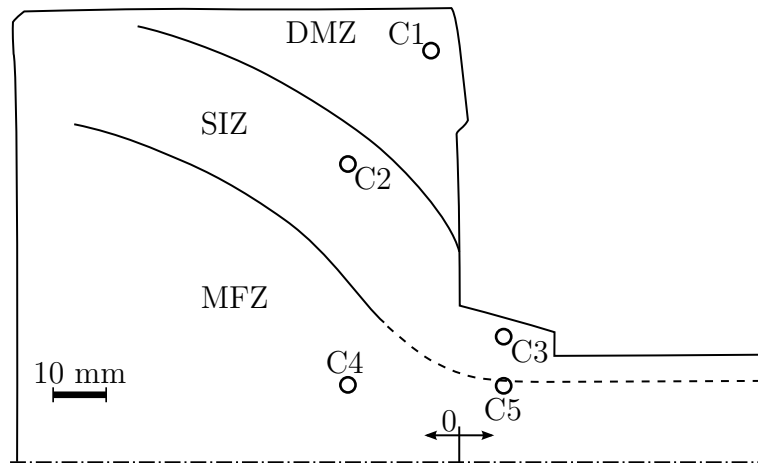


Figure 3.25: Contour of half section of a partly extruded billet of EN AW-7075. EBSD measurement point positions marked by circles. Black lines separate labeled deformation zones.

few subgrains. The missing subgrain structures and the absence of grain elongation suggest the occurrence of SRX in this region. The preferred grain orientations tend towards $\langle 111 \rangle$.

The EBSD measurements at the points C4 and C5, depicted in Figures 3.26e and 3.26f, are showing a coarse grain structure with significant larger mean sizes than observed in the DMZ. The grains at point C4 are all elongated in direction of material flow, whereas some grains at point C5 show a globular shape. At both points only few subgrain structures are found which affiliates the general occurrence of SRX in the MFZ. This assumption is supported by the fact that no strongly preferred orientation is found at point C5.

The recrystallization in the partly extruded billets of EN AW-7075 affects the MFZ and the die/die inflow region but not the SIZ at point C2 under the given experimental conditions. This situation is totally different from the recrystallization observed in EN AW-6060, where all regions undergoing significant plastic shear deformation (points A3 and A4, die inflow region) contained sufficient energy to drive SRX after interrupting the extrusion process.

3.6.3 Microstructure statistics

Grain size evolution

The grain size evolution in the three deformation zones in the partly extruded billet of EN AW-6082 shown in Figure 3.27 varies from the one observed for the billet of EN AW-6060 and EN AW-6082 due to a different occurrence of SRX. Here, the points C3 in the MFZ, as well as C4 and C5 in the die inflow region, show a grain coarsening caused by SRX which comes along with a significant reduction of subgrain structures inside the grains. According to the determination method of the subgrain sizes as discussed in Section 2.2.3, the obtained subgrain sizes are heavily overestimated for these three points and for C1. Therefore, only the grain size evolution of these grains is discussed here while the topic of LAGB development follows in the description of the normed LAGB fraction below. With respect to the observed maximum mean grain area sizes, the results of EN AW-7075 are $\sim 50\%$ of the size obtained for EN AW-6060 but $\sim 200\%$ compared to EN AW-6082.

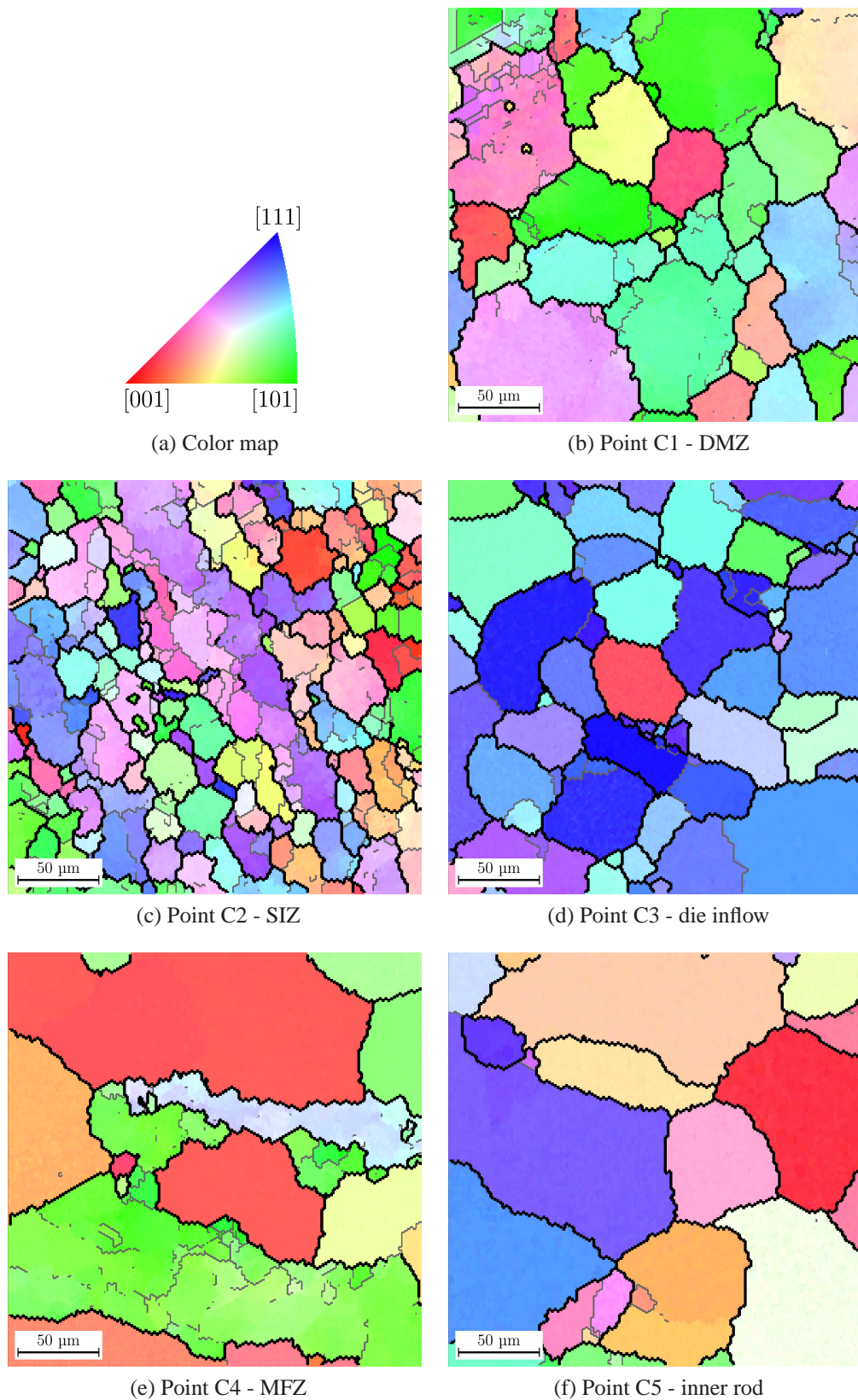


Figure 3.26: Restored EBSD based micrographs by Grainplot for different deformation zones in partly extruded billet of EN AW-7075. See Figure 3.25 for measurement point positions. Grain colors according to orientation triangle in subfigure a. Bold black lines indicate $HAGB \geq 15^\circ$, narrow gray lines indicate $LAGB \geq 3^\circ$. Minimum grain size filter is $17 \mu\text{m}^2$; minimum CI of 0.1.

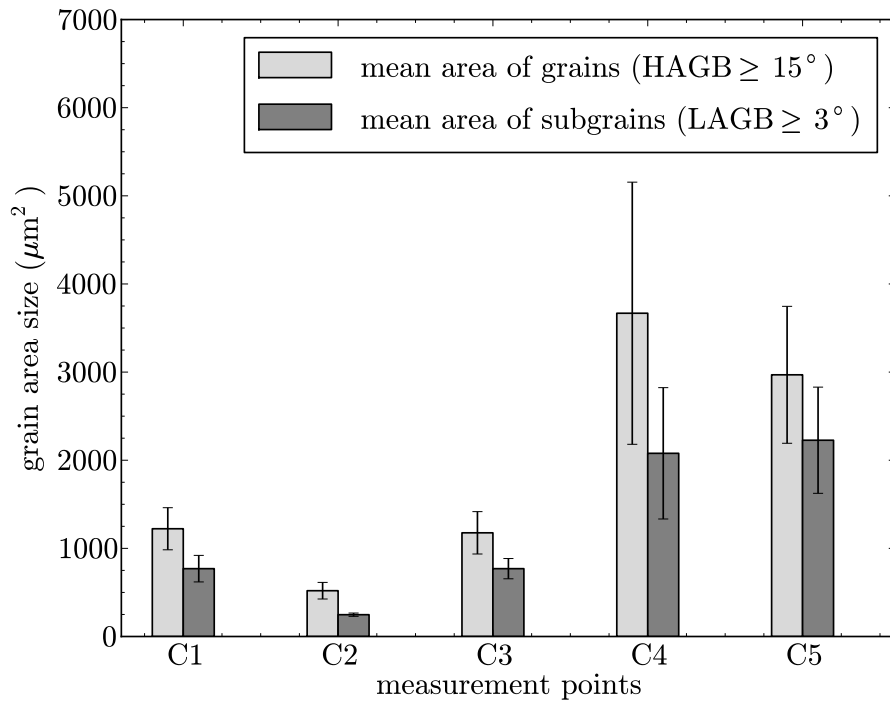


Figure 3.27: Mean grain area size in different deformation zones in partly extruded billet of EN AW-7075. See Figure 3.25 for measurement point positions. Statistics include grains and subgrains which are not completely located inside the micrographs.

The grain size found at point C1 in the DMZ has a mean grain area size of $1222 \mu\text{m}^2$. In the micrograph of point C2 located in the SIZ, the grain refinement due to GDX leads to a grain size reduction of $\sim 42\%$ of the initial value. The evolving subgrain structure results in a mean subgrain area size of $247 \mu\text{m}^2$ which is similar to the subgrain size determined at the analogous point B3, though which is located closer to the die inflow. The statically recrystallized grains at point C3 have an almost identical mean area as found for the initial microstructure at point C1 in the DMZ. This also includes the size variance displayed by the standard error bar. At points C4 and C5 in the MFZ the SRX generates larger grains with only a weak subgrain structure and mean grain area sizes of $3668 \mu\text{m}^2$ and $2969 \mu\text{m}^2$, respectively. Since most of the large grains observed at these points are not completely located inside the according micrographs, the mean grain area sizes of C4 and C5 are surely underestimated. To reduce the influence of incomplete grains in the micrograph on the grain size statistics, additional EBSD measurements covering a four times larger area of $500 \mu\text{m} \times 500 \mu\text{m}$ have been performed near points C3, C4 and C5. The mean grain areas determined at C4 then increase to $5669 \mu\text{m}^2$ while the result of $1100 \mu\text{m}^2$ at point C3 remains at the same level as for the measurement. To stay compatible with the grain size statistics of the other points, incomplete grains at the micrograph's edges are also included again. At point C5 the number of low quality data points with a $\text{CI} < 0.1$ is too large to perform a reliable micrograph reconstruction and - in consequence - to determine the microstructure statistics.

The normed grain boundary fraction diagram in Figure 3.28 reflects the grain size and grain boundary evolution due to SRX at the measurement points. Except for C2 in the SIZ, none of

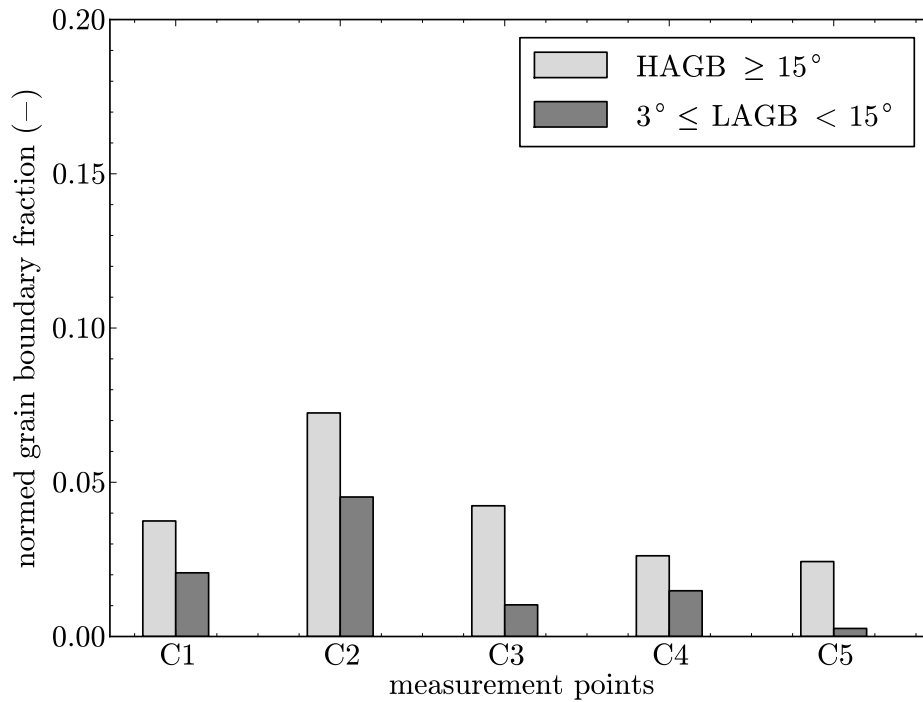


Figure 3.28: Normed grain boundary fraction development in different deformation zone of a partly extruded billet of EN AW-7075. See Figure 3.25 for measurement point positions inside billet.

the micrographs of EN AW-7075 in Figure 3.26 show elongated and fragmented grains from GDX. Accordingly, the highest normed HAGB fraction of 0.072 is found here. Furthermore the distinct subgrain structure evolving during shear deformation leads to a normed LAGB fraction of 0.045. Comparable to the grain area sizes determined for EN AW-7075, these values lie between the fraction of EN AW-6060 and EN AW-6082. The almost identical grain sizes of C1 and C3 also lead to similar normed HAGB fractions of ~ 0.04 . However, the subgrain structure in point C1 is more evident so that its normed LAGB fraction of 0.02 is twice as high as determined for point C3. The recrystallized microstructures at points C4 and C5 are characterized by a similar HAGB fraction of ~ 0.025 . A more obvious difference is revealed by the normed LAGB fraction which is extremely low at point C5 since almost no subgrain structure is evident. In contrast to this, the partial LAGB found in the micrograph of point C4 still show a significant normed LAGB fraction of 0.015.

Misorientation evolution

The misorientation angles determined in the different deformation zones in the partly extruded billet of EN AW-7075 are depicted in Figure 3.29. Taking into account the HAGBs $\geq 15^\circ$, the level of misorientations is comparable to the one obtained in the different deformations zones in the EN AW-6060 billet in Figure 3.14. The maximum misorientation angle of 4.8° is found at point C2. Here, the grain refinements due to GDX increase the number of grains in the micrograph which causes the raise of the misorientation. The microstructures of point C1 in the DMZ and point C3 in the SIZ at the die inflow are similar regarding mean grain area size and

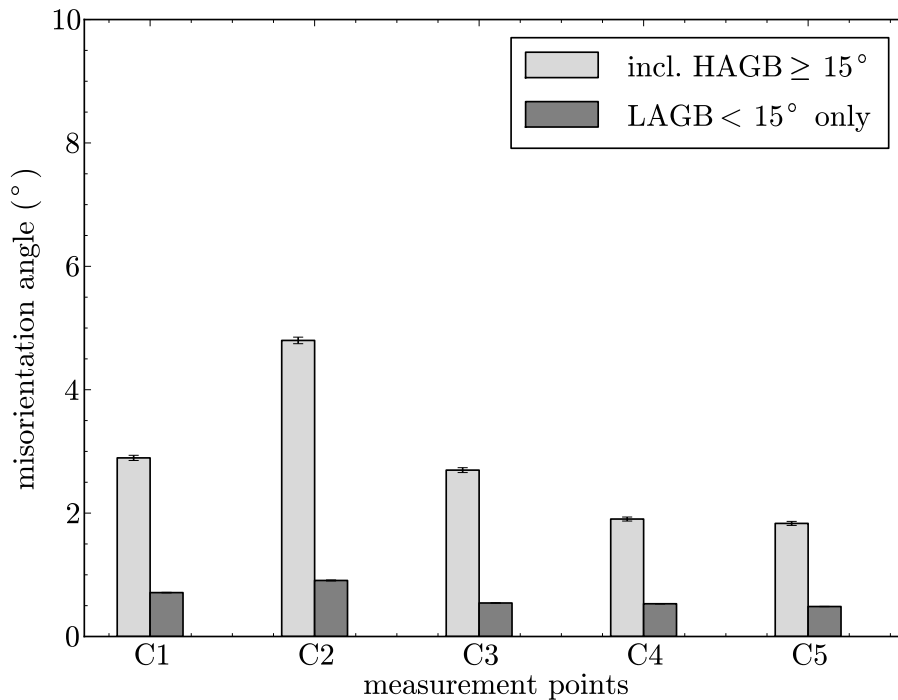


Figure 3.29: Evolution of misorientation at measurement points in different deformation zones in partly extruded billet of EN AW-7075. See Figure 3.25 for measurement point positions inside billet.

grain boundary fraction. This also holds true for the misorientations angles which are 2.9° and 2.7° . The misorientation angles obtained for the recrystallized points C4 and C5 both located in the MFZ have a lower value of $\sim 1.85^\circ$ although the micrographs reveal no distinct orientation texture in the micrographs. The comparably low misorientation angle rather results from the fact that only a few large grains can be evaluated which are mostly homogeneously orientated and contain no distinct subgrain structures.

The absence of distinct subgrain structures in the microstructures of points C3, C4 and C5 after SRX is responsible for the stagnation of the relative LAGB misorientation at $\sim 0.5^\circ$. The weak initial subgrain structure at point C1 in the DMZ with a relative LAGB misorientation of 0.711° evolves to a distinct network of LAGB splitting the elongated grains in the SIZ into several subgrains which comes along with an increase of the misorientation to 0.908° . Refer to Section B.3 in the appendix of this work for the misorientation histograms of the measurement points C1–C5 from which the mean misorientation angles are derived.

Inverse pole figures

Although a microstructure of rather globular-shaped grains is observed in the EBSD micrograph for point C1 in Figure 3.26b, the according RD IPF in Figure 3.30a indicates a significant texture varying between the directions $\langle 100 \rangle$ and $\langle 111 \rangle$. At least for the IPFs related to TD and RD a quite similar texture is found in the recrystallized point C5 in the inner rod at the die orifice as shown in Figure 3.30c. Due to SRX the grains at C5 are mostly free of LAGB and the resulting projection pattern are much sharper. In the SIZ of the EN AW-7075 billet a grain

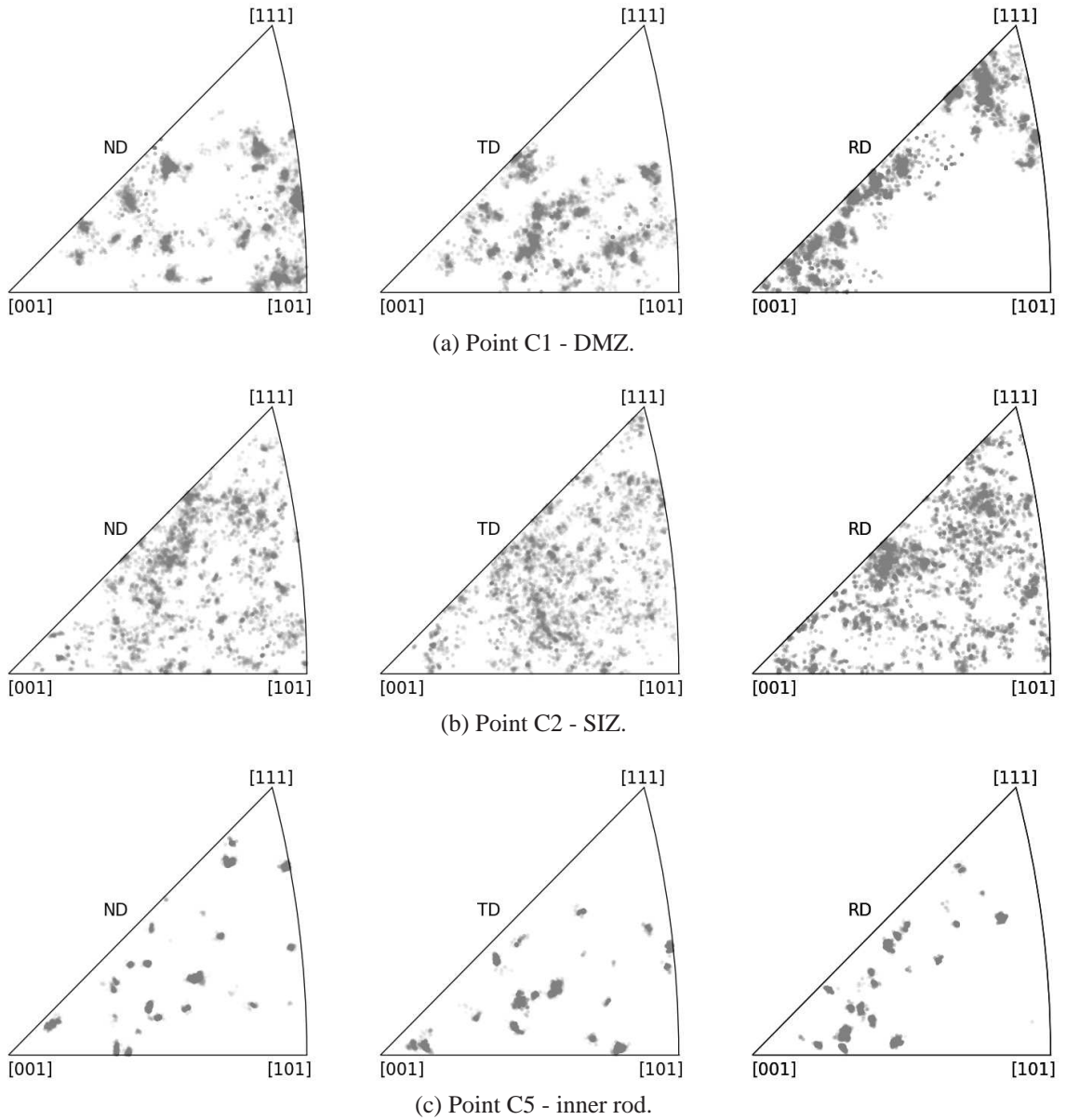


Figure 3.30: Selected discrete inverse pole figures by Grainplot of measurement points in different deformation zones in partly extruded billet of EN AW-7075. See Figure 3.25 for measurement point positions.

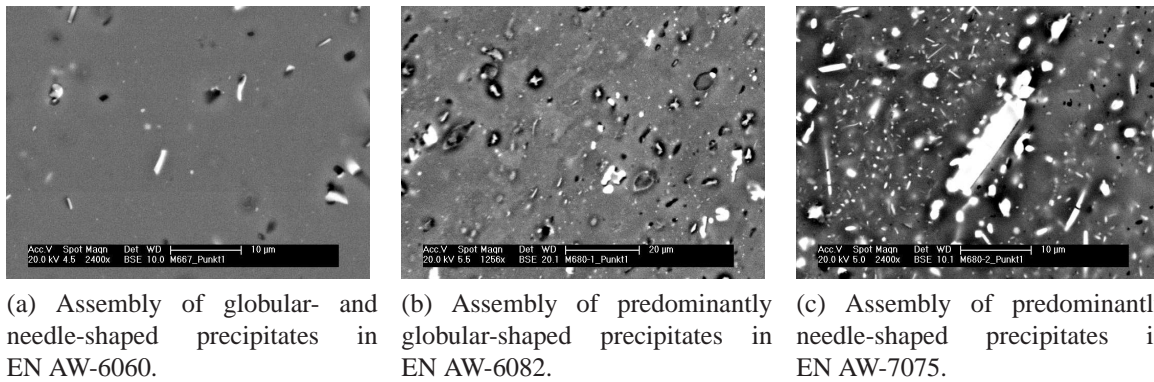


Figure 3.31: Precipitates in the DMZ of the different partly extruded billets. Courtesy of the Institute of Forming Technology and Lightweight Construction (IUL) at TU Dortmund University.

elongation in the microstructure is found which is likewise found at the SIZs of the other billets. However, a distinct texture evolution cannot be found in the IPFs of point C2 in Figure 3.30b. For completeness, the IPFs of the points C3 at the die inflow and C4 in the MFZ are attached in the appendix in Section C.3. At point C3 a texture is only found in the ND based IPF pointing towards $\langle 111 \rangle$ while the coarse recrystallized microstructure contains only a small number of grains which is not sufficient to pronounce a significant texture.

3.7 Precipitations in partly extruded billets

Since the EBSD measurements offer no information on the precipitate evolution, single BSE SEM images have been recorded at the Lehrstuhl für Werkstoffkunde (Materials Science), University of Paderborn. The SEM measurement points are located in the DMZ near point No. 1 marked in each of Figure 3.6 for EN AW-6060 and in Figures 3.18 as well as 3.25 for EN AW-6082 and EN AW-7075, respectively.

A comparison of the precipitate distribution and their shape for the different alloys is shown in the BSE SEM images in Figure 3.31. The precipitates in the DMZ of EN AW-6060 in Figure 3.31a have an almost equal fraction of globular- and needle-shaped particles with a distance of $5 \sim 10 \mu\text{m}$. The needle-shaped particles have a length of $3.5 \sim 4.0 \mu\text{m}$ and a diameter ten times smaller in size. The mean diameter of the globular-shaped precipitates is $3 \sim 4 \mu\text{m}$ which is almost the same dimension as the needle diameters. The precipitate distribution of EN AW-6082 is given in Figure 3.31b with a different scaling factor. Note that this image is tilted by 5° . The particles are predominantly globular shaped with a mean distance of $5 \sim 10 \mu\text{m}$ comparable to that of EN AW-6060. The mean size of the precipitates varies between $0.5 \sim 3 \mu\text{m}$ which is slightly smaller than in Figure 3.31a. Figure 3.31c showing the precipitate distribution of EN AW-7075 is dominated by a needle-shaped oversized particle of $14.5 \mu\text{m}$ in length and $2.9 \mu\text{m}$ in diameter. The size of the other predominantly needle-shaped precipitates varies between $0.5 \mu\text{m}$ and $5.0 \mu\text{m}$. On average, the corresponding diameters of the needles are one tenth of their length. Compared to the alloys of the 6000 series, EN AW-7075 shows a significantly higher density of precipitates with a mean particle distance of $1.0 \mu\text{m}$. Studies on

precipitate evolution due to thermo-mechanical processing and its modelling are carried out by of a number of different work groups.

The works of Myhr et al. (2001) and Myhr et al. (2004) describe the general modelling of precipitate evolution for Al-Mg-Si alloys. Although dealing with EN AW-6022, some of the results of Miao and Laughlin (1999) can also be adopted to other alloys of the 6000 series. Chang et al. (2009) focused on the effect of natural pre-aging on the age hardening of EN AW-6060 while Bergsma et al. (1998) investigated the strengthening of a related alloy EN AW-6069. Particle morphology and distribution in EN AW-6082 was discussed by Dadbakhsh et al. (2010) on the basis of TEM images, whereas the evolution of precipitates on atomic level was investigated by Marioara et al. (2001).

Due to its content of zinc, precipitate evolution and age hardening behavior of EN AW-7075 differ from the alloys of the 6000 series. The precipitation behavior during heat treatment of raw billets of EN AW-7075 produced by squeeze casting were investigated by Kim et al. (2001). The distribution of precipitates along grain boundaries was covered by the work of Park and Ardell (1986) and the relationship between particle distribution and grain boundary structure was investigated by Cai et al. (2007). However, the evolution of precipitates in the SIZ and MFZ strongly depends on the thermo-mechanical conditions during the extrusion process. These influences are not sufficiently reflected by the precipitates observed in the rather undeformed DMZ. Further investigations, especially under consideration of the precipitation mechanisms, are necessary in order to describe the mechanical properties in the extrudate depending on the extrusion parameters.

Chapter 4

Summary and outlook

Abstract – This work presents the results of a visual and statistical microstructure analysis of the aluminum alloys EN AW-6060, EN AW-6082 and EN AW-7075 after thermo-mechanical processing by direct hot extrusion. In order to capture different stages of plastic deformation of the material, the aluminum billets were partly extruded and cut along the middle axis in direction of extrusion to reveal the material flow and the associated microstructural evolution. Based on macroscopic LOM images, different deformation zones can be identified which are comparable in size and position for each of the partly extruded billets. A conical DMZ forms along the front face where the material only shows very little microstructure evolution due to the absence of plastic deformation in this region of the billet. The neighboring SIZ is characterized by a significant grain refinement caused by shear deformation, whereas the microstructure of the MFZ in the billet center consists of elongated grains which are oriented in direction of material flow towards the die.

Depending on the aluminum alloy, the microstructure inside the extruded solid rod significantly differs due to recrystallization effects. For EN AW-6060 three zones of microstructure are evident. In the rod center the fibrous grain structure of the MFZ mainly remains except for a few statically recrystallized grains. The material in the outer zones of the rod originates from the SIZ, and the stored energy of the plastic deformation facilitates a complete recrystallization due to SRX. Here, the material of the boundary layer between SIZ and DMZ which flows to the rod's surface shows finer globular grains than the microstructure located more towards the center line which is due to a larger number of recrystallization nuclei. This leads to a continuous gradient in grain size in this part of the extrudate. In contrast to this, the complete cross section of the EN AW-6082 extrudate shows no evidence of recrystallization so that the fibrous grain microstructure is preserved. The grains inside the rod of the third investigated alloy EN AW-7075 have completely recrystallized to a globular shape. Comparable to EN AW-6060 the grains at the rod surface have a smaller mean diameter which continuously increases with larger distance to the surface. In the region around the center line the fibrous grain structure remains preserved. Due to the experimental setup, the partly extruded billets rest for ~ 10 min in the heated press until they are released and cooled down to room temperature. Under these conditions SRX is also facilitated inside the billet, and recrystallized grains are observed in the die and die inflow regions as well as in parts of the SIZ of partly extruded billets of EN AW-6060 and EN AW-7075. In the billet of EN AW-6082 no recrystallized grains are found at all.

For a more in-depth analysis of the microstructure in the different deformation zones, EBSD measurements were performed at representative points of the billet. The visualization and statistical analysis of the EBSD data acquired by the commercial software OIM is done by the

newly developed in-house program Grainplot. The implementation of the basic concepts and algorithms is presented as pseudo-code. The generated and extensively commented Python code allows full access to every step of micrograph generation and statistical evaluation. A special focus of the software presentation lies in the grain identification and the handling of missing data points and those points with a low CI. The produced micrographs, IPFs and microstructure statistics are independently verified by comparison with the results of the commercial product OIM Analysis and the open source Matlab toolbox MTEX.

The EBSD based micrographs generally reflect the same results of the global grain microstructure evolution in the different deformation zones of the partly extruded billet. Furthermore, the EBSD data allows a distinction between grain and subgrain structures with flexible misorientation threshold values. For the investigated aluminum alloys the LAGBs are defined in the misorientation thresholds $3^\circ \sim 15^\circ$ and for HAGBs $\geq 15^\circ$. The development of GNBs and LAGBs due to DRV is observed at measurement points with low or moderate plastic deformation throughout all investigated alloys. With increasing strain the evolution of a serrate grain boundary shape during grain elongation is found which is coincident with the theory of GDX. In some micrographs the fragmentation of banded grains by pinching off leads to a characteristic chain of small scale, globular-shape grains of almost equal orientation which is typical for the grain refinement by GDX.

The grain and subgrain size distribution for each measurement point is presented in histogram plots. The evolution of the mean grain and subgrain sizes inside the billets allow to quantify the dynamic and static recovery and recrystallization processes for further material modeling which is beyond the scope of this particular work. The texture evolution and grain alignment during plastic deformation and material flow is given by discrete IPFs. Furthermore, the relative misorientation distributions between adjacent data points of the EBSD measurement are visualized by corresponding histograms. The evolution of the relative mean misorientation can be quantitatively derived from the given bar diagrams. To capture the evolution of grain and subgrain structures during the thermo-mechanical processing, the normed grain boundary fraction is introduced which is independently evaluated for LAGBs and HAGBs.

This work is embedded into the Collaborative Research Center Transregio TR 30, financially supported by the German Science Foundation (DFG). The results of the statistical microstructure characterization of the aluminum alloys EN AW-6060, EN AW-6082 and EN AW-7075 flow into material modeling for a thermo-mechanically coupled simulation of the extrusion process, the results of which are published by Parvizian et al. (2010a) and Parvizian et al. (2010b).

Both EBSD based or synthetic micrographs are used as input data for different types of microstructure simulations. Figure 4.1 exemplarily shows the results of a phase field based simulation of grain growth based on a real grain microstructure visualized by Grainplot. An adaptive meshing of the real or synthetic micrographs according to the grain boundaries can be used for simulations, for example in combination with crystal plasticity models. An exemplary crystal plasticity simulation result of a deformed microstructure is depicted in Figure 4.2. Due to their periodic conditions, the synthetic micrographs can serve representative volume elements (RVEs) for simulations based on homogenization methods.

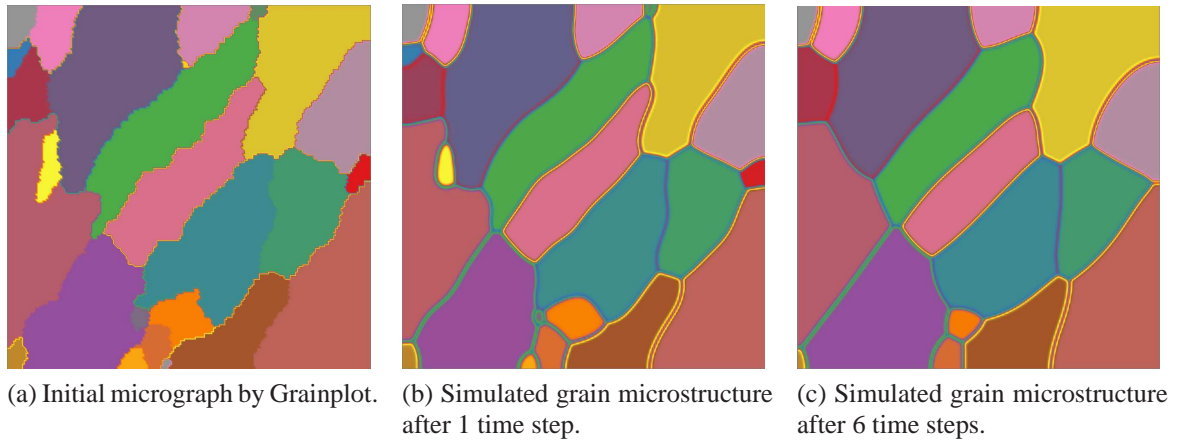


Figure 4.1: Simulated grain growth of a EBSD based grain microstructure based on a phase field model implemented in DEAL II. Grain colors corresponding to grain ID. Courtesy of S. Gladkov.

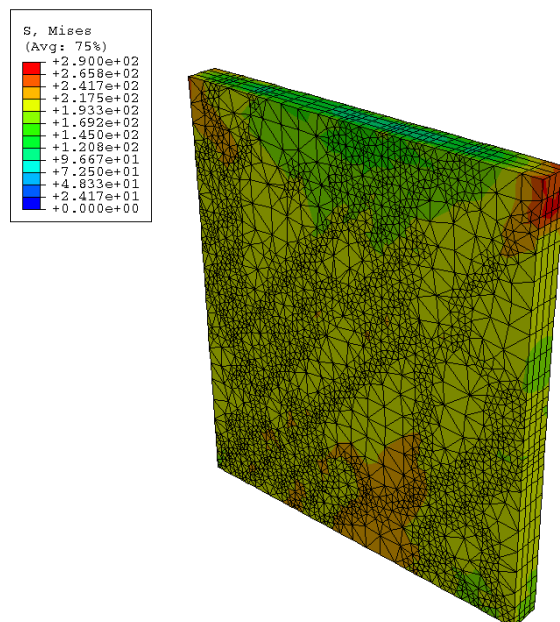


Figure 4.2: Von Mises stress distribution after elongation displacement of 0.285% simulated by a crystal elasticity model. Grain boundary adaptive meshing of an EBSD based micrograph and extension to third dimension. Courtesy of B. Klusemann.

Since the complete codes of Grainplot and Graingen are accessible for the user, further improvements can easily be implemented. This includes features such as statistical analysis or image processing of already present microstructure images not necessarily obtained by the EBSD technique (Wiederkehr et al., 2010).

Appendix A

Grain size histograms of all measurement points

A.1 EN AW-6060

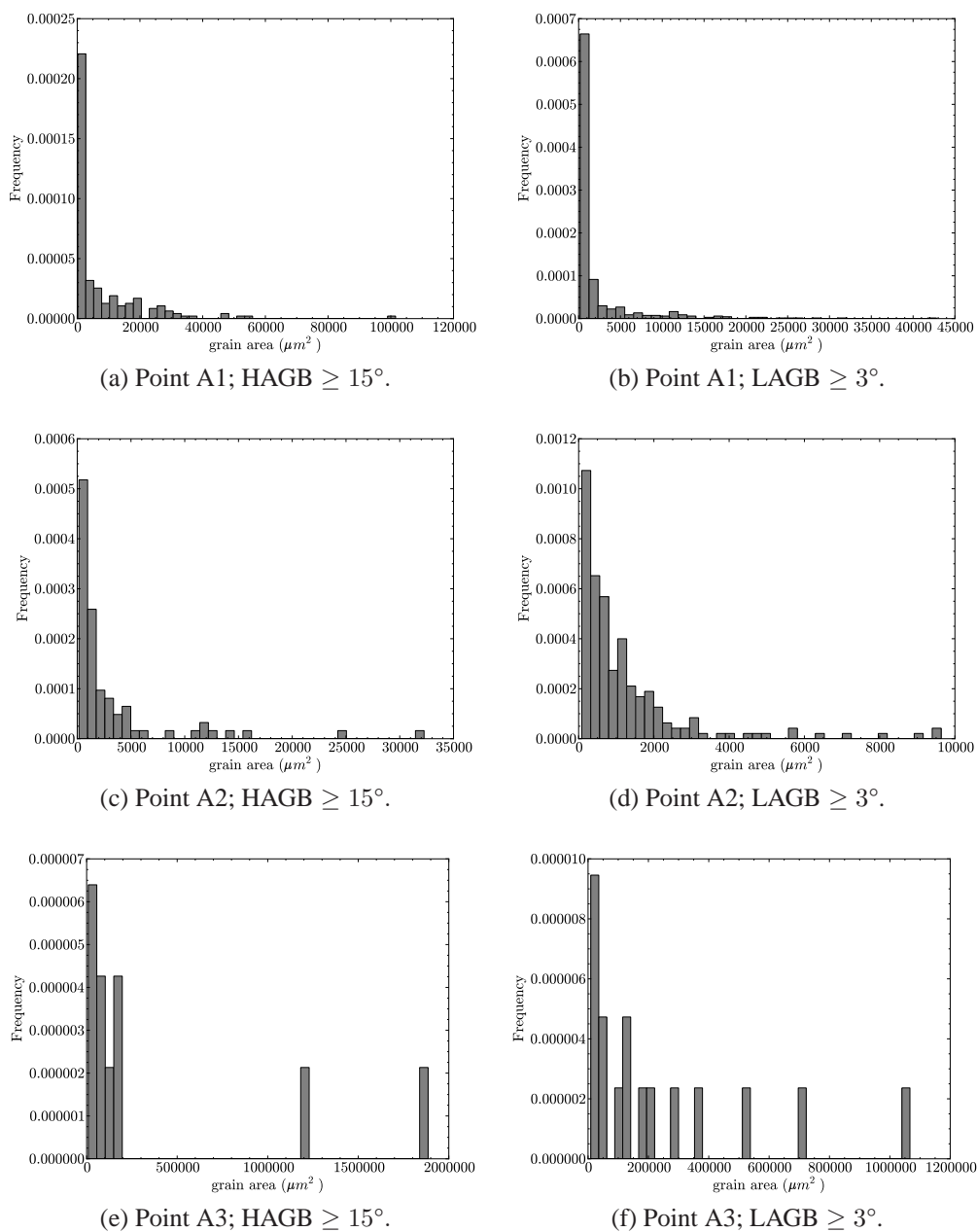
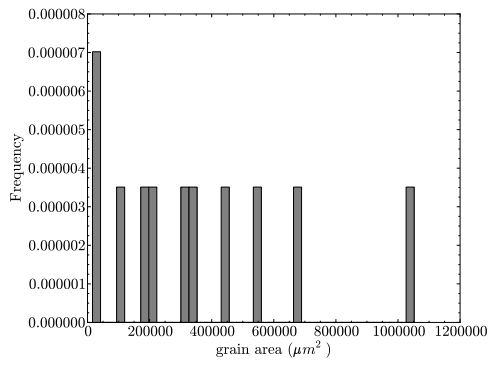
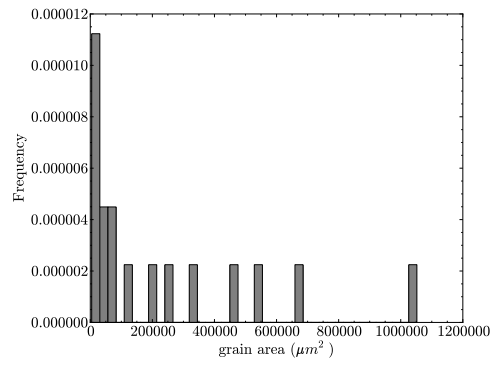


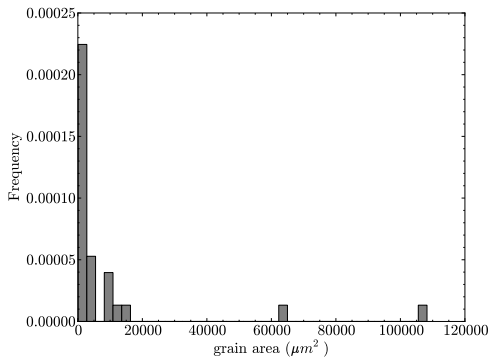
Figure A.1: Grain and subgrain area histograms of measurement points at different deformation zones in partly extruded billet of EN AW-6060. See Figure 3.6 for measurement point positions.



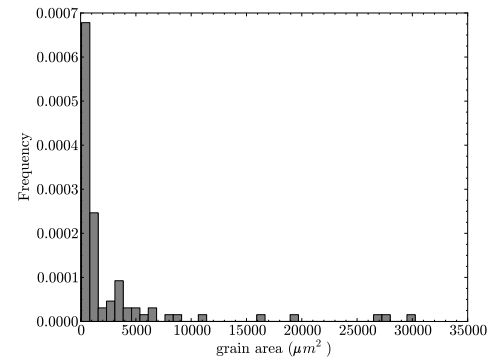
(a) Point A4; HAGB $\geq 15^\circ$.



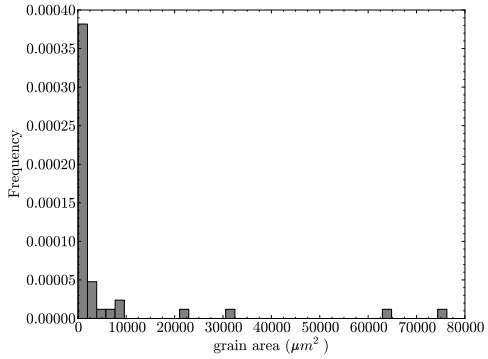
(b) Point A4; LAGB $\geq 3^\circ$.



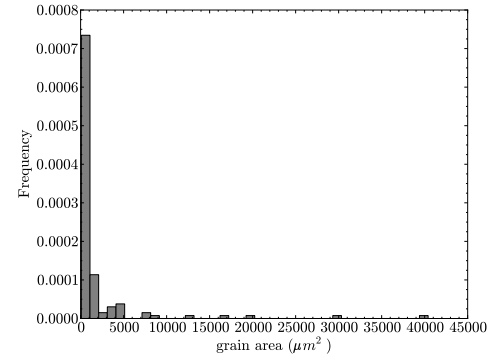
(c) Point A5; HAGB $\geq 15^\circ$.



(d) Point A5; LAGB $\geq 3^\circ$.

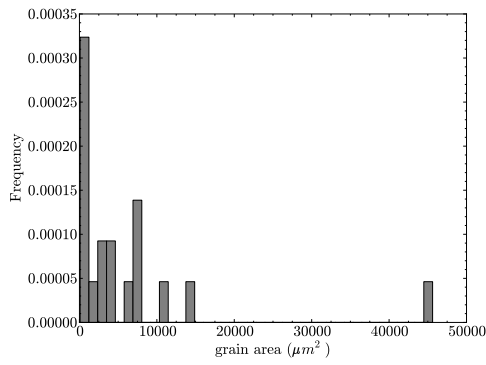


(e) Point A6; HAGB $\geq 15^\circ$.

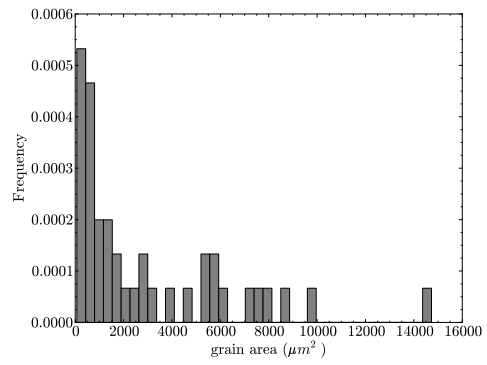


(f) Point A6; LAGB $\geq 3^\circ$.

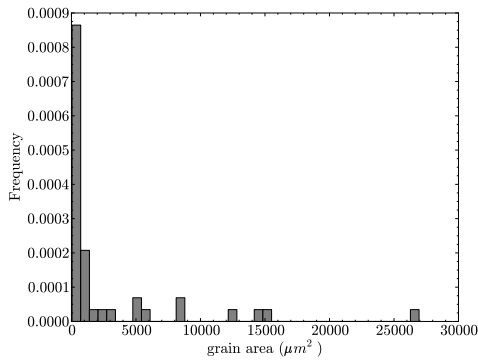
Figure A.2: Continuation - Grain and subgrain area histograms of measurement points at different deformation zones in partly extruded billet of EN AW-6060. See Figure 3.6 for measurement point positions.



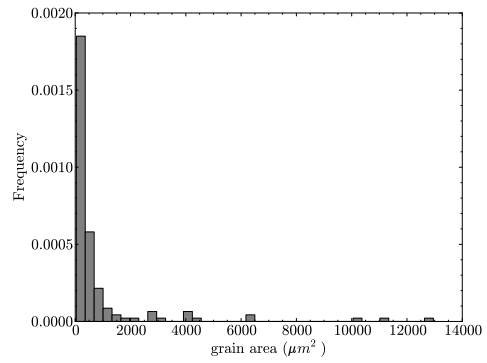
(a) Point M1; HAGB $\geq 15^\circ$.



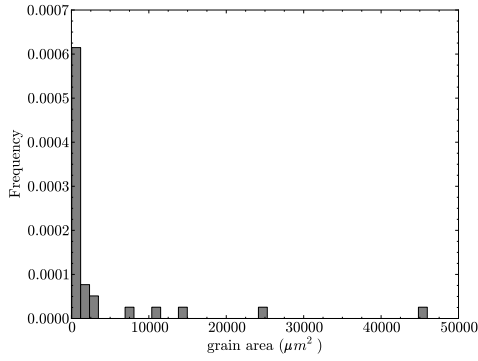
(b) Point M1; LAGB $\geq 3^\circ$.



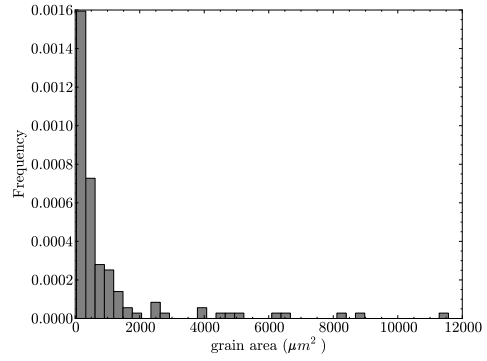
(c) Point M2; HAGB $\geq 15^\circ$.



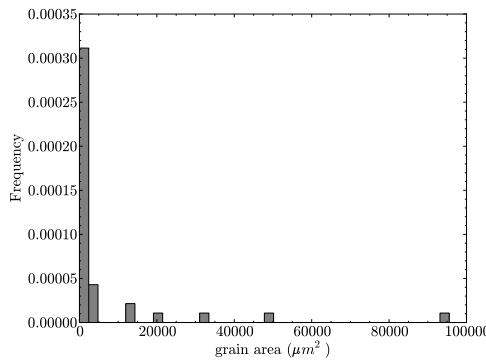
(d) Point M2; LAGB $\geq 3^\circ$.



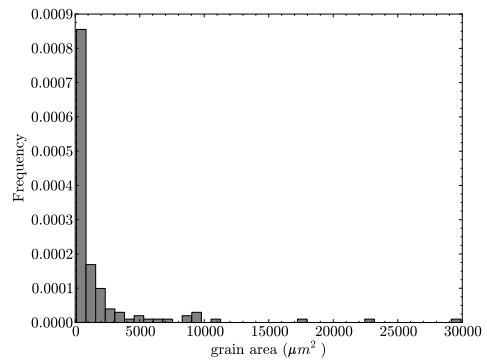
(e) Point M3; HAGB $\geq 15^\circ$.



(f) Point M3; LAGB $\geq 3^\circ$.



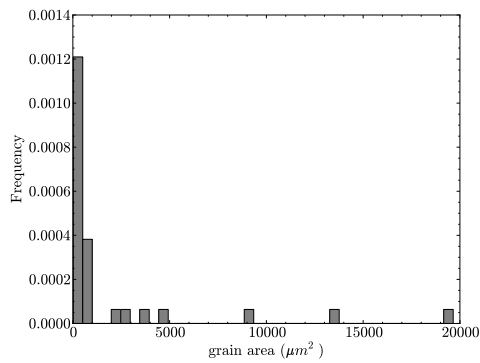
(g) Point M4; HAGB $\geq 15^\circ$.



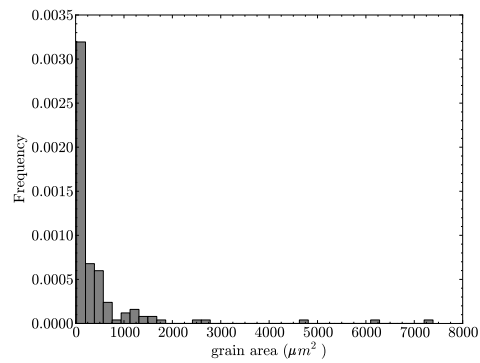
(h) Point M4; LAGB $\geq 3^\circ$.

Figure A.3: Grain and subgrain area histograms of measurement points along middle axis of partly extruded billet of EN AW-6060. See Figure 3.8 for measurement point positions.

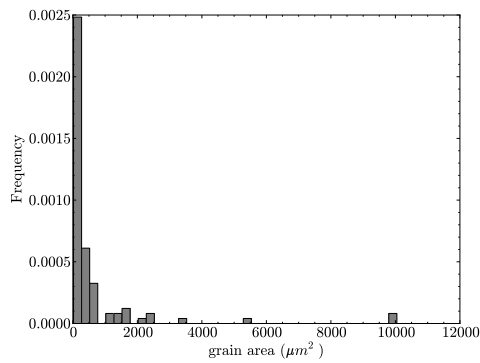
A.2 EN AW-6082



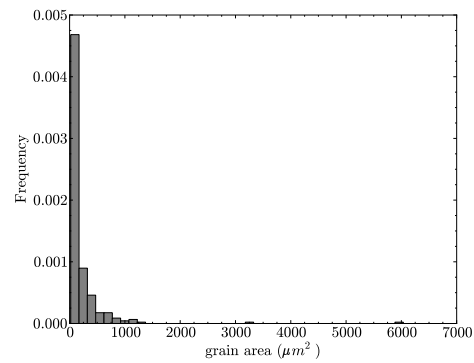
(a) Point B1; HAGB $\geq 15^\circ$.



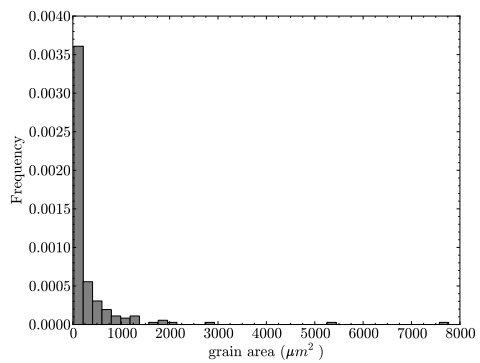
(b) Point B1; LAGB $\geq 3^\circ$.



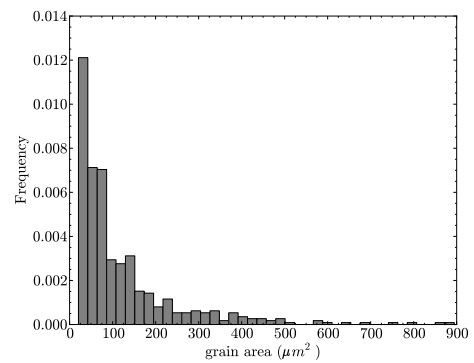
(c) Point B2; HAGB $\geq 15^\circ$.



(d) Point B2; LAGB $\geq 3^\circ$.



(e) Point B3; HAGB $\geq 15^\circ$.



(f) Point B3; LAGB $\geq 3^\circ$.

Figure A.4: Grain and subgrain area histograms of measurement points at different deformation zones in partly extruded billet of EN AW-6082. See Figure 3.18 for measurement point positions.

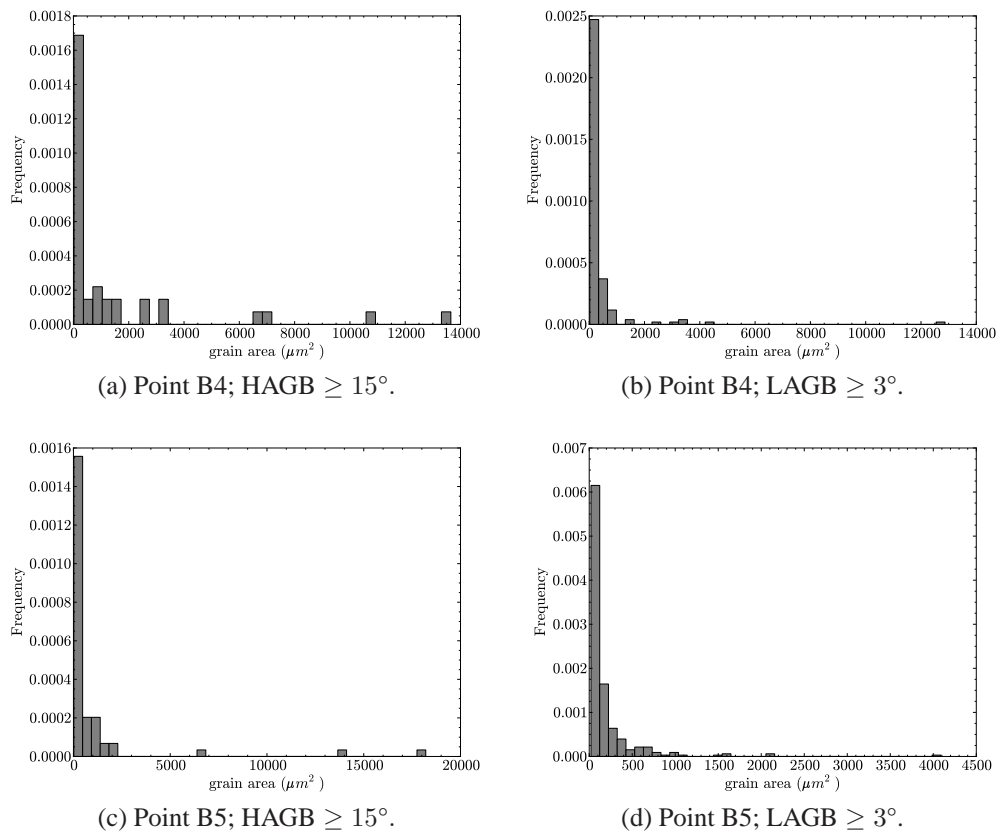


Figure A.5: Continuation - Grain and subgrain area histograms of measurement points at different deformation zones in partly extruded billet of EN AW-6082. See Figure 3.18 for measurement point positions.

A.3 EN AW-7075

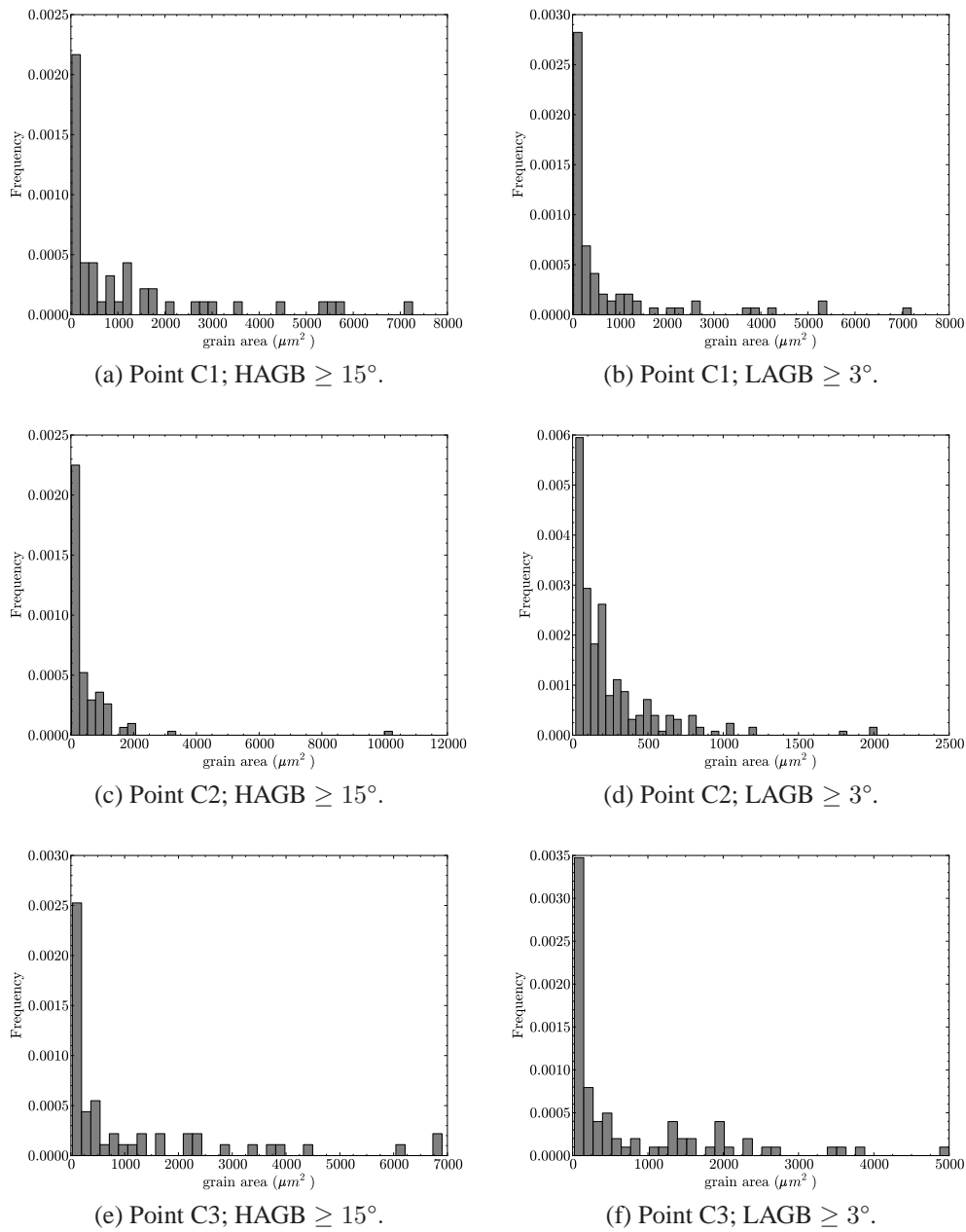
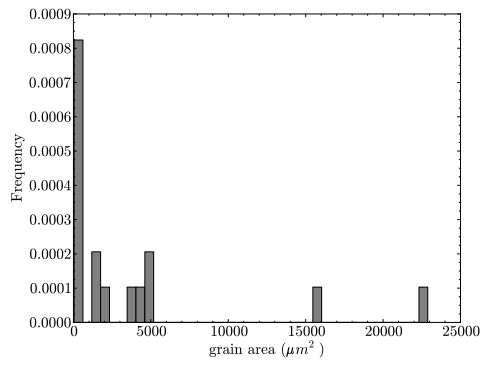
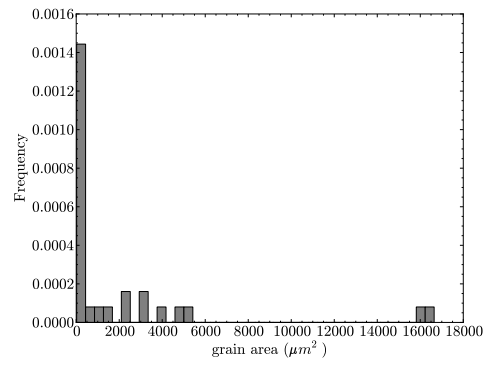


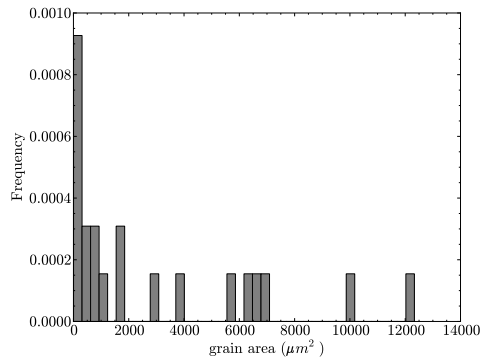
Figure A.6: Grain and subgrain area histograms of measurement points at different deformation zones in partly extruded billet of EN AW-7075. See Figure 3.25 for measurement point positions.



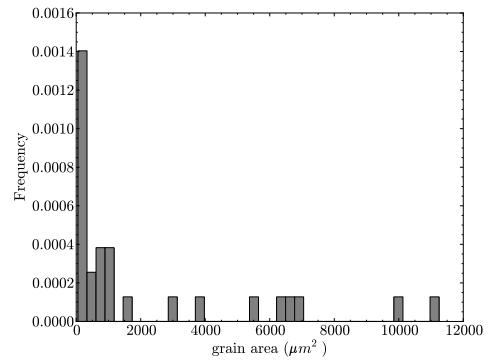
(a) Point C4; HAGB $\geq 15^\circ$.



(b) Point C4; LAGB $\geq 3^\circ$.



(c) Point C5; HAGB $\geq 15^\circ$.



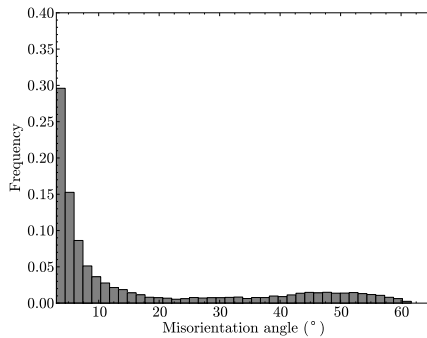
(d) Point C5; LAGB $\geq 3^\circ$.

Figure A.7: Continuation - Grain and subgrain area histograms of measurement points at different deformation zones in partly extruded billet of EN AW-7075. See Figure 3.25 for measurement point positions.

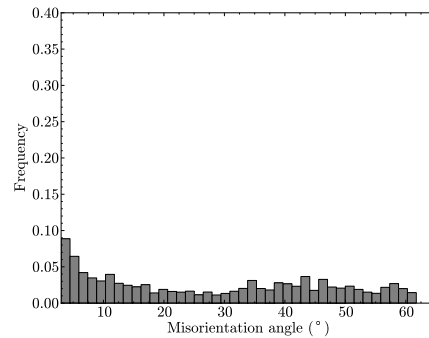
Appendix B

Misorientation histograms of all measurement points

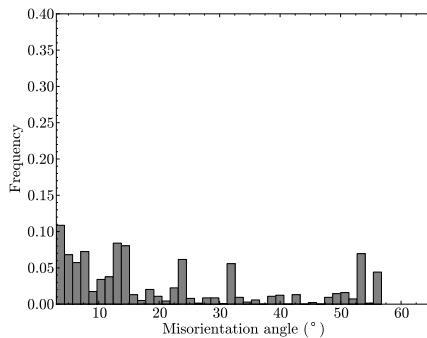
B.1 EN AW-6060



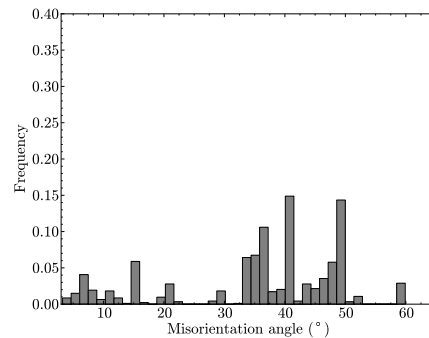
(a) Point A1 - DMZ.



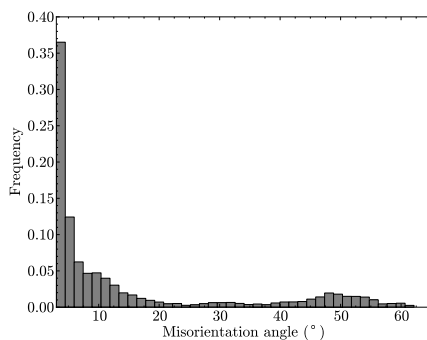
(b) Point A2 - SIZ.



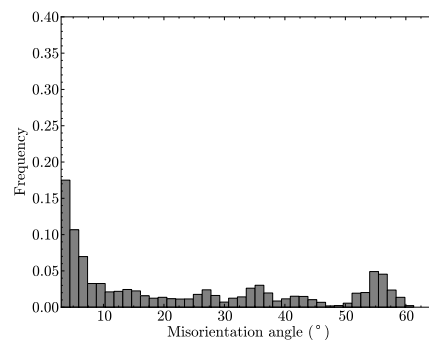
(c) Point A3 - die inflow.



(d) Point A4 - outer rod.

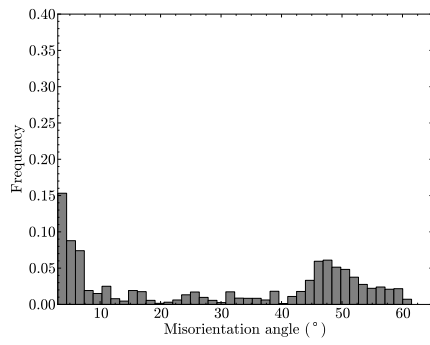


(e) Point A5 - MFZ.

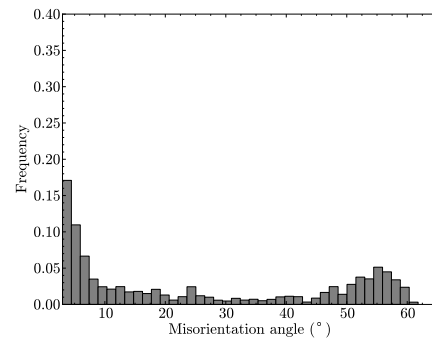


(f) Point A6 - inner rod.

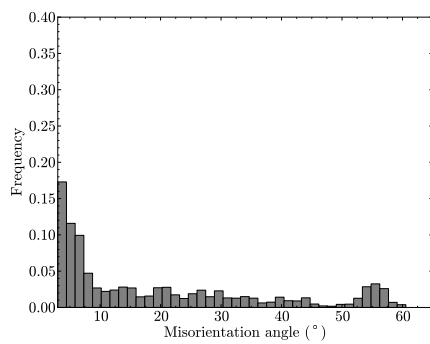
Figure B.1: Misorientation histograms of measurement points at different deformation zones in partly extruded billet of EN AW-6060. Minimum misorientation threshold 3° . See Figure 3.6 for measurement point positions.



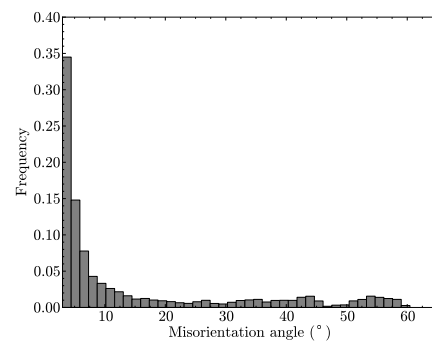
(a) Point M1 - MFZ.



(b) Point M2 - MFZ.

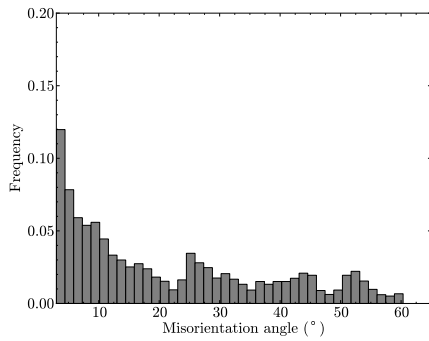


(c) Point M3 - die inflow.

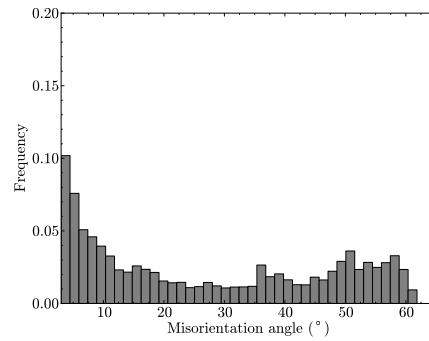


(d) Point M4 - die inflow.

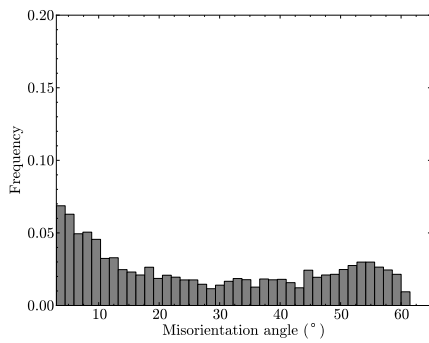
Figure B.2: Misorientation histograms of measurement points along middle axis of partly extruded billet of EN AW-6060. Minimum misorientation threshold 3° . See Figure 3.8 for measurement point positions.

B.2 EN AW-6082

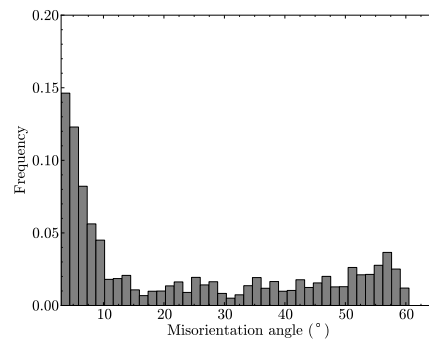
(a) Point B1 - DMZ.



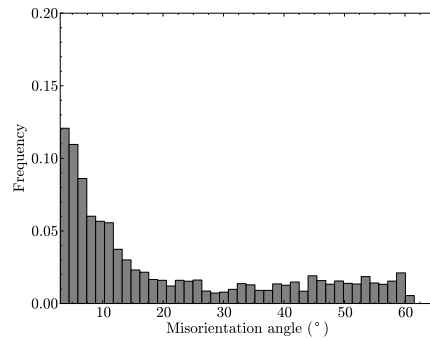
(b) Point B2 - SIZ.



(c) Point B3 - die inflow.



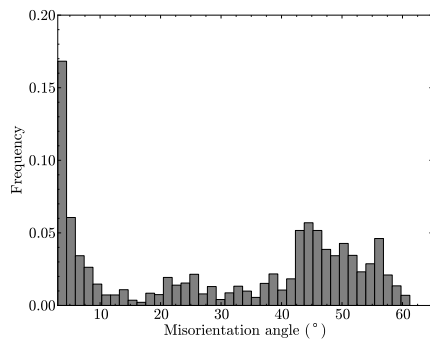
(d) Point B4 - MFZ.



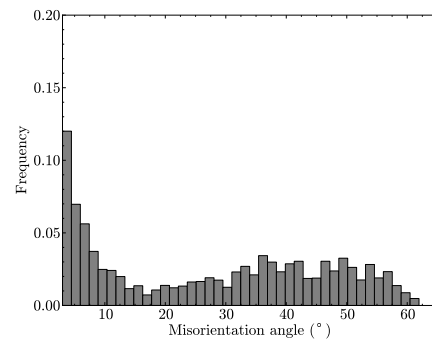
(e) Point A5 - inner rod.

Figure B.3: Misorientation histograms of measurement points at different deformation zones in partly extruded billet of EN AW-6082. Minimum misorientation threshold 3°. See Figure 3.18 for measurement point positions.

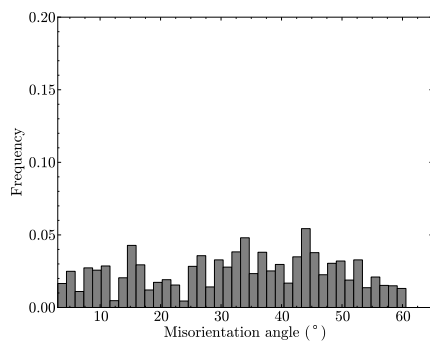
B.3 EN AW-7075



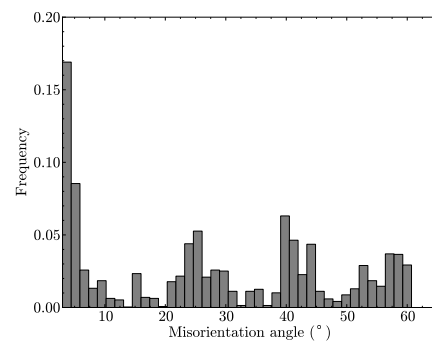
(a) Point C1 - DMZ.



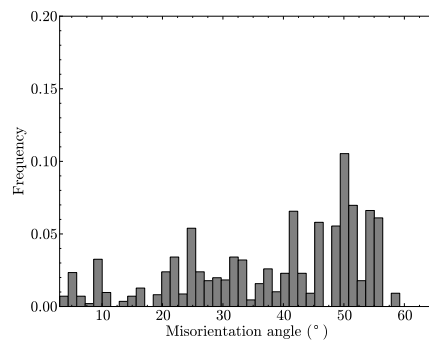
(b) Point C2 - SIZ.



(c) Point C3 - die inflow.



(d) Point C4 - MFZ.



(e) Point C5 - inner rod.

Figure B.4: Misorientation histograms of measurement points at different deformation zones in partly extruded billet of EN AW-6082. Minimum misorientation threshold 3° . See Figure 3.25 for measurement point positions.

Appendix C

Discrete inverse pole figures of all measurement points

C.1 EN AW-6060

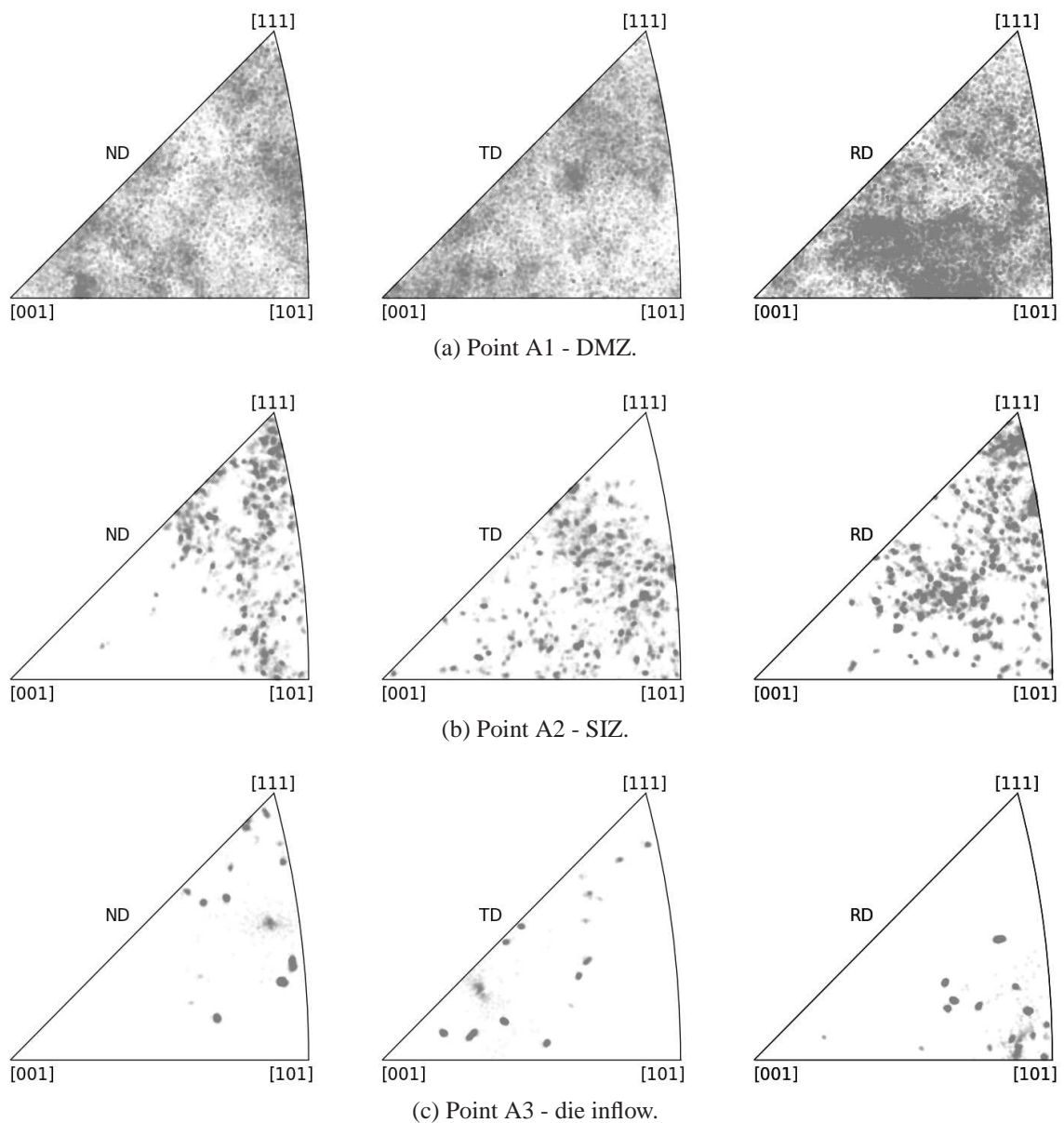


Figure C.1: Discrete inverse pole figures of measurement points at different deformation zones in partly extruded billet of EN AW-6060. See Figure 3.6 for measurement point positions.

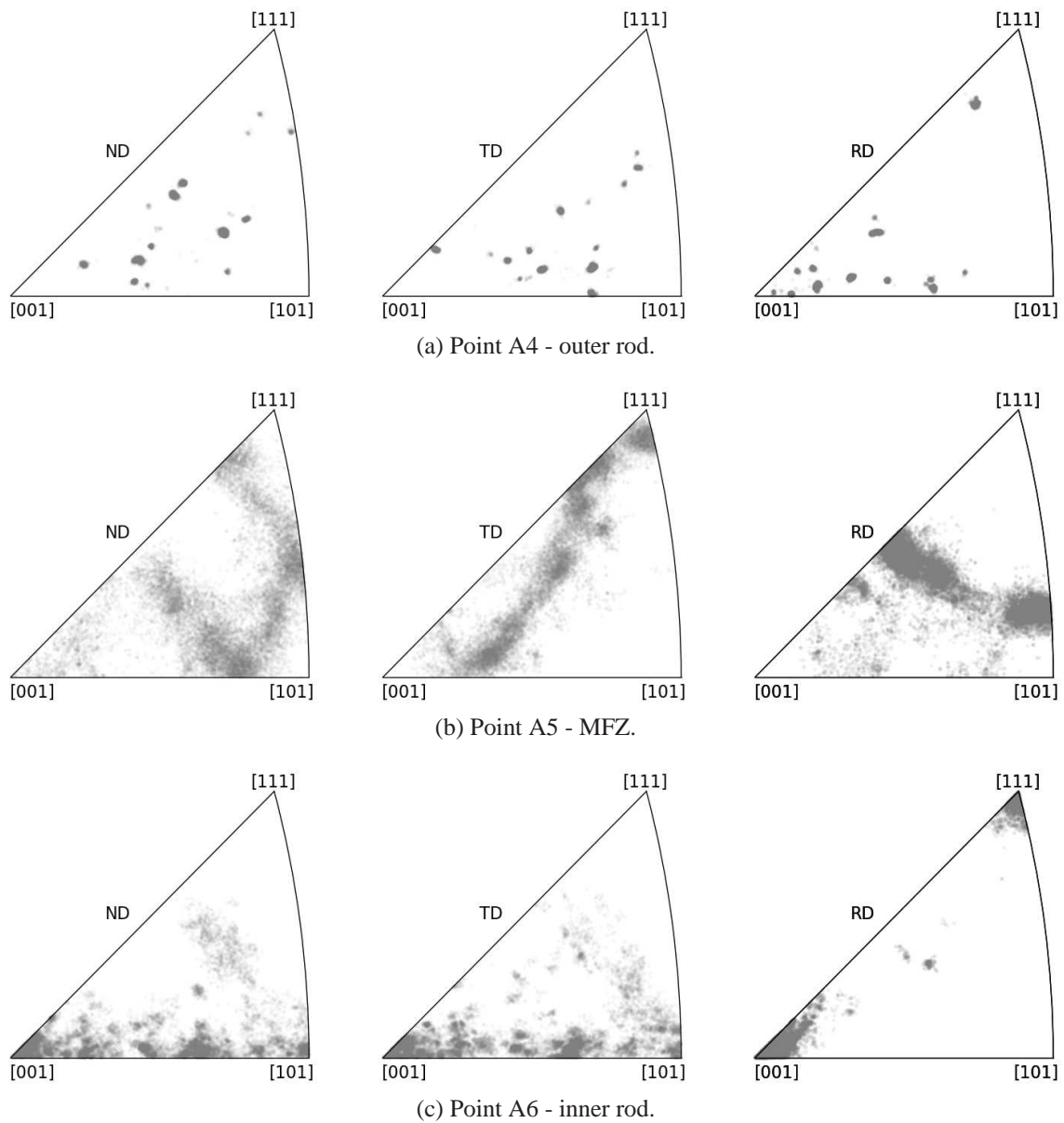


Figure C.2: Continuation - Discrete inverse pole figures of measurement points at different deformation zones in partly extruded billet of EN AW-6060. See Figure 3.6 for measurement point positions.

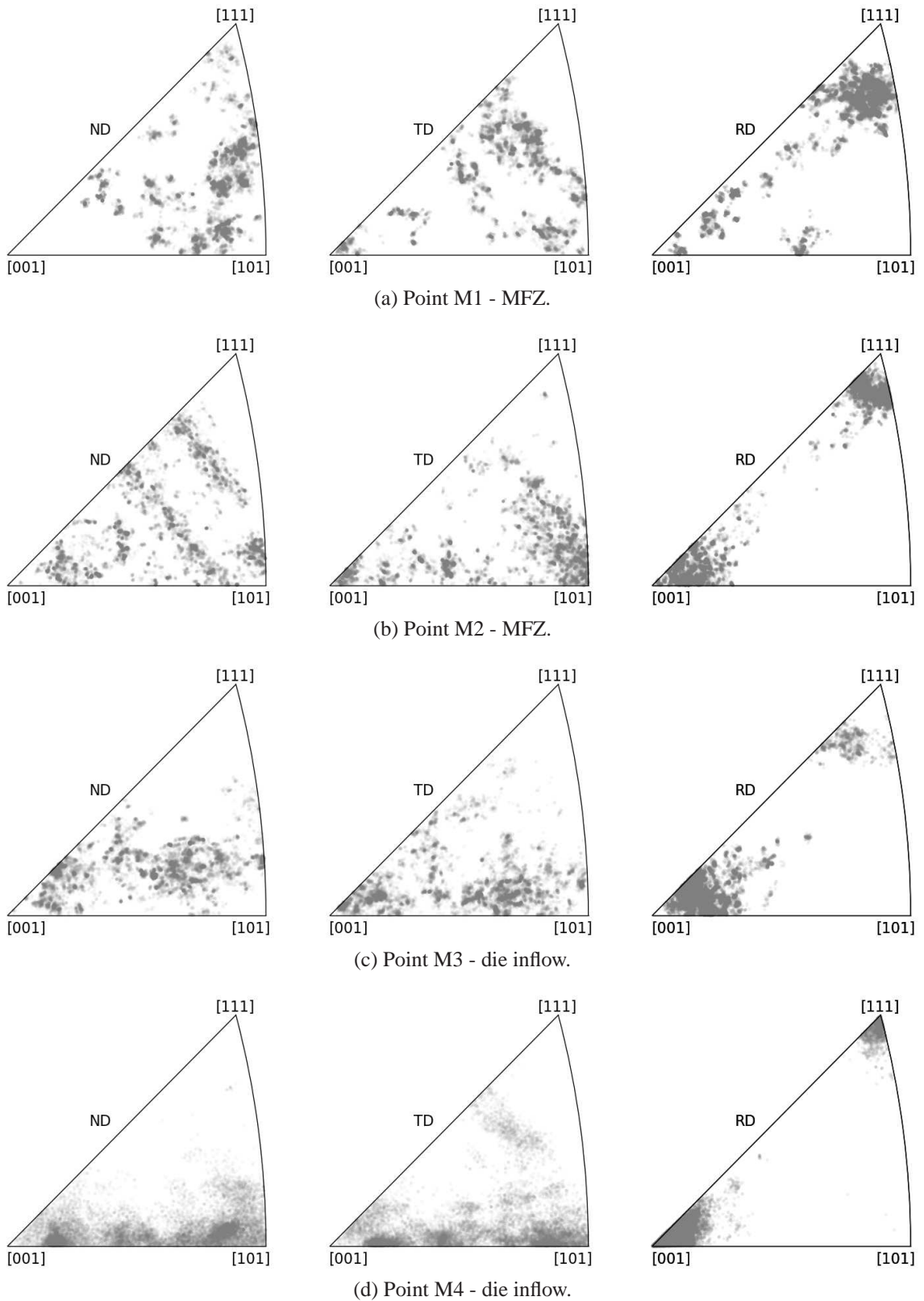


Figure C.3: Discrete inverse pole figures of measurement points along middle axis of partly extruded billet of EN AW-6060. See Figure 3.8 for measurement point positions.

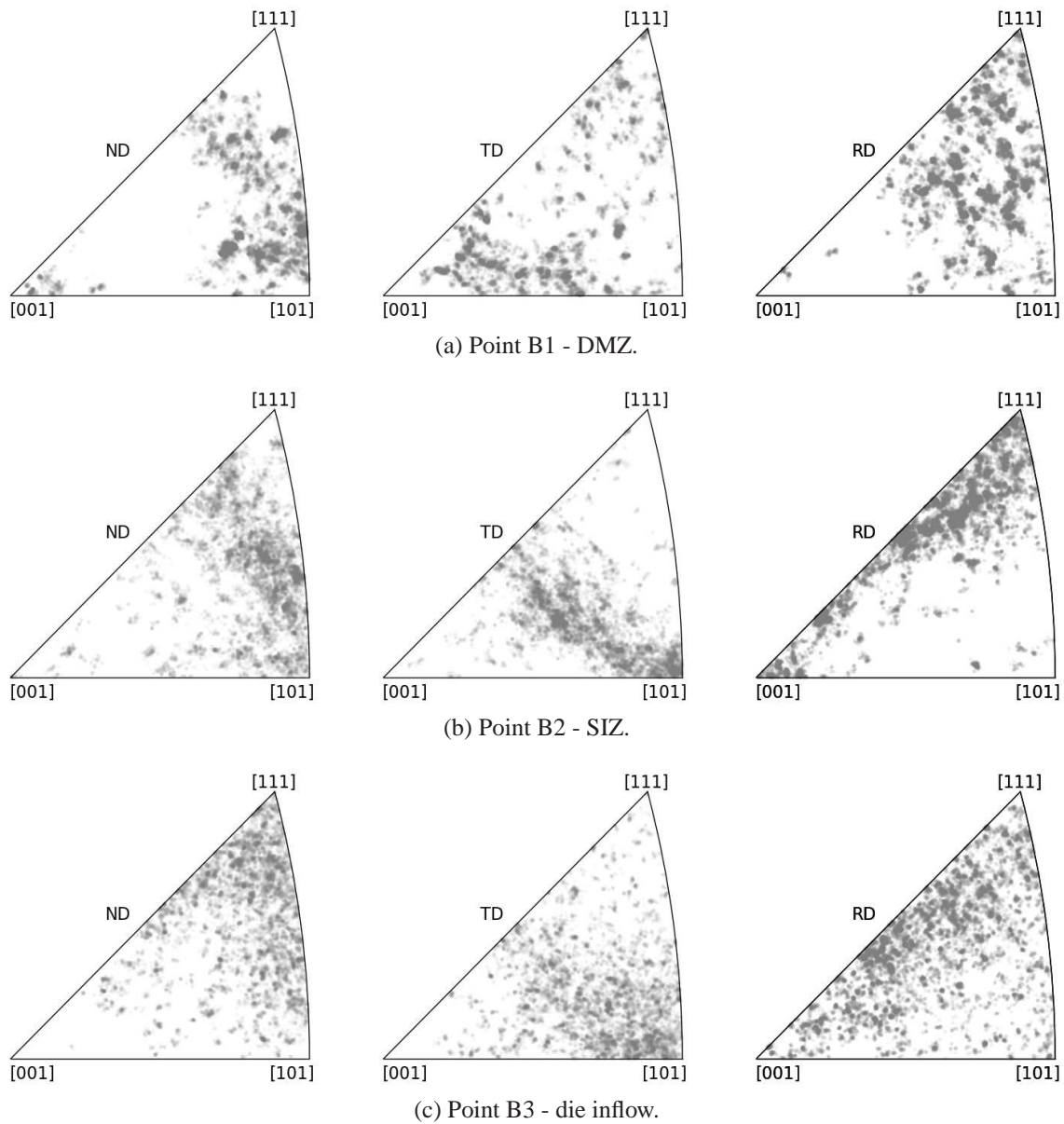
C.2 EN AW-6082

Figure C.4: Discrete inverse pole figures of measurement points at different deformation zones in partly extruded billet of EN AW-6082. See Figure 3.18 for measurement point positions.

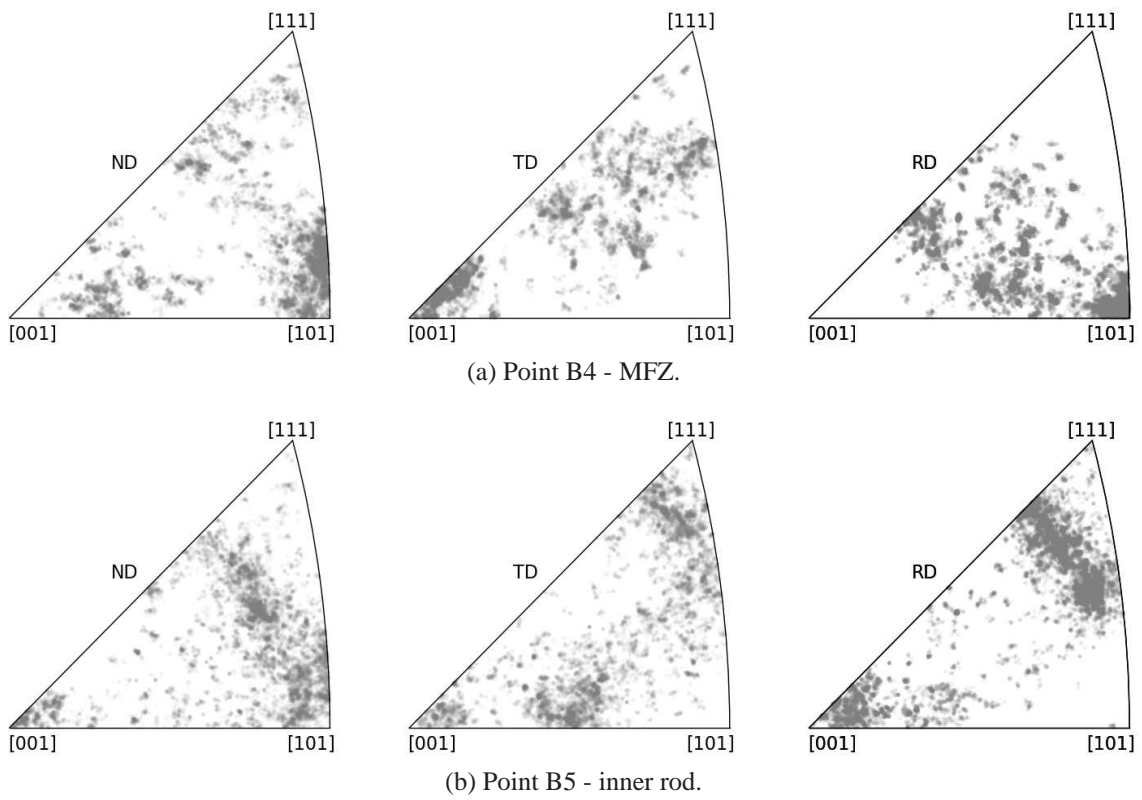


Figure C.5: Continuation - Discrete inverse pole figures of measurement points at different deformation zones in partly extruded billet of EN AW-6082. See Figure 3.18 for measurement point positions.

C.3 EN AW-7075

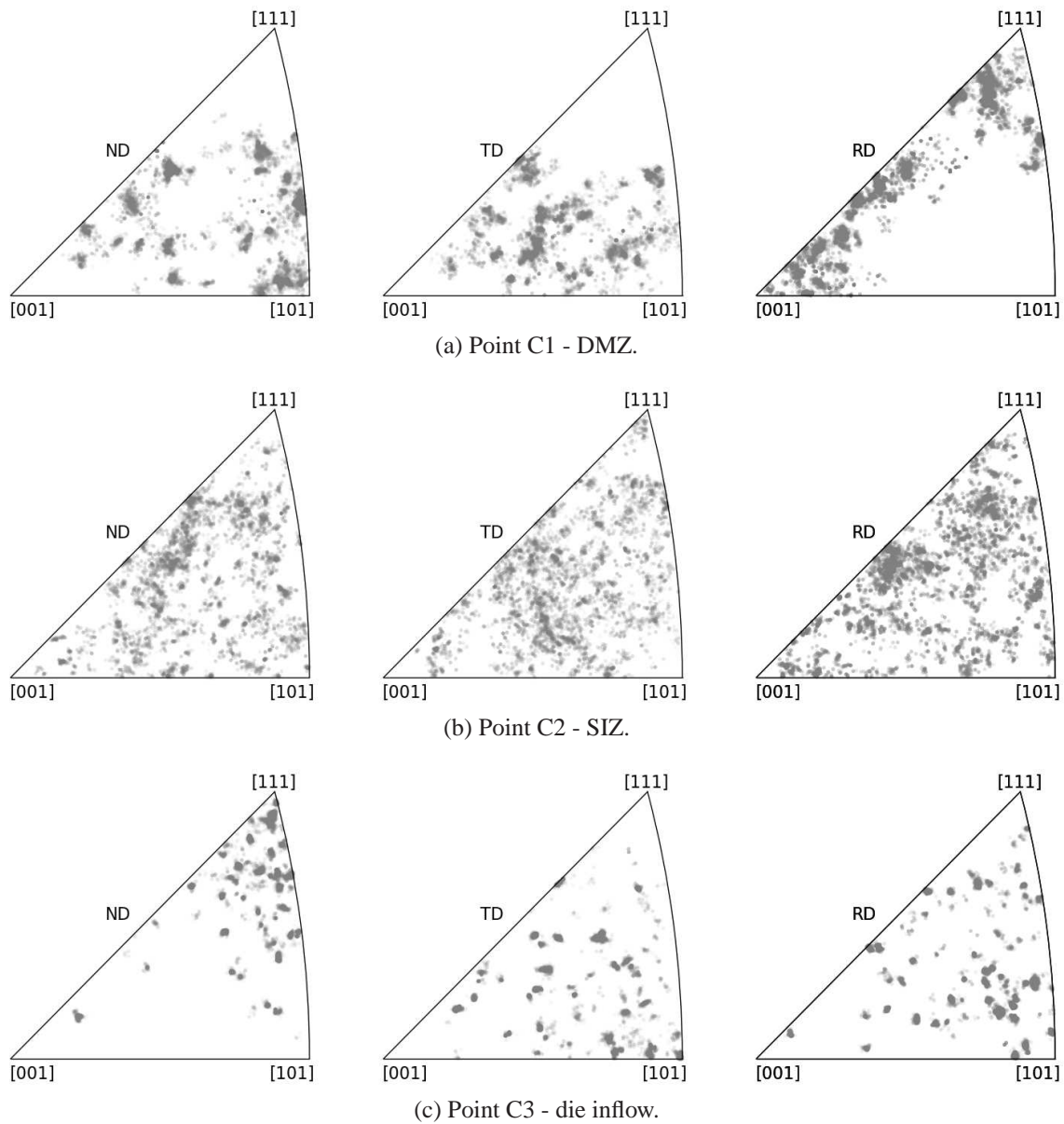


Figure C.6: Discrete inverse pole figures of measurement points at different deformation zones in partly extruded billet of EN AW-7075. See Figure 3.25 for measurement point positions.

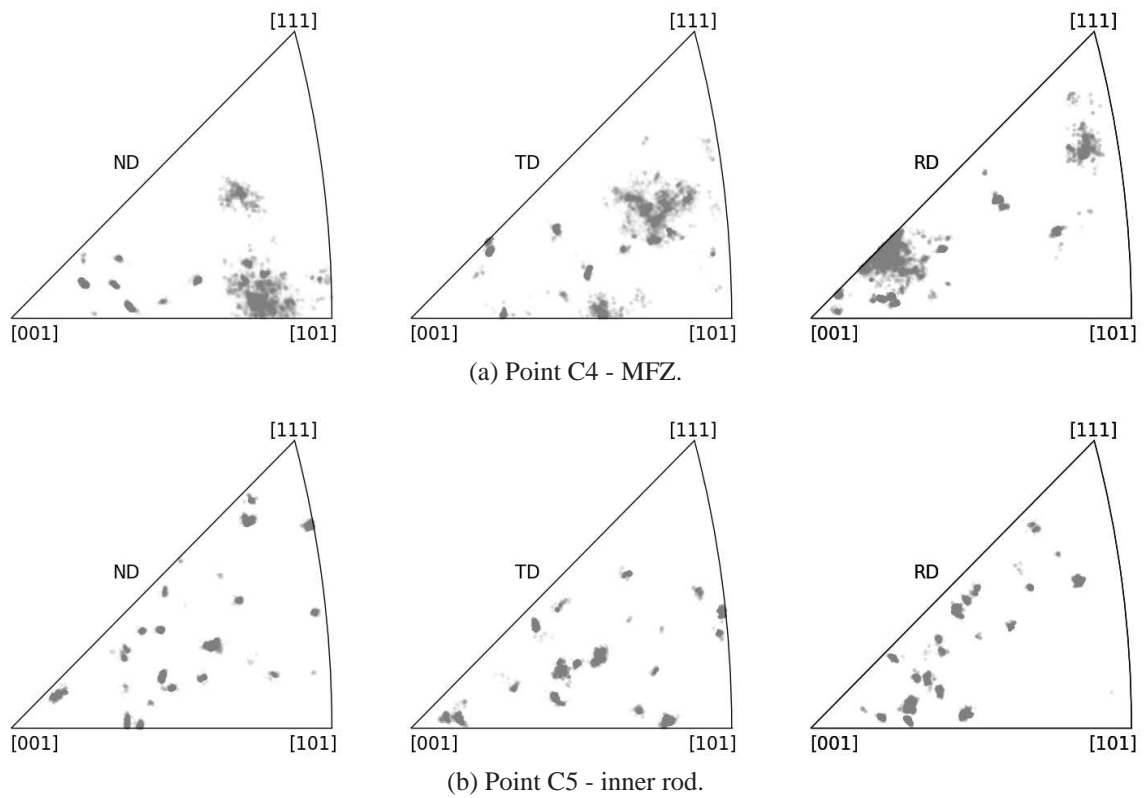


Figure C.7: Continuation - Discrete inverse pole figures of measurement points at different deformation zones in partly extruded billet of EN AW-7075. See Figure 3.25 for measurement point positions.

References

- Adams, B. L., Wright, S. I., Kunze, K., Orientation imaging: The emergence of a new microscopy, *Metallurgical Transactions A*, Volume 24, pp. 819–831, 1993.
- Ashby, M. F., The deformation of plastically non-homogeneous materials, *Philosophical Magazine*, Volume 21, pp. 399–424, 1970.
- Ashby, M. F., *Materials Selection in Mechanical Design*, Third Edition, 3rd edition, Butterworth-Heinemann, Oxford, GB, 2005.
- ASTM International, ASTM E 112 - Standard Test Methods for Determining Average Grain Size, 2004.
- Baba-Kishi, K. Z., Review Electron backscatter Kikuchi diffraction in the scanning electron microscope for crystallographic analysis, *Journal of Materials Science*, Volume 37, pp. 1715–1746, 2002.
- Bargel, H., Cardinal, P., Hilbrans, H., Hübner, K., Schulze, G., Wurzel, G., *Werkstoffkunde*, 6th edition, Springer, Berlin, 1999.
- Bauser, M., Sauer, G., Siegert, K. (editors), *Extrusion*, 2nd edition, ASM International, Materials Park, Ohio, 2006.
- Bergsma, S. C., Kassner, M. E., Li, X., Wall, M. A., Strengthening in the new aluminum alloy AA 6069, *Materials Science and Engineering: A*, Volume 254, pp. 112–118, 1998.
- Bhandari, Y., Sarkar, S., Groeber, M., Uchic, M. D., Dimiduk, D. M., Ghosh, S., 3D polycrystalline microstructure reconstruction from FIB generated serial sections for FE analysis, *Computational Materials Science*, Volume 41, pp. 222–235, 2007.
- Bunge, H. J., Entstehung von Verformungstexturen in metallischen Werkstoffen, *Kristall und Technik*, Volume 6, pp. 677–728, 1971.
- Bunge, H. J., Fabric analysis by orientation distribution functions, *Tectonophysics*, Volume 78, pp. 1–21, 1981.
- Burns, J. B., Hanson, A. R., Riseman, E. M., Extracting straight lines, *IEEE Transactions on Pattern Analysis and Machine Intelligence*, Volume 8, pp. 425–455, 1986.
- Cai, B., Adams, B. L., Nelson, T. W., Relation between precipitate-free zone width and grain boundary type in 7075-T7 Al alloy, *Acta Materialia*, Volume 55, pp. 1543–1553, 2007.
- Chang, C. S. T., Wieler, I., Wanderka, N., Banhart, J., Positive effect of natural pre-ageing on precipitation hardening in Al-0.44 at% Mg-0.38 at% Si alloy, *Ultramicroscopy*, Volume 109, pp. 585–592, 2009.
- Chawla, N., Patel, B. V., Koopman, M., Chawla, K. K., Saha, R., Patterson, B. R., Fuller, E. R., Langer, S. A., Microstructure-based simulation of thermomechanical behavior of composite materials by object-oriented finite element analysis, *Materials Characterization*, Volume 49, pp. 395–407, 2002.

- Chen, L., Phase-field models for microstructure evolution, *Annual Review of Materials Research*, Volume 32, pp. 113–140, 2002.
- Coates, D. G., Kikuchi-like reflection patterns obtained with the scanning electron microscope, *Philosophical Magazine*, Volume 16, pp. 1179–1184, 1967.
- Dadbakhsh, S., Taheri, A. K., Smith, C. W., Strengthening study on 6082 Al alloy after combination of aging treatment and ECAP process, *Materials Science and Engineering: A*, Volume 527, pp. 4758–4766, 2010.
- Davies, R., Randle, V., Secondary processing of electron backscatter data from an aluminum alloy, *Materials Characterization*, Volume 37, pp. 131–141, 1996.
- Ding, H. L., He, Y. Z., Liu, L. F., Ding, W. J., Cellular automata simulation of grain growth in three dimensions based on the lowest-energy principle, *Journal of Crystal Growth*, Volume 293, pp. 489–497, 2006.
- Ding, R., Guo, Z. X., Microstructural modelling of dynamic recrystallisation using an extended cellular automaton approach, *Computational Materials Science*, Volume 23, pp. 209–218, 2002.
- Doherty, R. D., Hughes, D. A., Humphreys, F. J., Jonas, J. J., Jensen, D. J., Kassner, M. E., King, W. E., McNelley, T. R., McQueen, H. J., Rollett, A. D., Current issues in recrystallization: a review, *Materials Science and Engineering A*, Volume 238, pp. 219–274, 1997.
- Fan, D., Chen, L. Q., Computer simulation of grain growth using a continuum field model, *Acta Materialia*, Volume 45, pp. 611–622, 1997.
- Flick, F. B., Etching Aluminum and Its Alloys for Macroscopic and Microscopic Examination, *Transactions of The American Institute of Mining, Metallurgical, and Petroleum Engineers*, Volume 71, pp. 816–827, 1925.
- Frank, F. C., Read, W. T., Multiplication Processes for Slow Moving Dislocations, *Physical Review*, Volume 79, p. 722, 1950.
- Geertruyden, W. V., Browne, H., Misiolek, W., Wang, P., Evolution of surface recrystallization during indirect extrusion of 6xxx aluminum alloys, *Metallurgical and Materials Transactions A*, Volume 36, pp. 1049–1056, 2005.
- Godfrey, A., Edge preservation near triple junctions during orientation averaging of EBSD data, *Scripta Materialia*, Volume 50, pp. 1097–1101, 2004.
- Godfrey, A., Hughes, D. A., Characterization of dislocation wall spacing distributions, in *Proceedings of Materials Week '97*, Indianapolis, IN, USA, 1997.
- Gottstein, G., *Physical Foundations of Materials Science*, 1st edition, Springer, Berlin, 2004.
- Gottstein, G., Shvindlerman, L. S., *Grain Boundary Migration in Metals: Thermodynamics, Kinetics, Applications*, 1st edition, CRC Press, Boca Raton, FL, 1999.
- Gourdet, S., Montheillet, F., A model of continuous dynamic recrystallization, *Acta Materialia*, Volume 51, pp. 2685–2699, 2003.

- Groeber, M., Ghosh, S., Uchic, M. D., Dimiduk, D. M., A framework for automated analysis and simulation of 3D polycrystalline microstructures.: Part 1: Statistical characterization, *Acta Materialia*, Volume 56, pp. 1257–1273, 2008a.
- Groeber, M., Ghosh, S., Uchic, M. D., Dimiduk, D. M., A framework for automated analysis and simulation of 3D polycrystalline microstructures. Part 2: Synthetic structure generation, *Acta Materialia*, Volume 56, pp. 1274–1287, 2008b.
- Gutierrez, I., Castro, F. R., Urcola, J. J., Fuentes, M., Static recrystallization kinetics of commercial purity aluminium after hot deformation within the steady state regime, *Materials Science and Engineering: A*, Volume 102, pp. 77–84, 1988.
- Hall, E. O., The Deformation and Ageing of Mild Steel: III Discussion of Results, *Proceedings of the Physical Society. Section B*, Volume 64, pp. 747–753, 1951.
- Hallberg, H., Wallin, M., Ristinmaa, M., Modeling of continuous dynamic recrystallization in commercial-purity aluminum, *Materials Science and Engineering: A*, Volume 527, pp. 1126–1134, 2010.
- Hansen, N., Huang, X., Hughes, D. A., Microstructural evolution and hardening parameters, *Materials Science and Engineering A*, Volume 317, pp. 3–11, 2001.
- He, W., Ma, W., Pantleon, W., Microstructure of individual grains in cold-rolled aluminium from orientation inhomogeneities resolved by electron backscattering diffraction, *Materials Science and Engineering: A*, Volume 494, pp. 21–27, 2008.
- Hielscher, R., The Inversion of the Radon Transform on the Rotational Group and Its Application to Texture Analysis, PhD thesis, Technische Universität Bergakademie Freiberg, Freiberg, 2007.
- Hielscher, R., Schaeben, H., A novel pole figure inversion method: specification of the MTEX algorithm, *Journal of Applied Crystallography*, Volume 41, pp. 1024–1037, 2008.
- Hirth, J. P., Lothe, J., *Theory of Dislocations*, 2nd edition, John Wiley & Sons, New York, 1982.
- Huang, Y., Humphreys, F. J., Transient dynamic recrystallization in an aluminium alloy subjected to large reductions in strain rate, *Acta Materialia*, Volume 45, pp. 4491–4503, 1997.
- Hughes, D. A., Microstructure evolution, slip patterns and flow stress, *Materials Science and Engineering A*, Volume 319-321, pp. 46–54, 2001.
- Hughes, D. A., Hansen, N., Bammann, D. J., Geometrically necessary boundaries, incidental dislocation boundaries and geometrically necessary dislocations, *Scripta Materialia*, Volume 48, pp. 147–153, 2003.
- Humphreys, F. J., Quantitative metallography by electron backscattered diffraction, *Journal of Microscopy*, Volume 195, pt 3, pp. 170–185, 1999.
- Humphreys, F. J., Review - Grain and subgrain characterisation by electron backscatter diffraction, *Journal of Materials Science*, Volume 36, pp. 3833–3854, 2001.
- Humphreys, F. J., Characterisation of fine-scale microstructures by electron backscatter diffraction (EBSD), *Scripta Materialia*, Volume 51, pp. 771–776, 2004a.

- Humphreys, F. J., Reconstruction of grains and subgrains from electron backscatter diffraction maps, *Journal of Microscopy*, Volume 213, pt 3, pp. 247–256, 2004b.
- Humphreys, F. J., Hatherly, M., *Recrystallization and Related Annealing Phenomena*, 2nd edition, Elsevier, Oxford, GB, 2004.
- Humphreys, F. J., Huang, Y., Brough, I., Harris, C., Electron backscatter diffraction of grain and subgrain structures - resolution considerations, *Journal of Microscopy*, Volume 195, pp. 212–216, 1999.
- Ishikawa, T., Sano, H., Yoshida, Y., Yukawa, N., Sakamoto, J., Tozawa, Y., Effect of Extrusion Conditions on Metal Flow and Microstructures of Aluminum Alloys, *CIRP Annals - Manufacturing Technology*, Volume 55, pp. 275–278, 2006.
- Kaibyshev, R., Shipilova, K., Musin, F., Motohashi, Y., Continuous dynamic recrystallization in an Al-Li-Mg-Sc alloy during equal-channel angular extrusion, *Materials Science and Engineering A*, Volume 396, pp. 341–351, 2005.
- Kammer, C., *Aluminium Taschenbuch*, Volume 1, 16th edition, Aluminium-Verlag Marketing & Kommunikation GmbH, Düsseldorf, 2009.
- Kayser, T., Klusemann, B., Lambers, H. G., Maier, H. J., Svendsen, B., Characterization of grain microstructure development in the aluminum alloy EN AW-6060 during extrusion, *Materials Science and Engineering: A*, Volume 527, pp. 6568–6573, 2010.
- Kayser, T., Parvizian, F., Klusemann, B., Svendsen, B., Experimental and theoretical investigation of the microstructural evolution in aluminium alloys during extrusion, in *Computational Methods and Experiments in Materials Characterisation IV*, 209–216, New Forest, UK, 2009.
- Kayser, T., Parvizian, F., Svendsen, B., Experimental and theoretical investigation on the microstructure of aluminum alloys during extrusion, *PAMM*, Volume 8, pp. 10431–10432, 2008.
- Kim, S. W., Kim, D. Y., Kim, W. G., Woo, K. D., The study on characteristics of heat treatment of the direct squeeze cast 7075 wrought Al alloy, *Materials Science and Engineering: A*, Volume 304-306, pp. 721–726, 2001.
- Kocks, U. F., A statistical theory of flow stress and work-hardening, *Philosophical Magazine*, Volume 13, pp. 541–566, 1966.
- Kraska, M., *Textursimulation bei großen inelastischen Verformungen mit der Technik des repräsentativen Volumenelements (RVE)*, PhD thesis, Technische Universität Berlin, Berlin, 1998.
- Krill III, C. E., Chen, L. Q., Computer simulation of 3-D grain growth using a phase-field model, *Acta Materialia*, Volume 50, pp. 3059–3075, 2002.
- Kumar, M., Schuh, C. A., Preface to the viewpoint set on grain boundary engineering, *Scripta Materialia*, Volume 54, pp. 961–962, 2006.
- Kunze, K., Wright, S. I., Adams, B. L., Dingley, D. J., Advances in automatic EBSD single orientation measurements, *Textures and Microstructures*, Volume 20, pp. 41–45, 1993.

- Langer, S. A., Fuller, E. R., Carter, W. C., OOF: An Image-Based Finite-Element Analysis of Material Microstructures, *Computing in Science and Engineering*, Volume 3, pp. 15–23, 2001.
- Li, S., Engler, O., Houtte, P. V., Plastic anisotropy and texture evolution during tensile testing of extruded aluminium profiles, *Modelling and Simulation in Materials Science and Engineering*, Volume 13, pp. 783–795, 2005.
- Lide, D. R. (editor), *CRC Handbook of Chemistry and Physics*, 90th edition, CRC Press/Taylor and Francis, Boca Raton, FL, 2010.
- Liu, Y., Baudin, T., Penelle, R., Simulation of normal grain growth by cellular automata, *Scripta Materialia*, Volume 34, pp. 1679–1683, 1996.
- Mackenzie, J. K., Second paper on statistics associated with the random disorientation of cubes, *Biometrika*, Volume 45, pp. 229–240, 1958.
- Marioara, C. D., Andersen, S. J., Jansen, J., Zandbergen, H. W., Atomic model for GP-zones in a 6082 Al-Mg-Si system, *Acta Materialia*, Volume 49, pp. 321–328, 2001.
- McQueen, H. J., Dynamic Recovery and Recrystallization, in Buschow, K. H. J., Cahn, R. W., Flemings, M. C., Ilschner, B., Kramer, E. J., Mahajan, S., Veyssi re, P. (editors), *Encyclopedia of Materials: Science and Technology*, 2375 – 2381, Elsevier, Oxford, 2001.
- McQueen, H. J., Development of dynamic recrystallization theory, *Materials Science and Engineering A*, Volume 387-389, pp. 203–208, 2004.
- McQueen, H. J., Blum, W., Dynamic recovery: sufficient mechanism in the hot deformation of Al (<99.99), *Materials Science and Engineering A*, Volume 290, pp. 95–107, 2000.
- McQueen, H. J., Celliers, O. C., Application of hot workability studies to extrusion processing: Part II. Microstructural development and extrusion of Al, Al-Mg, and Al-Mg-Mn Alloys, *Canadian Metallurgical Quarterly*, Volume 35, pp. 305–319, 1996.
- McQueen, H. J., Imbert, C. A. C., Dynamic recrystallization: plasticity enhancing structural development, *Journal of Alloys and Compounds*, Volume 378, pp. 35–43, 2004.
- McQueen, H. J., Kassner, M. E., Comments on 'a model of continuous dynamic recrystallization' proposed for aluminum, *Scripta Materialia*, Volume 51, pp. 461–465, 2004.
- Miao, W. F., Laughlin, D. E., Precipitation hardening in aluminum alloy 6022, *Scripta Materialia*, Volume 40, pp. 873–878, 1999.
- Miodownik, M. A., A review of microstructural computer models used to simulate grain growth and recrystallisation in aluminium alloys, *Journal of Light Metals*, Volume 2, pp. 125–135, 2002.
- Misiolek, W. Z., Kelly, R. D., Dead Metal Zones in Extrusion of Complex Shapes, in *Proceedings of the 5th International Aluminum Extrusion Technology Seminar ET'92*, Volume I, Volume I, pp. 315–318, Chicago, IL, 1992.
- Myhr, O., Grong,  ., Fj er, H., Marioara, C., Modelling of the microstructure and strength evolution in Al-Mg-Si alloys during multistage thermal processing, *Acta Materialia*, Volume 52,

- pp. 4997–5008, 2004.
- Myhr, O. R., Grong, Ø., Andersen, S. J., Modelling of the age hardening behaviour of Al-Mg-Si alloys, *Acta Materialia*, Volume 49, pp. 65–75, 2001.
- Nishikawa, S., Kikuchi, S., Diffraction of Cathode Rays by Mica, *Nature*, Volume 121, pp. 1019–1020, 1928.
- Owen, G., Randle, V., On the role of iterative processing in grain boundary engineering, *Scripta Materialia*, Volume 55, pp. 959–962, 2006.
- Park, J., Ardell, A., Precipitation at grain boundaries in the commercial alloy Al 7075, *Acta Metallurgica*, Volume 34, pp. 2399–2409, 1986.
- Parvizian, F., Güzel, A., Jäger, A., Lambers, H., Svendsen, B., Tekkaya, A., Maier, H., Modeling of dynamic microstructure evolution of EN AW-6082 alloy during hot forward extrusion, *Computational Materials Science*, Volume 50, pp. 1520–1525, 2011.
- Parvizian, F., Kayser, T., Klusemann, B., Svendsen, B., Modelling and simulation of dynamic microstructure evolution of aluminium alloys during thermomechanically coupled extrusion process, *International Journal of Material Forming*, Volume 3, pp. 363–366, 2010a.
- Parvizian, F., Kayser, T., Svendsen, B., Modelling and Simulation of Dynamic Microstructure Evolution of Aluminium Alloys during Hot Forming Processes, in *Proceedings of the 13th International Conference on Metal Forming*, 422–425, Steel research international, Toyohashi, Japan, 2010b.
- Peng, Z., Sheppard, T., Individual influence of forming parameters on surface recrystallization during aluminium extrusion, *Modelling and Simulation in Materials Science and Engineering*, Volume 12, pp. 43–57, 2004a.
- Peng, Z., Sheppard, T., Prediction of Static Recrystallisation after Extrusion of Shaped Aluminium Sections, *Materials Science Forum*, Volume 467-470, pp. 407–420, 2004b.
- Petch, N., The cleavage strength of polycrystals, *Journal of Iron and Steel Institute*, Volume 174, pp. 25–28, 1953.
- Pospiech, J., Lücke, K., Sztwiertnia, K., Orientation distribution and orientation correlation functions for description of microstructures, *Acta Metallurgica et Materialia*, Volume 41, pp. 305–321, 1993.
- Randle, V., Recent Developments in Electron Backscatter Diffraction, in *Advances in imaging and electron physics*, 1st edition, 363–416, Elsevier, Oxford, GB, 2008.
- Randle, V., Electron backscatter diffraction: Strategies for reliable data acquisition and processing, *Materials Characterization*, Volume 60, pp. 913–922, 2009.
- Randle, V., Engler, O., Introduction to Texture Analysis: Macrotecture, Microtexture, and Orientation Mapping, 2nd edition, CRC Press, Boca Raton, FL, 2009.
- Rauch, L., Madej, L., Kusiak, J., Modelling of Microstructure Deformation Based on Digital Material Representation Integrated with Watershed Image Segmentation Algorithm, in *Proceedings of the 13th International Conference on Metal Forming*, Wiley, Toyohashi, Japan,

- 2010.
- Reid, A. C., Langer, S. A., Lua, R. C., Coffman, V. R., Haan, S., García, R. E., Image-based finite element mesh construction for material microstructures, *Computational Materials Science*, Volume 43, pp. 989–999, 2008.
- Rezvanian, O., Zikry, M. A., Rajendran, A. M., Statistically stored, geometrically necessary and grain boundary dislocation densities: microstructural representation and modelling, *Proceedings of the Royal Society A: Mathematical, Physical and Engineering Science*, Volume 463, pp. 2833–2853, 2007.
- Saha, P., *Aluminum extrusion technology*, 1st edition, ASM International, Materials Park, Ohio, 2000.
- Santoro, A., Mighell, A. D., Coincidence-site lattices, *Acta Crystallographica Section A*, Volume 29, pp. 169–175, 1973.
- Schaeben, H., Hielscher, R., Funderberger, J., Potts, D., Prestin, J., Orientation density function-controlled pole probability density function measurements: automated adaptive control of texture goniometers, *Journal of Applied Crystallography*, Volume 40, pp. 570–579, 2007.
- Schikorra, M., Donati, L., Tomesani, L., Tekkaya, A. E., Microstructure analysis of aluminum extrusion: grain size distribution in AA6060, AA6082 and AA7075 alloys, *Journal of Mechanical Science and Technology*, Volume 21, pp. 1445–1451, 2007.
- Schikorra, M., Lambers, H. G., Donati, L., Maier, H. J., Tomesani, L., Tekkaya, A. E., Microstructure Development during Extrusion of AA6060, AA6082 and AA7075 alloys, in *Proceedings of ICTP 2008 (The 9th International Conference on Technology of Plasticity)*, 1471–1477, Gyeongju, Korea, 2008.
- Schuh, C. A., Kumar, M., King, W. E., Analysis of grain boundary networks and their evolution during grain boundary engineering, *Acta Materialia*, Volume 51, pp. 687–700, 2003.
- Schwartz, A. J., Kumar, M., Adams, B. L. (editors), *Electron Backscatter Diffraction in Materials Science*, 1st edition, Kluwer Academic/Plenum Publishers, New York, 2000.
- Schwartz, A. J., Kumar, M., Field, D. P., Adams, B. L. (editors), *Electron Backscatter Diffraction in Materials Science*, 2nd edition, Springer Science+Business Media, New York, 2009.
- Shackelford, J. F., *Introduction to materials science for engineers*, 7th edition, Prentice Hall, Upper Saddle River, NJ, 2009.
- Sheppard, T., *Extrusion of aluminium alloys*, 1st edition, Springer, Berlin, 1999.
- St-Pierre, L., Héripéré, E., Dexet, M., Crépin, J., Bertolino, G., Bilger, N., 3D simulations of microstructure and comparison with experimental microstructure coming from O.I.M analysis, *International Journal of Plasticity*, Volume 24, pp. 1516–1532, 2008.
- Svensen, B., Kayser, T., Parvizian, F., Characterization of the microstructural development in aluminum alloys during extrusion and cooling., in *Steinhoff, K., Maier, H. J., Biermann, D. (editors), Functionally graded materials in industrial mass production*, 211–219, Verlag

Wissenschaftliche Scripten, Auerbach, 2009.

- Trogolo, J. A., Kelly, R. D., Misiolek, W. Z., Use of EBSD Technique for Microstructural Characterization of the Deformation Zone in Aluminum Extrusion, in Proceedings of the 6th International Aluminum Extrusion Technology Seminar ET'96, 217–221, Chicago, IL, 1996.
- Valberg, H., Metal flow in the direct axisymmetric extrusion of aluminium, *Journal of Materials Processing Technology*, Volume 31, pp. 39–55, 1992.
- Vernon-Parry, K., Scanning electron microscopy: an introduction, *III-Vs Review*, Volume 13, pp. 40–44, 2000.
- Wiederkehr, T., Klusemann, B., Gies, D., Müller, H., Svendsen, B., An image morphing method for 3D reconstruction and FE-analysis of pore networks in thermal spray coatings, *Computational Materials Science*, Volume 47, pp. 881–889, 2010.
- Wilkinson, A. J., Hirsch, P. B., Electron diffraction based techniques in scanning electron microscopy of bulk materials, *Micron*, Volume 28, pp. 279–308, 1997.
- Wright, S. I., Fundamentals of Automated EBSD, in *Electron Backscatter Diffraction in Materials Science*, 1st edition, 51–63, Kluwer Academic/Plenum Publishers, New York, 2000.
- Wright, S. I., Adams, B. L., Automatic analysis of electron backscatter diffraction patterns, *Metallurgical Transactions A*, Volume 23, pp. 759–767, 1992.
- Wright, S. I., Adams, B. L., Kunze, K., Application of a new automatic lattice orientation measurement technique to polycrystalline aluminum, *Materials Science and Engineering: A*, Volume 160, pp. 229–240, 1993.
- Wright, S. I., Field, D. P., Dingley, D. J., Advanced software capabilities of automated EBSD, in *Electron Backscatter Diffraction in Materials Science*, 1st edition, 141–152, Kluwer Academic/Plenum Publishers, New York, 2000.

Acknowledgements

The work presented in this thesis has been carried out during my time as a research assistant at the Institute of Mechanics, TU Dortmund University, from 2005 till 2011. It was financially supported by the Deutsche Forschungsgemeinschaft DFG within the transregional research project SFB/TR TRR30. Now I would like to gratefully thank all the people who have supported me and my work in the preceding years.

First and foremost, I would like to express my heartfelt thanks to my academic supervisor Professor Bob Svendsen for his continuous scientific support and seasoned and inspiring guidance. His knowledge in the field of materials science and material modeling has been a great help while preparing my thesis.

Furthermore, I give thanks to Jun.-Professor Alexander Brosius for his interest in my work and for reviewing and commenting on my thesis. I am also grateful to Professor A. Erman Tekkaya for joining my examination committee and to Jun.-Professor Björn Kiefer for presiding as chairman during my defense.

Moreover, I would like to thank my colleagues at the Institute of Mechanics for the friendly atmosphere. Especially, I appreciate my colleague Dr.-Ing. Farhad Parvizian for the fruitful and interesting scientific discussions and for his friendship. I would also like to express my gratitude to Professor Andreas Menzel, Dr.-Ing. Benjamin Klusemann and Dr.-Ing. Christian Hortig for their help on different aspects of my work.

My special thanks go to Mrs. Kerstin Walter for her warm help in every organizational aspect during all the years and to Mrs. Christina McDonagh, Mrs. Christine Vu and Mrs. Daria Walenczyk for their excellent assistance in language correction of this thesis and other publications. And I'm in gratitude to Mr. Matthias Weiss for taking care of every hardware and software issue.

Special thanks also go to the group of Professor Hans Jürgen Maier, especially to Dr. Hans-Gerd Lambers and Mr. Sergej Tschumak, at the Lehrstuhl für Werkstoffkunde (Materials Science) at the University of Paderborn for performing the EBSD measurements. For providing and preparing the specimens my gratitude goes to Dr. Marco Schikorra, Mr. Andreas Jäger and Mr. Ahmet Güzel at the Institute of Forming Technology and Lightweight Construction (IUL) at TU Dortmund University. My thanks are also addressed to my colleagues participating in the TRR30 for the productive discussions and cooperations.

Finally I would particularly like to thank my parents, my brother, my family and all of my friends for supporting my work, each of them in different but very special and personal ways.

Curriculum Vitae

Personal

Name: Tobias Kayser
Date of Birth: September 1, 1978
Place of Birth: Werne, Germany
Nationality: German

Education

1999-2005 TU Dortmund, Diploma studies in mechanical engineering
1989-1998 Städtisches Gymnasium Kamen
1985-1989 Eichendorff-Grundschule, Kamen

Profession

09/2005-onwards Research Assistant, TU Dortmund
Institute of Mechanics (Prof. Dr. rer. nat. B. Svendsen)